NEW METHODS FOR SYNTHESIS OF INORGANIC NANOPARTICLES IN LIPID THIN FILMS AND IN SOLUTION

THESIS SUBMITTED TO

THE UNIVERSITY OF PUNE

FOR THE DEGREE OF

DOCTOR OF PHILOSOPHY

IN

CHEMISTRY

BY

S. Shiv Shankar

PHYSICAL & MATERIALS CHEMISTRY DIVISION

NATIONAL CHEMICAL LABORATORY

PUNE 411 008

INDIA

November 2005

Dedicated to my parents,
brother and teachers

DECLARATION

I hereby declare that the thesis entitled **"NEW METHODS FOR SYNTHESIS OF INORGANIC NANOPARTICLES IN LIPID THIN FILMS AND IN SOLUTION"** submitted for the degree of Doctor of Philosophy in Chemistry to the University of Pune, has been carried out by me at the Physical Chemistry Division of National Chemical Laboratory, Pune under the supervision of Dr. Murali Sastry. Such material as has been obtained by other sources has been duly acknowledged in this thesis. The work is original and has not been submitted in part or full by me for any other degree or diploma to other University.

Date: S. SHIV SHANKAR

Place: Pune (Research Student)

Acknowledgements

It is my great pleasure to take this as an opportunity to thank all the people because of whom this PhD thesis was possible.

I express my heartfelt gratitude and sincere thanks to Dr. Murali Sastry for introducing me to the field of nanoscience and providing me with an opportunity and resources to work under his valuable guidance. His ceaseless enthusiasm, resourcefulness, ingenuity in research and his constant motivation, support and constructive criticism have made a profound influence on me. It has been my great pleasure for being a part of his group and to work under such a close association with him. I owe him a lot for giving me a stable ground in all his capabilities and for the care he has shown towards me.

My special thanks to Dr. B. L. V. Prasad, especially for helping me out of the way by spending his valuable time in correcting and giving me important suggestions for compiling this thesis. I once again thank him along with Ms. Suguna Adyantaya and Dr. Poddar for their constant encouragement, support and their elderly advise thinking about my betterment.

My special thanks to Dr. Absar Ahmad from the Biochemical Sciences Division for his major contributions in plant extract based synthesis of metal nanoparticles. I thank him for his moral support and for facilitating all requirements as an eminent collaborator and scientist.

My sincere thanks to Ms. Renu Pasricha for helping me out with the transmission electron microscopy characterization at any odd time, giving me valuable training on using the instrument and for her caring gestures. I also like to take this opportunity to thank Dr. Sainkar, Dr. A. B. Mandale, Dr. Ms. Neela Pavasakar, Dr. Patil and Mr. Gaikwad of Center for Material Characterization for their help in different materials characterizations. Without their help progress of the work presented in this thesis was unimaginable.

My special thanks to Prof. G. U. Kulkarni of JNCASR, Bangalore and Dr. Satyam from IOP, Bhubaneswar for their kind willingness to make us available the HRTEM facility.

I thank Drs. Anand, Ashavani, Debabrata, Sumant, Saikat, Anita, Mr. Styanarayana and Kannan who readily extended their support to me as senior and fellow group members by helping me in all possible ways. I thank them for extending their friendly gesture and

providing me their great company at all times of need to make me feel very comfortable in this group.

I am thankful to Dr. Senthil, Dr. Jaspreet, Dr. Madhukumar and Dr. Vidya for their support in all possible ways and for showing their willingness to help me at all times of need.

My special thanks to fellow labmates, Hrushikesh, Ambarish, Akhilesh, Tanushree, Amit, Atul, Vipul, Sourabh, Deepti, Prathap, Sanjay, Minakshi and Mansi for always standing by my side and sharing a great relationship as compassionate friends. I will always cherish the warmth shown by them. I sincerely thank them for putting their efforts in correcting this thesis, many a times by keeping their own work aside. I especially thank Vipul, Amit and Sourabh for their valuable contribution in this regard.

My sincere thanks to Akhilesh, Amit and Dr. Ankamwar who were involved together with me in some crucial experiments. Their constant help and valuable contributions are greatly acknowledged.

My sincere thanks to Dr. Ms. S. P. Joshi who greatly helped us in carrying out the fractionation of the lemongrass leaf extract.

My special thanks to Mr. Jagdish and Mr. Santosh of University of Pune for their kind efforts to help in carrying out the irradiation experiments at any possible time.

My special thanks to Sayendev, Umesh, and Bapu who were associated with me for different periods in some very fruitful experiments and were of very kind and helping nature. I express my sincere thanks to some of the project students, Ajay, Amol, Anuja, Chinmay, Kaustav and Ganesh who have helped me in some or other way in the day to day research work.

I express my sincere thanks to Dr. K. N. Ganesh and Praveen for their out of the way help in carrying out the isothermal calorimetry experiments at all necessary stages of experiments.

My special thanks to the former Director, NCL, Dr. Paul Ratnaswamy and Present Director, Dr. S. Sivaram and to the former and present Heads of the Physical and Materials chemistry division Dr. P. Ganguly, Dr. S. K. Date and Dr. S. Pal, the for giving me an opportunity to work in this laboratory and maiking all facilities available for the pursued research.

I acknowledge the HRDG CSIR for providing me with the necessary funding and fellowship continue research in NCL. I am also grateful to HRDG CSIR for providing me with the necessary funding for attending an international conference in Germany.

I am grateful to my friends Santosh, Pushkar, Sumita, Janmajoy, Veena, Gagan, Shashi, Shubhenu, Ramaraju and Minita who have always believed in me and were an inspiration for me.

I am grateful to my friends, Manish, Sushim, Sreekant, Sameer, Ambrish, Dr. Joly, Rajshankar, Girish, Sanjay, Bhalchandar, Shekhar, Sasanka, Sneha, Prashant, Sarvesh, Govindraju, Gourishankar and Praveen from NCL who helped me in every possible way and cooperated at all times.

My special regards to many teachers because of whose teaching at different stages of education has made it possible for me to see this day. My special thanks to Dr. Ms. Sangeeta, who was my chemistry tutor, to my physics tutor, because of whose kindness I feel, was able to reach a stage where I could write this thesis.

My special regards to Dr. Mohan Bhadbhade, Dr. D. Srinivas, and Dr. S. B. Halligudi and their families who have always comforted me and helped me like a guardian.

At this moment and always, I pay my respectful regards to my beloved parents, who are for me, as is said in Sanskrit, Matrudevobhava pitrudevobhava. I express my deep affection and love to my late younger brother Raghu who would have duly cherished to see this thesis. I can still feel his presence.

S. Shiv Shanakar

CERTIFICATE

This is to certify that the work presented in the thesis entitled **"NEW METHODS FOR SYNTHESIS OF INORGANIC NANOPARTICLES IN LIPID THIN FILMS AND IN SOLUTION"** by **S. SHIV SHANKAR**, for the degree of Doctor of Philosophy in Chemistry was carried out under my supervision at the Physical Chemistry Division of National Chemical Laboratory, Pune. Such material as has been obtained by other sources has been duly acknowledged in this thesis. To the best of my knowledge, the present work or any part thereof, has not been submitted to any other University for the award of any other degree or diploma.

Date: Dr. MURALI SASTRY

Place: Pune (Research Guide)

Table of Contents

Chapter I

Introduction

This chapter is an introduction to the thesis and gives a brief overview about the interest in biological synthesis of nanomaterials that includes bioinorganic materials in naturally occurring systems as well as their recent application for deliberated synthesis of nanomaterials. It also discusses the various reported strategies used for the synthesis of anisotropic shaped metal nanoparticles and for the fabrication of nanoparticulate thin films of inorganic materials.

1.1 Introduction.

Nature has elegant and ingenious ways of creating the most efficient miniaturized functional materials. Recent spur in the interest towards nanoscience and nanotechnology by various researchers is due to the restless attempts to create functional miniaturized structures the nature's way. Richard Feynaman first propounded this concept in his seminal speech "There's plenty of room at the bottom" [1]. In attempts to create miniaturized structures, significant achievements have been achieved and structures of micron and nanodimensions can now be routinely fabricated (Figure 1.1) though the complexity manifested by the nature is yet a distant goal. To achieve this goal,

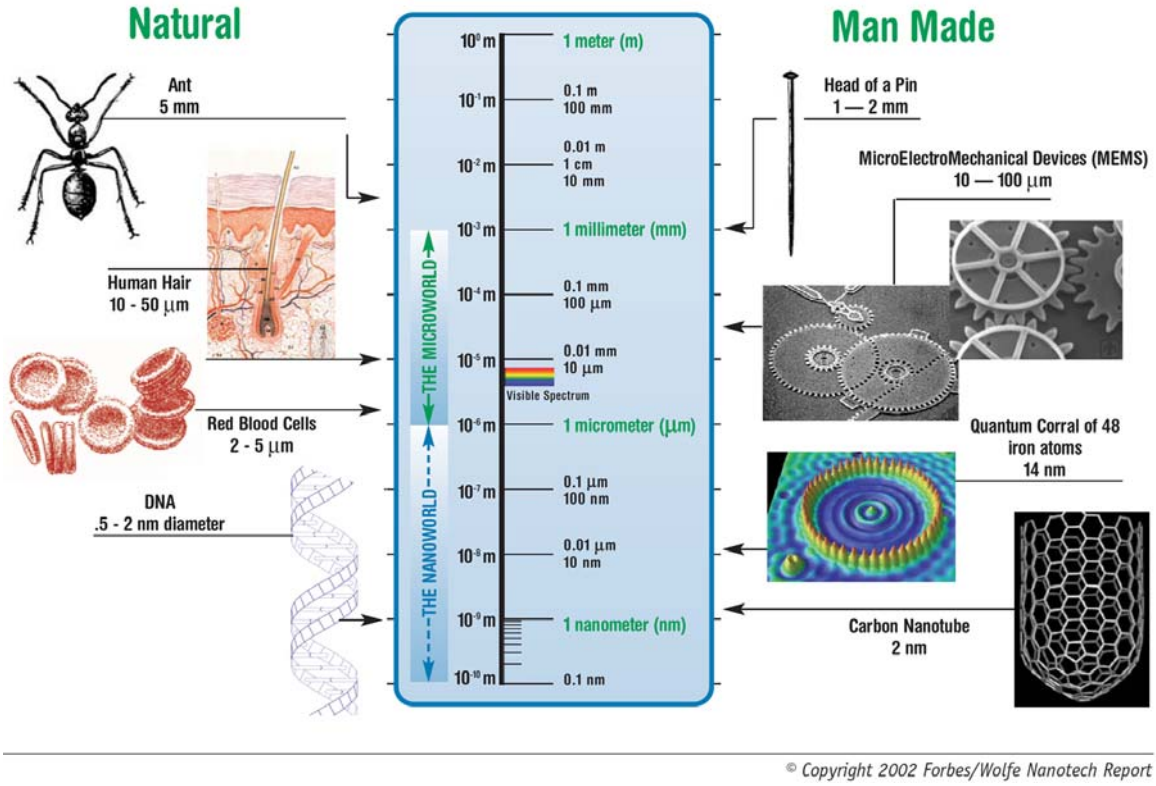

Figure 1.1: *Picture representing the relative sizes of various naturally occurring objects/species and man-made materials. Courtesy: Josh Wolfe's report on Nanotechnology, www.forbeswolfe.com.*

researchers are trying to follow both: "top down" and "bottom up" approach (Figure 1.2). Of these, top down approach can be considered as an approach with which the human race first learned to fabricate materials and in the course of time has perfected this art by being able to realize structures of submicron level. In attempts to create miniaturized materials it has been realized that materials in nanodimensions may exhibit properties

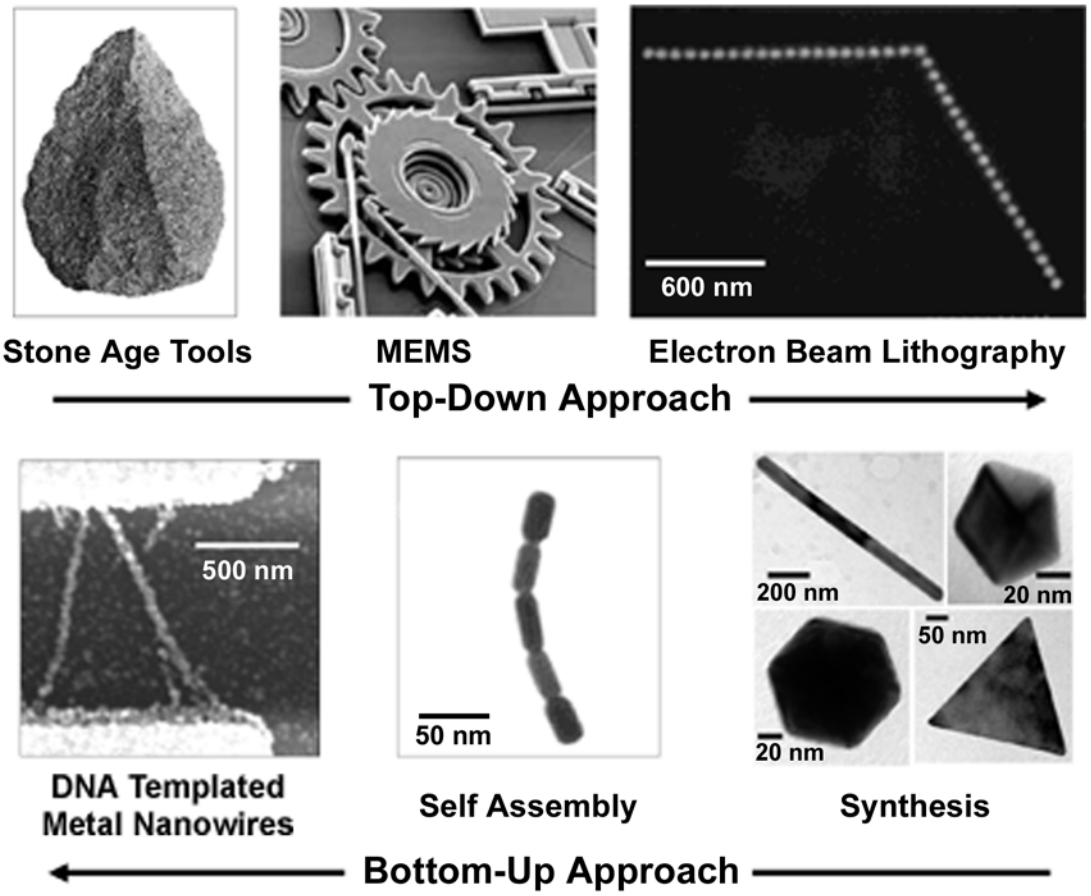

Figure 1.2: E*xamples that depict the fabrication of materials by the Top-down and Bottom-up approaches. Courtesy: Sandia National Laboratories (SUMMiT™ Technologies, www.mems.sandia.gov), Ref. 12a, Ref. 42d and Ref. 12a for the images of MEMS, electron beam lithography, DNA Templated metal nanowires and nanorod self-assembly, respectively.*

very different to their bulk counterparts. Increasing knowledge about the unique properties of nanoparticles has lead to renewed interest in them for potential applications. One of the oldest applications was the use of gold nanoparticles for staining glasses; a famous example is the Lycurgus cup that dates back to 4th century AD [2]. Around 17th century AD, colloidal solutions of gold nanoparticles started gaining importance for their supposed curative values [3]. In the present age, the applications of nanoparticles extend to wide-ranging areas such as catalysis [4], biosensors [5], diagnostics [6], cell labeling [7], solar cells [8], fuel cells [9], photonic bandgap materials [10], single electron transistors [11], nonlinear-optical devices [12] and surface enhanced Raman spectroscopy [13]. The realization of their various potential applications is only limited by our imagination [14].

An interesting aspect of nanomaterials is that a number of factors can influence their physical, chemical, optical, magnetic and electronic properties. The factors that can strongly modulate their properties include their size [15], shape [16], surface composition [17], dielectric environment of the particle [18] and the interparticle interactions [19]. The reasons for such remarkable variations are because of their dimensions comparable to the de Broglie wavelength of the charge carries and their high surface to volume ratio [20]. One of the readily perceptible properties in case of metal nanoparticles is their color. The color of metal nanoparticles originates from surface plasmons i.e., the coherent charge density oscillations [21]. The excitation of the surface plasmons by an electromagnetic field at an incident wavelength where resonance occurs results in strong light scattering, in the appearance of intense surface plasmon resonance (SPR) bands, and an enhancement of local electromagnetic fields [22]. When the size of the metal nanoparticles are below certain size, e.g., < 3 nm for gold nanoparticles, the size quantization effects become more important leading to discrete energy levels in the conduction band and can be understood by making analogy with the case of particle-in-box model [23]. The SPR band starts decreasing in intensity with the size of nanoparticles in this regime because of the increasing surface scattering of the delocalized electrons [24]. The quantum size effects have been better studied in case of semiconducting nanoparticles and the energy level spacing for a spherical particle is predicted to be inversely proportional to R^2 [25]. Thus, with decreasing size, the effective bandgap increases and the relevant absorption and emission spectra blue-shifts.

Apart from the optical properties, a beneficial consequence of the size of the nanoparticles is that they lead to a large increase in the surface to volume ratio of the corresponding material compared to their bulk counter parts. Greater availability of the surface facilitates better catalysis per unit amount of the catalyst [4b]. However, a further interesting consequence of the size of the nanoparticles is that, below a certain size limit, some of the nanoparticles start showing catalytic activity that is not demonstrated by their bulk counterparts [4b]. In fact, catalytic activities of some of the nanoparticles have also been demonstrated to be dependent on the shape of the nanoparticles. Similarly, size of the nanoparticles is also observed to significantly influence their melting point [15h], magnetic properties [15i] and even the lattice structure [15j,k].

The display of unique properties by the nanoparticles that can be controlled by many external and internal factors and the scope for diverse application makes it very predictable that the synthesis of such nanomaterials is equally important. Recorded methods for the synthesis of aqueous dispersion of gold existed since the beginning of 17^{th} century [3] and the awareness that the gold was present in a form that is not visible to the human eye also existed. However, Michael Faraday is considered to be the first to chemically synthesize aqueous colloidal gold solution with conscious efforts by reducing aqueous chloroaurate ion ($AuCl_4^-$) using phosphorus dispersed in CS_2 [26]. Though sols of aqueous dispersed particles have been in use since time immemorial, the term "Colloid" was first coined by Thomas Graham (1861) for suspended particles in liquid medium [27] and was categorized to be in the size range 1 nm to few μm. During recent rapid developments in this field, the term colloid has been alternatively replaced by nanoparticles to describe particles with size typically in the range 1 – 100 nm after introduction of the term "Nanotechnology" by Norio Taniguchi [28]. With increasing importance and applications of nanomaterials a number of physical and chemical routes for their synthesis has been reported and can be broadly classified as shown in Scheme 1.1.

In recent times, synthesis of inorganic nanoparticles has been demonstrated by many physical and chemical means. Some of the physical routes leading to successful synthesis of nanoparticles were achieved through photoirradiation [29], radiolysis [30], ultrasonication [31], physical vaporization, spray pyrolysis, solvated metal atom dispersion (SMAD) [32], chemical vaporization [33] and electrochemical [34] methods. However, chemical methods for synthesis of inorganic nanoparticles have received wide acceptance and are the most commonly followed route. Chemically, inorganic nanoparticles such as metal, metal oxide and semiconducting nanoparticles can be synthesized by reduction or oxidation of metal ions or by precipitation of the necessary precursor ions in solution phase. The control of size, shape, stability and the assembly of nanoparticles are achieved by incorporating different capping agents, solvents and templates. Capping agents that have been used range from simple ions to polymeric molecules and even biomolecules [35]. As a solvent, though water is largely used, organic solvents are preferred many times as non-aqueous solvent [36] and in few reports

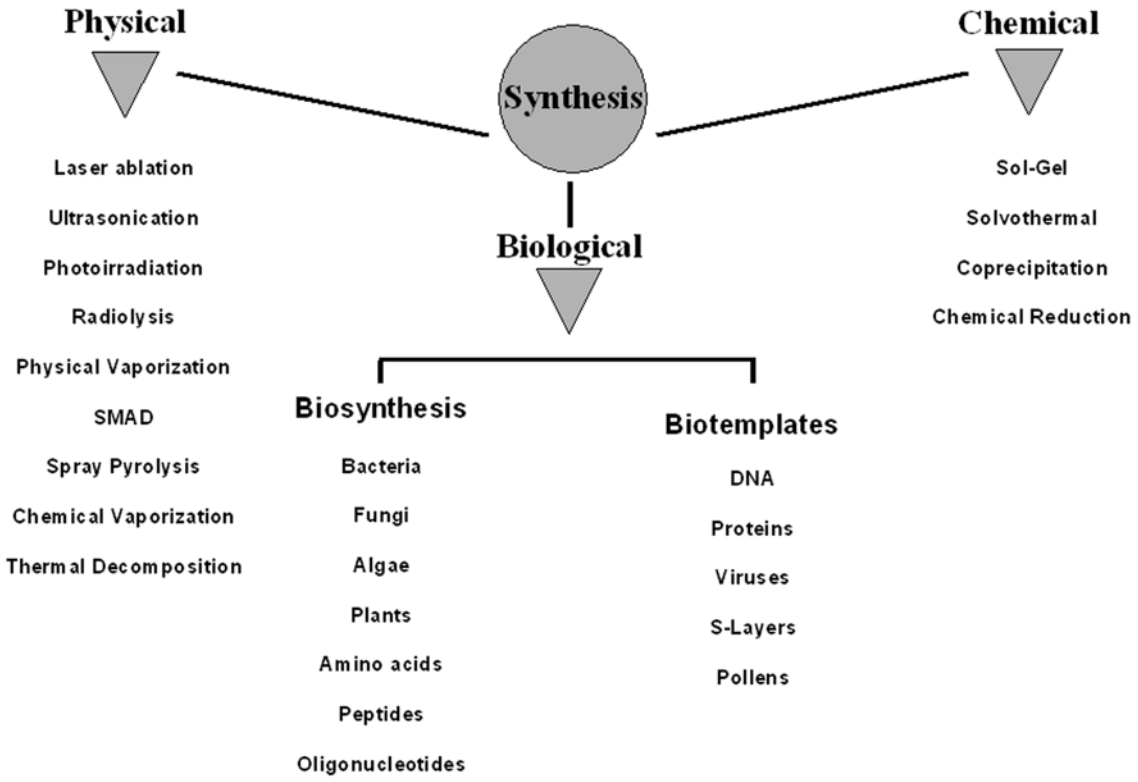

Scheme 1.1: *Schematic outlining the various approaches for the synthesis of nanoparticles.*

use of solvents such as ionic liquids [37] and supercritical fluids [38] have also been demonstrated. Similarly, many soft and rigid templates such as micelles [39], polymeric molecules [40], DNA [41], Tobacco Mosaic Virus [42], mesoporous materials and many more including the use of preformed nanoparticles [43], have been employed in order to gain control over the formation and assembly of nanoparticles.

Evidently, synthesis of nanoparticles has gained due focus and the scope for new synthetic methods have been constantly increasing with innovative contributions. Though the synthesis protocols have been largely dominated by chemical and physical methods, more recently, a part of the focus has also been on the advantageous use of biological means for nanoparticles synthesis. Yet another field of focus in nanotechnology has been the fabrication of nanoparticulate thin films. In the following sections of this chapter, brief introductions to i) various biological methods used for the synthesis of nanoparticles, ii) shape controlled synthesis of metal nanoparticles and iii) various methods used for fabrication of nanoparticulate thin films have been presented.

1.2 Biological Means for Synthesizing Nanomaterials.

The way biological systems fabricate structural and functional inorganic materials with precise dimensions and controlled morphology in a reproducible manner and above all in an environment nurturing manner, defies any possible description. These very basic features have lured the nanotechnologists towards these biological systems to learn and improve the skills for precise fabrication of nanomaterials. There exist several examples in biological systems demonstrating not only the efficient synthesis of macro materials like bones and teeth with precise positioning but also in making functional structures in the micro- and nanodimensions. The examples being, the eye-catching siliceous structures by diatoms and radiolarians [44] and calcareous structures synthesized by the coccoliths [45] in micro dimensions and the synthesis of aligned magnetite nanoparticles in magnetotactic bacteria [46]. The confinement of mineralization of silica and calcium carbonate leading to the various porous shell or aligned structures have been explained to be directed by the geometric patterning of the vesicles in the cells [47]. Mechanistically, biosilicification has been proposed be facilitated by polycationic peptides such as silaffins [48] and silicateins [49] in case of mineralization in diatoms and sponges respectively, and few other peptides such as frustulins [50] and pleuralins (formerly known as HF-extracted proteins, or HEPs) [51] have also been identified to play crucial role. Silaffins and silicateins were demonstrated to induce the formation of silica by hydrolyzing the dissolved silicic acid [52]. Calcite crystals mineralized by holococcoliths are generally extracellular and of simple rhombohedral or prismatic forms [53], whereas, in heterococcoliths the morphologies are quite complex and species specific occurring intracellularly [54]. Little is known regarding the molecular mechanism responsible for the transport of Ca^{2+} ions and HCO_3^- or CO_3^{2-} ions required for the calcite mineralization. It has been shown that the calcite minerals are coated with polyanions and some acidic polysaccharides [55]. Thorough research has been carried out in the identification of the formation of magnetic nanoparticles within bacteria. In naturally occurring magnetotactic bacteria both magnetite (Fe_3O_4) and greigite (Fe_3S_4) nanoparticles have been observed [56]. In fact, magnetite nanoparticles have been found in unicellular eukaryotic organisms such as Euglena algae [57], dinoflagellates [58] as

well as in higher species such as salmon [59], trout [60], carrier pigeons [61], army ants [62] and also in human brain [63]. In magnetotactic bacteria the magnetite nanoparticles are arranged linearly, surrounded by specific phospholipid membrane and are thus called magnetosomes [64]. The crystal morphologies found in the magnetotactic bacteria have been classified as cubooctahedral, pseudohexagonal and bullet shaped all having the cubic face-centered crystal lattice of magnetite [65]. In the mineralization of magnetite, it was shown that iron ions are taken up as Fe^{3+} ions and reduced to Fe^{2+} ions by the *soluble* and *cytoplamic* ferrireductase [66]. The oxidation of Fe^{2+} ions was attributed to a nitrite reductase, a cytochrome cd_1, in the periplasma that uses nitrate as electron acceptor [66]. The magnetite crystals in the magnetotactic bacteria are typically of size 30 – 120 nm with a permanent dipole moment that is large enough to align themselves in the Earth's magnetic field of 50 μT, overcoming the thermal forces [67]. In most cases the accumulated iron content in the magnetotactic bacteria is observed to be in the range 3 – 10 % of the dry biomass of the bacteria [68]. Similarly, bimineralization of MnO_2, gypsum ($CaSO_4$) and $CaCO_3$ is known to form on the S Layer of photosynthetic bateria [69] and the occurrence of nanocrystalline zinc-iron sulphide within tubes of hydrothermal vent worms, *Alvinella pompejana* [70].

While there exist a number of examples on the natural occurrence of biominerals, microorganisms have also been induced to synthesize biominerals and semiconducting or metal nanoparticles. This route for synthesis for nanoparticles was sought for because of the ability of microorganism to cope with high metal ion concentration through specific resistance mechanisms. The typical resistance mechanisms include: efflux systems; alteration of solubility and toxicity by changes in the redox state of the metal ions; extracellular complexation or precipitation of metals; and lack of specific metal transport systems [71]. The ability of the microorganisms to interact with heavy metal ions in such a manner has been utilized to tackle one of the current major environmental issues of detoxifying contaminated areas through bioremediation [72]. On the other hand, the metal accumulating ability of the microorganisms has also been proposed for industrial recovery of metals [73]. More recently, materials scientists have looked upon the detoxification of metal ions occurring by their reduction or sulphide formation with interest for the possible use of microoraginsms as eco-friendly nanofactories. Beveridge

and co-workers have demonstrated the synthesis of gold nanoparticles within the cell walls of the bacteria, *Bacillus subtilis* on incubation with Au^{3+} ions [74]. The deposition is supposed to occur first by a stoichiometric interaction between soluble metal ions and the reactive chemical groups of the cell wall followed by their nucleation in elemental form leading to further deposition of the metal in non-stoichiometric amounts. Tanja Klaus and co-workers using the bacteria, *Pseudomonas stutzeri* AG259 isolated from a silver mine, demonstrated the intracellular synthesis of silver nanoparticles. The silver nanoparticles of distinct shape and size were observed to grow within the periplasmic space, i.e., between the cell wall and the plasma membrane of the bacteria when cultured in presence of $AgNO_3$ [75]. The produced silver was reported to be 5 % of the total bacterial dry mass. Further, they have demonstrated that these nanoparticles after isolation and film formation on aluminum substrates followed by heat treatment could make materials with typical cermet properties [76]. These materials with interesting optical properties prepared by convenient low-cost method have been proposed to have technical application as coatings for efficient photothermal conversion of solar energy. Similarly, Nair and Pradeep by exposing the *Lactobacillus* strains isolated from buttermilk to gold and silver ions, showed the formation of gold, silver and gold-silver alloy nanoparticles [77]. The extent of metal deposited in them was reported to be 35 % of dry bacterial biomass. In an attempt to make the biological synthesis route competent with the chemical routes of synthesis, it was shown by Sastry and co-workers that a fair degree of mondisperse gold nanoparticles could be synthesized using the extremophilic actinomycete, *Thermomonospora* sp. [78]. Apart from metal nanoparticles, bacteria and yeast have been used for the synthesis of semiconducting nanoparticles such as ZnS [79], CdS [80] and PbS [81]. Holmes and co-workers [82] have shown that the bacterium, *Klebsiella aerogenes* when exposed to Cd^{2+} ions resulted in the intracellular formation of CdS nanoparticles in the size range 20–200 nm. Kowshik *et al*. [83] have shown that CdS quantum dots synthesized intracellularly in *Schizosaccharomyces pombe* yeast cells exhibit ideal diode characteristics. Kowshik and co-workers have also demonstrated the biological synthesis of PbS on exposing the yeast, *Torulopsis* sp. to aqueous Pb^{2+} ions [81].

Sastry and co-workers have demonstrated that other than prokaryotic microorganisms such as bacteria, fungi (eucaryotic) can also play efficient role as living nanofactories for the synthesis of nanomaterials. In their reports, using *Verticillium* sp. [84] and *Fusarium oxysporum* [85], synthesis of gold and silver nanoparticles was shown by the biological reduction of gold and silver ions. While the bioreduction of the metal ions in case of *Verticillium* sp. was observed to be intracellular, *Fusarium oxysporum* were shown to be capable of carrying out the bioreduction extracellularly. The advantage with the extracellular synthesis of nanoparticles is that, the nanoparticles can be readily isolated and the microorganism can be reused for further synthesis. Later, it was demonstrated that gold-silver alloy nanoparticles with varying composition could also be synthesized using *Fusarium oxysporum* [86]. Further, it has been shown that *Fusarium oxysporum* were also capable of synthesizing CdS nanoparticles on exposure to aqueous $CdSO_4$ solution by enzymatic reduction of the sulfate ions to sulphide ions [87].

From the above discussion it is evident that the synthesis of nanomaterials through biological route is largely focused on the use of microorganisms only. However, it is interesting to know that even plants are capable of biomineralizing many inorganic materials [88]. The most common and widely distributed biominerals in plants are especially calcium oxalates, calcium carbonates and silicon dioxides [89]. Such mineral accumulation is common in Cactaceae species in which all the three above-mentioned minerals can be found. In certain plants of the Cactaceae family silica in the form of α-quartz or opal is also found to be present [90]. Silica is also known to present in grasses [91]. Apart from these minerals, presence of nanocrystalline botanical magnetite in iron-rich extracts from disrupted grass cells has also been reported [92]. The majority of the magnetite nanocrystals extracted from the grass plants were reported to be of cubo-octahedral shapes, with a minority of hexagonal prism morphologies [92]. In addition to the constrained morphologies, each group was observed to have a narrow size distribution typical of intracellular-boundary organized biomineralization processes responsible for bacterial magnetite. The smallest cubo-octahedral botanical nanocrystals (4 ± 1 nm) were an order of magnitude smaller than their bacterial counterparts [92]. The botanical magnetite nanocrystals in plants are self-organized in ordered, micrometer-sized agglomerates [92], distinct from the linear chain like arrangement of magnetite

crystals in magnetotactic bacteria. Similar to bacteria, plants are also known to hyperaccumulate heavy metal ions within them and have thus been looked upon as means for phytoremediation of toxic metal ions to decontaminate polluted soil [93]. A number of plants have been reported to accumulate of gold in large percentage within them, one of them being the plant, *Equisetum* (horsetail) [94]. It has been proposed that plant secretions may aid the uptake of gold from the soil and that cyanide, in particular might render gold sufficiently soluble to enable plants to accumulate the metal. A number of plants have been reported to produce free cyanide by hydrolysis of cyanogenic glycosides within their tissues [95]. Macerated tissues of cyanogenic plants have been demonstrated to facilitate the uptake of gold in plants [96].

With such possibilities it would thus be interesting to explore plants as a means for synthesizing metal nanoparticles analogous to the use of microorganisms for their synthesis. Indeed, Jose-Yacaman and co-workers have shown that gold and silver nanoparticles are formed within different parts of live Alfalfa plant on uptaking the corresponding metal ions from solid media [97]. In an attempt to expand the scope of this successful demonstration of biosynthesis of metal nanoparticles, in this thesis studies have been presented demonstrating the synthesis of metal nanoparticles using extracts of different plants. The expected benefits by following this method is that, analogous to the biological synthesis of metal nanoparticles using microorganisms, efficient synthesis can still be achieved in an environmentally benign process. Since the procurement of plant based products are more convenient and can be obtained in large quantities as opposed to maintaining a pure culture of microorganisms in a protected environment, it is likely to be more cost effective with scope for large-scale production. Additionally, it may be noted that while in certain cases the synthesis could be achieved extracellularly, in most cases it was intracellular. When the microorganisms based procedures are followed, another matter of concern in these methods is the low amount of metal nanoparticles, that is usually less than 10 % of the dry biomass, except in case of *Lactobacillus* sp. wherein the amount of metal was reported to be nearly 35 % of the dry biomass as discussed above. These features of the microorganism-based synthesis of metal nanoparticles severely limit their applicability as feasible alternative to chemical approaches for efficient synthesis of nanoparticle. In the present study since extracts of plants are used

for the synthesis of metal nanoparticles, they can be conveniently used as a natural reducing agents alternative to potentially toxic chemical reagents or capital-intensive physical methods. Apart from these benefits, the presence of biomolecular complexing agents in the plant extracts with an ability to interact specifically with the surface of the nanoparticles may also lead to shape controlled synthesis of nanoparticles.

1.3 Shape controlled synthesis of metal nanoparticles.

From synthesis point of view, currently, more attention is being paid towards controlling the shape of the nanoparticles rather than the size of the nanoparticles for which a number of methods already exist. Nanoparticles of many anisotropic shapes such as nanorod/nanowires [98], nanotubes [99], nanodumbbells [100], nanocubes [101], nanohexagons [102], tetrahedrals [103], decahedrons [104], multipods [105], starshaped [106], nanodiscs [107], nanotriangles [108], dendritic shaped [109], etc. have been synthesized. Various strategies have been applied for the controlled synthesis of anisotropic shape metal nanoparticles. The usual methods include: 1) synthesis in micellar/surfactant solutions, 2) synthesis using soft and rigid templates, 2) controlling the growth of the nanoparticles using physical confinements 3) physical processes such as nanosphere lithography, vacuum vapor deposition, 4) direct synthesis in solution in presence or absence of additives and 5) morphological transformations of the preformed nanoparticles by thermal, photoirradiation or ion irradiation process.

1.3.1 Synthesis in micellar solutions:

This method has been the most common method for synthesizing specifically metal nanorods. Synthesis of metal nanorods in presence of surfactants has been demonstrated by electrochemical [110], photochemical [111] or seed-mediated methods [112]. Wang and co-workers demonstrated the synthesis of gold nanorods through an electrochemical method by using gold metal plate as anode and platinum plate as cathode in a micellar solution of hexadecyltrimethylammonium bromide (CTAB) [113]. In this method, the bulk gold metal from the anode was reported to get converted into gold nanoparticles at the interfacial region of the cathodic surface and the electrolytic solution. Esumi et al have shown the synthesis of gold nanorods by photochemical irradiation in a

micellar solution of hexadecyltrimethylammonium chloride (HTAC) [111a]. The formation of elongated gold nanorods instead of spherical nanoparticles was reported to form only when the concentration of HTAC was sufficient for the formation of rodlike micelles in solution. Kim et al have shown similar photochemical synthesis of gold nanorods by using CTAB as a surfactant and were able to both control the aspect ratio of gold nanorods and also improve the percentage of nanorods formed by adding different amounts of $AgNO_3$ [111b]. Murphy and co-workers had earlier demonstrated the effect of the added $AgNO_3$ in controlling the aspect ratio of gold nanorods [112c]. Their synthesis method was based on carrying out the reduction of $AuCl_4^-$ ions in presence of CTAB and preformed spherical nanoparticles as seeds [112]. For the reduction process, ascorbic acid was used specifically because it reduces $AuCl_4^-$ ions to Au^0 state in presence of CTAB only after addition gold seeds preventing any fresh nucleation. With slight changes in the experimental conditions they showed that morphologies such as blocks, cubes and tetrapods could be achieved [106]. The formation of rod shaped nanoparticles has been explained to occur either by the templating action of the micelles or because of the preferential binding of the CTAB molecules on the {110} faces of fcc gold [112j]. Further, they have reported that gold nanorods of larger aspect ratio are formed when smaller sized gold seeds are used [112i]. It has also been reported by Murphy and co-workers that the presence of Br^- ions as counter is essential for the rod formation and similar results were not obtained with Cl^- and I^- ions as counter ions [112a]. Pileni's group have demonstrated the synthesis of anisotropic shapes of copper nanoparticles such as cubes, rods and triangles using copper(II) bis(2-ethylhexyl)sulfosuccinate $Cu(AOT)_2$-isooctane-water system and salts of different anions as the reaction medium [113]. From the results obtained by them, it was demonstrated that though the structure of the AOT micellar structure did not change much with different added salts a drastic change the morphology could be observed. Mirkin's group have recently demonstrated the synthesis of gold nanotriangles following the seeded growth method in an aqueous solution containing the capping agent (cetyltrimethylammonium bromide (CTAB)), gold ions ($HAuCl_4 \cdot 3H_2O$), reducing agent (ascorbic acid), and NaOH [114]. Xie's group had demonstrated the synthesis of silver nanowires and dendrites in surfactant solution of CTAB and sodium dodecyl sulfate

(SDS) and stressed on the crucial role of added NaCl in its formation [115].

1.3.2 Synthesis in presence of templates:

Anisotropic metallic structures have been synthesized using both soft and rigid templates. DNA has been one such popular template because of its linear structure and negatively charged phosphate backbone. Fabrication of one-dimensional parallel and two-dimensional crossed Pd nanowire arrays, Cu nanowire, and Ag nanorod has been reported on a solid substrate surface templated by DNA with the direct reduction of metal ions [116]. Wei et al have recently demonstrated the synthesis of silver nanoparticles, nanorods and nanowires by first complexing the silver ions with the DNA network and then reducing with sodium borohydride [117]. In their synthesis, the diameter of the silver nanoparticles and the aspect ratio of the silver nanorods and nanowires were demonstrated to be controlled by adjusting the DNA concentration and reduction time. The formation of the uniform crystalline nanorods and nanowires was reported to be arising from a template-directed aggregation of small particles and subsequent recrystallization rather than simple aggregation of small particles. Block copolymers/polymers provide another class of versatile template for generating anisotropic nanostructures [118]. Under appropriate conditions, different segments of block copolymer form regular arrays of cylinders with a structure similar to that of self-assembled surfactants. Different regions of the arrayed structure can be easily designed with functional groups to selectively interact with the precursor metal ions through physical adsorption or chemical bonding, subsequent reduction of which results in 1D nanostructures. This templating procedure has been exploited for the synthesis of Ag nanowires [118a,b] Au nanowires and nanosheets [118c,d] using range of copolymers. Carbon nanotubes have also been used for the synthesis of metal nanoparticles. Nanowires of metals such as gold, silver, platinum and palladium were synthesized in the capillaries of singlewalled carbon nanotubes [119]. Schatz and co-workers have used polystyrene mesospheres as templates for the synthesis of silver nanodiscs [120]. In a separate approach, anisotropic metal nanoparticles such as silver nanocubes and nanotriangles themselves have also been used as templates for the synthesis of nanoboxes and triangular rings of gold [121]. In this method the synthesis is facilitated by the transmetallation reduction of the gold ions by silver in metallic form.

1.3.3 Controlling the growth of the nanoparticles using physical confinements:

Nanorods of various metals have been synthesized within the pores of rigid materials. Martin and co-workers have shown the synthesis of metal nanotubes and nanowires within the pores of polycarbonate and porous alumina membranes by both chemical reduction and electrochemical deposition [122]. Chemical reduction was reported to give better anisotropic structures and was demonstrated that the reduction is initiated at the walls of the pores. Similarly metal nanowires have also been synthesized within mesoporoous silica [123]. Sastry and co-workers have shown that the physical constraints of liquid-liquid and air-water interface are also capable of inducing anisotropic growth of gold nanoparticles. With these method gold tapes, plates and fractal structures have been successfully synthesized [124].

1.3.4 Physical methods:

Parallel to chemical routes for synthesis of anisotropic shaped nanoparticles physical methods have also been demonstrated for shape controlled synthesis. Nanosphere lithography technique has been used for synthesizing triangular, cup shaped and crescent shaped nanoparticles. In this procedure a monolayer of polystyrene spheres is drop-coated on a substrate and then metal is deposited on them by vacuum deposition. On removing the close packed sphere template, highly ordered triangular shaped nanoparticles deposited through the void spaces only remain [125]. Alternatively, the metal layer deposited on the spheres themselves can also be removed by dissolving the polystyrene spheres leading to formation of nanocups [126]. In a slight modification, Kreiter et al have demonstrated that using a well-separated layer of polystyrene spheres and carrying out deposition at angle rather than normal to the surface crescent shaped metal particles could also be achieved [127]. In a different physical approach, nanorods and nanowires have been obtained by vacuum vapor deposition of copper on carbon films. The rough surface of the carbon film was proposed to be the reason for re-nucleation of the copper vapor leading to the linear growth with uniform thickness [128]. Zhou et al have demonstrated the formation of silver nanowires by solid-liquid phase arc discharge arc. In this method the arc discharge of the silver filaments in $NaNO_3$ solution leads to the formation of linear structures [129].

1.3.5 Direct synthesis in absence or presence of additives:

Extensive work using polyol method for synthesis of anisotropic metal nanoparticles has been reported. Liz-Marzan and coworkers have demonstrated the synthesis of silver prisms by boiling $AgNO_3$ in N,N-dimethylformamide in presence of poly-(vinylpyrrolidone) [130]. Similarly, Xia and co-workers have demonstrated the synthesis of nanowires of silver and platinum and also the synthesis of nanocubes and nanotriangles of silver [131a-c]. Murphy's group have shown that the silver nanowires can be synthesized even in a templateless and seedless medium. In their method reduction of silver at 100 ^{o}C was carried out by sodium citrate in presence of NaOH [132]. Similarly, Turkevich et al have also reported synthesis of gold triangular nanoparticles using sodium citrate reduction method [133]. Plate like structures of gold have also been reported on reduction of gold ions using salicylic acid [134]. The growth of the plate like structures has been rationalized to occur by spiral growth mechanism and in some cases it has also been proposed to occur by an aggregation and recrystallization mechanism [135].

1.3.6 Synthesis by induced shape transformation:

Apart from the above mentioned methods anisotropic shaped nanoparticles have also been synthesized by transformation of spherical nanoparticles. Mirkin and co-workers have demonstrated the transformation of spherical silver nanoparticles to triangular nanoparticles by a photoirradiation [136]. Similarly, thermally induced transformation of spherical gold clusters to nanocubes has been demonstrated [137]. Fuhrhop and co-workers have demonstrated chemically induced transformation of gold from spherical to planar forms [138]. In an interesting approach, Roorda et al have demonstrated the formation of gold nanorods by ion beam irradiation of spherical gold-silica core-shell nanoparticles [139]. The ion beam irradiation was reported to deform the silica shell, consequently leading to the deformation of the core spherical gold nanoparticle. Similarly shape transformation by laser irradiation has also been observed to lead to the formation of Φ shaped nanoparticles from nanorods [140]. The transformation of gold nanorods to Φ shaped nanoparticles in small percentage was shown to occur on adjusting the laser irradiation fluence and the pulse width, which otherwise leads to spherical nanoparticles due to complete melting/fragmentation.

It is thus clear that the shape-controlled synthesis of various metal nanoparticles has been the focus of interest for many researchers. In this thesis an attempt has been made to synthesize anisotropic shape metal nanoparticles by solution based method in absence of any template or seeds. One of the objectives of this thesis is also to study the mechanism of the formation of gold nanotriangles synthesized using plant extracts and those synthesized following the citric acid reduction method.

1.4 Thin films of inorganic nanoparticles.

Analogous to the unique properties exhibited by the nanoparticles compared to their bulk counterparts, interesting collective properties are exhibited by the close packed thin films of nanoparticles. By controlling the size and the packing density of nanocrystals on planar surfaces, their electrical, magnetic, and optical properties can be tuned [141]. Because of these properties and other functional features suitable for device fabrication, thin film form an important class of commercially applicable materials. Some of the important applications of thin films are in high-density magnetic media, biosensors, solar cells, and in optical and electronic/optoelectronic devices [142]. For these applications, thin films have been routinely fabricated by chemical vapor deposition (CVD) [143], metal organic chemical vapor deposition (MOCVD) [144], molecular beam epitaxy (MBE) [145], rapid ion beam etching (RIE) [146], sputter deposition and other physical techniques [147]. Thin patterned films are also fabricated using lithographic techniques such as X-ray lithography [148], electron beam lithography [149] and microcontact printing [150]. Solution based methods for fabricating thin films can be more cost effective as compared to above-mentioned physicals methods. Solution based methods for fabrication of thin films depend on either self-assembly or two-dimensional synthesis of nanoparticles. Two-dimensional assembly has been achieved by solvent evaporation, electrophoretic deposition, Langmuir-Blodgett technique and layer-by-layer assembly. Nanoparticulate thin films can also be fabricated by either assembly or synthesis using templates such as self assembled monolayers (SAM) and multilayers, polymers, lipid thin films and biological molecules.

Several groups have demonstrated the formation of spontaneous ordered arrays of nanoparticles on solid substrates by solvent evaporation [151]. The success of the method

depends on various parameters such as nanoparticle concentration, rate of solvent evaporation, narrow size distribution, ionic strength, and surfactant concentration. The capping material stabilizing the nanoparticles also determines the interparticle distances of self-assembled structures. By comparing the measured separation between two neighbouring particles with twice the chain length of the capping molecules [152], it has been shown that the hydrocarbon chains of capping molecules are interdigitated. However, greater chemical control has been achieved by using bifunctional ligands [153], which are bound to the surface of the nanoparticles and can bind to a neighbouring particle during the assembly process via the second functional group. There are several examples in the literature for the evaporation induced 2D and 3D assembly of alkanethiol/alkylamine capped gold and silver nanoparticles [154]. Kiely et al. have shown that it is possible to produce ordered arrays of nanoparticles even from bimodal distribution of sizes of the same metal [155] and also of different metals [156].

Electrophoretic deposition technique also offers a convenient method for organizing nanoparticles in macrodimesions. In the process of electrophoretic deposition, two metal electrodes (usually indium tin oxide electrode) are immersed in a small glass cell containing colloidal solution. The charged nanoparticles migrate under the influence of electric field and get deposited on the electrode. The rate of nanoparticle deposition depends on both the applied voltage and initial concentration of colloidal solution. The formation of large monolayer domains has been rationalized by assuming that the colloidal particles migrate till they can find sites with the highest positive electrostatic potential. This directs the incoming colloidal particles to unoccupied surface sites preventing multilayer condensation of the colloid. The ability to modulate this "lateral attraction" between particles, by adjusting field strength or frequency, facilitates the reversible formation of 2D fluid and crystalline colloidal states on electrode surface [157]. Gersig and Mulveney [158] have succeeded in assembling aqueous citrate reduced gold nanoparticles [158a] as well as thiol capped gold nanoparticles [158b] as a 2D array on the copper grid. 2D organization of Pt nanoparticles by electrophoretic depostion has also been established by others [159].

The formation of SAM was first reported by Sagiv [160], who immersed scrupulously clean substrates into a dilute solution of *n*-octadecyltrichlorosilane (OTS) in

an organic solvent. Self-assembly involved chemisorption of OTS and subsequent hydrolysis of the Si-Cl bonds at the substrate surface to form a Si-O-Si network. Alternatively, thiol and disulfide-functionalized surfactants have been selfassembled onto coinage metal surfaces, primarily by chemisorption [161]. Alivisatos and coworkers [162] showed the capability of 2D SAM of 1,6 hexanedithiol, formed on gold thin film, in organization of CdS nanoparticles through covalent interactions. In another approach they have shown that carboxylic acid derivatized CdS nanoparticles can also be arranged on aluminium thin film [162]. The self-assembly in this case occurs through electrostatic interaction of the free carboxylic groups on the CdS surface with the aluminium atoms on the surface of the substrate [162]. Sastry and co-workers have demonstrated that SAMs of 4-aminothiophenol (4-ATP) chemisorbed on thin films of gold may be used to electrostatically bind with silver nanoparticles charged negatively with carboxylic acid functionality by simple immersion of the SAMs in the aqueous nanoparticle solution [163]. Using the electrostatic interactions Iler showed that oppositely charged silica and alumina particles could be electrostatically self-assembled in multilayer structures by alternatively immersing the substrate in the two colloidal solutions [164]. Decher and co-workers have demonstrated an alternate layer-by-layer deposition of oppositely charged polyelectrolytes and nanoparticles [165]. The electrostatically driven layer-by-layer assembly has been extensively used to realize structures containing polyelectrolye/inorganic nanoparticle sandwich structures with nano-magnetite [166], TiO_2/CdS [167], SiO_2, TiO_2 and CeO_2 [168], CdSe [169] and Au [170] as well as alternating layers of positively charged gold and negatively charged silver particles [171]. Sastry and co-workers have shown that amino acid capped gold nanoparticles can be electrostatically assembled in a layer-by-layer fashion by suitably changing the pH [172]. Two-dimensional assemblies of nanoparticles have also been synthesized using biological templates such as bacterial S-layer proteins. Bacterial S-layers deposited on planar substrates have a two dimensional crystalline structure and thus could be used for fabricating arrays of metallic/semiconducting nanostructures [173].

As a tool for two-dimensional organization of nanoparticles LB technique has been an area of extensive research. The LB technique consists the formation of monomolecular layers of amphiphilic molecules at the air-water interface and their

subsequent transfer onto solid substrates. These films have been used as templating organic structures for the synthesis of several nanostructures by exploiting their highly ordered lamellar structure to provide nanocrystals formation in a confined reaction geometry [174]. Fendler and co-workers first reported on using electrostatic interactions for the assembly of size-quantized CdS nanoparticles by Langmuir-Blodgett technique [175]. Nanoparticles of metals such as silver and gold [176], semiconductor quantum dots such as CdS [175,177] and CdTe [178], oxides such as SiO_2, TiO_2 [179], Fe_3O_4 [180] and γ-Fe_2O_3 [181] have been assembled from solution at the air-water interface using electrostatic interactions. In a slight variation to this method nanoparticles can be hydrophobized and then spread at the air water interface, leading to transfer of close-packed array of the nanoparticles by LB technique. This is a very general method and can be used to grow multilayer films consisting of different layers of nanoparticles in any desired sequence by using different troughs containing the desired nanoparticle solution successively [176j, 182]. Alternatively it was shown by Sastry and co-workers that mono- or multilayers of metal nanoparticles can also be achieved by spreading hydrophobized metal ions over a subphase phase consisting of reducing agent or conversely by spreading an amphiphilic reducing agent over an aqueous solution of necessary metal ions [183].

A part of this thesis focuses on the use of thermally evaporated lipid thin films of for the immobilization and synthesis of nanoparticles. This technique developed by Sastry and co-workers earlier, uses thermally evaporated thin films of ionizable long chain amphiphilic molecules for entrapment of oppositely charged species from an aqueous solution by a simple immersion method. These thermally evaporated thin films with entrapped metal ions have been reported to have an ordered lamellar structure of 'bilayer stacks' [184] analogous to multilayers of amphiphilic molecules deposited by LB technique. The flexible nature of these films renders them capable of immobilizing charged species of different size and shape. With this technique Sastry and co-workers, have demonstrated the formation of thin films of a wide variety of materials by entrapment e.g., DNA [185], enzymes [186], funtionalized gold [187], silver [188] and CdS [189] nanoparticles. Similarly the thermally evaporated lipid thin film based technique has also been used for the synthesis of nanoparticles by initial entrapment of metal ions and their subsequent chemical treatment [190].

1.5 Outline of the Thesis.

The work presented in this thesis describes the synthesis of metal nanoparticles using plant extracts as a natural reducing agent, in an attempt to extend the biological sysnthesis protocols used for its environmentally benign effects. An important outcome of this approach is the facile shape controlled synthesis of triangular and hexagonal gold particles by using lemongrass extract to reduce gold ions and has been discussed in detail. An attempt has been made to study the mechanism of formation of these flat gold particles synthesized using plant extract based gold ion reduction and has been compared with the gold nanotriangles formed with citric acid reduction method. Further, the biologically synthesized gold nanoparticles have been used for immobilization in cationic and anionic lipid thin films. Besides entrapment studies with thermally evaporated lipid thin films, synthesis of titania, zirconia and cadmium sulphide has been demonstrated. The chapter wise discussion of these studies is as follows:

The ***Second Chapter***, describes the instrumental techniques used for various experimental characterizations during synthesis of different nanoparticles. Instruments and experimental characterization techniques used for the work presented in this thesis include: vacuum deposition technique for lipid thin film coating, Quartz Crystal Microgravimetry (QCM), Fourier Transform Infrared Spectroscopy (FTIR), UV-visible-NIR Spectroscopy, X-ray diffraction (XRD), Energy Dispersive Analysis of X-Rays (EDAX), Scanning Electron Microscopy (SEM), Transmission Electron Microscopy (TEM), Atomic Force Microscopy (AFM), X-ray Photoelectron Spectroscopy (XPS), Light Scattering (LS) measurements, Isothermal Calorimetry (ITC) and IR-laser source used for irradiation of aqueous samples of metal nanoparticles etc. Applications of these techniques to understand various aspects of formation of nanoparticles in lipid thin films and in solution have been summarized.

The ***Third chapter*** describes the synthesis of metal nanoparticles in aqueous phase through an environmentally benign biosynthetic pathway. Leaf extracts and extracts from other parts of geranium plant and extract of neem leaves have been used for the reduction of metal ions to form very stable metal nanoparticles in aqueous phase. Extracts of different plants obtained by simply boiling the leaves or other parts of it in

water can be a very economic alternative for large-scale synthesis of metal nanoparticles. Aqueous solutions of gold and silver nanoparticles and their bimetallic nanoparticles with very good stability have been synthesized. Issues like the rate of reaction that is in general observed to be very slow when using other biosynthetic pathways involving microorganisms have been addressed. It has been also discussed that the biomolecules present in the plant extracts not only reduce the metal ions and stabilize the metal nanoparticles but also to some extent control the shape during their formation.

The ***Fourth chapter*** describes the use of lemon grass leaf extract to synthesize triangular gold nanoparticles in aqueous phase. Though the formation of gold nanotriangles is a relatively slow process, it challenges the chemical and physical methods available for the shape-controlled synthesis of metal nanoparticles. The chapter also describes the ease with which the size of the gold nanotriangles and consequently their optical properties can be tuned by simply varying the amount of the leaf extract used as a reducing agent for gold ions. The growth mechanism of the gold nanotriangles was studied by carrying out the TEM kinetic measurements and light scattering measurements during the formation of gold nanotriangles. Based on the interesting optical properties of the gold nanotriangles their potential application as a good NIR absorbing optical coating material for architectural applications has been demonstrated.

The ***Fifth chapter*** illustrates the possibility of achieving shape control by synthesizing gold nanotriangles using citric acid reduction method that has been very commonly used for the synthesis of spherical gold nanoparticles so far. The chapter emphasizes the possible factors that could be responsible for the formation of triangular gold nanoparticles. The formation of gold nanotriangles with citric acid reduction was studied by TEM measurements and compared to the gold nanotriangle growth mechanism observed in case of reduction with lemon grass extract. The chapter also describes the change in morphology of the triangular gold nanoparticles brought into effect by chemical and physical methods. The effect of different anions on the shape of gold nanoparticles during their synthesis has been studied and by comparing them with their effect on the morphology of the pre-formed gold nanotriangles, an attempt has been made to understand the nanocrystal growth process leading to nanotriangles. In this chapter, the effect of IR-laser irradiation leading to significant variation in the

morphology of the gold nanotriangles dispersed in aqueous medium has also been discussed.

The ***Sixth chapter*** discusses the use of an anisotropic constrained environment for entrapment and growth of nanoparticles by using thin films of thermally evaporated lipid bilayers as templates. In this chapter we demonstrate the possibility of immobilizing biologically synthesized gold nanoparticles into both anionic and cationic lipid thin films by just varying the pH of the metal nanoparticles solution. It is observed that on using a polydisperse solution of biologically synthesized gold nanoparticles solution, a size and shape dependent preferential immobilization occurs into the cationic and anionic lipid thin films. This successfully demonstrates yet another capability of lipid thin films and increases the scope of their applicability in nanotechnology. In this chapter the generality of the synthesis protocol of nanoparticles within lipid thin films has also been further shown. We have extended the use of lipid thin films to synthesize metal oxide and metal sulfide nanoparticles within the bilayer stacks by electrostatically entrapping suitable metal ions/complex ions followed by a suitable chemical treatment. Composite thin films of metal oxide nanoparticles such as TiO_2 and ZrO_2 were synthesized by sequential entrapment of TiF_6^{2-}, ZrF_6^{2} ions followed by a simple in situ hydrolysis. Similarly thin films of semiconducting CdS nanoparticles were synthesized by entrapping Cd^{2+} ions within thermally evaporated anionic sodium bis-2-ethylhexyl-sulfosuccinate (aerosol OT, AOT) thin films followed by treatment with S^{2-} ions.

The ***Seventh chapter*** includes a brief summary of the work presented in the thesis and scope for possible further research in these areas.

1.6 References:

1) Feynman, R. P. *Eng. Sci.* **1960**, *23*, 22.
2) Savage, G. *Glass and Glassware*; Octopus Book: London, 1975. b) Wagner, F. E.; Haslbeck, S.; Stievano, L.; Calogero, S.; Pankhurst, Q. A.; Martinek, K.-P. *Nature* **2000**, *407*, 691. c) Turkevich, J. *Gold Bull.* **1985**, *18*, 86.
3) a) Antonii, F. *Panacea Aurea-Auro Potabile*; Bibliopolio Frobeniano: Hamburg, **1618**. b) Kunckels, J. *Nuetliche Observationes oder Anmerkungen von Auro und Argento Potabili*; Schutzens: Hamburg, **1676**. c) Helcher, H. H. *Aurum Potabile oder Gold Tinstur*; J. Herbord Klossen: Breslau and Leipzig, **1718**. d) Ostwald, W. Zur Geschichte des Colloiden Goldes. *Kolloid Z.* **1909**, *4*, 5.
4) a) Roucoux, A.; Schulz, J.; Patin, H. *Chem. Rev.* **2002,** *102,* 3757. b) Lewis, L. N. *Chem. Rev.* **1993**, 93, 2693.
5) a) Niemeyer, C. M. *Angew. Chem. Int. Ed.* **2001**, *40*, 4128. b) Niemeyer, C. M. *Angew. Chem. Int. Ed.* **2003**, *42*, 5974. c) Parak, W. J.; Gerion, D.; Pellegrino, T.; Zanchet, D.; Micheel, C.; Williams, S. C.; Bodreau, R.; Gros, M. A. L.; Larabell, C. A.; Alivisatos, A. P. *Nanotechnology* **2003**, *14*, R15. d) Caski, A.; Maubach, G.; Born, D.; Reichert, J.; Fritzsche, W. *Single Mol.* **2002**, *3*, 275.
6) Rosi, N. L.; Mirkin, C. A. *Chem. Rev.* **2005**, *105*, 1547.
7) a) Parak, W. J.; Pellegrino, T.; Plank, C. *Nanotechnology* **2005**, *16*, R9; b) Bruchez, M.; Moronne, Jr., M.; Gin, P.; Weiss, S.; Alivisatos, A. P. *Science* **1998**, *281*, 2013; c) Chan, W. C. W.; Nie, S. M. *Science* **1998**, *281*, 2016.
8) a) Hagfeldt, A.; Graetzel, M. *Acc. Chem. Res.* **2000**, *33*, 269. b) Bueno, J. T.; Shchukina, N.; Ramos, A. A. *Nature*. **2004**, *430*, 326.
9) Fichtner, M. *Adv. Eng. Mater.* **2005**, *7*, 443.
10) Moran, C. E.; Steele, J. M.; Halas, N. J. *Nano Lett*. **2004**, *4*, 1497.
11) a) Simon, U. In *Nanoparticles: From Theory to Application*, Schmid, G., Ed. Wiley-VCH, Weinheim, 2004. b) *Nanomaterials: Synthesis, Properties, and Applications*, edited by A. S. Edelstein and R. C. Cammarata (Institute of Physics Publishing, Bristol, U.K., 1996).

12) a) Maier, S. A.; Brongersma, M. L.; Kik, P. G.; Meltzer, S.; Requicha, A. A. G.; Atwater, H. A. *Adv. Mater.* **2001**, *13*, 1501. b) Maier, S. A.; Brongersma, M. L.; Kik, P. G.; Atwater, H. A. *Phys. Rev. B*, **2002**, *65*, 193408. c) Wang, Y. *Acc. Chem. Res.* **1991**, *24*, 133. (b) Yoffe, A. D. *Adv. Phys.* **1993**, *42*, 173.

13) Li, X.; Xu, W.; Zhang, J.; Jia, H.; Yang, B.; Zhao, B.; Li, B.; Ozaki, Y. *Langmuir* **2004**, *20*, 1298.

14) a) Rouvray, D. *Chem. Br.* **2000**, *36*, 46. b) Lawton, G. *Chem. Ind. (London)* 2001, 174. c) Havancsak, K. *Mater. Sci. Forum* 2003, *414*, 85. d) Mazzola, L. *Nature Biotech.* **2003**, *21*, 1137. e) Hayat, M. A. Ed.; *Colloidal Gold : Principles, Methods and Application*; Academic Press : San Diego, 1989; Vol 1. f) Alivisatos, P. *Nature Biotech.* **2004**, *22*, 47.

15) a) Brust, M.; Kiely, C. J. *Colloids Surf. A: Physicochem. Eng. Asp.* **2002**, *202*, 175. b) Link, S.; El-Sayed, M. A. *J. Phys. Chem. B* **1999**, *103*, 4212. c) Brus, L. E. *J. Chem. Phys.* **1983**, *79*, 5566. d) J. P. Borel, *Surf. Sci.* **1981**, *106*, 1 e) Dick, K.; Dhanasekaran, T.; Zhang, Z.; Meisel, D. *J. Am. Chem. Soc.*, **2002**, *124*, 2312. f) Glinka, Y. D.; Lin, S. –H.; Hwang, L. –P.; Chen, Y. –T.; Tolk, N. H. *Phys. Rev. B*, **2001**, *64*, 085421. g) Eychmüller, A. *J. Phys. Chem. B* **2000**, *104*, 6514. h) Buffat, P.; Borel, J. P. *Phys. Rev. A* **1976**, *13*, 2287. i) Skomski, R *J. Phys.: Condens. Matter* **2003**, *15*, R841. j) McHale, J. M.,; Auroux, A.,; Perotta, A. J.; Navrotsky, A. *Science* **1997**, *277*, 788. k) Zhang, H.; Banfield, J. F. *J. Mater. Chem* **1998**, 8, 2073.

16) a) El-Sayed, M. A. *Acc. Chem. Res.* **2001**, *34*, 257. b) Link, S.; El-Sayed, M. A. *J. Phys. Chem. B* **1999**, *103*, 8410. c) Burda, C.; Chen, X.; Narayanan, R.; El-Sayed, M. A. *Chem. Rev.* **2005**, *105*, 1025.

17) a) Chen, S.; Huang, K. *Langmuir* **2000**, *16*, 2014. b) Li, D.; Li, J. *Chem. Phys. Lett.* **2003**, *372*, 668. c) Chen, S.; Ingram, R. S.; Hostetler, M. J.; Pietron, J. J.; Murray, R. W.; Schaaff, T. G.; Khoury, J. T.; Alvarez, M. M.; Whetten, R. L. *Science* **1998**, *280*, 2098. d) Miles, D. T.; Murray, R. W. *Anal. Chem.* **2003**, *75*, 1251 e) Chen, S.; Pei, R. *J. Am. Chem. Soc.* **2001**, *123*, 10607. f) Quinn, B. M.; Liljeroth, P.; Ruiz, V.; Laaksonen, T.; Kontturi, K. *J. Am. Chem. Soc.* **2003**, *125*, 6644. g) Zhang, P.; Sham, T. K. *Appl. Phys. Lett.* **2002**, *81*, 736.

18) a) Templeton, A. C.; Pietron, J. J.; Murray, R. W.; Mulvaney, P. *J. Phys. Chem. B* **2000**, *104*, 564. b) Itoh, T.; Asahi, T.; Masuhara, H. *Appl. Phys. Lett.* **2001**, *79*, 1667. c) Rechberger, W.; Hohenau, A.; Leitner, A.; Krenn, J. R.; Lamprecht, B.; Aussenegg, F. R. *Opt. Commun.* **2003**, *220*, 137. d) Link, S.; Mohamed, M. B.; El-Sayed, M. A. *J. Phys. Chem. B* **1999**, *103*, 3073. e) Yan, B.; Yang, Y.; Wang, Y. *J. Phys. Chem. B* **2003**, *107*, 9159. f) Swanson, N. L.; Billard, B. D. *Nanotechnology* **2003**, *14*, 353.

19) a) Su, K.-H.; Wei, Q.-H.; Zhang, X.; Mock, J. J.; Smith, D. R.; Schultz, S. *Nano Lett.* **2003**, *3*, 1087. b) Xu, H.; Bjerneld, E. J.; Kall, M.; Borjesson, L. *Phys. Rev. Lett.* **1999**, *83*, 4357. c) Kottmann, J. P.; Martin Oliver, J. F. *Opt. Lett.* **2001**, *26*, 1096. d) Kelly, K. L.; Coronado, E.; Zhao, L. L.; Schatz, G. C. *J. Phys. Chem. B* **2003**, *107*, 668. e) Jensen, T.; Kelly, L.; Lazarides, A.; Schatz, G. *Cluster Sci.* **1999**, *10*, 295. f) Al-Rawashdeh, N.; Foss, C. A., Jr. *Nanostruct. Mater*. **1997**, *9*, 383. h) Schmid G.; Simon U. *Chem. Commun.*, **2005**, *6*, 697.

20) a) Raimondi, F.; Scherer, G. G.; Kötz, R.; Wokaun, A. *Angew. Chem. Int. Ed.* **2005**, *44*, 2190. b) Henry, C. R. *Surf. Sci. Rep.* **1998**, *31*, 231. c) Zhang, J. H. *Acc. Chem. Res.* **1997,** *30*, 423.

21) Kreibieg, U.; Vollmer, M. *Optical properties of metal clusters*; Springer: Berlin and New York, 1995.

22) Hutter, E.; Fendler, J. H. *Adv. Mater.* **2004**, *16*, 1685.

23) a) Schaaf, T. G.; Shafigullen, M. N.; Khoury, J. T.; Vezmar, I.; Whetten, R. L.; Cullen, W. G.; First, P. N.; Guttierrez-Wing, C.; Ascencio, J.; Jose-Yacamun, M. J. *J. Phys. Chem. B* **1997**, *101*, 7885. b) Zaitoun, M. A.; Mason, W. R.; Lin, C. T. *J. Phys. Chem. B* **2001**, *105*, 6780. c) Melinger, J. S.; Kleiman, V. D.; McMorrow, D.; Gro¨hn, F.; Bauer, B. J.; Amis, E. *J. Phys. Chem. A* **2003**, *107*, 3424.

24) a) Logunov, S. L.; Ahmadi, T. S.; El-Sayed, M. A.; Khoury, J. T.; Whetten, R. L. *J. Phys. Chem. B* **1997**, *101*, 3713. b) Papavassiliou, G. C. *Prog. Solid State Chem*. **1979**, *12*, 185.

25) a) Alivisatos, A. P. *Science* **1996**, *271*, 933. b) Brus, L. E. *J. Phys. Chem.* **1986**, *90*, 2555 c) Heath, J. R. *Science* **1995**, *270*, 1315.

26) Faraday, M. *Philos. Trans. R. Soc. London* **1857**, *147*, 145.

27) Graham, T. *Philos. Trans. R. Soc*. **1861**, *151*, 183.

28) Taniguchi, N. 1974. On the Basic Concept of 'Nano-Technology'. In: *Proceedings of the international conference on production engineering. Tokyo, Part II,* Japan Society of Precision Engineering, 1974: 18-23: Tokyo: JSPE.

29) a) Itakura, T.; Torigoe, K.; Esumi, K. *Langmuir* **1995**,*11*, 4129. b) Ershov, B. G.; Henglein, A. *J. Phys. Chem.* **1993**, *97*, 3434. c) Gutierrez, M.; Henglein, A. *J. Phys. Chem.* **1993**, *97*, 11368. d) Henglein, A.; Mulvaney, P.; Holtzworth, A,; Sosebee, T. E.; Fojitik, A. *Ber. Bunsenges. Phys. Chem.* **1992**, *96*, 754. e) Yonezawa, Y.; Sato, T.; Ohno, M.; Hada, H. J. *Chem. Soc., Faraday Trans. 1* **1987**, *83*, 1559. f) Yonezawa, Y.; Sato, T.; Kuroda, *S.J . Chem. Soc.Faraday Trans. 1* **1991**, *87*, 1905. g) Torigoe, K.; Esumi, K. *Langmuir* **1993**, *9*, 1964. h) Itakura, T.; Torigoe, K.; Esumi, K. J. *Jpn. Soc. Colour Mater.* **1994**, *67*, 1695. i) Marignier, J. L.; Belloni, J.; Delcourt, M. 0.; Chevalier, J. P. *Nature* **1986**, *317*, 344. j) Kurihara, K.; Kizing, J.; Stenius, P.; Fender, J. H. *J. Am. Chem.Soc.* **1983**, *105*, 2574. k) T. Chen, S. Chen, H. Sheu, C. Yeh, *J. Phys. Chem. B* **2002**, *106*, 9717.

30) a) Henglein, A. *Langmuir* **1999,** *15,* 6738. b) A. Henglein, J. Phys. Chem. B **2000**, *104*, 1206.

31) R.A. Salkar, P. Jeevanandam, G. Kataby, S.T. Aruna, Y. Koltypin, O. Palchik, A. Gedanken, *J. Phys. Chem. B* **2000**, *104*, 893.

32) a) Wegner, K. ;Walker, B. ;Tsantilis, S. ;Pratsinis, S. E. *Chem. Eng. Sci* 2002, *57*, 1753. b) G. Vitulli, M. Bernini, S. Bertozzi, E. Pitzalis, P. Salvadori, S. Coluccia, G. Martra, *Chem. Mater.* **2002**,*14*, 1183. c) Klabunde, K. J.; Timms, P. S.; Skell, P. S.; Ittel, S. *Inorg. Synth.* **1979**, *19*, 59. e) Davis, S. C.; Klabunde, K. J. *Chem. Rev.* **1982**, *82*, 153. f) Kim, J. H.; Germer, T. A.; Mulholland, G. W.; Ehrman, S. H. *Adv. Mater.* **2002**, *14*, 518. g) Klabunde, K. J.; Groshens, T.; Brezinski, M.; Kennelly, W. *J. Am. Chem. Soc.* **1978**, *19*, 59.

33) a) Maisels, A.; Kruis F. E.; Fissan, H.; Rellinghaus, B.; Zahres, H.; *Appl. Phys. Lett*. **2000**, *77*, 4431. b) Swihart M. T. *Curr. Opin. Colloid Interface Sci.* **2003**, *8*, 127.

34) a) Reetz, M. T.; Helbig, W. *J. Am. Chem. Soc.* **1994**, *116*, 7401. b) Reetz, M. T.; Winter, M.; Breinbauer, R.; Thurn-Albrecht, T.; Vogel, W. *Chem. Eur. J.* **2001**, *7*, 1084. c) Reetz, M. T.; Helbig, W.; Quaiser, S. A.; Stimming, U.; Breuer, N.; Vogel, R. *Science* **1995**, *267*, 367. d) Natter, H.; Hempelmann, R. *Electrochim. Acta* **2003**, *49*, 51. e) Rodriguez-Sanchez, L.; Blanco, M. C.; Lopez-Quintela, M. A. *J. Phys. Chem. B* **2000**, *104*, 9683. f) Rodriguez-Sanchez, M. L.; Rodrigues, M. J.; Blanco, M. C.; Rivas, J.; Lopez-Quintela, M. A. *J. Phys. Chem. B* **2005**, *109*, 1183.

35) a) Tan, Y.; Dai, X.;Y. Li, ; Zhu, D. *J. Mater. Chem.* **2003**, *13*, 1069. b) Toshima, N.; Wang, Y. *Adv. Mater.* **1994**, *6*, 245. c) Toshima, N.; Harada, M.; Yonezawa, T.; Kushihashi, K.; Asakura, K. *J. Phys. Chem.* **1991**, *95*, 7448. 11 d) Bradley, J. S.; Hill, E. W.; Behal, S.; Klein, C. *Chem. Mater.* **1992**, *4*, 1234; e) Bradley, J. S.; Millar, J. M.; Hill, E. W.; Behal, S.; Chaudret, B.; Duteil, A. *Faraday Discuss.* **1991**, *92*, 255. f) Poulin, J. C.; Kagan, H. B.; Vargaftik, M. N.; Stolarov, I. P.; Moiseev, I. I. *J. Mol. Catal.* **1995**, *95*, 109. g) Amiens, C.; de Caro, D.; Chaudret, B.; Bradley, J. S.; Mazel, R.; Roucau, C. *J. Am. Chem. Soc.* **1993**, *115*, 11638. h) Jiang, X.; Xie, Y.; Lu, J.; Zhu, L.; He, W.; Qian, Y. *Langmuir*, **2001**, *17*, 3795. i) Naka, K.; Yaguchi, M.; Chujo, Y. *Chem. Mater.* **1999**, *11*, 849. j) Warner, M. G.; Reed, S. M.; Hutchison, J. E. *Chem. Mater.* **2000**, *12*, 3316.

36) a) Brust, M.; Walker, M.; Bethell, D.; Schiffrin, D. J.; Whyman, R. J. *J. Chem. Soc., Chem. Commun.* **1994**, 801. b) Brust, M.; Fink, J.; Bethell, D.; Schiffrin, D. J.; Kiely, C. J. *J. Chem. Soc., Chem. Commun*. **1995**, 1655. c) Cardenas-Trivino, G.; Klabunde, K. J.; Dale, E. B. *Langmuir* **1987**, *3*, 986.

37) Kim, K.-S.; Demberelnyamba, D.; Lee, H. Langmuir, ***2004***, *20*, 556.

38) a) Chattopadhyay, P.; Gupta, R. B. *Ind. Eng. Chem. Res.* **2003**, *42*, 465. Ohde, H.; Hunt, F.; Wai, C. M. *Chem. Mater.* **2001**, *13*, 4130. Viswanathan, R.; Lilly, G. D.; Gale, W. F.; Gupta, R. B. *Ind. Eng. Chem. Res.*, **2003**, *42*, 5535.

39) a) Capek, I. *Advances in Colloid and Interface Science* **2004**, *110*, 49. b) Meyer, M.; Wallberg, C.; Kurihara, K.; Fendler, J. H. *Chem. Commun.* **1984**, 90. c) Lianos, P.; Thomas, J. K. *Chem. Phys. Lett.* **1986**, *125*, 299. d) Pileni, M. P.; Motte, L.; Petit, C. *Chem. Mater.* **1992**, *4*, 338. e) Petit, C.; Lixon, P.; Pileni, M.

P. *J. Phys. Chem.* **1990**, *94*, 1598. f) Petit, C.; Jain, T. K.; Billoudet, F.; Pileni, M. P. *Langmuir* **1994**, *10*, 4446. g) Antonietti, M.; Wenz, E.; Bronstein, L.; Seregina, M. *Adv. Mater.* **1995**, *7*, 1000. T.; Krieger, M.; Boyen, H. G.; Ziemann, P.; Kabius, B. *Langmuir* **2000**, *16*, 407. h) Fo¨rster, S.; Antonietti, M. *Adv. Mater.* **1998**, *10*, 195.

40) a) Zhang, M.; Drechsler, M.; Muller, A. H. E. *Chem. Mater.* **2004**, *16*, 537. b) Crooks, R. M.; Lemon, B. I., III; Sun, L.; Yeung, L. K.; Zhao, M. *Top. Curr. Chem.* **2001**, *212*, 81. c) Minko, S.; Kiriy, A.; Gorodyska, G.; Stamm, M. *J. Am. Chem. Soc.* **2002**, *124*, 10192.

41) a) Braun, E.; Eichen, Y.; Sivan, U.; Ben-Yoseph, G. *Nature* **1998**, *391*, 775. b) Richter, J.; Seidel, R.; Kirsch, R.; Mertig, M.; Pompe, W.; Plaschke, J.; Schackert, H. K. *Adv. Mater.* **2000**, *12*, 507.

42) a) Shenton, W.; Douglas, T.; Young, M.; Stubbs, G.; Mann, S. *Ad*v. *Mater.* **1999**, *11*, 253. b) Fowler, C. E.; Shenton, W.; Stubbs, G.; Mann, S. *Ad*v. *Mater.* **2001**, *13*, 126 c) Dujardin, E.; Peet, C.; Stubbs, G.; Culver, J. N.; Mann, S. *Nano Lett.* **2003**, *3*, 413. d) Ongaro, A.; Griffin, F.; Beecher, P.; Nagle, L.; Iacopino, D.; Quinn, A.; Redmond, G.; Fitzmaurice, D. *Chem. Mater.* **2005**, *17*, 1959.

43) Wiesner, J.; Wokaun, A. *Chem. Phys. Lett.* **1989**, *57*, 569.

44) a) Mann, S., *Nature*, **1993**, *365*, 499.b) Oliver, S., Kupermann, A., Coombs, N., Lough, A. and Ozin, G. A., *Nature*, 1995, *378*, 47. b) Kroger, N., Deutzmann, R. and Sumper, M., *Science*, 1999, *286*, 1129. c) Parkinson, J.; Gordon, R. *Trends Biotech.* **1999**, *17*, 190.

45) Young, J. R.; Davis, S. A.; Bown, P. R.; Mann, S. *J. Struct. Biol.* **1999**, *126***,** 195.

46) a) Lovley, D. R., Stolz, J. F., Nord, G. L. and Phillips, E. J. P., *Nature*, **1987**, *330*, 252. b) Spring, H. and Schleifer, K. H., *Sys. Appl. Microbiol*. **1995**, *18*, 147. c) Dickson, D. P. E., *J. Magn. Magn. Mater.*, **1999**, *203*, 46.

47) Mann, S. Angew. Chem. Int. Ed. **2000**, *39*, 3392.

48) a) Kroger, N.; Deuzmann, R.; Sumper, M. *Science* **1999**, *286*, 1129. b) Kroger, N.; Lorenz, S.; Brunner, E.; Sumper, M. *Science* **1999**, *286*, 1129. c) Kroger, N.; Deuzmann, R.; Sumper, M. *J. Biol. Chem.* **2001**, *276*, 26066. d) Kroger, N.;

Deuzmann, R.; Bergsdorf, C.; Sumper, M. *Proc. Natl. Acad. Sci. USA* **2000**, *97*, 14133.

49) a) Shimizu, K.; Cha, J.; Stucky, G. D.; Morse, D. E. *Proc. Natl. Acad. Sci. USA* **1998**, *95*, 6234. b) Cha, J.; Shimizu, K.; Zhou, Y.; Christiansen, S. C.; Chmelka, B. F.; Stucky, G. D.; Morse, D. E. *Proc. Natl. Acad. Sci. USA* **1999**, *96*, 361.

50) Kroger, N.; Bergsdorf, C.; Sumper, M. *Eur. J. Biochem.* **1996**, *239*, 259.

51) a) Kroger, N.; Wetherbee, R. *Protist* **2000**, *151*, 263. b) Kroger, N.; Lehmann, G.; Rachel, R.; Sumper, M. *Eur. J. Biochem.* **1997**, *250*, 99.

52) a) Hecky, R. E.; Mopper, K.; Kilham, P.; Degans, E. T. *Mar. Biol.* **1973**, *19*, 323. b) Nakajima, T.; Volcani, B. E. *Science* **1969**, *164*, 1400. c) Swift, D.; Wheeler, A. *J. Phycol.* **1992**, *28*, 202.

53) Rowson, J. D.; Leadbeater, B. S. C.; Green, J. C. *Br. Phycol. J.* **1986**, *21*, 359.

54) a) Marsh, M. E. In Biomineralization (Ed. Baeuerlein, E.), Wiley-VCH, Weinheim, 2000, p. 251-268. b) Marsh, M. E. *Protoplasma* **1999**, *207*, 54-66. c) Young, I. R.; Didymus, I. M.; Brown, P. R.; Prins, N.; Mann, S. *Nature* **1992**, *356*, 516. d) van der Wal, P; de Jong, E. W.; Westbrock, P.; de Bruijn, W. C.; Hulder-Stapel A. A. *J. Ultrastructure. Res.* **1983**, *85*, 139.

55) Bauerlein, E *Angew. Chem. Int. Ed.* **2003**, *42*, 614.

56) a) Devouard, B.; Posfai, M.; Hua, X.; Bazylinski, D. A.; Frankel, R. B.; Busek, P. R. *Am. Mineral.* **1998**, *83*, 1387, b) Pósfai M.; Cziner K.; Márton E.; Márton P.; Buseck P.R.; Frankel R.R.B.; Bazylinski D.A. *Eur. J. Mineral.* **2001**, *13*, 691.

57) Torres de Araujo, F. F.; Pires, M. A.; Frankel, R. B.; Bicudo, C. E. M. *Biophys. J.* **1986**, *50*, 375.

58) Bazylinski, D. A.; Frankel, R. B. *Biomineralization* (Ed.: E. Baeuerlein), Wiley-VCH, Weinheim 2000, p. 41-43.

59) Mann, S.; Sparks, N. H.; Walker, M. M.; Kirschvink, J. L. *J. Exp. Biol.* **1988**,*140*, 35.

60) a) Walker, M. M.; Diebel, C. E.; Haugh, C. V.; Pankhurst, P. M.; Montgomery, J. C.; Green, C. R. *Nature* **1997**, *390*, 371. b) Diebel, C. E.; Proksch, R.; Green, C. R.; Neilson, P.; Walker, M. M. *Nature* **2000**, *406*, 299.

61) Hanzlik, M.; Heunemann, C.; Holtkamp-Rötzler, E.; Winklhofer, M.; Petersen, N.; Fleissner, G. *Biometal*, **2000**, *13*, 325.

62) Acosta-Avalos, D.; Wajnberg, E.; Oliveira, P. S.; Leal, I.; Farina, M.; Esquivel, D. M. *J. Exp. Biol.* **1999**, *202*, 2687.

63) a) Kirschvink, J. L.; Kobayashi-Kirschvink, A.; Woodford, B. J. *Proc. Natl. Acad. Sci USA* **1992**, *89*, 7683; b) Dobson, J.; Grassi, P. P. *Brain Res. Bull.* **1996**, *39*, 255. c) Schultheiss-Grassi, P. P.; Wessiken, R.; Dobson, J. *Biochem. Biophys. Acta* **1999**, *1426*, 212. d) Schultheiss-Grassi, P. P.; Dobson, J. *BioMetals* **1999**, *12*, 67.

64) Balkwill, D.; Marata, D.; Blakemore, R. P. *J. Bacteriol.* **1980**, *141*, 1399.

65) a) Bauerlein, E *Angew. Chem. Int. Ed.* **2003**, *42*, 614. b) Schueler, D. and Frankel, R. B. *Appl. Microbiol. Biotechnol.* **1999**, *52*, 464.

66) a) Fukumori, Y. In *Biomineralization* (Ed.: Baeuerlin), Wiley-VCH, Weinheim, **2000**, p. 93 – 107. b) Noguchi, Y.; Fujiwara, T.; Yoshimatsu, K.; Fukumori, Y. *J. Bacteriol.* **1999**, *181*, 2142. c) Abe, M.; Tamaura, Y. *Jpn. J. Appl. Phys.* **1983**, *22*, L511. d) Yamazaki, T.; Oyanagi, H.; Fujiwara, T.; Fukumori, Y. *Eur. J. Biochem.* **1995**, *233*, 665.

67) Blakemore, R. P. Blakemore, N. A. In *Iron Biominerals* (Eds.: Frankel, R.; Blakemore, R. P., Plenum Press, New York **1991**, p. 51-67.

68) a) Amann, R.; Rosello-Mora, R.; Schuler, D. *Biomineralization* (Ed.: E. Baeuerlein), Wiley-VCH, Weinheim 2000, p 47-59. b) Spring, S.; Amann, R. Ludwig, W.; Schleifer, K. –H.; van Gemerden, H.; Petersen, N. *Appl. Environ. Microbiol.* **1993**, *59*, 2397.

69) Bauerlein, E *Angew. Chem. Int. Ed.* **2003**, *42*, 614.

70) Zbinden M.; Martinez I.; Guyot F.; Cambon-Bonavita M-A.; Gaill F. *Eur. J. Mineral.* **2001**, *13*, 653.

71) a) Beveridge, J. T.; Hughes, M. N.; Lee, H.; Leung, K. T.; Poole, R. K.; Savvaides, I.; Silver, S.; Trevors, J. T. *Adv. Microb. Physiol.* **1997**, 38, 178 b) Silver, S. *Gene* **1996**, *179*, 9. c) Rouch, D.A. Lee, B. T.; Morby, A. T. *J. Ind. Micro.* **1995**, *14*, 132.

72) Stephen, J. R.; Macnaughton, S. J. *Curr. Opin. Biotechnol.* **1999**,*10*, 230.

73) Beveridge, T. J.; Doyle, R. J., Ed. *Metal Ions and Bacteria*; Wiley: New York, 1989.

74) a) Southam, G. and Beveridge, T. J., *Geochim. Cosmochim. Acta*, **1996**, *60*, 4369. b) Beveridge, T. J. and Murray, R. G. E., *J. Bacteriol*., **1980**, *141*, 876. c) Fortin, D. and Beveridge, T. J., in *Biomineralization. From Biology to Biotechnology and Medical Applications* (ed. Baeuerien, E.), Wiley-VCH, Weinheim, 2000, p. 7.

75) a) Klaus, T.; Joerger, R.; Olsson, E.; Granqvist, C. G.; *Proc*. *Natl. Acad. Sci*. *USA*, **1999**, *96*, 13611. b) Klaus-Joerger, T.; Joerger, R.; Olsson, E.; Granqvist, C. G. *Trends Biotechnol*. **2001**, *19*, 15.

76) Joerger, R.; Klaus, T.; Granqvist, C. G., *Adv. Mater*. **2000**, *12*, 407.

77) Nair, B.; Pradeep, T. *Cryst. Growth Des.* **2002**, *2*, 293.

78) Ahmad, A.; Senapati, S.; Khan, M. I.; Kumar, R.; Sastry, M. *Langmuir* **2003,** *19,* 3550.

79) Labrenz, M.; Druschel, G. K.; Thomsen-Ebert, T.; Gilbert, B.; Welch, S. A.; Kemner, K. M.; Logan, G. A.; Summons, R. E.; De Stasio, G.; Bond, P. L.; Lai, B.; Kelly, S. D.; Banfield, J. F. *Science*, **2000**, *290*, 252.

80) a) Cinningham, D. P.; Lundie, L. L. *Appl. Environ. Microbiol.* **1993**, *59*, 7. b) Smith, P. R.; Holmes, J. D.; Richardson, D. J.; Russell, D. A.; Sodeau, J. R., *J. Chem. Soc., Faraday Trans.* **1998**, *94*, 1235.

81) Kowshik, M.; Vogel, W.; Urban, J.; Kulkarni, S. K.; Paknikar, K. M. *Adv. Mater*. **2002**, *14*, 815.

82) Holmes, J. D.; Smith, P. R.; Evans-Gowing, R.; Richardson, D. J.; Russell, D. A.; Sodeau, J. R. *Arch. Microbiol*. **1995**, *163*, 143.

83) Kowshik, M.; Deshmukh, N.; Vogel, W.; Urban, J.; Kulkarni, S. K.; Paknikar, K. M. *Biotechnol. Bioeng*., **2002**, *78*, 583.

84) a) Mukherjee,P.; Ahmad,A.; Mandal,D.; Senapati,S.; Sainkar,S.R.; Khan,M.I.; Ramani,R.; Parischa,R.; Ajayakumar, P. V.; Alam, M.;Sastry,M.; Kumar.R *Angew. Chem. Int. Ed.* **2001**, *40*, 3585. b) Mukherjee, P.; Ahmad, A.;. Mandal, D.; Senapati, S.; Sainkar, S. R.; Khan, M. I.; Parischa, R.; Ajayakumar, P. V.; Alam, M.; Kumar, R.; Sastry, M.; *Nano Lett.* **2001**, *1*, 515.

85) a) Mukherjee, P.; Senapati, S.; Mandal, D.; Ahmad, A.; Khan, M.I.; Kumar, R.; Sastry, M. *ChemBioChem* **2002**, *3*, 461. b) Ahmad, A.; Mukherjee, P.; Senapati, S.; Mandal, D.; Khan, M.I.; Kumar, R.; Sastry, M. *Colloids Surf. B* **2003**, *28*, 313.

86) Senapati, S.; Ahmad, A.; Khan, M.I.; Sastry, M.; Kumar.;R *Small* **2005**, *1*, 517.

87) Ahmad, A.; Mukherjee, P.; Mandal, D.; Senapati, S.; Khan, M.I.; Kumar, R.; Sastry, M.; *J. Am. Chem. Soc.* **2002**, *124*, 12 108.

88) a) Cheavin, W.H.S., *The crystals and cystholites found in plant cells. Part 1:* Crystals. Microscope **1938**, *2*, 155. b) Monje, P.V., Baran, E.J., *J. Plant Physiol.* 2004, *161*, 121.

89) a) Arnott, H.J., 1982. *Three systems of biomineralization in plants with comments on the associated organic matrix.* In (Ed.: Nancollas, G. H.), Biological Mineralization and Demineralization. Springer Verlag, Berlin, pp. 199–218. b) Monje, P.V., Baran, E.J., 2004a. *Plant biomineralization.* In (Ed.: Hemantaranjan, H.), Advances in Plant Physiology, vol. 7. Scientific Publishers, Jodhpur, pp. 403–419.

90) Monje, P.V., Baran, E.J., *J. Plant Physiol.* **2000**, *157*, 457.

91) Harrison, C. C. *Phytochemistry* **1996**, *41*, 37.

92) Gajdardziska-Josifovska M.; McClean R.G.; Schofield M.A.; Sommer C.V.; Kean W.F. *Eur. J. Mineral.* **2001**, *13*, 863.

93) Gardea-Torresdey, J. L.; Peralta-Videa, J. R.; de la Rosa, G.; Parsons, J. G. *Coord. Chem. Rev.* **2005,** *249*, 1797.

94) a) Cannon, H. L.; Shacklette, H. T.; Bastron, H. 1968: Metal absorption by *Equisetum* (horsetail). *United States Geological Survey Bulletin 1278-A:* A1-A21. b) Shacklette, H. T.; Lakin, H. W.; Hubert, A. E.; Curtin, G. C. 1970: Absorption of gold by plants. *United States Geological Survey Bulletin 1314-B:* 1-23. c) Lakin, H. W.; Curtin, G. C.; Hubert, A. E.; Shacklette, H. T.; Doxtader, K. G. 1974: Geochemistry of gold in the weathering cycle. *United States Geological Survey Bulletin 1330:* 1-80.

95) Conn, E. E. *J. Agric. Food Chem.* **1969**, *17*, 519.

96) Shacklette, H. T.; Lakin, H. W.; Hubert, A. E.; Curtin, G. C. *U.S. Geol. Surv. Bull.* **1970**, *1314-B*, 1.

97) a) J.L. Gardea-Torresdey, J.G. Parsons, E. Gomez, J.R. Peralta-Videa, H.E. Troiani, P. Santiago, M. Jose-Yacaman, *Nano Lett.* **2002, 2,** 397. b) J.L. Gardea-Torresdey, E. Gomez, J.R. Peralta-Videa, J.G. Parsons, H. Troiani, M. Jose-Yacaman, *Langmuir*. 2003, 19, 1357.

98) Jana, N. R.; Gearheart, L. A.: Murphy, C. J. *Chem. Commun*. **2001**, 617.

99) Qu, L.; Shi, G.; Wu, X.; Fan, B. *Adv. Mater.* **2004**, *16*, 1200.

100) Huang, C. –C.; Yang, Z.; Chang, H. –T. *Langmuir* **2004,** *20,* 6089.

101) Xiong, Y.; Chen, J.; Wiley, B.; Xia, Y.; Yin, Y.; Li, Z.-Y. *Nano Lett.* **2005**, *5*, 1237.

102) Kuo, C.-H.; Chiang, T.-F.; Chen, L.-J.; Huang, M. H. *Langmuir* **2004**, *20*, 7820.

103) Ahmadi, T. S.; Wang, Z. L.; Green, T. C.; Henglein, A.; El-Sayed, M. A. *Science* **1996**, *272*, 1924.

104) Chen, Y.; Gu, X.; Nie, C.-G.; Jiang, Z.-Y.; Xie, Z.-X.; Lin, C.-J. *Chem. Commun.* **2005**, 4181.

105) Teng, X.; Yang, H. *Nano Lett.* **2005**, *5*, 885.

106) Sau, T. K. ; Murphy, C. J. *J. Am. Chem. Soc.* **2004**, *126*, 8648.

107) Maillard, M.; Giorgio, S.; Pileni, M.-P. *Adv. Mater.* **2002**, *14*, 1084.

108) Jin, R.; Cao, Y. W.; Mirkin, C. A.; Kelly, K. L.; Schatz, G. C.;. Zheng, J. G *Science* **2001**, *294*, 1901.

109) Zhou, Y.; Yu, S. H.; Wang, C. Y.; Li, X. G.; Zhu, Y. R.; Chen, Z. Y. **1999**, *11*, 850.

110) a) Yu, Y.-Y.; Chang, S.-S.; Lee, C.-L.; Wang, C. R. C. *J. Phys. Chem. B.* **1997**, *101*, 6661. b) Wang, Z. L.; Mohamed, M. B.; Link, S.; El-Sayed, M. A. *Surf. Sci.* **1999**, *440*, L809.

111) a) Esumi, K.; Matsuhisa, K.; Torigoe, K. *Langmuir;* **1995**; *11*, 3285. b) Kim, F.; Song, J. H.; Yang, P. *J. Am. Chem. Soc.* **2002**, *124*, 14316.

112) a) Murphy, C. J.; Sau, T. K.; Gole, A. M.; Orendorff, C. J.; Gao, J.; Gou, L.; Hunyadi, S. E.; Li, T. *J. Phys. Chem. B.* **2005**, *109*, 13857. b) Gole, A.; Murphy, C. J. *Chem. Mater.* **2004**, *16*, 3633. c) Jana, N. R.; Gearheart, L.; Murphy, C. J. *J.*

Phys. Chem. B **2001**, *105*, 4065-4067. d) Murphy, C. J.; Jana, N. R. *Ad*v. *Mater*. **2002**, *14*, 80-82. e) Sau, T. K.; Murphy, C. J. *Langmuir* **2004**, *20*, 6416-6420. f) Jana, N. R.; Gearheart, L.; Murphy, C. J. *Ad*v. *Mater.* **2001**, *13*, 1389-1393. g) Jana, N.; Gearheart, L.; Murphy, C. J. *Langmuir* **2001**, *17*, 6782- 6786. h) Johnson, C. J.; Dujardin, E.; Davis, S. A.; Murphy, C. J.; Mann, S. *J. Mater. Chem*. **2002**, *12*, 1765-1770. i) Busbee, B. D.; Obare, S. O.; Murphy, C. J. *Ad*v. *Mater*. **2003**, *15*, 414-416. j) Gole, A.; Murphy, C. J. *Chem. Mater*. **2004**, *16*, 3633-3640. k) Murphy, C. J.; Sau, T. K.; Gole, A.; Orendorff, C. J. *MRS Bull.* **2005**, *30*, 349.

113) Pileni, M. P. Nature Mater. **2003**, *2*, 145.

114) Millstone, J. E.; Park, S.; Shuford, K. L.; Qin, L.; Schatz, G. C.; Mirkin, C. A. *J. Am. Chem. Soc.* **2005**, *127*, 5312.

115) Zheng, X.; Zhu, L.; Yan, A.; Wang, X.; Xie, Y. *J. Colloid Interface Sci.* **2003**, *268*, 257.

116) a) Deng, Z.; Mao, C. *Nano Lett.* **2003**, *3*, 545. Monson, C. F.; Woolley, A. T. *Nano Lett.* **2003**, *3*, 359. b) Becerril, H. A.; Stoltenberg, R. M.; Monson, C. F.; Woolley, A. T. *J. Mater. Chem.* **2004**, *14*, 611.

117) Wei, G.; Zhou, H.; Liu, Z.; Song, Y.; Wang, L.; Sun, L.; Li, Z. *J. Phys. Chem. B.* **2005**, *109*, 8738.

118) a) Zhang, D.; Qi, L.; Ma, J.; Cheng, H. *Chem. Mater.* **2001**, *13*, 2753. b) Cornelissen, J. J. L. M.; Heerbeek, R. V.; Kamer, P. C. J.; Reek, J. N. H.; Sommerdijk, N. A. J. M.; Nolte, R. J. M. Adv. Mater. **2002**, *14*, 489. c) Kim, U. K.; Cha, S. H.; Shin, K.; Jho, J. Y.; Lee, J. C. *Adv. Mater.* **2004**, *16*, 459. d) Djalali, R.; Li, S.Y.; Schmidt, M. Macromolecules **2002**, *35*, 4282.

119) a) Govindraj, A.; Satishkumar, B. C.; Nath, M.; Rao, C. N. R. *Chem. Mater.* **2000**, *12*, 202. b) Sloan, J.; Wright, D. M.; Woo, H.-G.; Bailey, S.; Brown, G.; York, A. P. E.; Coleman, K. S.; Huchison, J. L.; Green, M. L. H. *Chem. Commun.* **1999**, 699. c) Kyotani, T.; Tsai, L. F.; Tomita, A. *J. Chem. Soc., Chem. Commun.* **1997**, 701.

120) Hao, E.; Kelly, K. L.; Hupp, J. T.; Schatz, G. C. *J. Am. Chem. Soc.* **2002**, *124*, 15182.

121) a) Y. Sun, B. Mayers, Y. Xia *Adv. Mater.* **2003**, *15*, 641. b) Sun, Y.; Xia, Y. *J. Am. Chem. Soc.* **2004**, *126*, 3892.

122) a) Hornyak, G. L.; Patrissi, C. J.; Martin, C. R. *J. Phys. Chem. B* 1997, **101**, 1548. b) Nishizawa, M.; Menon, V. P.; Martin, C. R. *Science* 1995, **268**, 700. c) Jirage, K. B.; Hulteen, J. C.; Martin, C. R. *Science* 1997, **278**, 655. d) Hulteen, J. C.; Jirage, K. B.; Martin, C. R. *J. Am. Chem. Soc.* 1998, **120**, 6603. e) Jirage, K. B.; Hulteen, J. C.; Martin, C. R. *Anal. Chem.* 1999, **71**, 4913. f) Penner, R. M.; Martin, C. R. *Anal. Chem.* 1987, **59**, 2625. g) Menon, V. P.; Martin, C. R. *Anal. Chem.* 1995, **67**, 1920. h) Kang, M. S.; Martin, C. R. *Langmuir* 2001, **17**, 2753. i) Lee, S. B.; Martin, C. R. *Anal. Chem.* 2001, **73**, 768.

123) Wang, D.; Zhou, W. L.; McCaughy, B. F.; Hampsey, J. E.; Ji, X.; Jiang, Y.-B.; Xu, H.; Tang, J.; Schmehl, R. H.; O'Connor, C.; Brinker , C. J.; Lu, Y. *Adv. Mater.* **2003**,*15*, 130.

124) a) Sanyal,A.; Sastry, M.; *Chem.Commun.* **2003** 1236. b) Anita Swami, Kumar, A.; Selvakannan, PR.; Mandal, S.; Pasricha, R.; Sastry, M *Chem. Mater*. **2003**, *15*, 17. c) Swami, A.; Kumar, A.; D`Costa, M.; Sastry, M. *J. Mater.Chem.* **2004**, *14*, 2696. d) Swami, A.; Kasture, M.; Pasricha, R.; Sastry, M. *J.Mater. Chem.* **2004**, *14*, 709. e) Sastry, M.; Swami, A.; Mandal, S.; Selvakannan, PR. *J. Mater. Chem.* **2005**, *15*, 3161.

125) Haes, A. J.; Zhao, J.; Zou, S.; Own, C. S.; Marks, L. D.; Schatz, G. C.; Van Duyne, R. P. *J. Phys. Chem. B* **2005**, *109*, 11158.

126) a) Charnay, C.; Lee, A.; Man, S.-Q.; Moran, C. E.; Radloff, C.; Bradley, R. K.; Halas, N. J. *J. Phys. Chem. B.* **2003**, *107*, 7327. b) Love, J. C.; Gates, B. D.; Wolfe, D. B.; Paul, K. E.; Whitesides, G. M.; *Nano Lett.* **2002**, *2*, 891.

127) a) Lu, Y.; Liu, G. L.; Kim, J.; Mejia, Y. X.; Lee, L. P. *Nano Lett.* **2005**, *5*, 119. b) Shumaker-Parry, J. S.; Rochholz, H.; Kreiter, M. *Adv. Mater.* **2005**, *17*, 2131.

128) Liu, Z.; Bando, Y. *Adv. Mater.* **2003**, *15*, 303.

129) Zhou, Y.; Yu, S. H.; Cui, X. P.; Wang, C. Y.; Chen, Z. Y. *Chem. Mater.* **1999**, *11*, 545.

130) Pastoriza-Santos. I.; Liz-Marzan. L. M. *Nano Lett.* **2002**, *2*, 903.

131) a)Sun, Y.; Xia. Y. *Adv. Mater.* **2003**, *15*, 695. b) Chen, J.;Herricks, T.;Geissler, M.;Xia.Y. *J.Am.Chem.Soc*. **2004**, *126*, 10854. c) Sun, Y.; Xia, Y. *Avd.Mater*. 2002, *298*, 2176.

132) Caswell, K. K.; Bender, C. M.; Murphy, C. J. *Nano Lett.* **2003**, *3*, 667.

133) Turkevich, J.; Hiller, J.; Stevenson, P. C. *Discussions Faraday Soc.* **1951**, *11*, 55.

134) Suito, E.; Uyeda, N. *Proc. Intern. Conf. Elect. Micro.*, London, **1954**, 224.

135) a) Suito, E.; Uyeda. N. *Nature* **1960,** *185*, 453. b) Suito. E.; Uyeda. N. *J. Electronmicroscopy.* **1960,** *8*, 25. c) Frank, F. C. *Discussions Faraday Soc.* **1949**, *5*, 48. d) Fran, F. C. *Acta.Cryst.* 1951, 4,497. e) Kossel, W. *Ann.Physik.* **1934**, *21*, 457. f) Stranski, I. N. *Z.Phys.Chem.* **1928**, *136*, 259. g) Chiang, Y. S.; Turkevich.J. *J.Colloid.Sci.* **1963**,*18*, 772.

136) Jin, R.; Cao, C.; Hao, E.; Metraux, G. S.; Schatz, G. C.; Mirkin, C. A. *Nature* **2003**, *425*, 487.

137) Jin, R.; Egusa. S.; Scherer. N. F. *J. Am. Chem. Soc.* **2004**, *126*, 9900.

138) ,Li, G.; Lauer, M.; Schulz, A.; Boettcher, C.; Li. F.; Fuhrhop, J.-H. *Langmuir.* **2003**, *19*, 6483.

139) Roorda, S.; van Dillen, T.; Polman, A.; Graf, C.; van Blaaferen, A.; Kooi, B. J. *Adv. Mater.* **2004**, *16*, 235.

140) Link, S.; Burda. C.; Nikoobakht El-Sayed. M. A. *J. Phys. Chem. B* **2000**, *104*, 6152.

141) a) A. N. Shipway, E. Katz, I. Willner, *ChemPhysChem* **2000**, *1*, 18-52. b) Daniel, M.; Astrue, D. *Chem.Rev.***2004**, *104*, 293. c) Beverly, K .C.; Sample, J.L.; Sampaio, J.F.; Remacle, F.; Heath, J. R.; Levine, R. D. *Proc. Natl. Acad. Sci.* U.S.A. **2002**, *99*, 6456. d) Murray, C. B.; Kangan, C. R.; Bawendi, M. G. *Annu.Rev.Mater.* **2002**, 30, 545. e) Murray, C. B.; Norris, D. J.; Bawendi, M. G. *J.Am.Chem.Soc*. **1993**, *115*, 8706. f) O'Brien, S.; Brus, L.; Murray, C. B. *J.Am.Chem.Soc.* **2001**, *123*, 12085. g) Puntes, V. F.; Krishnan, K. M.; Alivisatos, A. P. *Appl.Phys.Lett.* **2001**, *78*, 2187. h) Micic, O. I.; Jones, K. M.; Cahill, A.; Nozik, A. J. *J.Phys.Chem.B* **1998**, *102*, 9791. i) Harfenist, S. A.; Wang, Z.L.; Alvarez, M. M.; Vezmar, I.; Whetten, R. L. *J.Phys.Chem*. **1996**, 100, 13904. j) Petit, C.; Taleb, A.; Pileni, M.P. *J.Phys.Chem.B* **1999**, *103,* 1805. k) Wong, K. K.

W.; Douglas, T.; Gider, S.;Awschalom, D.D.; Mann, S. *Chem. Mater.* **1998**, *10*, 279. l) Liu, X. G.; Fu, L.; Hong, S.H.; Dravid, V.P.;Mirkin, C.A. *Adv.Mater.* **2002**, *14*, 231. m) Park, S. –J.;Taton, T. A.; Mirkin, C. A. *Science*. **2002**, *295*, 1503. n) Yamamuro, S.; Farrell, D. F.; Majetich, S. A. *Phys.Rev.B* **2002**, *65*, 224431. o) Rengarajan, R.; Jiang, P.; Larrabee, D. C.; Colvin, V. L.; Mittleman, D.M. *Phys.Rev.B* **2001**, 64, 205103. p) Doty, R. C.; Yu, H. B.; Shih, C.K. Korgel,B.A. *J.Phys.Chem.B* **2001**,*105*,8291. q) Tripp, S. L.; Puszaty, S. V.; Ribbe, A. E.; Wei, A. *J.Am.Chem.Soc*. **2002**, *124*, 7914.

142) a) Liu, X.; Fu, L.; Hong, S.; Dravid, V. P.; Mirkin, C. A. *Adv. Mater.* **2002**, *14*, 231. b) Koike, K.; Matsuyama, H.; Hirayama, Y.; Tanahashi, K.; Kanemura, T.; Kitakami, O.; Shimada, Y. *Appl. Phys. Lett.* **2001**, *78*, 784. c) Jacobs, H. O.; Whitesides, G. M. *Science* **2001**, *291*, 1763. d) Ho, P. K. H.; Thomas, D. S.; Friend, R. H.; Tessler, N. *Science* **1999**, *285*, 233. e) Renault, J. P.; Bernard, A.; Juncker, D.; Michel, B.; Bosshard, H. R.; Delamarache, E. *Angew. Chem., Int Ed.* **2002**, *41*, 2320. f) Pirrung, M. C. *Angew. Chem., Int Ed.* **2002**, *41*, 1276.

143) Fendler, J. H.; Meldrum, F. *Adv. Mater.* **1995**, *7*, 607.

144) Etzkorn, J.; Therese, H. A.; Rocker, F.; Zink, N.; Kolb, U.; Tremel, W. *Adv.Mater.* **2005**, *17*, 2372.

145) Herman, M. A.; Richter, W.; Sitter, H. *Epitaxy. Physical Principles and Technical Implementation*, Springer Series in Materials Science, Vol. 62, Springer, Berlin 2004.

146) a) Liang, J.; Chik, H.; Yin, A.; Xu. J. *J. Appl. Phys.* **2002**, *91*, 2544. b) Crouse, D.; Lo, Y. –H.; Miller, A. E.; Crouse, M. *Appl. Phys. Lett.* **2000**, *76*, 49.

147) a) Bullen, H. A.; Garrett, S. J;. *Nano Let*. **2002**, *2*, 739. b) H. Masuda, K.; Yasui, K.; Nishio K. *Adv. Mater.* **2000**, *12*, 1031. c) H. Masuda, K.; Yasui, K.; Sakamoto, Y.; Nakao, M.; Tamamura, T.; Nishio, K. Jpn. *J. Appl. Phys*. **2001**, *40*, L1267. d) Sander, M. S.; Tan, L.-S. *Adv. Func. Mater.* **2003**, *13*, 393.

148) a) Craighead, H. G. *Science* **2000**, *290*, 1532. b) Knaack, S. A.; Eddington, J.; Leonard, Q.; Cerrina, F.; Onellion, M. *Appl. Phys. Lett.* **2004**, *84*, 3388.

149) Soong, R. K.; Bachand, G. D.; Neves, H. P.; Olkhovets, A. G.; Craighead, H. G.; Montenango, G. D. *Science* **2000**, *290*, 1555.

150) a) Xia, Y.; Whitesides, G. M. *Annu. Rev. Mater. Sci.* **1998**, *28*, 153. b) Chou, S. Y.; Krauss, P. R.; Zhang, W.; Guo, L.; Zhuang, L. *J. Vac, Sci Technol. B* **1997**, *15*, 28.

151) a) Nikoobakht, B.; Wang, Z. L.; El-Sayed, M. A;. *J. Phys. Chem. B* **2000**, *104*, 8635. b) Korgel, B. A.; Fullam, S.; Connoly, S.; Fitzmaurice, D. *J. Phys. Chem. B* **1998**, *122*, 4640. c) Harfenist, S. A.; Wang, Z. L.; Alvarez, M. M.; Vezmar, I.; Whetten R. L. *J. Phys. Chem.* **1996**, *100*, 13904. d) Pileni, M. P *Langmuir*. **1997**, *13*, 3266. e) Pileni, M. P. *New J. Chem.* **1998**, *22*, 693.

152) a) Pileni, M. P. *J. Phys. Chem. B* **2001**, *105*, 3358. b) Collier, C. P.; Vossmeyer, T.; Heath, J. R. *Ann. Rev. Phys. Chem.* **1998**, *49*, 71. c) Wang, Z. L. *Adv. Mater.* **1998**, *10*, 13.

153) Andres, R. P.; Bielefeld, J. D.; Henderson, J. I.; Janes, D. B.; Kolagunta, *V. R. Science.* **1996**, *273*, 1690.

154) a) Selvakannan, PR.; Mandal, S.; Pasricha, R.; Sastry, M. *J. Colloid Int. Sci* . **2004**, *279*, 124. b) Sarathy, K. V.; Raina, G.; Yadav, R. T.; Kulkarni, G. U.; Rao, C. N. R. *J. Phys. Chem. B* **1997**, *101*, 9876. c) Brown, L. O.; Hutchison, J. E. *J. Phys. Chem. B* **2001**, *105*, 8911. d) He, S.; Yao, J.; Jiang, P.; Shi, D.; Zhang, H.; Xie, S.; Pang, S.; Gao, H.; *Langmui.* **2001**, *17*, 1571. e) Zhao, S.Y.; Wang, S.; Kimura, K. *Langmuir* **2004**, *20*, 1977. f) Stoeva, S.; Klabunde, K. J.; Sorensen, C.M.; Dragieva, I. J. *Am. Chem. Soc.* **2002**, *124*, 2305. g) Liu, S.; Zhu, T.; Hu, R.; Liu, Z. *Phys. Chem. Chem. Phys*. **2002**, *4*, 6059.

155) Kiely, C. J.; Fink, J.; Brust, M.; Bethell D.; Schiffrin, D. J. *Nature*. **1998**, *396*, 444.

156) Kiely, C. J.; Fink, J., Zheng, J. G.; Brust, M.; Bethell D.; Schiffrin, D. J. *Adv. Mater.* **2000**, *12*, 640.

157) Trou, M.; Saville, D. A.; Aksay, I. A. *Science*. **1996**, *272*, 706.

158) a) Giersig, M.; Mulvaney, P. J. Phys. Chem. **1993**, *97*, 6334. b) Giersig, M.; Mulvaney, P. *Langmuir* **1993**, *9*, 3408.

159) Teranishi, T.; Hosoe, M.; Tanaka, T.; Miyake, M. *J. Phys. Chem. B* **1999**, *103*, 3818.

160) Sagiv, J. *J. Am. Chem. Soc*. **1980**, *102*, 92.

161) Nuzzo, R. G.; Allara, D. L.; Nuzzo, R. G.; Allara, D. L. *J. Am. Chem. Soc*. **1983**, *105*, 4481.

162) Colvin, V. L.; Goldstein, A. N.; Alivisatos, A. P. *J. Am. Chem. Soc.* **1992**, *114*, 5221.

163) Gole, A.; Sainkar, S.R.; Sastry, M. *Chem.Mater*. **2000**, *12*, 1234.

164) Iler, R.K. *J.Colloid Interface Sci.* **1966**, *21*, 569.

165) a) Decher, G.; Hong, J. –D.; Schmitt, J. *Thin Solid Films*. **1992**, *210*, 504. b) Lvov, Y.; Essler, F.; Decher, G.; *J. Phys. Chem.* **1993**, *97*, 13773.

166) Mamedov, A.; Ostrander, J.; Aliev, F.; Kotov, N.A. *Langmuir*. **2000**, *16*, 3941.

167) Hao, E.; Yang, B.; Ren, H.; Qian, X.; Xie, R.; Shen, J.; Li, D. *Mater.Sci.Engg.C.* **1999**, *10*, 119.

168) Lvov, Y.; Ariga, K.; Onda, M.; Ichinose, I.; Kunitake, T. *Langmuir.* **1997**, *13*, 6195.

169) Cassagneau, T.; Mallouk, T.E.; Fendler, J.H. *J.Am.Chem.Soc.* **1998**, *120*, 7848.

170) a) Maya, L.; Muralidharan, G.; Thundat, T.G.; Kenik, E.A. *Langmuir*. **2000**, *16*, 9151. b) Feldheim, D.L.; Grabar, K.C.; Natan, M.J.; Mallouk, T.E.; *J.Am.Chem.Soc.* **1996**, *118*, 7640. c) He, J.-A.; Valluzzi, R.; Yang, K.; Dolukhanyan, T.; Sung, C.; Kumar, J.; Tripathy, S.K.; Samuelson, L.; Balogh, L.; Tomalia, D.A. *Chem.Mater.* **1999**, *11*, 3268.

171) Kumar, A.; Mandale, A.B.; Sastry, M. *Langmuir.* **2000**, *16*, 6921.

172) Kumar, A.; Mukherjee, P.; Guha, A.; Adyantaya, S.D.; Mandale, A.B.; Kumar, R.; Sastry, M. *Langmuir.* **2000**, *16*, 9775.

173) a) Shenton, W.; Pum, D.; Sleytr, B.; Mann, S. *Nature*. **1997**, *389*, 585. b) Bergkvist, M.; Mark, S. S.; Yang, X.; Angert, E. R.; Batt, C. A. *J. Phys. Chem. B* **2004**, *108*, 8241.

174) Swami, A.; Kumar, A.; Selvakannan, PR.; Mandal, S.; Pasricha, R.; Sastry, M. *Chem. Mater.* **2003**, *15*, 17.

175) Tian, Y.; Wu, C.; Fendler, J.H. *J.Phys.Chem.* **1995**, *98*, 4913.

176) a) Sastry, M.; Patil, V.; Mayya, K. S. *Langmuir*. **1997**, *13*, 4490. b) Sastry, M.; Patil, V.; Sainkar, S. R. *J. Phys. Chem. B* **1998**, *102*, 1404. c) Patil, V.; Sastry, M. *Langmuir*. **2000**, *16*, 2207. d) Patil, V.; Sastry, M. *Langmuir*. **1997**, *13*, 5511. e)

Sastry, M.; Mayya, K. S.; Patil, V.; Paranjape, D. V.; Hegde, S. G. *J. Phys. Chem. B* **1997**, *101*, 4954. f) Mayya, K. S.; Sastry, M. *J. Phys. Chem. B* **1997**, *101*, 9790. g) Mayya, K. S.; Sastry, M. *Langmuir*. **1998**, *14*, 74. h) Mayya, K. S.; Patil, V.; Sastry, M. *Langmuir.* **1997**, *13*, 2575. i) Mayya, K. S.; Patil, V.; Sastry, M. *J. Chem. Soc., Faraday Trans.* **1997**, *93*, 3377. j) Sastry, M.; Mayya, K.S. *J.Nano.Res.* **2000**, *2*, 183.

177) a) Mayya, K. S.; Patil, V.; Kumar, P. M.; Sastry, M. *Thin Solid Films*, **1998**, *312*, 300. b) Zhavnerko, G. K.; Agabekov, V. E.; Gallyamov, M. O.; Yaminsky, I. V.; Rogach, A. L. *Coll.Surf.A.* **2002**, *202*, 233.

178) Zhavnerko, G. K.; Agabekov, V. E.; Gallyamov, M. O.; Yaminsky, I. V.; Rogach, A. L. *Coll.Surf.A.*, **2002**, *202*, 233.

179) Muramatsu, K.; Takahashi, M.; Tajima, K.; Kobayashi, K. *J.Colloid Interface Sci.*, **2001**, *242*, 127.

180) Lee, D. K.; Kang, Y. S.; Lee, C. S.; Stroeve, P. *J.Phys.Chem.B*. **2002**, *106*, 7267.

181) Kang, Y. S.; Lee, D. K.; Lee, C. S.; Stroeve, P. *J.Phys.Chem.B*. **2002**, *106*, 9341.

182) Sastry, M.; Rao, M.; Ganesh, K. N. *Acc. Chem. Res*. **2002**, *35*, 847.

183) Swami, A.; Selvakannan, PR.; Pasricha, R.; Sastry, M. *J. Phys. Chem. B.* **2004**, *108*, 19269.

184) Ganguly, P.; Sastry, M.; Pal S.; Shashikala, M.N. *Langmuir*, **1995**, *11*, 1078.

185) a) Sastry, M.; Ramakrishnan, V.; Pattarkine, M.; Ganesh, K. N. *J. Phys. Chem. B*, **2001**, *105*, 4409. b) Sastry, M. *Trends Biotech.*, **2002**, *20*, 185.

186) a) Gole, A.; Dash, C.; Rao, M.; Sastry, M. *J. Chem. Soc., Chem. Commun.* **2000**, 297. b) Gole, A.; Dash, C.; Mandale, A. B.; Rao, M.; Sastry, M. *Anal. Chem.*, **2000**, *72*, 4301. c) Gole, A.; Sastry, M. *Biotechnol. Bioeng.*, **2001**, *74*, 172. d) Gole, A.; Chaudhari, P.; Kaur, J.; Sastry, M. *Langmuir*, **2001**, *17*, 5646. e) Gole, A.; Vyas, S.; Sainkar, S. R.; Lachke, A. L.; Sastry, M. *Langmuir*, **2001**, *17*, 5964. f) Phadtare, S.; Parekh, P.; Gole, A.; Patil, M.; Pundle, A.;Prabhune, A.; Sastry, M. *Biotechnol. Prog.*, 2002, *18,* 483.

187) Patil,V.; Malvankar,R.B.; Sastry, M. *Langmuir* **1999,** *15,* 8197.

188) a) Sastry, M.; Patil,V.; Sainkar,S.R. *J.Phys.Chem.B.* **1998,** *102,* 1404. b) Patil,V.; Sastry, M. *Langmuir.* **1998** *14* 2707.

189) Patil,V.; Sastry,M. *J.Chem.Soc. Faraday Trans.* **1997,** *93,* 4347.

190) a) Mandal,S.; Sainkar,S.R.; Sastry,M. *Nanotechnology* **2001,** *12,* 358. b) Gole, A.; Kumar, A.; Phadthare,S.; Mandale,A.B.; Sastry,M. *PhysChemComm.* **2001,** *4,* 92.

Chapter II

Characterization techniques

The different experimental techniques used during the course of the present work are discussed in this chapter.

2.1 Introduction.

The work presented in this thesis lays emphasis on the following aspects: 1) synthesis of metal nanoparticles through an environmentally benign process using plant extracts as natural reducing agents, 2) shape controlled synthesis of triangular and hexagonal gold particles using lemongrass leaf extract as a reducing agent, 3) study of the growth of gold nanotriangles using citric acid reduction method as a model system, and the shape transformation of gold nanotriangles by chemical and physical methods and 4) fabrication of thin films of inorganic nanoparticles by either entrapment of preformed nanoparticles or the precursor metal ions in chargeable lipid films. Various characterization techniques such as UV-visible spectroscopy, Fourier Transform Infrared Spectroscopy (FTIR), Transmission Electron Microscopy (TEM), Scanning Electron Microscopy (SEM), Energy dispersive microanalysis (EDAX), X-ray diffraction (XRD), X-ray photoelectron spectroscopy (XPS), Nuclear Magnetic resonance spectroscopy (NMR), Light scattering, Isothermal titration calorimetry (ITC), Laser (Nd YAG), Thermal vapor deposition, Quartz crystal microgravimetry (QCM), have been used to characterize while pursuing these aspects. This chapter is devoted to explain the basic principles and the techniques used for the characterization.

2.2 Uv-vis spectroscopy.

In the work described in this thesis, UV-visible spectroscopy was used for monitoring the signatures of spherical and anisotropic gold nanoparticles during their formation in the different reaction mixtures. This technique was also used to monitor the entrapment or formation of inorganic nanoparticles within lipid thin films.

Theory: The total energy of a molecule is the sum of its electronic energy, vibrational energy and rotational energy. The magnitude of these energies decreases in the following order: E_{elec}, E_{vib} and E_{rot}. Energy absorbed in the UV region produces changes in the electronic energy of the molecule resulting from transitions of valence electrons in the molecule. The relationship between the energy absorbed in an electronic transition and the frequency (ν), wavelength (λ) and wavenumber ($\bar{\nu}$) of radiation producing the transition is

$$\Delta E = h\nu = hc/\lambda = h \cdot \nu c$$

where, h is Planck's constant, c is the velocity of light and ΔE is the energy absorbed in an electronic transition in a molecule from a low-energy state (ground state) to a high energy state (excited state). The energy absorbed is dependent on the energy difference between the ground state and the excited state; the smaller the difference in energy, the longer the wavelength of absorption. Since UV energy is quantized, the absorption spectrum arising from a single electronic transition should consist of a single, discrete line. A discrete line is not obtained since electronic absorption is superimposed on rotational and vibrational sublevels as shown in Fig. 2.1. The principal characteristics of an absorption band are its position and intensity. The position of an absorption band correspond to the wavelength of radiation whose energy is equal to that required for an electronic transition. The intensity of absorption is largely dependent on two factors: the probability of interaction between the radiation energy and the electronic system and the difference between the ground and excited state. The intensity of absorption may be expressed as transmittance (T), defined by

$$T = I/I_0$$

where I_0 is the intensity of the radiant energy striking the sample, and I is the intensity of the radiation emerging from the sample. A more convenient expression of absorption intensity is that derived from the Lambert-Beer law, which establishes a relationship between the absorbance, the sample thickness and the concentration of the absorbing species. The relationship is expressed as

$$A = abc$$

where, A is the measured absorbance, a is absorptivity , b is the cell-path length, and c is the analyte concentration.

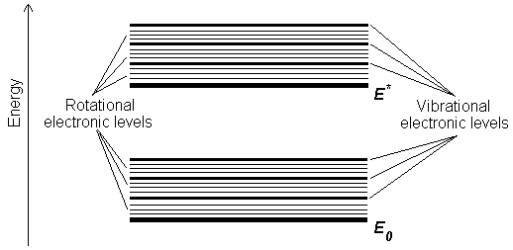

Figure 2.1: *Energy level diagram of a diatomic molecule.*

UV-visible spectroscopy is a powerful tool for the characterization of colloidal particles [1]. In particular, noble metal particles are ideal candidates for study with UV

vis spectroscopy, since they exhibit strong surface plasmon resonance absorption in the visible region and are highly sensitive to the surface modification. The light absorption by small metal particles is described by Mie theory [1]. The absorption spectrum of particles in a given solvent can be calculated from optical constants of the bulk metal [2]. The absorption spectrum of spherical particles of sizes between 3 to 30 nm does not strongly depend on particle size. This is because the particles are below the size at which higher order term in the Mie formulae for the absorption constant becomes significant. Thus one has to regard only the dipole term, which depends only on the total metal concentration in the solution and not on particle size. The absorption coefficient α (mol-1 L cm-1) is calculated from the relation 2.1

$$\alpha = \frac{18\pi}{\ln 10} \frac{10^5}{\lambda} \frac{Mn_0^3}{\rho} \frac{\varepsilon_2}{(\varepsilon_1 + 2n_0^2) + \varepsilon_2^2} \qquad \text{..... (2.1)}$$

where λ is the wavelength of light, M and ρ are the molecular weight and density of the metal, n_o is the refractive index of the solvent and ε_1 and ε_2 are the real and imaginary parts of the dielectric constant of the metal. When the size of the particles becomes smaller than the mean free path of the electrons, the absorption bands are broadened this is accounted by using size-corrected values of ε_2 [3].

$$\varepsilon_2 = \varepsilon_{2(bulk)} + \left(\omega_p^2 / \omega^3\right) (V_F / R) \qquad \text{..... (2.2)}$$

where ω is the frequency of light, ω_p the plasmon frequency, V_F the electron velocity at the Fermi level and R the particle radius (R/V_F, mean time of the free movement of the electrons). Resonance with the incident light is reached at the wavelength where the negative value of ε_1 of the metal is equal to twice the dielectric constant of the medium.

Gold nanoparticles possess plasmon resonances in the visible range (~514 nm). Resonance is produced by a collective excitation of all the free electrons in the particles. As shown in Fig.2.2 the movement of the electrons under the influence of electric field vector of the incoming light leads to a dipole oscillations across the particle sphere, the positive polarization charge acting as a restoring force which makes the electrons oscillate. Thus the electron density within surface layer, the thickness of which is about equal to the screening length of a few angstroms, oscillate whereas the density in the

interior of the particle remains constant ("surface plasmon"). Therefore, any changes in the electron density of this surface layer will lead to changes in the plasmon absorption [4].

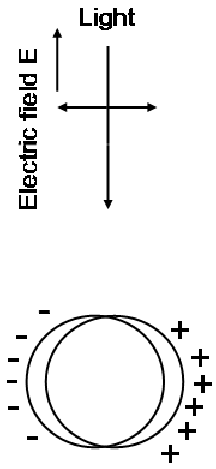

Figure 2.2: *Schematic representation of polarization of a spherical metal particle by the electrical field vector of the incoming light.*

Higher order modes become more dominant with increasing particle size, causing the plasmon absorption band to red shift and resulting in increased bandwidth, because for larger particles, the light cannot polarize the nanoparticles homogeneously and retardation effects lead to the excitation of higher order modes [4]. Within the size range of 25 nm the nanoparticles can be treated with dipolar approximation and is independent of the particle size. Though, below the size limit of 10 nm the particles start showing size dependence of the plasmon resonance band and ultimately disappear for particles of size less than 2 nm. This is attributed to the decreasing validity of the free electron gas model assumption [4].

Gans extended the Mie's theory for spherically shaped particles to cylindrical or oblate nanoparticles within the dipole approximation [5]. The plasmon resonance for nanorods is observed to split into two bands. The high energy band corresponds to the oscillation of the electrons perpendicular to the major axis of the rods and is referred to as the transverse plasmon absorption. The other absorption band, which is red-shifted to lower energies, is caused by the oscillation of the electrons along the major axis of the nanorods and is known as the longitudinal surface plasmon absorption. The transverse

plasmon absorption has linear dependence on the aspect ratio (ratio between the length and width of the particle) and the dielectric constant of the medium [4].

Similarly in case of flat triangular metal nanoparticles, the electronic oscillations are said to set up in the plane of the particle and out of the plane of the particle. These lead to the appearance of a strong band at higher wavelength and a weak band at lower wavelength. For gold nanoprisms, the higher wavelength band is assigned to the in plane dipolar plasmon resonance that is observed to be very sensitive to the edge length and the lower wavelength (usually around ~ 530 nm) to out of the plane dipolar plasmon resonance. In certain cases even a weak band intermediate to these two regions is observed and is assigned to the in plane quadrupole mode of plasmon resonance [6].

Optical absorption features are also exhibited by semiconducting nanoparticles and explained by the excitation of the valence shell electrons to the conduction band, creating an electron-hole pair in the system. As discussed in the introduction chapter, the semiconducting nanoparticles display size quantization effect. The dependence of the in crease in the band gap energy (ΔE_{BG}) in the semiconducting nanoparticles on their size in terms of the radius (R) of spherical nanopaticle is expressed as [7]:

$$\Delta E_{BG} = \frac{\hbar^2 \pi^2}{2}\left(\frac{1}{m_e}+\frac{1}{m_h}\right)\frac{1}{R^2} - \frac{1.8e^2}{\varepsilon}\cdot\frac{1}{R} \qquad \text{..... (2.3)}$$

where m_e and m_h correspond to the effective masses of electron and hole, respectively and ε is the dielectric constant of the semiconducting material.

The work described in this thesis, UV-Vis spectroscopy was used to monitor the formation of gold and silver nanoparticles during the reduction $AuCl_4^-$ and Ag^+ ions using different plant extracts. UV-vis-NIR measurements were also carried out to monitor the growth of the gold nanoparticles during the citric acid reduction of aqueous $AuCl_4^-$ ions leading to the formation of triangular and spherical nanoparticles. In the synthesis of nanoparticulate thin films using thermally evaporated lipid films, UV-vis spectroscopy was used for monitoring the entrapment of gold nanoparticles and for the formation of TiO_2, ZrO_2 and CdS nanoparticles. These measurements were done on Hewlett-Packard diode array spectrophotometer (model HP-8452) operated at a resolution of 2 nm and on JASCO V570 UV/VIS/NIR operated at a resolution of 1 nm.

2.3 Fourier transform infrared spectroscopy (FTIR).

Principle: The atoms in a molecule do not remain in a fixed relative position and vibrate about some mean position. Due to this vibrational motion, if there is a periodic alternation in the dipole moment then such mode of vibration is infrared (IR) active. The IR region of the electromagnetic spectrum is 100 μm – 1 μm wavelength. The vibrating molecule absorbs energy only from radiation with which it can coherently interact, i.e. the radiation of its own oscillation frequency. The appearance or non-appearance of certain vibrational frequencies gives valuable information about the structure of a particular molecule. Each functional group have specific range of vibrational frequencies and are very sensitive to the chemical environment and the neighbouring, thus provide valuable information regarding the presence of certain functional groups in the specific sample for their further characterization and identification. The frequency of vibration is given by the relation:

$$\nu = \frac{1}{2\pi} \sqrt{\frac{k}{\mu}} \qquad \text{..... (2.4)}$$

where, k is force constant; μ is reduced mass.

Silicon is the most commonly used substrate for IR measurements, for variety of reasons. It is chemically very stable and generally not very reactive even at high temperatures. It is excellent for optical studies of deposited films in the visible region using reflection techniques. It does not have strong lattice absorption bands in the useful regions of the infrared and thus can be used for transmission studies in this region. To correct for the lattice absorption bands in silicon, a reference silicon sample is used as a reference.

FTIR measurements of the films of nanoparticles in the present study were carried out in the diffuse reflectance mode at a resolution of 4 cm^{-1} on a Perkin-Elmer FTIR Spectrum One spectrophotometer.

2.4 Transmission electron microscopy (TEM).

Working principle: In TEM analysis, a thin specimen is illuminated with electrons in

which the electron intensity is uniform over the illuminated area. As the electrons travel through the specimen, they are either scattered by a variety of processes or they may remain unaffected by the specimen. The end result is that a nonuniform distribution of electrons emerges from the exit surface of the specimen, that contains all the structural and chemical information about the specimen. Electron microscope is constructed to display this nonuniform distribution of electrons in two different ways. Angular distribution of scattering can be viewed in the form of scattering patterns, usually called diffraction patterns, and spatial distribution of scattering can be observed as contrast in

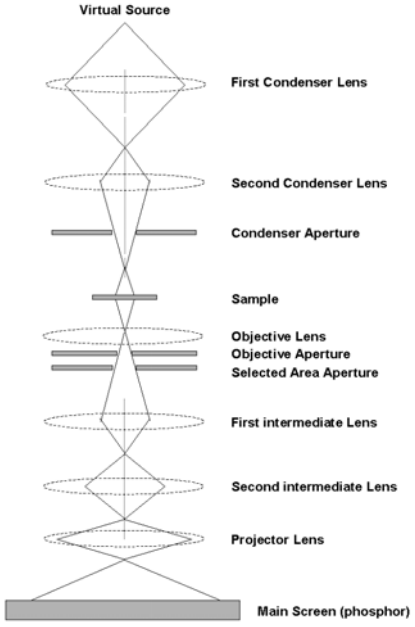

Figure 2.3: *Diagram showing the various elements of the TEM instrument.*

images of the specimen. The advantage of this arrangement is the possibility of directly viewing the area from which the diffraction pattern arises. The basic components of transmission electron microscope are shown in Fig. 2.4.

A technical explanation of a typical TEMs workings is as follows :

1. The virtual source that is an electron gun, producing a stream of monochromatic electrons.
2. This stream is focused to a small, thin, coherent beam by the use of condenser lenses 1 and 2. The first lens usually controlled by a spot size knob largely determines the spot size; the general size range of the final spot that strikes the

sample. The second lens usually controlled by the intensity or brightness knob actually changes the size of the spot on the sample; changing it from a wide dispersed spot to a pinpoint beam.

3. The beam is restricted by the condenser aperture, knocking out high angle electrons.
4. The beam strikes the specimen and parts of it are transmitted.
5. This transmitted portion is focused by the objective lens into an image.
6. Optional objective and selected area metal apertures can restrict the beam; the objective aperture enhancing contrast by blocking out high-angle diffracted electrons, the selected area aperture enabling the user to examine the periodic diffraction of electrons by ordered arrangements of atoms in the sample
7. The image is passed down the column through the intermediate and projector lenses, being enlarged all the way.

The image strikes the phosphor image screen and light is generated, allowing the user to see the image. The darker areas of the image represent those areas of the sample that fewer electrons were transmitted through (they are thicker or denser). The lighter areas of the image represent those areas of the sample that more electrons were transmitted through (they are thinner or less dense)

In the present study, TEM has been used for observing the size and shape distribution of gold and silver nanoparticles synthesized using different plant extracts. TEM measurements were also carried out to monitor the growth of triangular gold nanoparticles during synthesis by lemongrass leaf extract and citric acid reduction of $AuCl_4^-$ ions. Further, TEM was used for observing the particles size and shape distribution of gold nanoparticles entrapped and for observing TiO_2, ZrO_2 and CdS nanoparticles synthesized in the lipid thin films. The samples for the metal nanoparticles synthesized using different plant extracts were prepared by drop coating on a carbon coated copper grid. For measuring the growth of gold nanotriangles by TEM measurements, samples were prepared by evaporating the drop coated carbon coated copper grid in vacuum. By this method samples on the carbon coated copper grid could be made within 2 minutes. For imaging the gold nanoparticles entrapped in lipid thin films and TiO_2, ZrO_2 and CdS nanoparticles synthesized within lipid thin films, the

samples were prepared by following the entrapment and synthesis of nanoparticles within thermally evaporated lipid thin films deposited on carbon coated copper grids. The TEM measurements were done on a JEOL model 1200EX instrument operated at an accelerating voltage of 120 kV. High resolution transmission electron microscopy (HRTEM) of the gold triangular and hexagonal particles samples prepared on carbon coated grids were carried on a JEOL model 3010 operated at an accelerating voltage of 300 kV.

2.5 Scanning electron microscopy.

Scanning Electron Microscopy is extremely useful for the direct observations of surfaces because they offer better resolution and depth of field than optical microscope. The two major components of an SEM are the electron column and control console [8]. The electron column consists of an electron gun and two or more electron lenses, which influence the path of electrons travelling down an evacuated tube. The control console consists of a cathode ray tube (CRT) viewing screen and computer to control the electron beam. The base of the column is usually taken up with vacuum pumps that produce a vacuum of about 10-6 Torr. The purpose of electron gun is to provide a stable beam of electrons. Generally, tungsten or Lanthanum hexaboride (LaB6) thermionic emitters are used as electron gun. The most common electron gun consists of three components: tungsten wire filament serving as cathode, grid cap and anode. A tungsten filament is heated resistively by a current to a temperature of 2000-2700 K. This results in an emission of thermionic electrons from the tip over an area about 100 μm x 150 μm. The electron gun generates electrons and accelerates them to energy in the range 0.1 – 30 keV. The spot size from a tungsten hairpin gun is too large to produce a sharp image unless electron lenses are used to demagnify it and place a much smaller focused electron spot on the specimen. Most SEMs can produce an electron beam at the specimen with a spot size less than 10 nm that contains sufficient probe current to form an acceptable image. The beam emerges from the final lenses into the specimen chamber, where it interacts with the specimen to a depth of approximately 1 μm and generates the signals used to form an image. The scanned image is formed point by point. The deflection system causes the beam to move to a series of discrete locations along a line and then

along another line below the first and so on, until a rectangular 'raster' is generated on the specimen. Simultaneously, the same scan generator creates a similar raster on the viewing screen. Two pairs of the electromagnetic deflection coils (scan coils) are used to sweep the beam across the specimen. The first pair of the coils deflects the beam off the optical axis of the microscope and the second pair bends the beam back onto the axis at the pivot point of the scan. Contrast in an image arises when the signal collected from the beam specimen interactions varies from one location to another. When the electron beam impinges on the specimen, many types of signals are generated and any of these can be displayed as an image. The two signals most often used to produce SEM images are secondary electrons (SE) and backscattered electrons (BSE). Most of the electrons are scattered at large angles (from 0^o to 180^o) when they interact with the positively charged nucleus. These elastically scattered electrons usually called 'backscattered electrons' (BSE) are used for SEM imaging. Some electrons scatter inelastically due to the loss in kinetic energy upon their interaction with orbital shell electrons. Due to electron bombardment, phonons are set up in the specimen resulting considerable heating of the specimen. Incident electrons may knock off loosely bound conduction electrons out of the sample. These are secondary electrons (SE) and along with backscattered electrons are widely used for SEM topographical imaging. Both SE and BSE signals are collected when a positive voltage is applied to the collector screen in front of detector. When a negative voltage is applied on the collector screen only BSE signal is captured because the low energy SEs are repelled. Electrons captured by the scintillator/ photomultiplier are then amplified and used to form an image in the SEM. If the electron beam knocks off an inner shell electron, the atom rearranges by dropping an outer shell electron to an inner one. This excited or ionized atom emits an electron commonly known as the Auger electron. Recently Auger electron spectroscopy (AES) is useful to provide compositional information. Instead of excited atom releasing Auger electron, it can release a photon of electromagnetic radiation. If the amount of energy released is high, the photon will be an X-ray photon. These electrons are characteristic of the sample and can be used for analysis. This type of analysis is known as Energy Dispersive analysis of X-rays (EDAX). SEM measurements were carried out to image the micron size triangular and hexagonal gold particles synthesized using lemongrass leaf extract. EDAX attachment of

the SEM instrument was used for the elemental analysis of crude geranium leaf extract and for analysing the presence of Cd and S species in the AOT thin films after sequential immersion in aqueous $CdCl_2$ and Na_2S solutions for the formation of CdS nanoparticles. These measurements were performed on a Leica Stereoscan-440 scanning electron microscopy (SEM) equipped with a Phoenix EDAX attachment.

2.6 X-ray diffraction (XRD).

X-ray Generation & Properties: X-rays are electromagnetic radiations with typical photon energies in the range of 100 eV - 100 keV. For diffraction applications, only short wavelength x-rays (hard x-rays) in the range of a few angstroms to 0.1 angstrom (1 keV - 120 keV) are used. Because the wavelength of x-rays is comparable to the size of atoms, they are ideally suited for probing the structural arrangement of atoms and molecules in a wide range of materials. The energetic x-rays can penetrate deep into the materials and provide information about the bulk structure. X-rays are produced generally by either x-ray tubes or synchrotron radiation. In a x-ray tube, which is the primary x-ray source used in laboratory x-ray instruments, x-rays are generated when a focused electron beam accelerated across a high voltage field bombards a stationary or rotating solid target. As electrons collide with atoms in the target and slow down, a continuous spectrum of x-rays are emitted, which are termed Bremsstrahlung radiation. The high energy electrons also eject inner shell electrons in atoms through the ionization process. When a free electron fills the shell, a x-ray photon with energy characteristic of the target material is emitted. Common targets used in x-ray tubes include Cu and Mo, which emit 8 keV and 14 keV x-rays with corresponding wavelengths of 1.54 Å and 0.8 Å, respectively. (The energy E of a x-ray photon and it's wavelength is related by the equation $E = hc/\lambda$, where h is Planck's constant and c the speed of light). In recent years synchrotron facilities have become widely used as preferred sources for x-ray diffraction measurements. Synchrotron radiation is emitted by electrons or positrons traveling at near light speed in a circular storage ring. These powerful sources, which are thousands to millions of times more intense than laboratory x-ray tubes, have become indispensable tools for a wide range of structural investigations and brought have advances in numerous fields of science and technology.

Lattice Planes and Bragg's Law: X-rays primarily interact with electrons in atoms. When x-ray photons collide with electrons, some photons from the incident beam will be deflected away from the direction where they originally travel, much like billiard balls bouncing off one another. If the wavelength of these scattered x-rays did not change (meaning that x-ray photons did not lose any energy), the process is called elastic scattering (Thompson Scattering) in that only momentum has been transferred in the scattering process. These are the x-rays that we measure in diffraction experiments, as the scattered x-rays carry information about the electron distribution in materials. On the other hand, in the inelastic scattering process (Compton Scattering), x-rays transfer some of their energy to the electrons and the scattered x-rays will have different wavelength than the incident x-rays. Diffracted waves from different atoms can interfere with each other and the resultant intensity distribution is strongly modulated by this interaction. If the atoms are arranged in a periodic fashion, as in crystals, the diffracted waves will consist of sharp interference maxima (peaks) with the same symmetry as in the distribution of atoms. Measuring the diffraction pattern therefore allows one to deduce the distribution of atoms in a material. The peaks in a x-ray diffraction pattern are directly related to the atomic distances. Fig. 2.4 shows incident x-ray beam interacting with the atoms arranged in a periodic manner as shown in 2 dimensions. The atoms, represented as spheres in the figure, can be viewed as forming different sets of planes in the crystal.

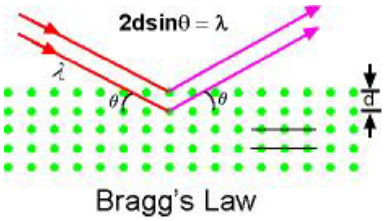

Figure 2.4: *X-ray reflections from a crystal.*

For a given set of lattice plane with an inter-plane distance of d, the condition for a diffraction (peak) to occur can be simply written as:

$$2d \sin\theta = n \lambda \qquad \ldots\ldots (2.5)$$

which is known as the Bragg's law, after W.L. Bragg, who first proposed it. In the equation, λ is the wavelength of the x-ray, θ the scattering angle, and n an integer representing the order of the diffraction peak. The Bragg's Law is one of most important

laws used for interpreting x-ray diffraction data. It is important to point out that Bragg's Law applies to scattering centers consisting of any periodic distribution of electron density. In other words, the law holds true if the atoms are replaced by molecules or collections of molecules, such as colloids, polymers, proteins and virus particles.

Powder Diffraction: Powder XRD, Debye-Scherrer method is particularly used for characterizing samples in the present work. As the name suggests, the sample is usually in a powdery form, consisting of fine grains of single crystalline material to be studied. The technique is used also widely for studying particles in liquid suspensions or polycrystalline solids (bulk or thin film materials). The term 'powder' really means that the crystalline domains are randomly oriented in the sample. Therefore when the 2-D diffraction pattern is recorded, it shows concentric rings of scattering peaks corresponding to the various d spacings in the crystal lattice. The positions and the intensities of the peaks are used for identifying the underlying structure (or phase) of the material. For example, the diffraction lines of graphite would be different from diamond even though they both are made of carbon atoms. This phase identification is important because the material properties are highly dependent on structure. Powder diffraction data can be collected using either transmission or reflection geometry. Because the particles in the powder sample are randomly oriented, these two methods yield the same data.

Samples for the XRD measurements of gold and silver nanoparticles synthesized using different plant extracts were prepared by drop coating on glass substrates followed by air-drying. In case of TiO2, ZrO2 and CdS nanoparticles the samples were prepared by synthesizing them within the thermally evaporated lipid thin films coated on glass substrates. The XRD measurements were carried out on a Phillips PW 1830 instrument operating at a voltage of 40 kV and a current of 30 mA with Cu-Ka radiation.

2.7 X-ray photoelectron spectroscopy (XPS).

X-ray Photoelectron Spectroscopy known as XPS has been developed from the Fifties by Professor K. Siegbahn for which he was awarded the Physics Nobel Prize in 1981. XPS is surface science technique used to study the composition and electronic state of the surface region of a sample. Since, the technique provides a quantitative analysis of

the surface composition is sometimes known by the alternative acronym, ESCA (**E**lectron **S**pectroscopy for **C**hemical **A**nalysis).

Working Principle: XPS is based on well-known photoelectric effect (a single photon in/electron out process) first explained by Einstein in 1905. Photoelectron spectroscopy uses monochromatic sources of radiation (i.e. photons of fixed energy given by relation, $E = h\nu$). In XPS the photon is absorbed by an atom in a molecule or solid, leading to ionization and the emission of a core (inner shell) electron. The kinetic energy distribution of the emitted photoelectrons (i.e. the number of emitted photoelectrons as a function of their kinetic energy) can be measured using any appropriate electron energy analyser and a photoelectron spectrum can thus be recorded. The one way to look at the overall process of photoionization is follows :

$$A + h\nu = A^{+} + e^{-}$$

Conservation of energy then requires that:

$$\mathbf{E(A) + h\nu = E(A^{+}) + E(e^{-})} \qquad \text{..... (2.6)}$$

Since the electron's energy is present solely as kinetic energy (KE) this can be rearranged to give the following expression for the KE of the photoelectron:

$$\mathbf{KE = h\nu - (E(A^{+}) - E(A))} \qquad \text{..... (2.7)}$$

The final term in brackets, representing the difference in energy between the ionized and neutral atoms, is generally called the *binding energy* (BE) of the electron - this then leads to the following commonly quoted equation:

$$\mathbf{KE = h\nu - BE} \qquad \text{..... (2.8)}$$

the binding energies (BE) of energy levels in solids are conventionally measured with respect to the Fermi-level of the solid, rather than the vacuum level. This involves a small correction to the equation given above in order to account for the work function (ϕ) of the solid,

$$\mathbf{KE = h\nu - BE - \phi} \qquad \text{..... (2.9)}$$

Employing photons with fixed energy $h\nu$, it is obvious that if kinetic energy KE and work function ϕ of the sample are measured, it is possible to measure binding energy of electron in solid. Binding energies being characteristic of atoms, different elements present in the sample under investigation are identified. Electrons traveling through a

material have a relatively high probability of experiencing inelastic collisions with locally bound electrons as a result of which they suffer energy loss and contribute to the background of the spectrum rather than a specific peak. Due to inelastic scattering process, the flux of photoelectrons emerging from the sample is much attenuated.

Why is the XPS technique surface sensitive? The soft X-rays employed in XPS penetrate a substantial distance into the sample (~ few μm). Thus this method of excitation imparts no surface sensitivity at the required atomic scale. However the photoelectrons can escape from only a very short distance beneath the surface (< 100 Å). The surface sensitivity thus arises from the emission and detection of the photoemitted electrons.

Chemical shift: The exact binding energy of an electron depends not only upon the level from which photoemission is occurring, but also upon:

(1) the formal oxidation state of the atom

(2) the local chemical and physical environment

changes in either (1) or (2) give rise to small shifts in the peak positions in the spectrum - so-called *chemical shifts.* Atoms of a higher positive oxidation state exhibit a higher binding energy due to the extra coulombic interaction between the photo-emitted electron and the ion core. This ability to discriminate between different oxidation states and chemical environments is one of the major strengths of the XPS technique.

The basic requirements for a XPS experiment are:

(1) x-ray source of fixed-energy radiation (usually Mg Kα with $h\nu$ = 1253.6 eV or Al Kα with $h\nu$ = 1486.6 eV)

(2) Concentric hemispherical analyser (CHA), which uses an electric field between two hemispherical surfaces to disperse the electrons according to their kinetic energy, and thereby measure the flux of emitted electrons of a particular energy.

(3) a high vacuum environment (to enable the emitted photoelectrons to be analysed without interference from gas phase collisions)

For the work described in this thesis, the XP spectra of C 1s and Au 4f core levels were recorded for the samples of gold nanoparticles solution synthesized by the reduction of aqueous $AuCl_4^-$ ions using lemongrass leaf extract and sodium borohydride. XP

spectra of F 1s, Cl 2p, Br 3d and I 3d core levels were also recorded from the gold nanoparticles solution synthesized by the reduction of aqueous $AuCl_4^-$ ions by citric acid in presence and absence of potassium halides (KF, KCl, KBr and KI). The Samples were prepared by drop-coating the solution on Si (111) substrate. XPS measurements were carried out on a VG Microtech ESCA 3000 instrument at a base pressure better than 1 x 10^{-9} Torr with un-monochromatized Mg Kα radiation (1253.6 eV energy). The measurements were made in the constant analyzer energy (CAE) mode at a pass energy of 50 eV and electron takeoff angle (angle between electron emission direction and surface plane) of 60°. This leads to an overall resolution of ~ 1 eV in the measurements. The chemically distinct components in the core level spectra were resolved by a non-linear least squares fitting algorithm after background removal by the Shirley method [9].

2.8 Nuclear magnetic resonance spectroscopy (^{1}H NMR).

Magnetic properties of nuclei: All atomic nuclei possess nuclear spin, I, which may be integral (i.e. 1,2,3 etc.) or half integral (i.e ½, 3/2, 5/2 etc.) Since nucleus possesses an electric charge, the spinning nucleus gives rise to a magnetic field whose axis coincides with the axis of spin. Thus each nucleus can be thought of being equivalent to a minute magnet having magnetic moment μ. Each nucleus with I > 0 has magnetic moment. If a magnetic nucleus is placed in a uniform magnetic field, it is found that the magnetic dipole assumes only a discrete set of orientations. The system is said to be quantized. The magnetic nucleus may assume any one of (2I + 1) orientations with respect to the direction of the applied magnetic field. Thus, a proton (I = ½) will be able to assume only one of two possible orientations that correspond to energy levels of ± μH in a applied magnetic field, where H is the strength of the external magnetic field. The transition of a proton from one possible orientation to another may be affected by the absorption or emission of a discrete amount of energy such that

$$E = h\nu = 2\mu H, \qquad \text{..... (2.10)}$$

where ν is the frequency of electromagnetic radiation absorbed or emitted.

Unless the axis of the nuclear magnet is oriented exactly parallel or antiparallel with the applied magnetic field, there will be a certain force by the external field to so orient it.

But because the nucleus is spinning the effect is that its rotatioanl axis draws out a circle perpendicular to the applied field. This motion of nucleus is called precession and is of exceptional importance in the nuclear resonance phenomenon.

Theory of nuclear resonance: The precessional frequency of the spinning nucleus is exactly equal to the frequency of electromagnetic radiation necessary to induce a transition from one nuclear spin state to another. The nucler transition corresponds to a change in the angle that the axis of the nuclear magnet makes with the applied magnetic field. This change can be brought about through the application of electromagnetic radiation whose magnetic vector component is rotating in a plane perpendicular to the main magnetic field. When the frequency of the rotating magnetic field and the frequency of the precessing nucleus become equal, they are said to be in resonance, and absorption or emission of energy by the nucleus can occur.

Chemical shift: If the resonance frequencies for all protons in a molecule were the same, the nuclear resonance technique would be of little use- one would observe only one peak for the compound, regardless of the number or nature of protons present. The utility of the nuclear resonance phenomenon depends on the fact that nuclear magnetic resonane frequencies are to a small degree dependent on the molecular environment of the nucleus. The surrounding electrons shield the nucleus, so the effective magnetic field felt by the nucleus is not quite the same as the applied field. Electronic shielding arises from an induced circulation of electrons about a nucleus. These circulations are induced by the applied field and are in a plane perpendicular to the applied magnetic field. They produce a magnetic field that, in the region of the nucleus, is usually in a direction opposed to the direction of the applied field. The magnitude of the induced field is directly proportional to the magnitude of the applied field. The effective magnetic field experienced by the nucleus is changed by this small local field such that

$$H_{eff} = H_0 - \sigma H_0 \qquad \text{..... (2.11)}$$

where, σH_0 is the induced field owing to electronic circulations. Protons in different environments are shielded by the circulations of surrounding electrons to different extents. Hence, different values of σH_0, each dependent on the magnitude of the applied field H_0 are obtained for different protons. Because the strength of the applied magnetic

field cannot be determined to the reequired degree of accuracy, the absolute position of absorption cannot be obtained directly from the instrument. However relative proton frequencies can readily be determined. The separation of resonance frequencies of nuclei in different structural environments from some arbitrarily chosen standard is termed the chemical shift.

Proton NMR spectra of a fraction isolated from the aqueous lemongrass leaf extract by solvent column chromatography, used for the synthesis of triangular and hexagonal gold particles, were recorded on a Bruker AC 200 MHz instrument and scanned in the range 0–15 ppm using D_2O as a solvent.

2.9 Light scattering.

When light strikes particles, scattering (diffraction) occurs. The light scatters in all directions, but for larger particles there is relatively more scattering to the front while for smaller particles there is relatively more scattering to the sides and back as shown in figure 2.5. It is therefore possible to calculate particle size distributions if the intensity of light scattered from a sample are measured as a function of angle.

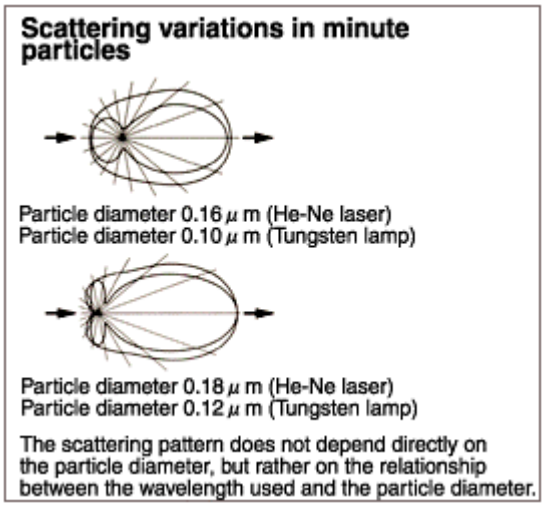

Figure 2.5: *Diagram showing the scattering pattern depending on the size of the particle.*

The general relationship for scattered intensity relative to the incident intensity is:

$$\frac{I(\theta)}{I_0} = \frac{\lambda^2}{8\pi R^2}(i_1 + i_2)(N \times V) \qquad \text{..... (2.12)}$$

where θ = angle of the scattered beam, relative to the incident beam

R = distance from the particles to the viewing point

i_1, i_2 = scattering intensity coefficients or Mie parameters, dimensionless

N = number of particles per unit volume

V = sensing volume of instrument

The subscripts on the coefficients *i* correspond to the planes of polarization, if any, of the incident light. For spheres, with unpolarized incident light (the usual case) the value of the intensity coefficients depends again on the range of values for the particle size parameter, α:

Rayleigh region $(i_1 + i_2) = \alpha^6 \left[\frac{m^2 - 1}{m^2 + 2}\right]^2 (1 + \cos^2\theta)$ ..... (2.13)

Classical region $(i_1 + i_2) \propto d_p^2$ ..... (2.14)

Mie region: $(i_1 + i_2) \propto d_p^3$ ..... (2.15)

where, m is the refractive index of the particles, and $\alpha = \frac{\pi . d_p}{\lambda}$, λ = wavelength of the light, and d_p is the particles diameter. For α > about 20, the interaction is described accurately by classical optical theory, and this range of diameters is called Classical Region. For α < about 1.0, the interaction is more complex, but is described accurately by the Rayleigh optical theory. For values of α between 1 and 20, the optical behavior is most complex, and is described by the Mie theory, which is most complete of the three physical descriptions of particle optics.

The angular dependence is such that scattered intensity is least at angles near 90°, and is highest at angles near zero ("forward-scattering") and 180° ("backward scattering"). However, the forward scattering intensity doesn't show great variation for particles under 0.2μm, while there are distinct variations in intensity to the sides and back.

For a fixed scattering angle, within the Rayleigh region, $(i_1 + i_2) \propto d_p^6$ and scattered light intensity is low but strongly dependent on wavelength and particle diameter. In the Mie region, the intensity parameters are approximately proportional to d_p^3 with oscillations, while in the classical region the parameters are proportional to d_p^2.

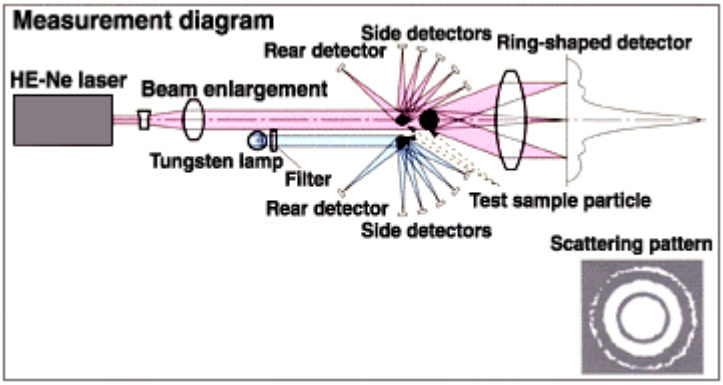

Figure 2.6: *Diagram showing the various elements in light scattering instrument.*

To measure particle size with the laser scattering method, the light scattering instrument detects the correlation between the intensity and the angle of light scattered from a particle (Figure 2.6), then calculates the particle size distribution based on the Mie-scattering theory. The Mie theory is the rigorous solution for light scattered from a sphere. For particles smaller than the wavelength of the incident light, the Mie theory is reduced to the Rayleigh theory. When particles are much larger (typically>30 μm) than the wavelength of the incident light, the Mie theory simplifies to the classical theory.The technique has a very large dynamic range, from 3.5mm to below 100nm, as defined by the range of angles over which the scattering pattern is collected and the instruments optical configuration.

Light scattering measurements were carried out to monitor The kinetics of formation of gold nanoparticles during reduction of $AuCl_4^-$ ions using lemongrass leaf extract on a Horiba model LA-910 laser light scattering particle size distribution analyzer.

2.10 Isothermal titration calorimetry.

Every molecular interaction either generates or absorbs small amounts of heat;

ultra sensitive isothermal titration calorimetry (ITC) can detect these small changes in heat. Recent advances in ITC systems permit the complete characterization of molecular interactions with as little as a few nanomoles of material. An ITC experiment takes only 30–60 min to complete and is highly automated, including instrument operation, data collection and analysis. Each ITC experiment provides a complete thermodynamic profile of the interaction including the binding constant (Ka), the number of binding sites (*n*), enthalpy (ΔH), entropy (ΔS), and free energy (ΔG). Since heat is universally generated or absorbed during any molecular interaction, ITC may be viewed as a universal detector for such interactions. ITC may be used to study interactions using native, modified, or immobilized substances and is the only bioanalytical method that directly measures enthalpy.

Instrument operation: The instrument utilizes a differential design with two identical cells. All binding processes occur in the sample cell, whose temperature is continuously compared to that of the reference cell, where no reaction takes place. The cells are surrounded by an inner shield, which is maintained at the same temperature as the cells in order to minimize any heat flow to or from the cells. The outer shield is also maintained at the same temperature, to compensate for any changes in room temperature. During operation, a very small constant power is supplied to a heater on the reference cell. The amount of power supplied to the sample cell (feedback power) is continuously adjusted so that its temperature is always identical to that of the reference cell. If, for example, an exothermic reaction occurs in the sample cell, then the feedback power to the sample cell will automatically be reduced to nullify the temperature difference caused by the heat released in the sample cell. The precise amount of heat released by the exothermic process can then be determined since it is exactly equal to the reduction in the amount of feedback heat necessary to reestablish the temperature null between the cells [10].

We have used MicroCal VP-ITC instrument, which is an ultrasensitive ITC system that requires less sample and is easier to use than preceding models. These characteristics allow ITC to be used as a routine method for studying molecular interactions. ITC is an extremely powerful thermodynamic technique that has been used with much success in understanding biomolecular binding processes [11-15]. It is widely used in biochemistry to study protein-ligand [11], protein-protein [12], DNA-RNA [13],

DNA-protein [14] and protein-lipid [15] interactions. In this thesis, we have used ITC in order to understand the ability of halide ions to bind to the surface of gold nanoparticles on addition of different potassium halides (KF, KCl, KBr and KI) to the citric acid reduced gold nanoparticles solution.

2.11 Laser.

The laser source used for the irradiation of gold triangles solution is Neodynium doped Yetterium aluminum garnet (Nd-YAG) laser. The laser instrument consists of a Yetterium aluminum garnet ($Y_3Al_5O_{12}$) rod (6 mm × 7.5 mm) doped with 0.9 % of Nd and is pumped by a xenon filled flash lamp, FXQ 274-3, housed in an elliptical reflecting cavity. This ensemble forms the pump cavity. The efficient transfer of radiation from flash lamp to the laser rod is the main function of pump cavity and controls the over all efficiency of the laser system. The pump cavity provides good coupling between the source and laser rod. It is responsible for the pump density distribution in the laser rod, which affects uniformity, divergence and optical distortion of the output beam.

The lasing medium is the colorless, isotropic crystal $Y_2Al_5O_{12}$ (YAG). When used in a laser, about 0.9% of the Yttrium is replaced by Neodymium. For Nd:YAG crystal the main absorption line occurs at 808 nm. Population inversion results from shining light on this crystal due to excitation of electrons to higher energy levels. The emission at 1064 nm is due to stimulated dexcitation, from $^4F_{3/2} \rightarrow {}^4I_{11/2}$ level. The radiative decays to the ground-state have long life-times, on the order of micro-seconds, as compared to the fast transitions to the upper energy levels (on the order of nano-seconds). Approximately 99% of the ions that are excited to the absorption band transfer to the upper energy levels. These levels are characterized by a relatively long lifetime, on the order of milli-seconds. Due to this long life-time, they de-excite almost solely due to spontaneous emission.

The Nd-YAG crystal forms the laser cavity and is in between reflective mirrors. The back mirror is 100 % reflective, and the front mirror is 99.9 % reflective (Figure 2.7) to allow only part of the amplified light to pass and enough feed-back so that oscillation

may occur. The light energy is amplified in this manner until sufficient energy is built up for a burst of laser light to be transmitted through the partially reflecting mirror.

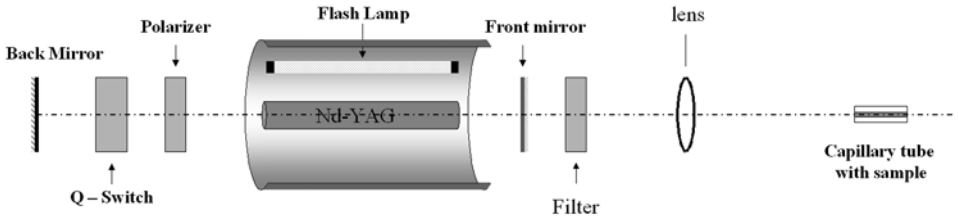

Figure 2.7: *Diagram showing the construction of a laser source instrument.*

When the laser is operated in free running pulsed mode, the out put shows individual burst or spikes in the form of relaxation of oscillations. This reduces the peak power of the laser. The peak power of the laser is enhanced by the technique of Q-switching. There are of two types of Q-switching modes: pulse reflection mode and pulse transmission mode. In the present laser system pulse reflection mode is used. A fast shutter is inserted in between the Nd:YAG rod and one of the reflecting mirrors. When the shutter is closed, energy is stored in the amplifying medium and the gain in the rod is high. The cavity losses are high and the lasing action is prohibited. The population inversion reaches a level far above the threshold for normal lasing action. When the shutter is opened, the stored energy is released in the form of very short pulse (few ns) of laser radiation. Switching elements in Q-switching are of different types namely mechanical, electro-optic, acousto-optic, saturable absorber. In the present laser system electro- optic switch is used.

Nd-YAG laser source was used to study the morphological change during irradiation of the NIR absorbing gold triangular and hexagonal particles synthesized by the reduction of $AuCl_4^-$ ions using lemongrass leaf extract. The Q-switched Nd:YAG laser source used for the experiments was a built at the Department of Physics, University of Pune, India. The energy could be tuned between 1 to 35 mJ per pulse at 1064 nm, with, 1Hz repetition rate, and 20ns pulse width . The laser radiation was filtered by a 1064nm pass filter (Melles Griot) to minimize the background intensity. The laser beam was

focused using a lens (focal length 14cm) having diameter 0.2mm (spot size) in a capillary tube of diameter 2mm and length 2.5cm.

2.12 Thermal deposition of organic thin films.

Thermally evaporated stearic acid (STA), octadecylamine (ODA) and bis(2-ethylhexyl)sulfosuccinate (AOT) thin films used for the entrapment of biologically synthesized gold nanoparticles and for the synthesis of TiO_2, ZrO_2 and CdS nanoparticles in this thesis have been deposited using Edwards E306 coating unit. The coating unit consists of a rotary pump used for backing and roughing the chamber where deposition is done and can produce a vacuum upto 10^{-3} Torr. Below this pressure, oil diffusion pump is employed to produce high vacuum of 10^{-7} Torr [16] and the deposition rate was 10 Å /min. Both these pumps are used in conjunction for backing and roughing of the deposition chamber. A liquid nitrogen trap was also used. Deposition of organic thin films is done under vacuum due to the following reasons: 1) The quality of deposition is better due to the increased mean free path of a molecule under vacuum as compared to atmosphere, resulting in a linear trajectory of the thermally evaporated molecule. 2) The melting point of fatty acid/ amine lipids is reduced under vacuum, enabling low current requirements for thermal evaporation. The fatty acid/amine lipids (amphiphilic molecules) used for deposition, were taken in a molybdenum boat and subjected to low tension DC of about 20 amps under 10^{-7} Torr vacuum and heated. The substrates such as Si(111), glass and quartz were kept at a suitable distance above the molybdenum boat. The molecules when heated evaporated and condensed onto these substrates giving nearly same thickness of the uniform films on each substrate. The rate of deposition and the thickness of the lipid films was monitored *in-situ* using Edwards FTM5 quartz crystal microbalance. The films were tested for stability by using infrared spectroscopy, and it was found that the films did not decompose on deposition in vacuum.

Amphiphilic molecules: An amphiphilic molecule has a hydrophobic and a hydrophilic part. The hydrophobic end is normally a long chain of hydrocarbons called the tail and the hydrophilic moiety is called the polar head group as shown in the fig. 2.8.

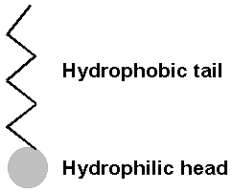

Figure 2.8: *A schematic of an amphiphilic molecule showing hydrophobic (long hydrocarbon chain) and hydrophilic (polar group) parts.*

The amphiphilic molecules we have used in this work are: Stearic acid [StA; CH_3-$(CH_2)_{16}$-COOH] and octadecylamine [ODA; CH_3-$(CH_2)_{17}$-NH_2].

2.13 Quartz Crystal Microgravimetry (QCM).

Quartz crystal based microgravimetry is a powerful tool to study various adsorption processes and has been used to study adsorption of gases, self-assembled monolayers (SAMs), Langmuir-Blodgett films, nanoparticles, and biomolecules. For the work discussed in this thesis, QCM has been extensively used for measuring the uptake of the metal nanoparticles and the metal ions during immersion of the thermally evaporated lipid thin films in the metal nanoparticles solution or the metal ions solutions respectively.

Working principle: One can describe the QCM to be an ultra-sensitive mass sensor. The heart of the QCM is the piezoelectric AT-cut quartz crystal sandwiched between a pair of electrodes. When the electrodes are connected to an oscillator and an AC voltage is applied over the electrodes the quart crystal starts to oscillate at its resonance frequency due to the piezoelectric effect. This resonance frequency is sensitive to the mass changes of the crystal and its electrodes.

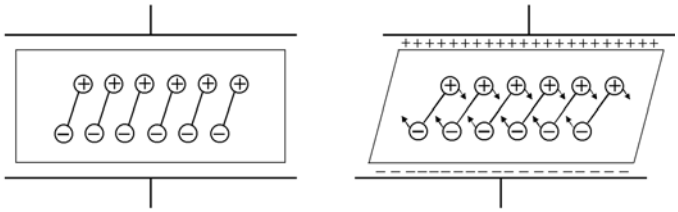

Figure 2.9: *Schematic representation of the converse piezoelectric effect for shear motion.*

Piezoelectric effect: In 1880, Jacques and Pierre Curie discovered that a mechanical stress applied to the surfaces of various crystals, including quartz, rochelle salt

($NaKC_4H_4O_6$-$4H_2O$) and tourmaline, afforded a corresponding electrical potential across the crystal whose magnitude was proportional to the applied stress [17]. This behaviour is referred to as piezoelectric effect; "piezo" comes from the Greek word piezen meaning to "to press". Not predicted by the Curies, the converse piezoelectric effect was later suggested by Lippman. According to the converse piezoelectric effect application of an electrical field across any piezoelectric material results in corresponding mechanical strain in it. This converse piezoelectric effect is the basis of quartz crystal microgravimetry (QCM) technique. This property only exits in materials that are acentric, viz. those crystallize in non-centrosymmetric space groups. A single crystal of an acentric material will possess a polar axis due to dipoles associated with the orientation of atoms in the crystalline lattice. When stress is applied across an appropriate direction, there is a shift of dipoles resulting from the displacement of atoms. This atomic displacement leads to a corresponding change in the net dipole moment. This will produce a net change in electrical charge on the faces of the crystal. This is depicted above in Fig. 2.9.

Application of electric field across the crystal causes a vibrational motion of the quartz crystal, with amplitude parallel to the surface of the crystal [18]. The result of the vibrational motion of the quartz crystal is the establishment of a transverse acoustic wave that propagates across the thickness of the crystal, reflecting back into the crystal at the

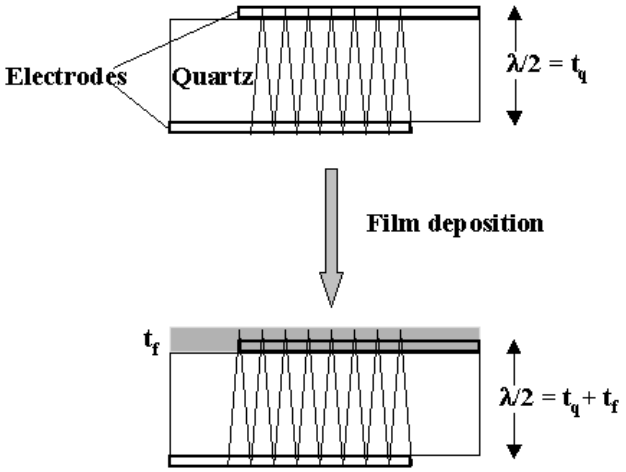

Figure 2.10: *Schematic representation of the transverse shear wave in a quartz crystal and a composite resonator comprising the quartz crystal and a layer of a foreign material*

surfaces. When a uniform layer of foreign material is added to the surface of the quartz crystal, the acoustic wave will travel across the interface, and will propagate through the

layer as shown in Fig. 2.10. This leads to decrease in the frequency of the crystal. The Frequency changes on deposition of the film can be converted to mass loading using the Saurbrey formula [19].

Saurbrey formula:

$$\Delta f = -2f_0^2 \frac{\Delta m}{A \times (\mu_q \times \rho_q)} \quad \text{..... (2.16)}$$

where, Δf - frequency shift, f_0 - frequency of the crystal prior to a mass change, Δm – mass change, A - Piezo electrically active area, ρ_q - density of quartz, μ_q - shear modulus for quartz. ($\mu_q = 2.95 \times 10^{11}$ g cm^{-1} s^{-2}, $\rho_q = 2.65$ g/cm^3).

Why AT-cut Quartz Resonators? Although 20 of the 32 crystal systems lack a center of inversion and can exhibit piezoelectricity, the most commonly used piezoelectric material is crystalline α quartz (SiO_2). The advantage of using quartz over other crystals is that it is a completely oxidized material and insoluble in water. It can also resist temperatures up to 579 ^{0}C still maintaining its piezoelectricity. Only quartz provides the unique combination of mechanical, electrical, chemical and thermal properties that has led to its commercial significance. Crystals cut with the proper angles with respect to the crystalline axes exhibit shear displacements. Depending on the cut angle, a large number of different resonator types such as thickness-shear mode, plate and flexural resonators can be obtained from a mother crystal with eigen frequencies ranging from 5×10^2 – 3×10^8 Hz. Generally AT-cut quartz crystals are used for QCM purposes in which thin quartz wafer is prepared by slicing a quartz rod at an angle of 35.25^0 with respect to the X-axis of the crystal, resonates in the *thickness shear mode*. AT cut quartz crystals exhibit a high frequency stability of $\Delta f/f \sim 10^{-8}$, which makes them well suited for many electronic devices. Since AT-cut quartz crystals have a temperature coefficient that is almost zero between 0-50 ^{0}C, this particular cut is the most suitable one for QCM sensors.

In the work described in this thesis we have used a gold coated AT-cut 6 MHz quartz crystal. The frequency counter used was an Edwards FTM5 instrument operating at a frequency stability and resolution of ± 1 Hz. At this resolution and the type of quartz

crystal used, the mass resolution would be 12 ng/cm^2. Films of different thickness of STA, ODA and AOT were deposited onto the QCM crystals and the frequency changes during their immersion in the metal nanoparticles or the metal ions solution (and their subsequent hydrolysis or sulfudization, in case of metal oxides and CdS respecitvely) were measured *ex situ* after removing the coated crystals from the respective solutions followed by their thorough washing and drying at regular intervals. The frequency changes were converted to a mass uptake by using the standard Saurbrey formula [19]. The Sauerbrey equation does not apply for thick films, viscous liquids, elastic solids and viscoelastic bodies. Most reported QCM investigations have assumed ideal rigid behavior and no slip at the resonator-fluid boundary while using the Sauerbrey equation [20]. These assumptions are valid when dealing with studies on inorganic thin films, wherein the film deposited is rigid enough to be considered "quartz like". However while dealing with thermally deposited films that are being intercalated with nanoparticles, one would need to consider factors such as viscoelastic effects, high mass loadings, surface roughness, surface stress, interfacial slippage and non uniform mass distribution in any piezoelectric measurement [20]. The thin films (about 250 Å), low mass loadings (about 8-50 μg) as compared to total weight of the crystal, and assuming uniform mass distribution over the film surface supports the validity of the use of Sauerbrey equation in our case.

2.14 References:

1) a) Mie, G. *Ann. Phys*. **1908**, *25*, 377. b) Greighton, J. A.; Eadon, D. G. *J. Chem. Soc. Faraday Trans.* **1991**, *87*, 3881. c) Mulvaney, P. *Langmuir* **1996**, *12*, 788.
2) Johnson, P. B.; Christy, R. W. *Phys. Rev. B* **1972**, *6*, 4370.
3) Henglein, A. *J. Phys. Chem.* **1993**, *97*, 5457.
4) Burda, C.; Chen, X.; Narayanan, R.; El-Sayed, M. A. *Chem. Rev.* **2005**, *105*, 1025.
5) Gans, R. *Ann. Phys.* **1915**, *47*, 270.
6) Millstone, J. E.; Park, S.; Shuford, K. L.; Qin, L.; Schatz, G. C.; Mirkin, C. A. *J. Am. Chem. Soc.* **2005**, *127*, 5312.
7) Brus L. *J. Phys. Chem.;* **1986**, *90*, 2555.
8) Lawes, G. *Scanning electron microscopy and X-ray microanalysis: Analytical chemistry by open learning*, John Wiley & sons, **1987**.
9) Shirley, D. A. *Phys. Rev. B* **1972**, *5*, 4709.
10) Chellani, M. *Application Notes* **1999**, 14.
11) Qin, K.; Srivastava, D. K. *Biochemistry* **1998**, *37*, 3499.
12) Pierce, M. M.; Raman, C. S.; Nall, B. T. *Methods* **1999**, *19*, 213.
13) Barbieri, C. M.; Li, T. K.; Guo, S.; Wang, G.; Shallop, A. J.; Pan, W.; Yang, G.; Gaffney, B. L.; Jones, R. A.; Pilch, D. S.; *J. Am. Chem. Soc.* **2003**, *125*, 6469.
14) Kunne, A.; Sieber, M.; Meierhans, D.; Allemann, R. K. *Biochemistry* **1998**, *37*, 4217.
15) Wenk, M. R.; Seelig, J. *Biochemistry* **1998**, *37*, 3909.
16) Maissel, L. I.; Glang, R. *Handbook of thin film technology*, McGraw Hill Book Company, NewYork, **1970**.
17) Curie, P.; Curie, J. C. R. *Acad. Sci.* **1880**, *91*, 294.
18) Buttry, D. A.; Ward, M.D. *Chem. Rev.* **1992**, *92*, 1356.
19) Sauerbrey, G. *Z. Phys. (Munich)* **1959**, *155*, 206.
20) a) Wang, J.; Frostman, L.M.; Ward, M.D. *J. Phys. Chem.* **1992**, *96*, 5224. b) Buttry, D. A.; Ward, M.D. *Chem. Rev.* **1992**, *92*, 1356.

Chapter III

Synthesis of Metal Nanoparticles Using Plant Extracts as Natural Reducing Agents

Materials syntheses following biological routes are presently confined largely to the use of organisms like diatoms, fungi, bacteria, viruses, etc. or mimicking biological systems by using biomolecules isolated from them. In this chapter an attempt has been made to extend these green chemistry approaches for synthesizing nanomaterials from these lower class of organisms to higher forms of plants. Extracellular synthesis of metal nanoparticles using extracts of plants viz., geranium (Pelargonium graveolens) and neem (Azadirachta indica) has been demonstrated. On treating the metal ions with different plant extracts, a rapid reduction occurs leading to the formation of highly stable metal nanoparticles. The synthesis of nanoparticles was observed to occur within few hours of reaction as compared to 2 - 4 days required by microorganisms. A tendency towards directing the shape of gold nanoparticles during their growth is also observed when using geranium leaf extract as a natural reducing agent.

Part of the work presented in this chapter has been published:

(1) Shankar, S. S.; Ahmad, A.; Pasricha, R.; Sastry, M. *J. Mater. Chem.* **2003**, *13*, 1822. (2) Shankar, S. S.; Ahmad, A.; Sastry, M. *Biotechnol. Prog.*, **2003**, *19*, 1627. (3) Shankar, S. S.; Rai, A.; Ahmad, A.; Sastry, M. *Applied Nanoscience* **2004**, *1*, 69. (4) Shankar, S. S.; Rai, A.; Ahmad, A.; Sastry, M. *J. Colloid Interface Sci.*, **2004**, *275*, 496.

3.1 Introduction.

The intricacies and the functional efficacies of the biological world fascinate both the scientist and the common person alike. From a materials scientist's point of view, the formation of the appealing siliceous structures of the Diatoms, [1] calcareous structures produced by the Haptophytes [2] and the aligned magnetic nanoparticles synthesized by the magnetotactic bacteria, [3] are very inspirational. Numerous reports have been published in literature related to various aspects of biomineralisation. Recently, synthesis of metal nanoparticles using microorganisms is also being looked into with interest. Beveridge and coworkers demonstrated the deposition of gold nanoparticles within bacterial cells [4]. Reduction of Ag^+ ions and formation of silver nanoparticles within the periplasmic space of the bacterium *Pseudomonas stutzeri* AG259 was shown by Klaus-Joerger and coworkers [5]. Similarly Nair and Pradeep synthesized silver, gold and their alloy nanoparticles intracellularly using L*actobacillus* strains common in buttermilk [6]. From this laboratory it was shown earlier that fungi are also capable of synthesizing nanoparticles of different chemical compositions and sizes, both intracelluarly as well as extracellularly [7]. Syntheses of nanoparticles of gold, silver and technologically important CdS were reported using fungi as biofactories [7]. Later it was demonstrated that parallel to the chemical process, it is also possible to synthesize gold nanoparticles of uniform size extracellularly using extremophilic actinomycete *Thermomonospora* sp. [8].

While microorganisms continue to be investigated for biomineralization and metal nanoparticles synthesis, the use of plants/plant extracts in similar nanoparticles biosynthesis methodologies is an exciting possibility and is relatively unexplored and under-exploited. Plants have been known to biomineralize calcium carbonate [9], silica [10] and even magnetite [11] internally. Similar to microorganisms, plants have also been used for remediation of heavy metal ions from contaminated soil and water [12]. Certain plants are known to hyperaccumulate these heavy metals or can even be induced to hyperaccumulate within different parts of plants [12,13]. The internal accumulation of metal can occur both via complexation of the metal ion with a suitable bio-ligand in its native oxidation state or after its reduction to a lower oxidation state [12]. The possibility of reduction of metal ions and the presence of metal complexing agents in plants would entice a materials scientist, with a goal of synthesizing nanoparticles and controlling their

size and shape and to experiment on the likelihood of forming nanoparticles of low reduction potential metals. The possibility of synthesizing nanoparticles of different compositions using plants, would offer an environmentally benign alternative to the existing potentially toxic chemical and physical methods of preparations. This would also help stave off the growing apprehensions related to environmental degradation and biological hazards that accompany the enthusiasm of emerging nanoscience and nanotechnology [14], apart from being a cost effective process with potential to scale up for large scale synthesis. In fact Jose-Yacaman and co-workers have shown that live alfalfa plants when supplied with Au^{3+} ions, reduce them to Au^{0} state and absorb them resulting in the internal formation of gold nanoparticles [15]. Jose-Yacaman's group have also extended this to demonstrate the synthesis of assemblies of silver nanoparticles within alfalfa shoots by supplying the plants with Ag^{+} ions [16]. While these reports demonstrated the possibility of synthesizing metal nanoparticles using plants, they suffer with the inherent complication of being intracellular, making the isolation of particles an additional difficult job.

In this chapter an attempt has been made to use plants for the synthesis of metal nanoparticles and demonstrate their capabilities as an alternative to chemical synthetic processes. To circumvent the problem of internalization of nanoparticles, i.e. to achieve nanoparticles synthesis extracellularly in order to get a well-dispersed and stable solution, an attempt has been made to use the extracts of plant were used instead of live plants. One of the objectives in using plant extracts was also to achieve rapid synthesis of nanoparticles unlike the usual biosynthetic process involving microorganisms that consume minimum of 2 to 4 days for complete reduction of metal ions [4-7]. The choice of plants for this purpose was biased towards those containing medicinal and aromatic compounds, in order to make the nanoparticles biologically more beneficial and to obtain any possible shape controlling effect due to these molecules as is observed following chemical synthesis in presence of aromatic compounds [17].

This chapter describes:

1) Synthesis of gold and silver nanoparticles using aqueous extracts of different parts of the plant geranium, *Pelargonium graveolens*.

2) Synthesis of gold, silver and gold-silver bimetallic nanoparticles using the aqueous leaf extract of the neem, *Azadirachta Indica*.

3.2 Synthesis of silver and gold nanoparticles using extracts of different parts of geranium plant.

3.2.1 Experimental details:

The reduction of Ag^+ and $AuCl_4^-$ ions to Ag^0 and Au^0 can be easily achieved by reacting them with extracts of different parts of the plant, geranium, *Pelargonium graveolens*. The extracts were prepared by taking 20 g each of its thoroughly washed and finely cut leaves, stem and root in separate 500 mL Erlenmeyer flasks with 100 mL sterile distilled water and then boiling them for 1 min. The process of boiling the different parts of the plant leads to rupture of the cell walls and thus, release larger amount of intra-cellular material into solution. After boiling, the solutions were decanted, filtered and 5 mL of each of the extracts were added to separate 100 mL aqueous solutions of 10^{-3} M $AgNO_3$ and 10^{-3} M $HAuCl_4$. The kinetics of bioreduction of the metal ions in solution were monitored by periodic sampling of aliquots (2 mL) of the aqueous component and measuring the UV-vis spectrum of the solution.

Further characterization of the metal nanoparticles after their purification by repeated centrifugation was carried out by X-ray diffraction (XRD) and Fourier transform infrared (FTIR) spectroscopy and transmission electron microscopy (TEM) measurements.

3.2.2 UV-vis measurements:

Reduction of the aqueous Ag^+ ions and $AuCl_4^-$ ions during exposure to the extracts of different parts of the plant geranium, *Pelargonium graveolens*, may be easily followed by UV-vis spectroscopy. It is well known that silver nanoparticles exhibit yellowish-brown color and gold nanoparticles exhibit an impressive pink-ruby red colors in water; these colors arise due to excitation of surface plasmon vibrations in the metal nanoparticles [18]. The surface plasmon resonance (SPR) band for spherical silver and gold nanoparticles occur in the range 380-440 nm and 510-560 nm respectively in an aqueous medium. Figure 3.1A shows the UV-vis spectra recorded from the aqueous

silver nitrate-geranium leaf extract reaction medium as a function of time of reaction. It is observed that the silver surface plasmon resonance band occurs at ca. 440 nm and steadily increases in intensity as a function of time of reaction without any shift in the position of peak maximum. In addition to the peak at 440 nm, another peak at 370 nm is also seen which increases in intensity with time and merges with the band at 440 nm, appearing as a shoulder in the UV-vis spectra after 4 h of reaction. The observation of such asymmetric peak form could indicate the formation of some anisotropic structures or

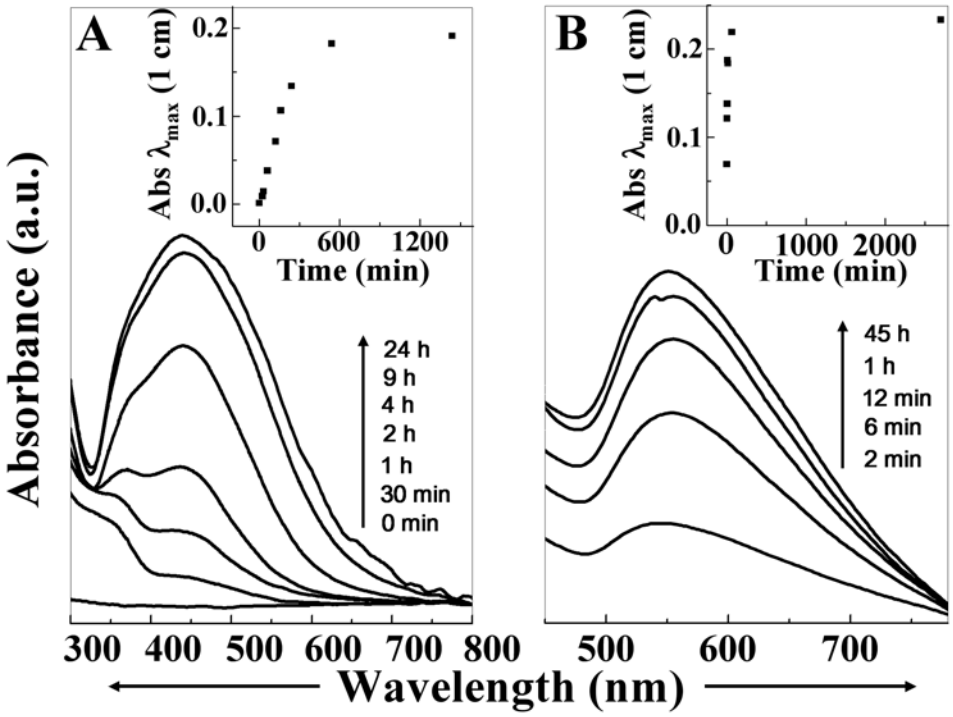

Figure 3.1: *UV-vis spectra recorded as a function of time of reaction of A) 10^{-3} M aqueous solution of $AgNO_3$ and B) 10^{-3} M aqueous solution of $HAuCl_4$ with geranium leaf extract. The insets of A and B are plots of maximum absorbance vs time of reaction for the silver and gold solutions respectively (for brevity, all time-dependent UV-vis spectra have not been shown).*

some degree of aggregation. The shoulder at 370 nm would correspond to the transverse plasmon vibration in the silver nanoparticles whereas the peak at 440 nm is due to excitation of longitudinal plasmon vibrations of either anisotropic Ag nanoparticles or aggregates of spherical Ag nanoparticles. The inset of Figure 3.1A is a plot of absorbance at 440 nm (λ_{max}) vs time of reaction of geranium leaf broth with Ag^+ ions and it can be inferred that the reduction of the silver ions occurs fairly rapidly, more than 90 % of which is complete within 9 h of reaction (Figure 3.1A). In earlier studies on the synthesis of silver nanoparticles using bacteria [5,6] or fungi [7c,7d], the time required for

completion of the reaction (i.e., complete reduction of the metal ions) ranged from 24 h to 120 h and is thus rather slow. The silver particles were observed to be extremely stable in solution even 4 weeks after their synthesis. Figure 3.1B shows the UV-vis spectra recorded from the aqueous chloroauric acid-geranium leaf extract reaction medium as a function of time of reaction. It is observed that the gold surface plasmon resonance band occurs initially at ca. 547 nm after 2 min and steadily increases in intensity as a function of time of reaction. After completion of the reaction, the wavelength of the surface plasmon band stabilizes at 551 nm. The absorption band for the gold nanoparticles solution is broad and slightly asymmetrical with indications of an additional weaker component at ca. 610 nm. The appearance of this feature indicates either formation of stable aggregates of the gold nanoparticles in solution or shape anisotropy in the particles, as was the case with silver nanoparticles. This issue will be addressed subsequently during TEM analysis of the nanoparticles solution. From the inset of Figure 3.1B representing the plot of absorbance at λ_{max} of the SPR band of gold nanoparticles vs time of reaction of geranium leaf broth with $AuCl_4^-$ ions, reduction of the $AuCl_4^-$ ions is observed to be complete after 60 min of reaction. The rate of formation of gold nanoparticles is fairly rapid even when compared with silver nanoparticles formation using the same geranium leaf extract. As with silver nanoparticles, formation of gold nanoparticles has also been achieved in a much shorter time when compared to earlier studies from this laboratory on the use of the fungus *Fusarium oxysporum* [7b] and the actinomycete *Thermomonospora* sp. [8] for extra-cellular gold nanoparticles synthesis, in which case the time for complete reduction of the gold ions was 48 and 120 h respectively (under nearly identical reaction conditions). As observed, the significant reduction in the reaction time of the Ag^+ and $AuCl_4^-$ ions with the geranium leaf extract is an important result and will enable nanoparticles synthesis using natural products to compete favorably with chemical methods that are currently much more rapid and reproducible. Long reaction times is one disadvantage of the biosynthetic procedures and the reduction in reaction time observed for the extract of geranium leaves is a significant advance in this direction. There has been a report by Ping Yong and co-workers on the accelerated synthesis of palladium nanoparticles using the sulfate-reducing bacterium *Desulfovibrio desulfuricans* (NCIMB 8307) wherein the reduction of the metal ions was

achieved in a very short time (3 min) [19]. However, the process was not purely biosynthetic and depended on an exogenous electron donor to accomplish reduction of the metal ions. Furthermore, the Pd nanoparticles were not formed in solution and were adsorbed on the surface of the microorganism.

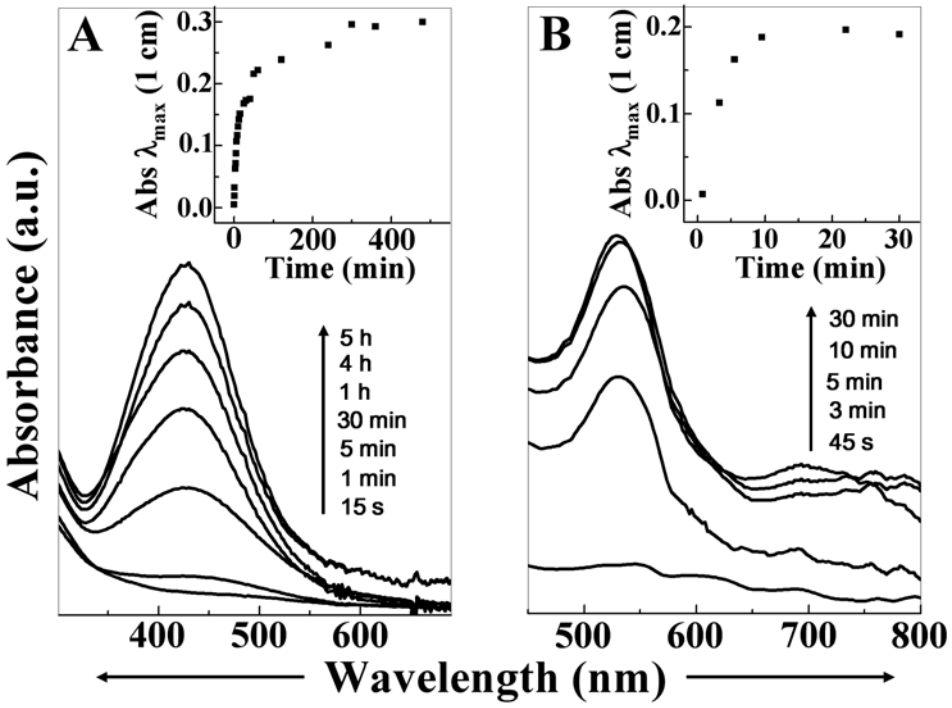

Figure 3.2: *UV-vis spectra recorded as a function of time of reaction of geranium stem extract with, A) 10^{-3} M aqueous solution of $AgNO_3$ and B) 10^{-3} M aqueous solution of $HAuCl_4$. The insets of A and B are plots of maximum absorbance vs time of reaction for the silver and gold solutions respectively.*

Figure 3.2A shows the UV-vis spectra recorded as a function of time of reaction of Ag^+ ions with geranium stem extract. The band corresponding to the surface plasmon vibrations of Ag nanoparticles is observed at 430 nm. The intensity of the surface plasmon band is seen to saturate after 5 h of reaction (inset of Figure 3.2A, plot of absorbance at 430 nm vs time of reaction). The SPR band appears more symmetric and blue shifted by 10 nm relative to the silver nanoparticles synthesized using geranium leaf extract (Figure 3.1A). Figure 3.2B shows the UV-vis spectra recorded from the aqueous $AuCl_4^-$ ion solution as a function of time of reaction. It is seen that the surface plasmon band initially is centered at 536 nm and subsequently shifts to 527 nm. This trend is contrary to that observed with gold nanoparticles formation using geranium leaf extract, where a red shift of the SPR band was observed as the reaction progressed. Additionally

it is also observed that a weak absorption band above 700 nm also appears during the later stage of reduction of gold ions to form gold nanoparticles. The long wavelength band is observed to extend well into the near infrared region of the electromagnetic spectrum. This is attributed to the significant anisotropy in the shape of the gold nanoparticles with excitation of the in-plane SPR contributing to this feature or to the aggregation of particles in solution [20,21] and is attributed to excitation of the in-plane SPR. These observations will be discussed later along with TEM analysis of the gold nanoparticles. The reaction of gold ions with the geranium stem extract saturates after 9-10 min of reaction (inset of Figure 3.2B, plot of absorbance at 530 nm vs. time of reaction) and is thus faster than that of geranium leaf extract.

Figures 3.3A and 3.3B show the UV-vis spectra recorded from the aqueous solution of $AgNO_3$ and $HAuCl_4$ respectively reacted with the geranium root extract as a function of time of reaction. It is observed that the silver SPR band is centered at ca. 435 nm and its absorbance steadily increases as a function of time of reaction as shown in the inset of Figure 3.3A respresenting the plot of absorbance value at λ_{max} of the SPR band as a function of time. The nanoparticles absorption band is slightly asymmetrical with

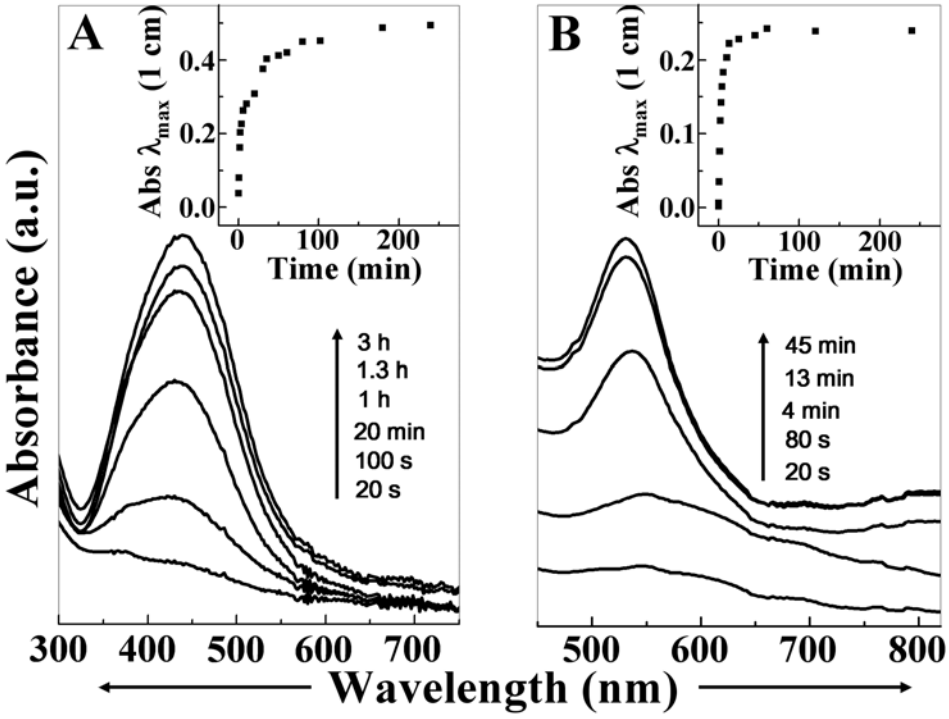

Figure 3.3: *UV-vis spectra recorded as a function of time of reaction of geranium root extract with aqueous solutions of A) 10^{-3} M $AgNO_3$ and B) 10^{-3} M $HAuCl_4$. The insets of A and B are plots of maximum absorbance vs time of reaction for the silver and gold solutions respectively.*

indications of an additional weaker component at ca. 380 nm that is more prominent during the initial time of formation of silver nanoparticles and its prominence is lost as the intensity of the band at 435 nm increases with time. This again suggests some anisotropy in the shape of the silver nanoparticles formed on reduction with geranium root extract. The variation in SPR intensity (intensity at 435 nm) with time of reaction of the silver ions with geranium root extract is shown in the inset of Figure 3.3A. The reduction of the silver ions as inferred from the plot of absorbance at λ_{max} vs time of reaction (inset, Figure 3.3A), saturates within 3 h of reaction.

The UV-vis spectra of the gold solution as a function of time of reaction with geranium root extract is shown in Figure 3.3B while the inset shows the variation in absorbance at λ_{max} (~ 530 nm) due to SPR band of gold nanoparticles in solution as a function of time of reaction. Compared to silver ions, reduction of $AuCl_4^-$ ions is much faster with the SPR centered at around 530 nm reaching saturation within 30 min of reaction (Figure 3.3B, inset). As observed in the UV-vis spectrum measured during gold nanoparticles formation using geranium stem broth, an additional band above 700 nm is also observed when using geranium root extract (Figure 3.3B) for synthesis and can be similarly attributed to excitation of the in-plane SPR. The silver and gold nanoparticles were observed to be very stable in solution with little evidence for aggregation even months after their synthesis.

In all the above instances of reduction of Ag^+ and $AuCl_4^-$ ions using extracts of different parts of the plant geranium, a simple experiment was performed to find out whether the entire amount of metal ions were reduced for the formation of metal nanoparticles. The reaction mixtures were first allowed to react with different plant extracts and reach saturation and left undisturbed for two days. As discussed earlier the saturation is reached within few hours time after which no further appreciable change in the UV-vis spectra is observed. These reaction mixtures after two days were treated with excess amount of $NaBH_4$ solution to observe any additional change in the optical absorption spectra due to reduction of metal ions present after the reaction between the extract and metal ion reaches saturation. Following this experiment it was observed that reduction of $AuCl_4^-$ ions with geranium plant extracts proceeds towards completion while

during synthesis of silver nanoparticles, some unreduced Ag^+ ions are still present after the system reaches equilibrium.

3.2.3 XRD measurements:

Figure 3.4 shows the XRD pattern obtained for silver nanoparticles synthesized using the geranium leaf, stem and root extract represented by the curves 1, 2, and 3 respectively. A number of Bragg reflections are observed for the silver nanoparticles synthesized with each of the geranium plant extracts, which may be indexed based on the fcc structure of silver and is shown in Table 3.1. The XRD pattern thus clearly shows that the silver nanoparticles formed by the reduction of Ag^+ ions by the geranium leaf extract are crystalline in nature. From the calculated d spacing values corresponding to each 2θ values, it appears that the (111) and (200) lattice spacing are broadened as compared to the bulk form and this phenomenon is more pronounced in case of the (111) planes. In addition to the Bragg peaks representative of fcc silver nanocrystals, extra peaks (marked by asterisk) at 2θ values 46, 54.5, 57.1 and 67.2^o are also observed. These values correspond to that of AgCl with standard 2θ values 46.231, 54.826, 57.476 and 67.468^o (JCPDS—International Center for Diffraction Data, PCPDFWIN v. 1.30, 31-1238)

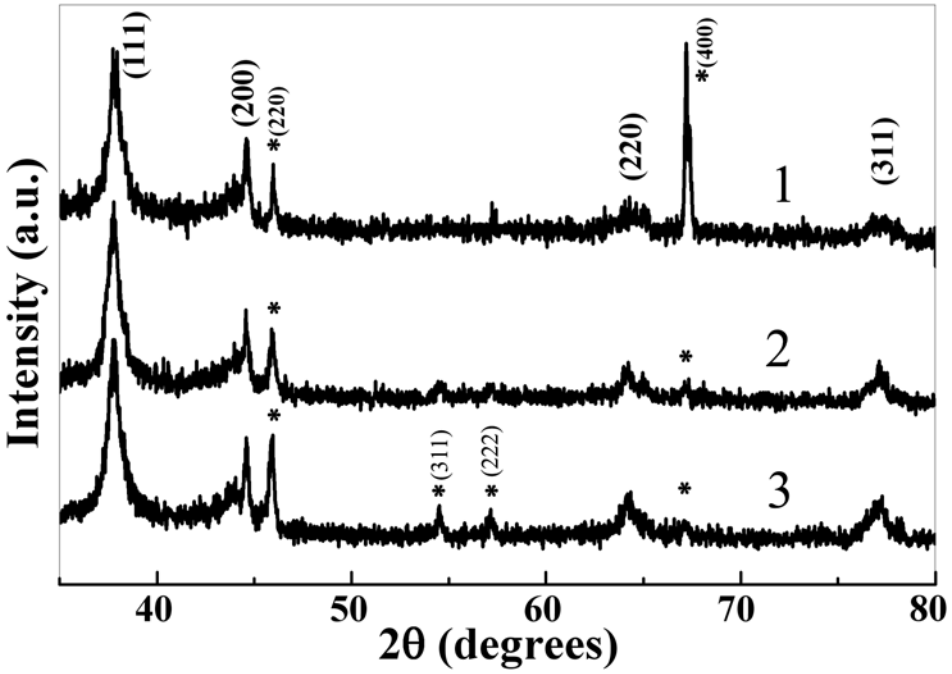

Figure 3.4: *XRD pattern of silver nanoparticles synthesized using geranium leaf, stem and root extracts, represented by the curves 1, 2 and 3 respectively. The asterisk represents the lattice indexing for AgCl phase*

Table 3.1: *Lattice spacing values calculated from the 2θ values obtained from the XRD pattern of silver nanoparticles synthesized using geranium leaf, stem and root extract that are represented by the curves 1, 2 and 3 as shown in Figure 3.4 respectively. Standard values of Ag were obtained from JCPDS—International Center for Diffraction Data, PCPDFWIN v. 1.30, 04-0783.*

Lattice planes (hkl)	Standard Ag (Å)	1) Geranium leaf– Ag (Å)	2) Geranium stem - Ag (Å)	3) Geranium root - Ag (Å)
(111)	2.359	2.38	2.38	2.38
(200)	2.044	2.06	2.06	2.06
(220)	1.445	1.44	1.45	1.45
(311)	1.231	1.24	1.24	1.24

corresponding to the lattice planes (220), (311), (222) and (400) respectively. The origin of Cl^- ions resulting in the precipitation of Ag^+ ions as AgCl could be the plant extract itself, and possibly explains the incomplete reduction of silver ions on reaction with mild reducing agents present in the extracts of different parts of geranium plant. Figure 3.5 shows the energy dispersive analysis by X- rays (EDAX) spectrum of the plain geranium leaf extract and it is observed that the broth consists of a number of inorganic ions apart from the presence of carbon and oxygen originating from the bioorganic component of the extract. Clearly a large percentage of chlorine can be seen that can explain the AgCl formation observed in the XRD measurements. Apart from chlorine the extract contains

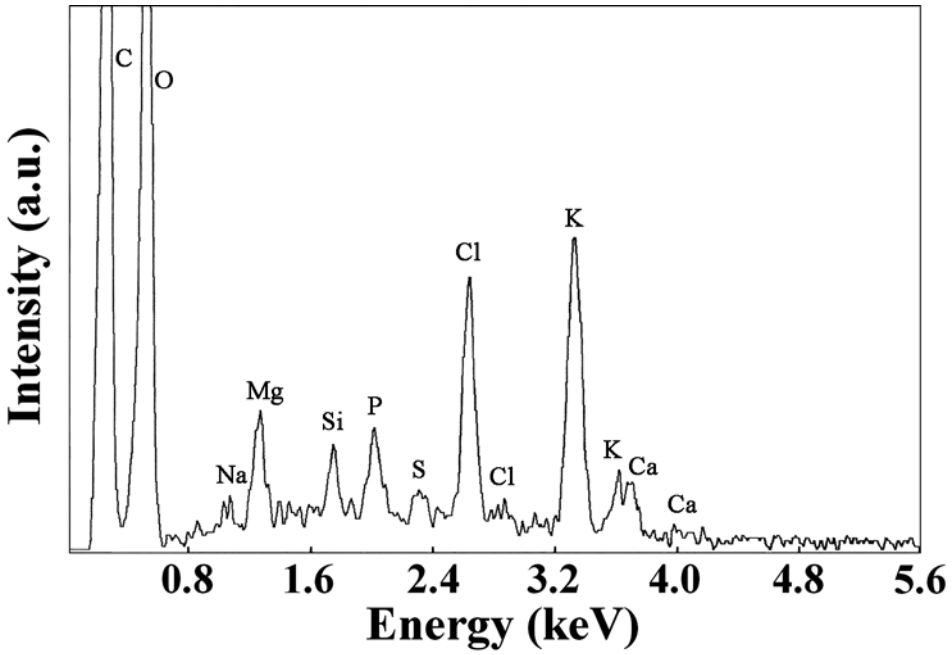

Figure 3.5: *EDAX of crude extract of geranium leaf in absence of any external additive.*

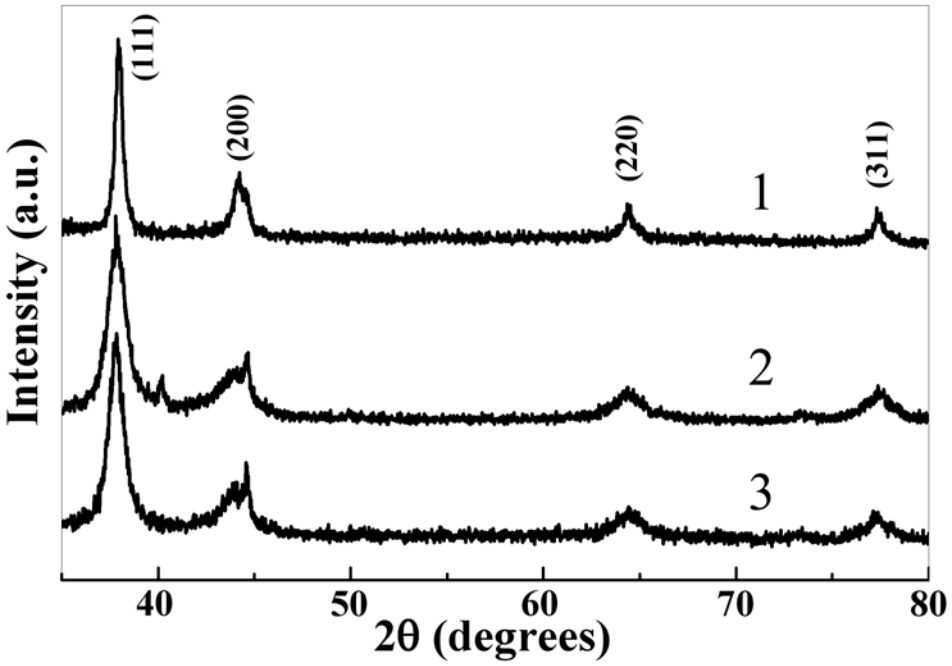

Figure 3.6: *XRD pattern of gold nanoparticles synthesized using extract of geranium leaf, stem and root represented by the curves 1, 2 and 3 respectively.*

potassium, calcium and magnesium in appreciable amounts. Presence of magnesium possibly indicates that the extract also consists of considerable amount of chlorophyll in it. Similar XRD measurements were carried for the gold nanoparticles synthesized using extracts of different parts of geranium plant and are shown in Figure 3.6. The Bragg reflections observed in each case could be indexed based on the fcc structure of gold and is shown in Table 3.2. Similar to silver nanoparticles the lattice spacing of the (111) and (200) planes appear to be expanded (Table 3.2) and it may be noticed that the expansion

Table 3.2: *Lattice spacing values calculated from the 2θ values obtained from the XRD pattern of gold nanoparticles synthesized using geranium leaf, stem and root extract that are represented by the curves 1, 2 and 3 as shown in Figure 3.6 respectively. Standard values of Au were obtained from JCPDS—International Center for Diffraction Data, PCPDFWIN v. 1.30, 04-0784.*

Lattice planes (hkl)	Standard Au (Å)	1) Geranium leaf – Au (Å)	2) Geranium stem – Au (Å)	3) Geranium root – Au (Å)
(111)	2.355	2.37	2.38	2.38
(200)	2.039	2.05	2.06	2.06
(220)	1.442	1.45	1.44	1.44
(311)	1.230	1.23	1.23	1.23

is least for the gold nanoparticles synthesized using geranium leaf extract. It may also be observed that the peak width of the gold nanoparticles synthesized using geranium leaf extract is the least (Figure 3.6, curve 1) suggesting that the average particle size in this case is large as compared to other two cases. From these observations it may be inferred that the lattice spacing of (111) and (200) planes tend to expand with decreasing particle sizes that have greater surface to volume ratio.

3.2.4 TEM measurements:

Figure 3.7 shows representative TEM images recorded from drop-coated films of the silver nanoparticles synthesized by treating silver nitrate solution with geranium leaf extract for 24 hrs. At low magnification (Figure 3.7A), a very large density of silver nanoparticles can be seen and the silver nanoparticles are quite polydisperse ranged in size from 16 to 40 nm with an average size ca. 27 nm. At higher magnification, the morphology of the silver nanoparticles is more clearly seen (Figures 3.7B and 3.7C). The particles are predominantly spherical with a small percentage being elongated (ellipsoidal). What is striking is that the nanoparticles appear to have assembled into very open, quasi-linear superstructures rather than a dense, close-packed assembly as normally is observed for TEM images obtained from aqueous nanoparticles solutions. The assembly of the silver nanoparticles into string-like structures thus explains the appearance of a longitudinal component in the UV-vis spectra recorded from the silver nanoparticles solutions as discussed earlier (Figure 3.1A) and indicates that the assemblies exist in solution and are not formed during sample preparation by evaporation of the solvent. The assembly of the silver particles in the manner observed might be driven by the presence of the bioorganic molecules. While the TEM pictures do not provide direct evidence of the presence of a bioorganic material on the silver nanoparticles, it is interesting to note that most of the particles in the TEM pictures are not in physical contact but are separated by a fairly uniform inter-particle distance. From the higher magnification TEM images (Figure 3.7D) it can be seen that each silver nanoparticle is surrounded by a material with a lower contrast as indicated by an arrow for one of the particles. We believe that this coating material with an average thickness of 5 nm is a bioorganic component of the geranium leaf extract acting as a stabilizing agent for the nanoparticles. In the inset of Figure 3.7D an enlarged view of the indicated

particles is shown and it appears to have further internal core shell kind of structure, demarcated partially by a dashed line. It is possible that the coating material around the nanoparticles could also consist of AgCl as indicated from the XRD measurements. A closer observation of the particles in Figure 3.7A reveals that there are a few particles that exhibit lower contrast as compared to the rest and are possibly the AgCl nanocrystals precipitated from the solution on the reaction of the $AgNO_3$ with the geranium leaf extract.

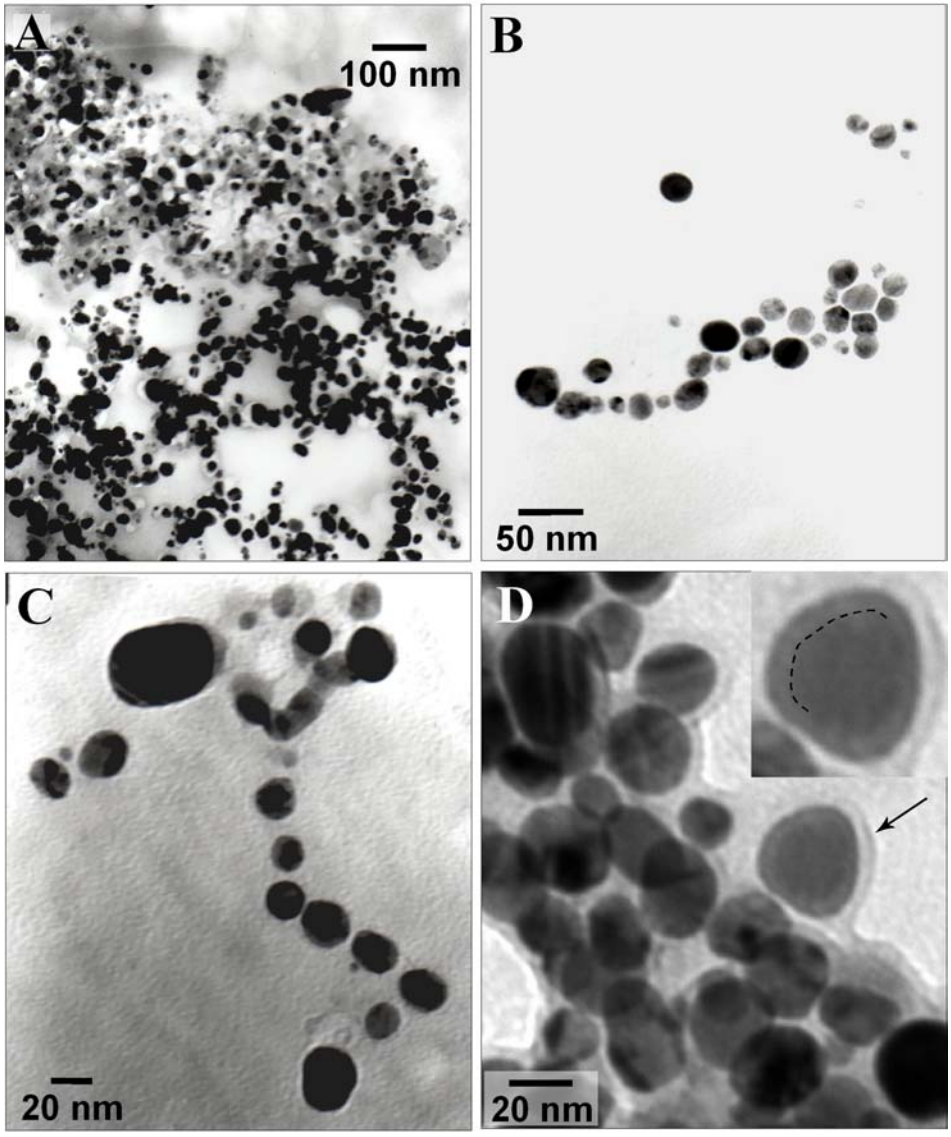

Figure 3.7: *A-D: TEM images of silver nanoparticles at different magnifications formed using geranium leaf extract.*

Figure 3.8 shows TEM images recorded for gold nanoparticles synthesized using geranium leaf extract after reaction with 10^{-3} M $HAuCl_4$ solution for 48 h. The low magnification TEM image (Figure 3.8A) clearly shows a number of gold nanoparticles of a range of sizes and shapes. The structural features of the individual gold nanoparticles are more clearly seen in the higher magnification TEM images (Figures 3.8B-D). The particles are predominantly decahedral and icosahedral in shape, ranging in size from 20-40 nm and exhibit contrast that suggests that they are multiply twinned particles (MTPs).

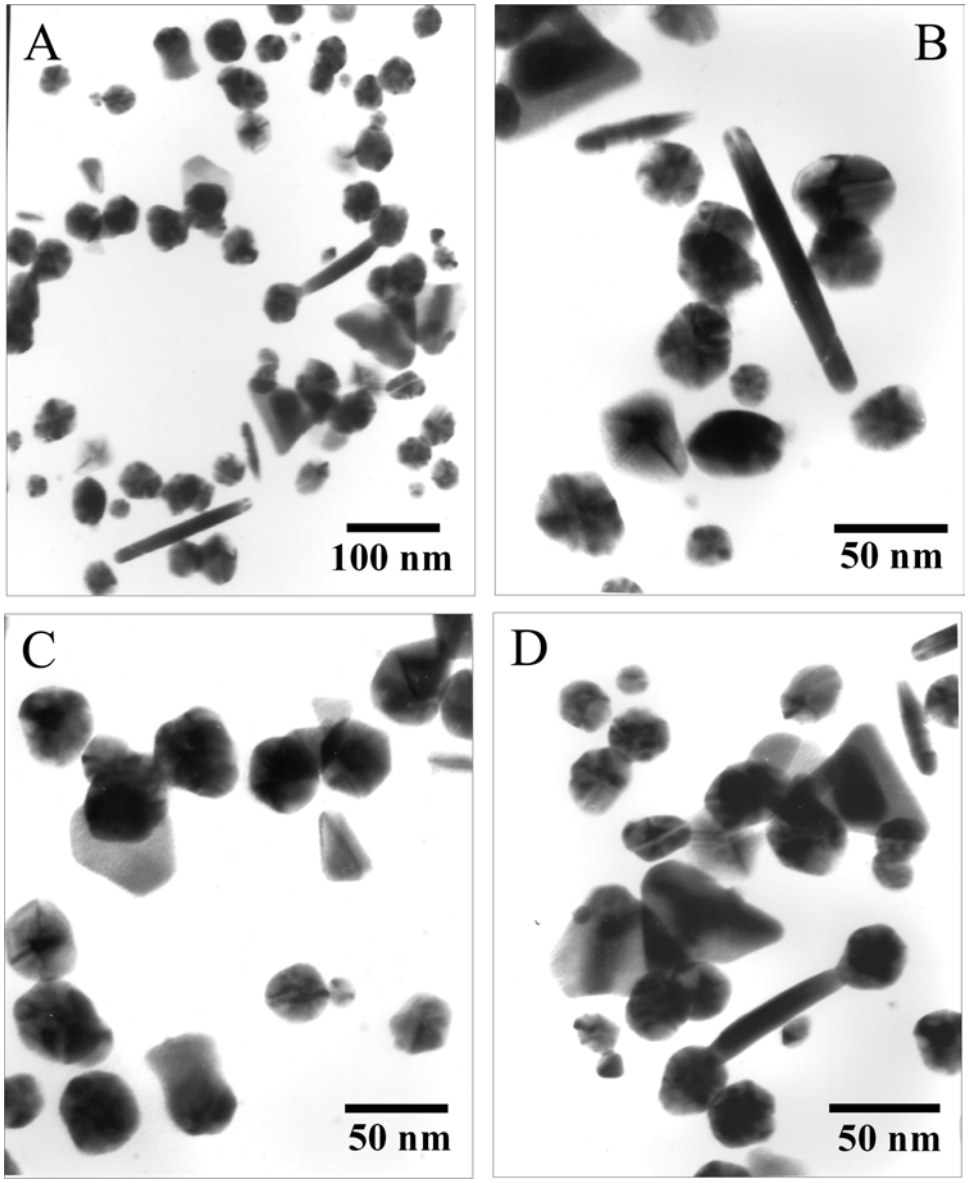

Figure 3.8: *A-D: TEM images at different magnifications of gold nanoparticles formed using geranium leaf extract.*

What is more interesting is the existence of triangular and rod shaped gold nanoparticles of fairly high density in the ensembles. While triangular nanoparticles of silver and gold have been observed in earlier studies [5a,7b], there have been no reports on biogenic gold nanorods. The large nanorod seen in Figure 3.8B shows contrast in the terminal regions implicating possible involvement of MTPs in their growth process. Figure 3.8D shows a gold nanorod straddled by two MTPs in a dumbbell configuration. Whether this is due to a fortuitous juxtaposition of the nanorod and MTPs or if the nanorod is actually growing outwards from the MTPs is not clear at this stage. Gai and Harmer have recently presented a detailed electron microscopy investigation of gold nanorods synthesized by wet chemical methods involving cetyltrimethylammonium bromide (CTAB) as a templating surfactant [22]. They have shown that gold nanorods grow by diffusion of gold atoms to sites within weaker bonded twinned regions of MTPs. This leads to growth of gold nanorods along the (100) direction, an important prerequisite for this process being stabilization of the highly unstable (110) faces by CTAB molecules [22]. The presence of a large density of MTPs and gold nanorods in the TEM images suggests that a similar templating effect involving MTPs as seeds for growth of the nanorods could be operative in the geranium leaf extract experiment of this study.

Seemingly flat gold nanoparticles of predominantly triangular (prismatic) shape were frequently observed in the TEM images (Figure 3.8C and 3.8D). The edges of the triangles are truncated in some cases and the inference that they are extremely thin (on a nanoscale) can clearly be made from Figure 3.8D, which shows increased contrast in the region of overlap of two triangular particles. It may be recollected that in UV-vis spectrum a broad and asymmetric SPR band for the gold nanoparticles solutions synthesized using geranium leaf extract was observed (Figure 3.1B) that can now be attributed to the presence of the polydisperse nanoparticles consisting of bigger spherical particles and the anisotropic shaped gold nanoparticles. Similar argument would also explain the observation of smaller peak width in the XRD measurements (Figure 3.6) for these gold nanoparticles. The ability to grow gold nanoparticles of rod-like and prismatic morphology by biological methods is tremendously exciting given that the optical, electronic and catalytic properties of metal nanoparticles is a strong function of not only particle size but shape as well [23].

Representative TEM images of the silver nanoparticles synthesized using geranium stem extract are shown in Figure 3.9. The silver nanoparticles are essentially spherical in shape and range in size between 9 to 35 nm with average size of ca. 20 nm. A

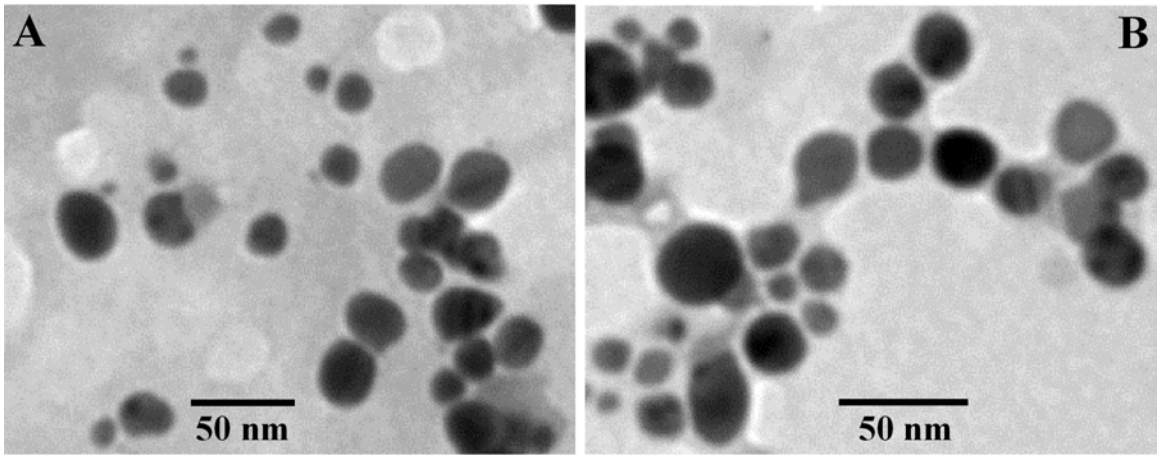

Figure 3.9: *Representative TEM images of silver nanoparticles synthesized by reacting 10^{-3} M $AgNO_3$ solutions with geranium stem extract.*

closer inspection of the TEM images in Figure 3.9 will reveal that all the particles do not have a similar contrast, while some appear dark, few others appear faint in comparison and are possibly the AgCl nanocrystals that contribute to the appearance of corresponding Bragg reflections in the XRD measurements (curve 2, Figure 3.4). The UV-vis absorption spectra (Figure 3.2A) are consistent with the spherical shape of the Ag nanoparticles. Figure 3.10 shows representative TEM images of the gold nanoparticles synthesized using geranium stem extract. The gold nanoparticles appear to be spherical and also

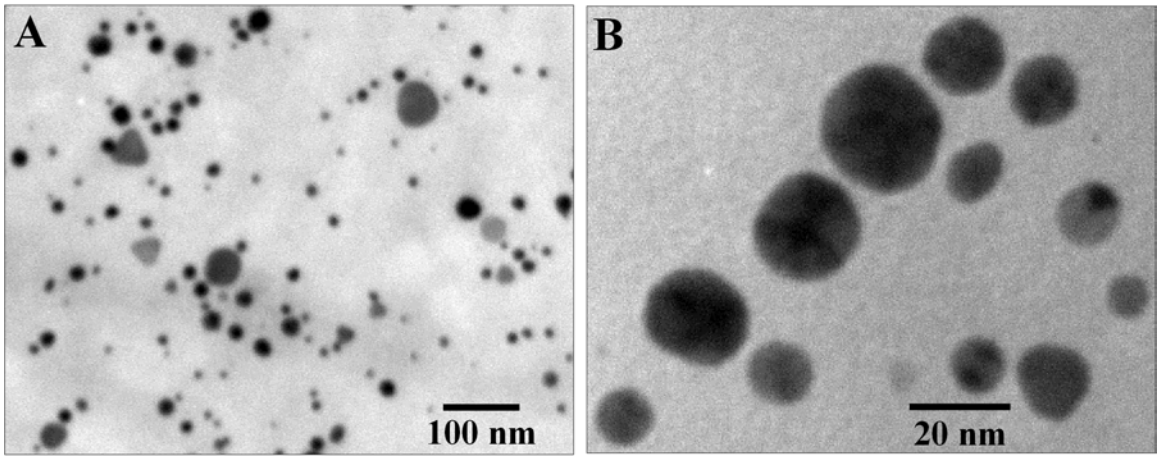

Figure 3.10: *Representative TEM images of gold nanoparticles synthesized by reacting 10^{-3} M $HAuCl_4$ solutions with geranium stem extract.*

consist of some flat particles few of which are triangular in shape. The spherical particles range in size between 8 to 24 nm with average size of ca. 14 nm. The presence of the flat gold nanoparticles is believed to be responsible for the absorption in the UV-vis spectra above 700 nm (Figure 3.2B) and its low intensity indicates their presence as a small fraction. Figures 3.11 show representative TEM images recorded for the Ag nanoparticles synthesized by treating $AgNO_3$ solution with geranium root extract for 24 h. The silver nanoparticles are observed to range in size from 8 to 31 nm with an average size of ca. 19 nm (Figure 3.11A). The morphology of the Ag nanoparticles is predominantly spherical with occasional disk-like particles. Interesting contrast is observed within the physical boundaries of a large percentage of silver nanoparticles and is a well-known feature in twinned and multiply-twinned nanocrystals [24]. Few of the particles indicated by the arrows in Figure 3.11B, appear to have coreshell like structure and this feature is similar to that observed for silver nanoparticles synthesized using geranium leaf broth (inset of Figure 3.7D). The coreshell features of some of the particles can be analogously attributed to the presence of AgCl in the solution as indicated from the XRD measurements (Figure 3.4). As stated before, morphology of some of the particles appear to be disk like, while an exact estimate of the thickness of these apparent flat, disk-like

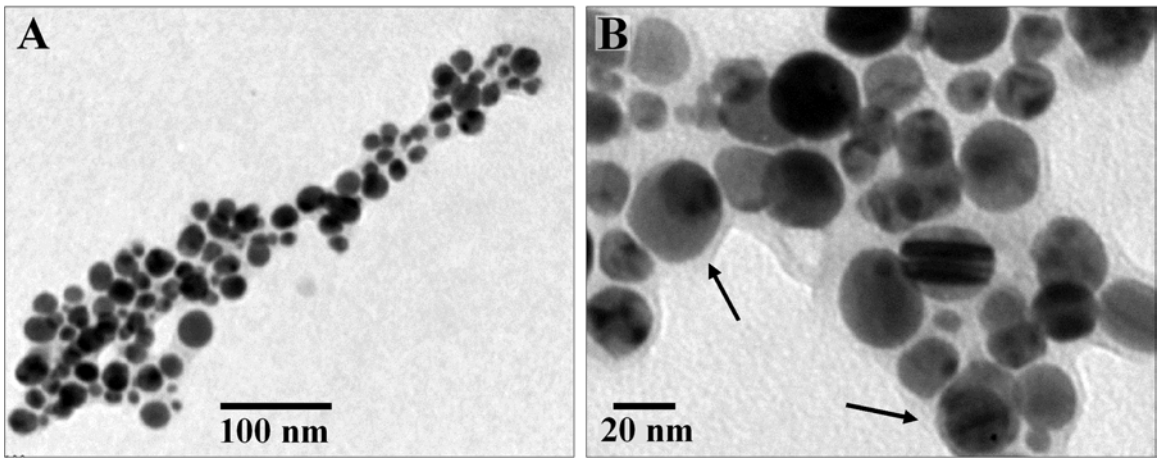

Figure 3.11: *Representative TEM images of silver nanoparticles synthesized by reacting $AgNO_3$ with geranium root extract.*

particles could not be made, the fact that the thickness of these structures is less than that of the spherical particles is inferred from the increased contrast in places where such nanoparticles overlap. The presence of these disk-shaped Ag nanoparticles along with

spherical nanoparticles is consistent with the asymmetric absorption band in the UV-vis absorption spectrum (Figure 3.3A). The asymmetry in the SPR band of the silver nanoparticle solution results primarily due to two distinct absorption bands centered at ca. 380 nm and 435 nm and a much weaker component in the range 475-530 nm. Based on the TEM studies, we tentatively assign 380 nm band to the out-of-plane SPR excitation in the flat, disk-like particles while the weaker band at longer wavelengths (475-530 nm) is attributed to excitation of the corresponding in-plane surface plasmons in flat nanoparticles [25]. The 435 nm resonance is due to the degenerate in-plane and out-of-plane surface plasmons in spherical silver nanoparticles [25]. As briefly mentioned previously, these bands could arise either due to coupling of nanoparticles in solution by aggregation or due to shape anisotropy in the particles. From the TEM images, it is safe to conclude that the features in the UV-vis absorption spectra are due to formation of flat, disk-like silver nanoparticles since little aggregation of the silver nanoparticles is observed.

The TEM image of gold nanoparticles synthesized using geranium root extract (Figure 3.12) shows that the gold nanoparticles are quite polydisperse and range in size from 11 to 34 nm with an average size of ca. 21 nm. The morphology of the nanoparticles is interesting and as in the case of the silver particles, there exists a propensity to form rather flat nanoparticulate structures. The presence of a small percentage of triangular, prismatic gold nanoparticles is observed. Recently, there has been much excitement in the

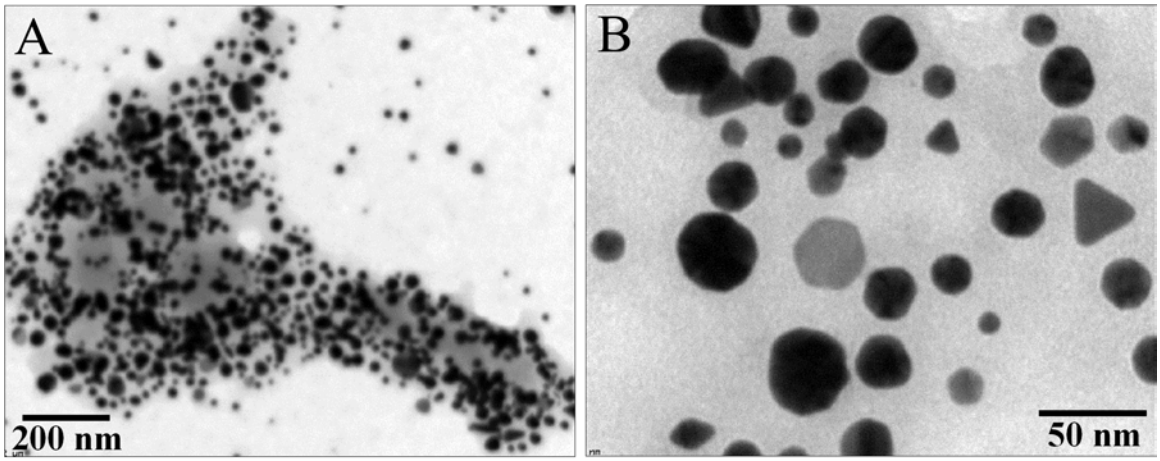

Figure 3.12: *Representative TEM images of Au nanoparticles synthesized by reacting $HAuCl_4$ solutions with geranium root extract.*

synthesis of gold and silver nanoparticles of triangular morphology by chemical methods due to their unusual optical properties [23a, 26] and it is gratifying that biological methods may also be developed to yield such morphology control (albeit after considerable development). Thus, the TEM studies of the geranium root extract synthesized gold nanoparticles clearly show that the absorption in the near infrared region observed in the UV-vis absorption spectra (Figure 3.3B) of the gold nanoparticles is due to in-plane surface plasmon excitation in the triangular nanoparticles while the 530 nm band is due to SPR from spherical nanoparticles and due to out-of-plane plasmons from triangular gold nanoparticles [26b].

3.2.5 FTIR measurements:

FTIR measurements were carried out to identify the nature of the biomolecules that are capping the metal nanoparticles synthesized using extracts of different parts of geranium plant. The metal nanoparticles solutions after complete formation were

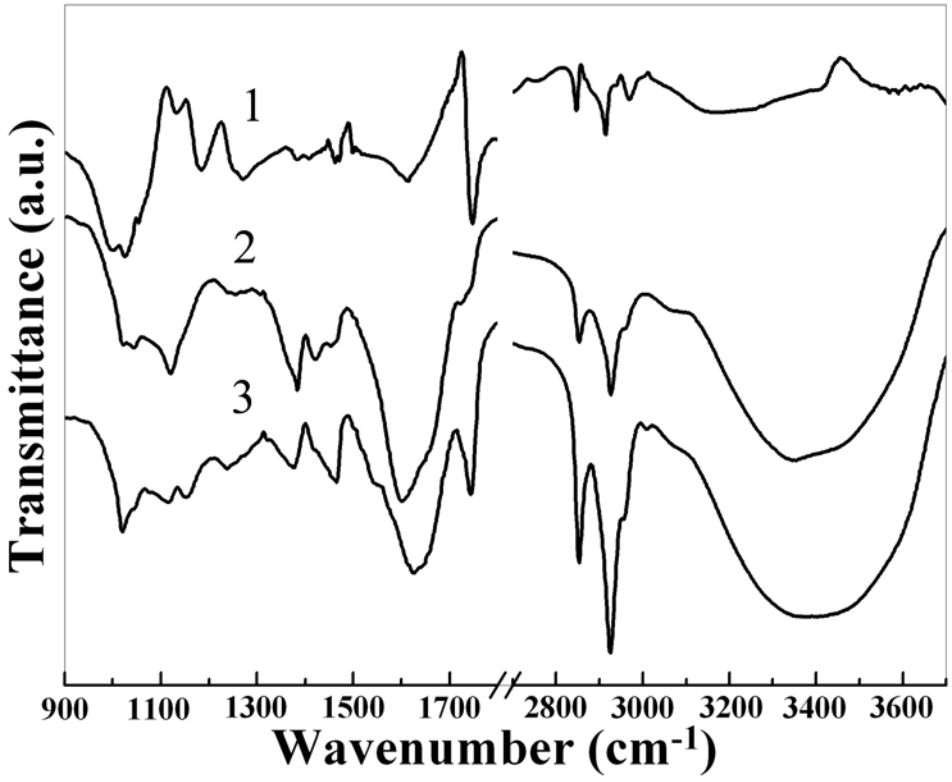

Figure 3.13: *FTIR spectra of silver nanoparticles synthesized by reacting 10^{-3} M $AgNO_3$ solutions with 1) geranium leaf extract 2) geranium stem extract and 3) geranium root extract.*

Table 3.3: *Vibrational frequency assignments for the peaks observed in FTIR spectra of silver nanoparticles synthesized using geranium leaf, stem and root extract, represented by the curves 1, 2 and 3 in Figure 3.13.*

Vibration modes	(1) Leaf-Ag (cm^{-1})	(2) Stem-Ag (cm^{-1})	(3) Root-Ag (cm^{-1})
Ether linkages C-O-C, C–O (ν) of polysaccharides	997		
	1026	1022	1021
	1054	1044	
C–O (ν)	1134	1120	1113
	1184		1152
$-CH_2$ (δ), O–H (δ), C–O (ν) of COOH groups	1272	1256	1237
$-CH_3$ (δ_s)	1384	1384	1375
-C–C–H (δ_{as}), aliphatic C-H close to carbonyl group	1407	1422	1418
-O–C–H (δ), CH_2 (δ_{as})	1462	1454	1464
	1471		
carboxylate anion, aromatic -C=C- (ν)	1615	1602	1625
-C=O (ν)	1748	1726	1743
CH_2 (ν_s)	2847	2853	2853
CH_2(ν_{as})	2915	2926	2926
CH_3 (ν_{as})	2969	2961	2957
O–H (ν)	3178	3350	3370
(δ) bending (ν) stretching			

pretreated for isolating free biomolecules from the capped metal nanoparticles as discussed in the experimental section. Figure 3.13 shows the FTIR spectra of the silver nanoparticles synthesized using the extracts of leaf, stem and root of geranium plantrepresented by the curves 1, 2 and 3 respectively. The different vibrational frequencies shown in the FTIR spectra 1, 2 and 3 of Figure 3.13 are given in Table 3.3

and have been assigned to probable vibrational modes. The broad band in the region 3100 – 3400 cm^{-1} is due to O–H stretching vibrational frequencies and the presence of bands in these regions in the spectra strongly indicates the presence of organic molecules with alcohol functional groups. The observed vibrational frequencies in the range 2840 – 2970 cm^{-1} correspond to the C–H asymmetric (ν_{as}) and symmetric (ν_s) stretching vibrations of the CH_3 and CH_2 groups. The presence of distinct strong peak at 2969 cm^{-1} corresponding to asymmetrical stretching mode of CH_3 group in case of geranium leaf extract synthesized Ag nanoparticle indicates that the capping molecules are highly branched or of smaller chain length. Compared to this, in Ag nanoparticles synthesized using stem and root extract of geranium plant the ν_{as} CH_3 appears as weak shoulder as compared to the strong peaks corresponding to asymmetric and symmetric stretching vibrational mode of CH_2 vibrational frequencies. From the peak position of the C=O stretching vibrational mode at 1748 and 1743 cm^{-1} for Ag nanoparticles synthesized using geranium leaf and root extract it may be inferred that the capping molecules have ester

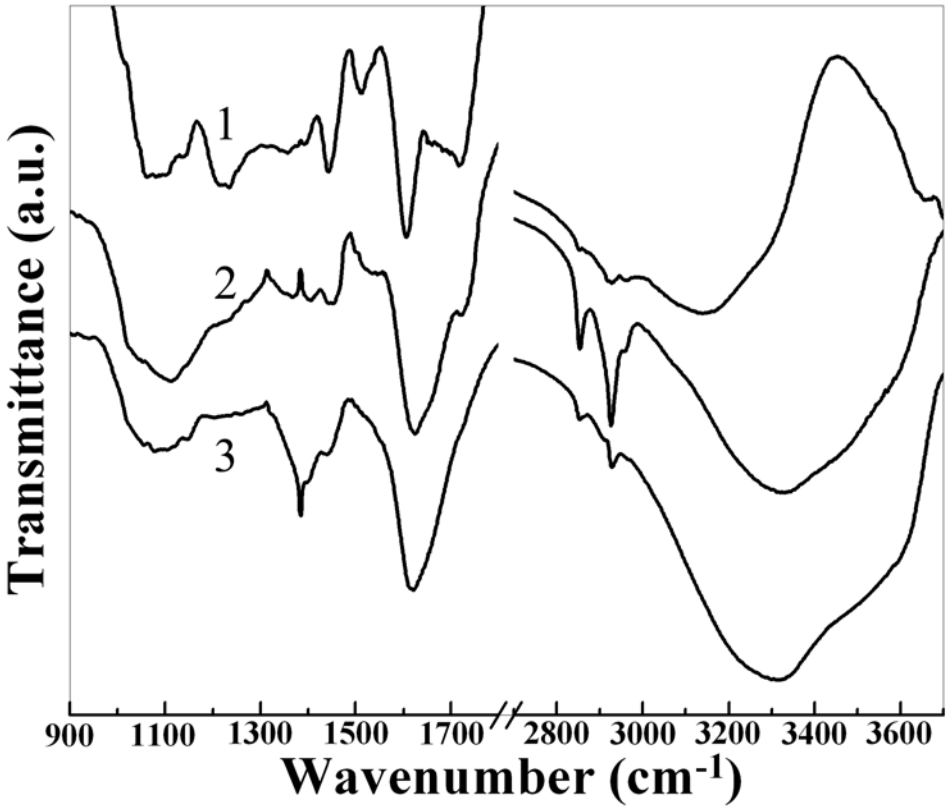

Figure 3.14: *FTIR spectra of Au nanoparticles synthesized by reacting 10^{-3} M $HAuCl_4$ solutions with 1) geranium leaf extract 2) geranium stem extract and 3) geranium root extract.*

Table 3.4: *Vibrational frequency assignments for the peaks observed in FTIR spectra of gold nanoparticles synthesized using geranium leaf, stem and root extract, represented by the curves 1, 2 and 3 in Figure 3.14.*

Vibration modes	(1) Leaf-Au (cm^{-1})	(2) Stem-Au (cm^{-1})	(3) Root-Au (cm^{-1})
Ether linkages, C-O str (ν) of polysaccharides	1061		1088
	1082		
C-O (ν)	1135	1113	
$-CH_2$ (δ), O–H (δ), C–O (ν) of COOH groups	1215		
	1235		
$-CH_3$ (δ_s)	1357	1371	1385
aliphatic C-H (δ) close to carbonyl group		1406	
CH_2 (δ_{as})	1442	1451	1441
-O-C-H (δ)	1512		
Aromatic -C=C- (ν)	1608	1623	1621
-C=O str (ν)	1716	1722	
$-CH_3$ and $-CH_2$ (ν_{as}, ν_s)	2851	2854	2854
	2928	2926	2928
	2963		
O-H (ν)	3149	3328	3316
(δ) = bending (ν) = stretching			

groups. The capping molecules of Ag nanoparticles synthesized using extract of geranium stem exhibit a weak shoulder at 1726 cm^{-1} and possibly originates from a ketonic moiety and not an aldehydic moiety as the corresponding aldehydic C–H stretching modes around 2700 and 2800 cm^{-1} are not observed. The strong and broad peaks at 1615, 1602 and 1625 cm^{-1} observed in spectra 1, 2 and 3 respectively of Figure

3.13 could have contributions from both anionic carboxylate group and aromatic C=C stretching vibrational modes and possibly these different peaks in the region 1370 – 1480 cm^{-1} all correspond to the various bending modes of the methyl groups. Medium to weak and broad peaks observed at 1272, 1256 and 1237 cm^{-1} in the spectra 1, 2 and 3 respectively of Figure 3.13 are possibly molecules bind to the surface of the Ag nanoparticle through the carboxylate groups. The originating from the O–H bending vibrational modes from alcohol functional groups or from C–O stretching and O–H bending vibrations from COOH groups. The vibrational frequencies in the range 960 – 1190 cm^{-1} originate from the C-O stretching modes usually from the ether linkages at lower wave numbers. The appearance of peaks in the region 990–1070 cm^{-1} is characteristic of polysaccharides. From the above assignments made to the observed vibrational frequencies it appears that the biomolecules capping the Ag nanoparticles have alcohol and carboxylic functional groups along with some ester, ketonic and aromatic moieties. Possibly the molecules capping Ag nanoparticles are the oxidized products of terpenoids (e.g. gereniol, citrenellol, etc.) [27] or polysaccharides that are the usually present as large fraction in the plant extracts. The oxidation of reducable alcoholic or aldehydic group to carboxylic group possibly leads to the reduction of the Ag^{+} ions to Ag^{0} state and formation of nanoparticles stabilized by the carboxylic functionality. Similar FTIR measurements were carried for the gold nanoparticles synthesized using geranium leaf, stem and root extract (Figure 3.14). Many of the features seem analogous to that observed for Ag nanoparticles excepting few aspects as follows. The peak intensity of the asymmetric and stretching vibration modes appear to be reduced as compared to that observed for Ag nanoparticles. The carbonyl stretching frequencies 1716 and 1722 cm^{-1} observed in case of gold nanoparticles synthesized using geranium leaf and stem extract respectively are more close to ketonic groups and not to ester groups and the gold nanoparticles synthesized using root extract of geranium plant did not have any noticeable signatures of carbonyl group. Similarly peaks corresponding to carboxyl groups in the region around 1200 cm^{-1} are observed only in case of gold nanoparticles synthesized using geranium leaf extract. The absence of carboxyl group signatures around 1200 cm^{-1} implies that the peak at around 1620 has greater contribution from aromatic C=C stretching frequencies in case of gold nanoparticles synthesized using

geranium stem and root extract. This possibly indicates that gold nanoparticles have less affinity towards adsorbing molecules with carboxylic group and based on the assignments of the peak values the capping molecules are some flavanones, alkaloids or polysaccharides.

3.3 Synthesis of Au, Ag and bimetallic Au core-Ag shell nanoparticles using neem (*Azadirachta indica*) leaf extract.

3.3.1 Experimental section:

The neem (*Azadirachta indica*) leaf extract was prepared by taking 20 g of thoroughly washed and finely cut *Azadirachta indica* leaves in a 500 mL Erlenmeyer flask with 100 mL of sterile distilled water and then boiled the mixture for 2 min before finally decanting it. For reduction of Ag^+ ions, 5 mL of neem leaf extract was added to 45 mL of 10^{-3} M aqueous $AgNO_3$ solution. Similarly, 5 mL of neem leaf extract was added to 45 mL of 10^{-3} M $HAuCl_4$ solution for reduction of $AuCl_4^-$ ions. For synthesis of Ag-Au bimetallic nanoparticles, 90 mL of a 1 : 1 mixture of 10^{-3} M solutions of $AgNO_3$ and $HAuCl_4$ was taken along with 10 mL of neem extract. The reduction of pure Ag^+ and Au^{3+} ions and that of the 1 : 1 $Ag^+/AuCl_4^-$ mixture was monitored by measuring the UV-vis spectra of the solution at regular intervals after diluting a small aliquot (0.2 mL) of the sample 20 times. X-ray diffraction (XRD) measurements of the neem leaf extract-reduced Ag, Au and Au-Ag nanoparticles were carried out on films of the respective solutions drop-coated onto glass substrates on a Phillips PW 1830 instrument operating at a voltage of 40 kV and a current of 30 mA with Cu Kα radiation. For Fourier transform infrared (FTIR) spectroscopy measurements, dry powders of the nanoparticles were obtained in the following manner. The Ag, Au and Au-Ag nanoparticles synthesized after 24 h of reaction of the different salt solutions with the neem leaf extract were centrifuged at 10000 rpm for 15 min following which the pellet was redispersed in sterile distilled water to get rid of any uncoordinated biological molecules. The process of centrifugation and redispersion in sterile distilled water was repeated three times to ensure better separation of free entities from the metal nanoparticles. The purified pellets were then dried and powders subjected to FTIR spectroscopy measurement in diffuse reflectance mode. Samples for transmission electron microscopy (TEM) analysis were prepared by drop-

coating Ag, Au and Au-Ag nanoparticle solutions onto carbon-coated copper TEM grids. The films on the TEM grids were allowed to stand for 2 min following which the extra solution was removed using a blotting paper and the grid allowed to dry prior to measurement.

3.3.2 Synthesis of monometallic silver and gold nanoparticles:

3.3.2a UV-vis measurements:

Formation of the metal nanoparticles by reduction of the aqueous metal ions during exposure to the extract of boiled neem leaves was followed by UV-vis spectroscopy. Figures 3.15A and 3.15B show the UV-vis spectra recorded from the aqueous silver nitrate-neem leaf extract and $HAuCl_4$ acid-neem leaf extract reaction

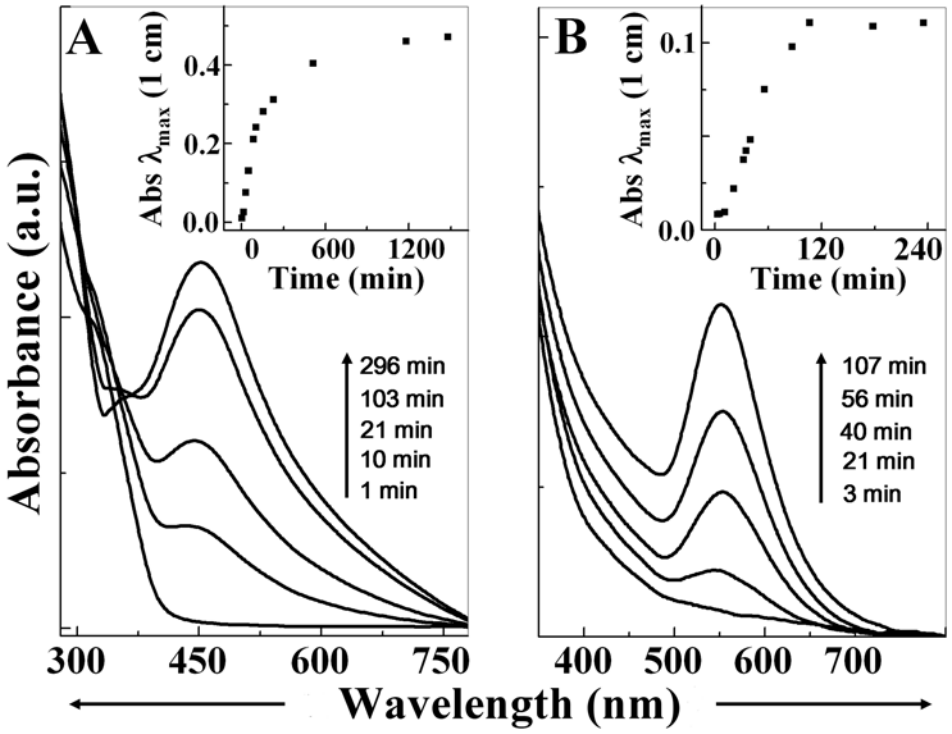

Figure 3.15: *UV-vis spectra recorded as a function of time of reaction of 10^{-3} M aqueous solutions of A) $AgNO_3$ and B) $HAuCl_4$ with neem leaf extract. The insets in A and B represent the respective plots of absorbance at λ_{max} (= 450 nm in case of silver and = 550 nm in case of gold) as a function of time.*

medium as a function of time of reaction. It is observed that the silver surface plasmon resonance band occurs at ca. 450 nm and steadily increases in intensity as a function of time of reaction without any shift in the peak wavelength. In case of gold ion reduction,

the band corresponding to the surface plasmon resonance occurred at 550 nm as shown in Figure 3.15B. The insets of Figure 3.15A and 3.15B represents the plot of absorbance at λ_{max} (i.e at 450 nm for silver nanoparticles and at 550 nm for gold nanoparticles formation respectively) vs time of reaction. The reduction of the metal ions occurs fairly rapidly. More than 90 % of reduction of Ag^{+} and $AuCl_4^{-}$ ions is complete within 4 hrs and 2 hrs respectively after addition of the neem leaf extract to the metal ion solutions (Figures 3.15A and 3.15B) and hence these reactions are efficient as compared to the microbial synthesis of metal nanoparticles [5-8]. The comparatively slower reduction rate of silver ions relative to that of gold ions is most likely due to differences in the reduction potential of the two metal ions because of which all the biomolecules present in the extract having the reducing capability will not be able to reduce the Ag^{+} ions as against the $AuCl_4^{-}$ ions. The metal particles were observed to be stable in solution even 4 weeks

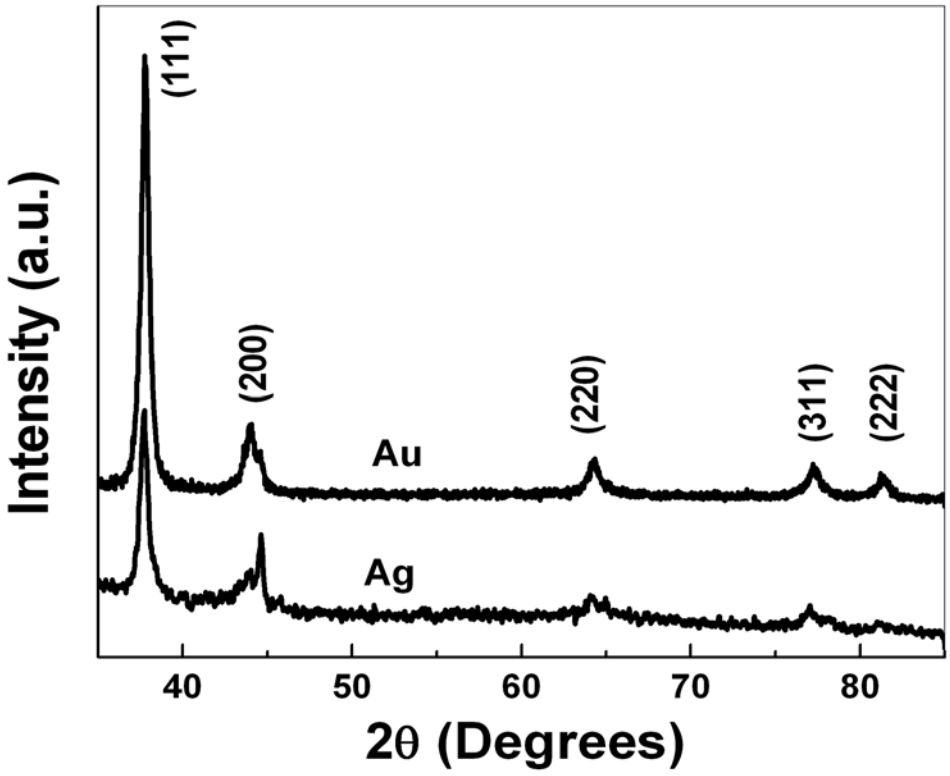

Figure 3.16: *XRD patterns of silver and gold nanoparticles synthesized by treating neem leaf extract with $AgNO_3$ and $HAuCl_4$ aqueous solutions respectively.*

after their synthesis. By stability, we mean that there was no observable variation in the optical properties of the nanoparticles solutions with time. No significant changes were detected in the particle size distributions by TEM during this time interval as well.

3.3.2b XRD measurements:

Figure 3.16 shows the XRD patterns obtained for silver and gold nanoparticles synthesized using the neem leaf extract. A number of Bragg reflections which may be indexed based on the fcc structure of silver and gold are observed and correspond to the (111), (200), (220), (311) and (222) set of lattice planes. The XRD pattern thus clearly shows that the silver and gold nanoparticles formed by the reduction of Ag^+ ions and $AuCl_4^-$ by the neem leaf extract are crystalline in nature.

3.3.2c FTIR measurements:

FTIR measurements were carried out to identify the possible biomolecules responsible for capping and efficient stabilization of the metal nanoparticles synthesized by the neem leaf extract. The silver nitrate and chloroauric acid solutions after complete

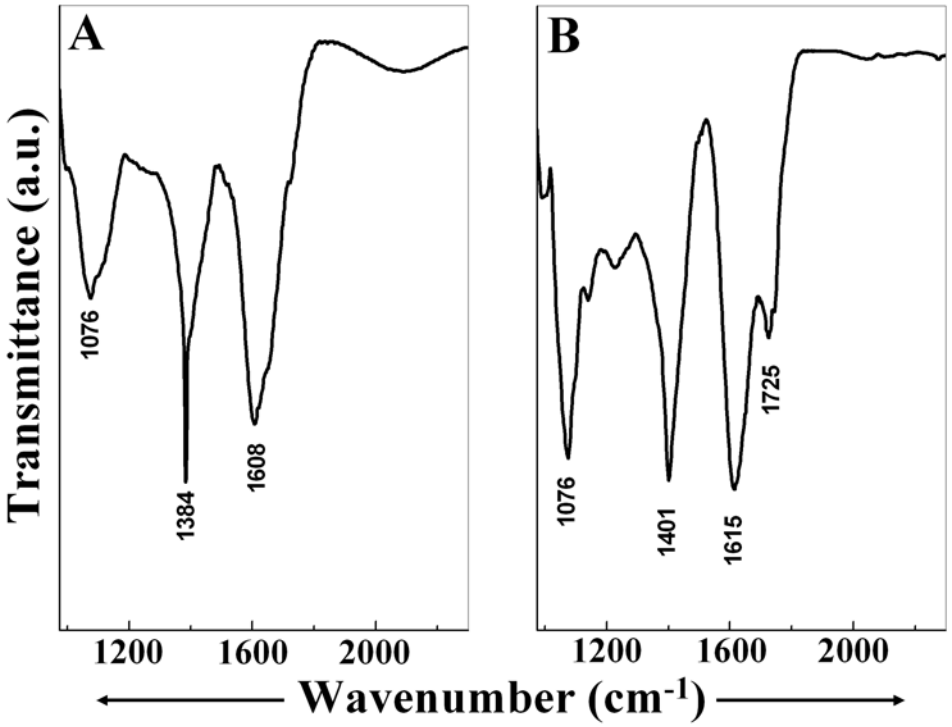

Figure 3.17: FTIR spectra of A) silver nanoparticles synthesized by the reduction of Ag^+ ions and B) gold nanoparticles synthesized by reduction of $AuCl_4^-$ ions using neem leaf extract.

reduction of the respective metal ions and formation of silver and gold nanoparticles were centrifuged at 10000 rpm for 15 min, the pellet obtained was further dialyzed to isolate the metal nanoparticles from free proteins or other compounds present in the solution prior to FTIR analysis. Figures 3.17A and 3.17B show the FTIR spectra of silver and

gold nanoparticles respectively synthesized using the neem leaf extract. The silver nanoparticles sample shows peaks at 1608, 1384 and 1076 cm^{-1} (Figure 3.17A) while the gold nanoparticles show peaks at 1725, 1615, 1401, 1228, 1140 and 1076 cm^{-1} (Figure 3.17B). There appear to be no peaks in the amide I and amide II regions characteristic of proteins/enzymes which have been found to be responsible for the reduction of metal ions when using microorganisms such as fungi for synthesis of metal nanoparticles [7a-7d]. The observed peaks are more characteristic of flavanones and terpenoids that are very abundant in neem plant extracts [28]. The peaks observed for the silver nanoparticles at 1608 cm^{-1} (C=C groups or from aromatic rings), 1384 cm^{-1} (geminal methyls) and 1076 cm^{-1} (ether linkages) and for gold nanoparticles at 1725 cm^{-1} (carbonyls of α,β unsaturated ketone and ester), 1615 cm^{-1} (C=C or aromatic groups), 1401 cm^{-1} (geminal methyls) and at 1140 and 1076 (ether linkages) suggest the presence of the flavanones or terpenoids adsorbed on the surface of metal nanoparticles [28]. It is evident from the differences in the peaks and small shifts in the peak position that the capping species could be different for silver and gold nanoparticles and also that the nature of coordination with the metal surface could be quite different in both cases. Flavanones or terpenoids could be adsorbed on the surface of metal nanoparticles, possibly by interaction through carbonyl groups or the π-electrons in absence of other strong ligating agents in sufficient concentration. Presence of reducing sugars in the extract could be responsible for the reduction of metal ions and formation of the corresponding metal nanoparticles. It is also possible that the terpenoids play a role in reduction of metal ions by oxidation of aldehydic groups in the molecules to carboxylic acids.

3.3.2d TEM measurements:

Figure 3.18 shows representative TEM images recorded from drop-coated films of the silver nanoparticles synthesized by treating 10^{-3} M $AgNO_3$ solution with neem leaf extract for 24 hrs. The silver nanoparticles formed were predominantly spherical and are polydisperse with diameters in the range 5 to 35 nm. Under careful observation, it is noticed that the silver nanoparticles are surrounded by a faint thin layer of other material, which we suppose is the capping organic material from the neem leaf extract. On the other hand, gold nanoparticles synthesized using the neem leaf extract appear to have a

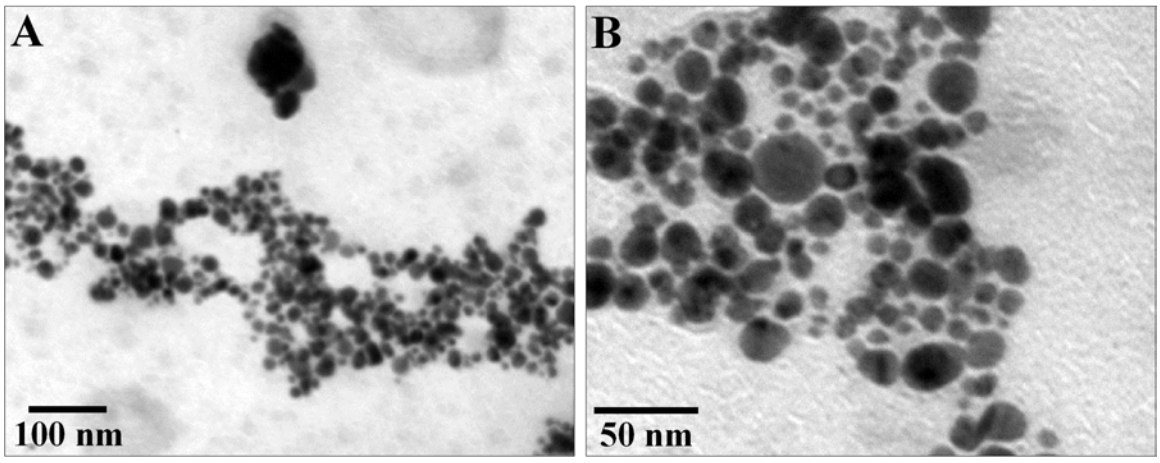

Figure 3.18: *TEM images of silver nanoparticles synthesized by the reduction of Ag^+ ions using Neem leaf extract.*

propensity towards forming thin, planar structures rather than just spherical particles (Figure 3.19). The planar particles formed are predominantly triangular with a very small percentage of hexagonal shaped particles. It is known that the shape of metalnanoparticles considerably changes their optical and electronic properties [20]. The ability to modulate the shape of nanoparticles as observed in this study for gold nanoparticles opens up the exciting possibility of developing further synthetic routes to these structures, employing biological sources. Due to the ease and speed with which silver and gold nanoparticles can be synthesized using neem leaf extract, we proceeded to test this extract in the synthesis of Au-Ag bimetallic nanoparticles.

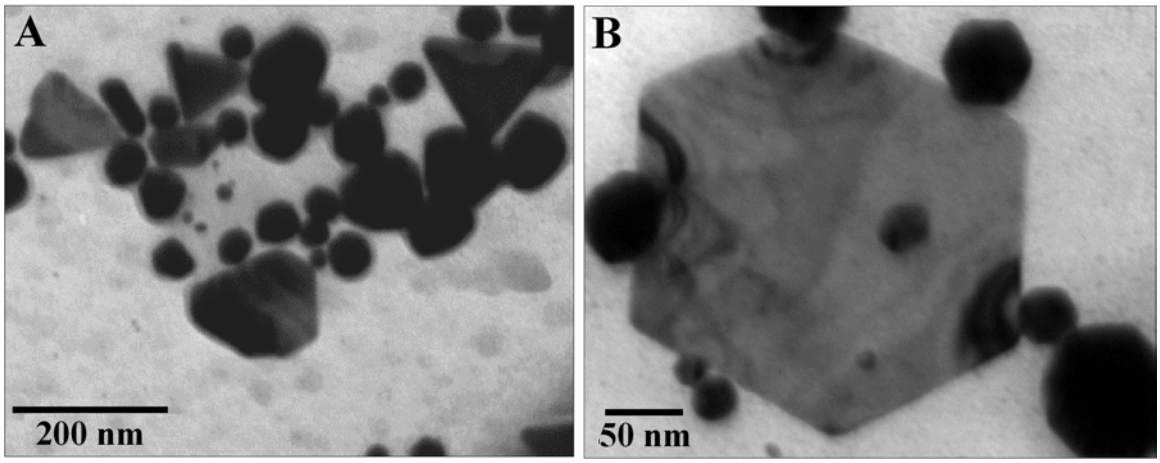

Figure 3.19: *TEM images of gold nanoparticles synthesized by the reduction of $AuCl_4^-$ ions using Neem leaf extract.*

3.3.3 Synthesis of bimetallic Au/Ag nanoparticles:

3.3.3a UV-vis measurements:

Reduction of the silver and gold ions in the 1 : 1 mixture by the neem leaf extract was monitored as a function of time of reaction by UV-vis spectroscopy measurements and the spectra obtained are shown in Figure 3.20. It is Interesting to note that the rate of increase of absorbance at λ_{max}= 557 nm that originates from surface plasmon resonance from the gold nanoparticles (Figure 3.20B) is much faster in the case of the 1 : 1 Ag^{+} : $AuCl_4^{-}$ mixture than in the case of the pure $AuCl_4^{-}$ ions (inset of Figure 3.20B). The increase in absorbance of the surface plasmon resonance of gold nanoparticles formed from the bimetallic solution reaches saturation within 30 min as compared to nearly 2 hrs in case of reduction from $HAuCl_4$ solution alone. This indicates that in a competitive process involving both silver and gold ions, the reduction of gold ions is accelerated and is an important feature of this work. At present, the reason for this unusual behavior is not understood. While the increase in intensity of the gold surface plasmon band is quite

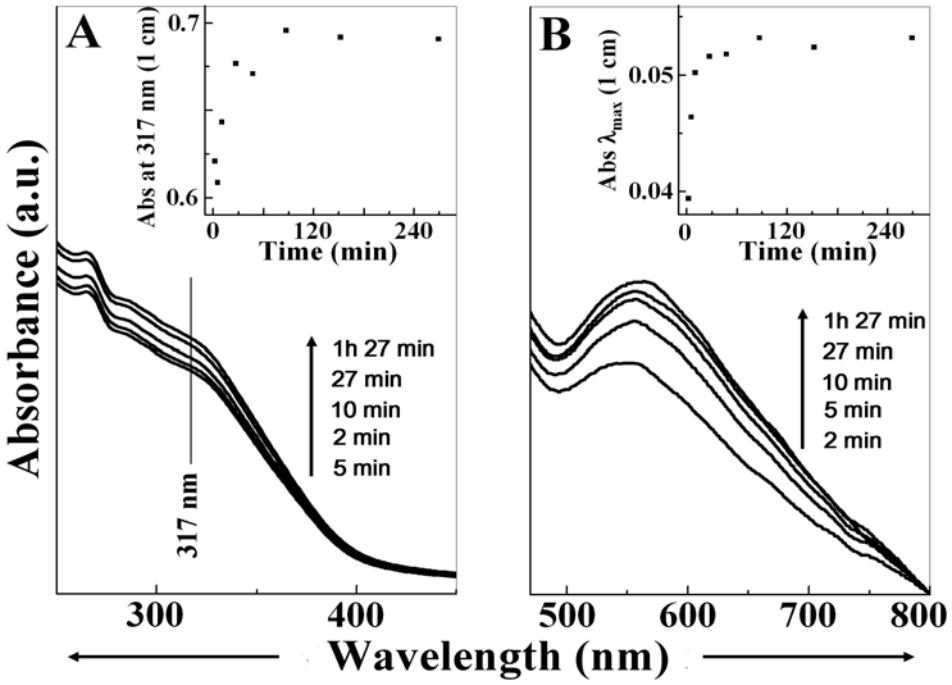

Figure 3.20: *UV-vis spectra recorded as a function of time of reaction of a 1 : 1 solution of gold and silver ions by Neem leaf extract in the range A) 250-450 nm and B) 470-800 nm. The insets of A and B show plots of the absorbance at 317 nm and at λ_{max} (= 557 nm) as a function of time respectively.*

distinct and clear (Figure 3.20B), a well-defined band corresponding to silver nanoparticles is not observed (Figure 3.20A). A small and rigid vertical shift in the UV-vis absorption spectra in the spectral window close to the silver plasmon band is observed (Figure 3.20A) and is symptomatic of some degree of reduction of the silver ions. As the inset of Figure 3.20A shows, the increase in intensity with time at 317 nm stabilizes within 180 min of reaction. We believe the silver particles are rather small in this case and donot form a uniform layer around the gold nanoparticles since this would have led to considerable damping of the gold surface plasmon band and appearance of a distinct silver plasmon vibration band at ca. 400 nm. As will be seen from the TEM results of the bimetallic solution, small silver particles do indeed decorate larger gold nanoparticles that are very rapidly formed in the reaction with neem leaf extract.

3.3.3b FTIR measurements:

The FTIR spectrum recorded from the bimetallic Au/Ag nanoparticles is shown in Figure 3.21. The peaks observed at 1615 (conjugated C=C or aromatic ring), 1400 (geminal methyls) and 1077 cm^{-1} (ether linkages) were similar to those observed in the FTIR spectrum of pure silver and gold nanoparticles.

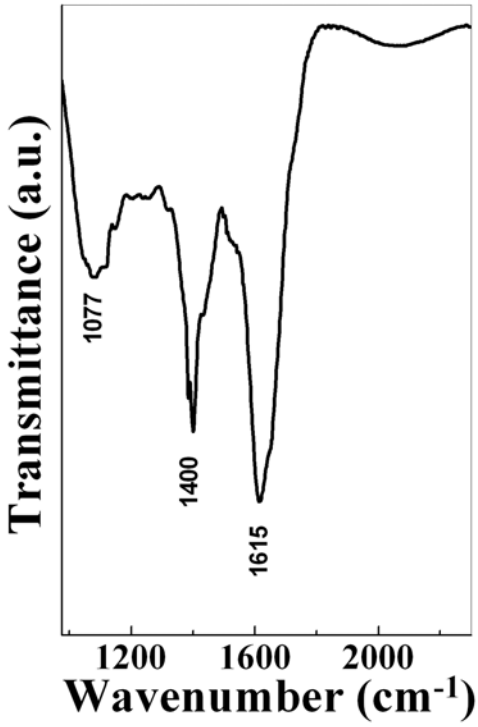

Figure 3.21: *FTIR spectrum of bimetallic Au-Ag nanoparticles synthesized by simultaneous reduction of Ag^+ and $AuCl_4^-$ ions using neem leaf extract*

3.3.3c XRD measurements:

XRD measurement of the solution after treatment of the 1 : 1 10^{-3} M $AgNO_3$ and $HAuCl_4$ solution with neem leaf extract for 24 h was performed. Figure 3.22 shows the XRD pattern of the sample with a number of Bragg reflections. The lattice spacing of fcc silver and gold are almost similar and thus give Bragg reflections at nearly same 2θ values and hence makes it difficult to distinguish between the formation of core-shell or alloy phase of the bimetallic Au-Ag nanoparticles. In the XRD pattern of the bimetallic

nanoparticles prominent Bragg reflection at 37.83^o and 44.67^o are observed that can be indexed to the (111) and (200) lattice of gold and silver fcc phase. Additional Bragg reflections are observed at 45.81, 54.47 and 57.03^o that correspond to AgCl crystals. The low intensity of Bragg reflection corresponding to AgCl phase indicates their presence as a small fraction in the entire solution of nanoparticles. The formation of AgCl in this case is due to the release of Cl^- ions into the reaction medium during the reduction of $AuCl_4^-$ ions to Au^0.

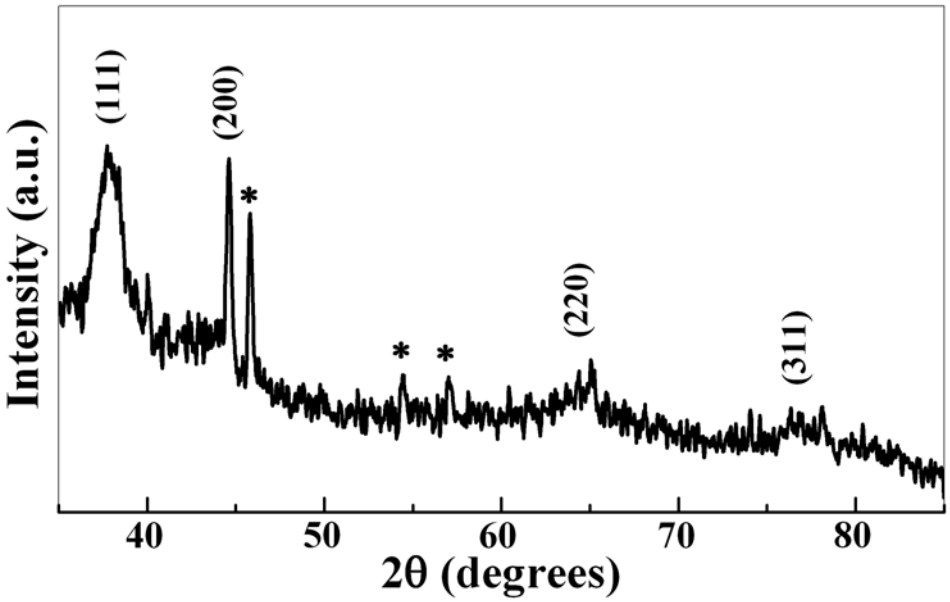

Figure 3.22: *XRD patterns of bimetallic Au-Ag nanoparticles synthesized by treating Neem leaf extract with 1 : 1 mixture of $AgNO_3$ and $HAuCl_4$ aqueous solutions.*

3.3.3d EDAX measurements:

Preliminary EDAX measurements indicated that the sample is composed of gold, silver and chlorine and is shown in Figure 3.23. Gold and silver were present approximately in the ratio 2:1. It may be noted here that for EDAX measurements, same purified sample used for FTIR analysis was used. This eliminates any possibility of the presence of free ions of either gold or silver in the reaction medium and thus the observed amount of silver is present both as reduced metal and as AgCl precipitate. The low percentage of silver in the reduced state is the reason for the low absorbance in the region corresponding to silver nanoparticles (Figure 3.20).

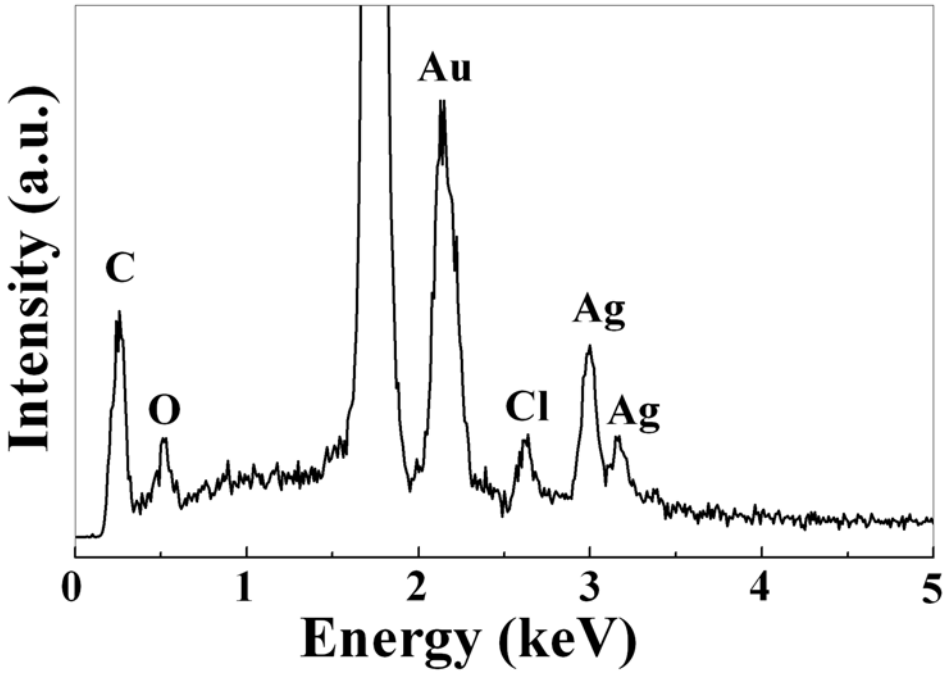

Figure 3.23: *EDAX of bimetallic Au-Ag nanoparticles synthesized by treating neem leaf extract with 1 : 1 mixture of 10^{-3} M $AgNO_3$ and $HAuCl_4$ aqueous solutions.*

3.3.3e TEM measurements:

Figure 3.24 shows representative TEM micrographs of bimetallic Au/Ag nanoparticles. The nanoparticles are in the range of 50 to 100 nm. It is seen that while the particles are predominantly spherical in morphology, they are not well separated from each other and tend to form structures wherein large particles (dimensions in the range 50-70 nm) are capped with smaller particles (15-20 nm diameter). As discussed above, the rate of formation of silver nanoparticles is relatively slow compared to gold nanoparticles formation, and hence it is possible that gold nanoparticles are formed initially and formation of silver nanoparticles is delayed. The silver nanoparticles formed after equilibration of the gold nanoparticles density then assemble onto the surface of the larger gold nanoparticles thus forming the peculiar core-shell structures observed (Figure 3.24). The reasons for this mode of assembly are not understood and may by due to electrostatic interactions, hydrogen bonding between the capped bioorganic etc. Careful comparison of the TEM images of silver, gold and bimetallic Au/Ag nanoparticles shows that the cores in the bimetallic Au/Ag nanoparticles resemble that of pure gold nanoparticles and the particles constituting the shell resemble pure silver nanoparticles

both in terms of their size and shape. It can be stressed here that the aggregation seen is not random and appears to be driven by specific interactions. Randomly aggregated structures would have been observed had the assembly of gold nanoparticles been driven by, for example, screening of repulsive electrostatic interactions by silver ions. In conjunction with the EDAX, FTIR and UV-vis measurements it is thus shown that with neem leaf extract, high density of stable bimetallic core-shell nanoparticles can be formed.

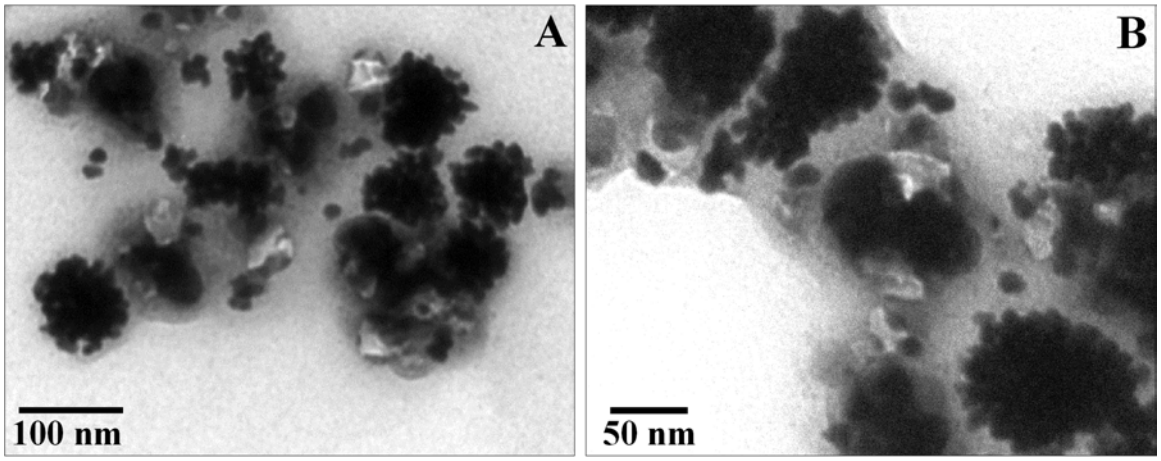

Figure 3.24: *TEM images of bimetallic Au-Ag nanoparticles synthesized by simultaneous reduction of Ag^+ and $AuCl_4^-$ ions from an aqueous bimetallic solution of 1 : 1 molar ratio $AgNO_3$ and $HAuCl_4$ using neem leaf extract.*

3.4 Conclusions.

In conclusion, through a green chemistry approach rapid synthesis of stable silver, gold and bimetallic Au-Ag core-shell nanoparticles at high concentration using plant extracts such as leaf, stem and root extract of geranium plant and neem leaf extract has been demonstrated. It has been demonstrated that plant extracts apart from being a more convenient way of synthesizing nanoparticles as compared to microbial synthesis have also a propensity to exhibit some shape control of the metal nanoparticles formed. The formation of pure metallic and bimetallic nanoparticles by reduction of the metal ions is possibly facilitated by reducing sugars and/or terpenoids present in the plant extracts. The present study opens up a new possibility of very conveniently synthesizing metal nanoparticles using natural products. Achievement of such rapid time scales for synthesis of metallic nanoparticles contributes to an increase in the efficiency of synthetic

procedures utilizing environmentally benign natural resources as an alternative to chemical synthesis protocols. Issues such as monodispersity and shape selectivity for obtaining phase pure monodisperse nanoparticles of a particular shape have to be addressed.

3.5 References:

1) a) Mann, S. *Nature* **1993**, *365*, 499. b) Oliver, S.; Kupermann, A.; Coombs, N.; Lough, A.; Ozin, G. A. *Nature* **1995**, *378*, 47.

2) Young, J. R.; Davis, S. A.; Bown, P. R.; Mann S. *Journal of Structural Biology* **1999**, *126*, 195.

3) a) Lovley, D. R.; Stolz, J. F.; Nord, G. L.; Phillips, E. J. P. *Nature* **1987**, *330*, 252. b) Philse, A. P.; Maas, D. *Langmuir*, **2002**, *18*, 9977.

4) a) Southam, G.; Beveridge, T. J. *Geochim .Cosmochim. Acta* **1996**, *60*, 4369. b) Beveridge, T. J.; Murray, R. G. E. *J.Bacteriol.* **1980**, *141*, 876. c) Fortin, D.; Beveridge, T. J. in *Biomineralization. From Biology to Biotechnology and Medical Applications* (Ed. E. Baeuerien), Wiley-VCH, Weinheim **2000**, *7*.

5) a) Klaus, T.; Joerger, R.; Olsson, E.; Granqvist, C. G. *Proc. Nat. Acad. Sci.* **1999**, *96*, 13611. b) Klaus-Joerger, T.; Joerger, R.; Olsson, E.; Granqvist, C. G *Trends Biotech.* **2001**, *19*, 15. c) Joerger, R.; Klaus, T.; Granqvist, C. G. *Adv.Mater.* **2000**, *12,* 407.

6) Nair, B.; Pradeep, T. *Crystal Growth & Design* **2002**, *2*, 293.

7) a) Mukherjee, P.; Ahmad, A.; Mandal, D.; Senapati, S.; Sainkar, S. R.; Khan, M. I.; Ramani, R.; Parischa, R.; Ajaykumar, P. V.; Alam, M.; Sastry, M.; Kumar, R. *Angew. Chem. Int. Ed.* **2001**, *40*, 3585. b) Mukherjee, P.; Senapati, S.; Mandal, D.; Ahmad, A.; Khan, M. I.; Kumar, R.; Sastry, M. *ChemBioChem* **2002**, *3*, 461. c) Mukherjee, P.; Ahmad, A.; Mandal, D.; Senapati, S.; Sainkar, S. R.; Khan, M. I.; Parischa, R.; Ajayakumar, P. V.; Alam, M.; Kumar, R.; Sastry, M. *Nano Lett.* **2001**, *1*, 515. d) Ahmad, A.; Mukherjee, P.; Senapati, S.; Mandal, D.; Khan, M. I.; Kumar, R.; Sastry, M. *Coll. Surf. B.* **2003**, *28*, 313. e) Ahmad, A.; Mukherjee, P.; Mandal, D.; Senapati, S.; Khan, M. I.; Kumar, R.; Sastry, M. *J. Am. Chem. Soc.* **2002**, *124*, 12108.

8) Ahmad, A.; Senapati, S.; Khan, M. I.; Kumar, R.; Sastry, M. *Langmuir*, **2003**, *19*, 3550.

9) Monje, P. V., ;Baran, E. J., *J. Plant Physiol.* **2004**, *161*, 121.

10) Monje, P.V. ;Baran, E.J., *J. Plant Physiol.* **2000**, *157*, 457.

11) Gajdardziska-Josifovska M.; McClean R. G.; Schofield M. A.; Sommer C. V.; Kean W. F. *Eur. J. Mineral.* **2001**, *13*, 863.

12) Gardea-Torresdey, J. L.; Peralta-Videa, J. R.; de la Rosa, G.; Parsons, J.G. *Coord. Chem. Rev.* **2005**, *249*, 1797.

13) Anderson, C. W. N.; Brooks, R. R.; Stewart, R. B.; Simcock, R. *Nature*, **1998**, *395*, 553.

14) a) Brumfiel G., *Nature*, **2003**, *424*, 246. b) *The big down*, available at the link http://www.etcgroup.org/documents/TheBigDown.pdf

15) Gardea-Torresdey, J. L.; Parsons, J. G.; Gomez, E.; Peralta-Videa, J.; Troiani, H. E.; Santiago, P.; Jose-Yacaman, M., *Nano Lett.* **2002**, *2*, 397.

16) Gardea-Torresdey, J. L.: Gomez, E.; Peralta-Videa, J. R.; Parsons, J. G.; Troiani, H.; Jose-Yacaman, M. *Langmuir* **2003,** *19*, 1357.

17) Sanyal A.; Sastry M. *Chemical Communications***, 2003,** *11***,** 1236**.**

18) Mulvaney, P. *Langmuir* **1996**, *12***,** 788.

19) Yong, P.; Rowson, N. A.; Farr, J. P. G.; Harris, I. R.; Macaskie, L. R. *Biotechnol. Bioeng.* **2002**, *80*, 369.

20) a) Kelly, K. L.; Coronado E.; Zhao, L. L.; Schatz G. C. *J. Phys. Chem. B* **2003**, *107*, 668. b) El-Sayed, M. A. *Acc. Chem. Res.* **2001**, *34*, 257.

21) a) Maye, M.; Chun, S. C.; Han, L.; Rabinovich, D.; Zhong, C. J. *J. Am. Chem. Soc.* **2002**, *124*, 4958. b) Norman, T. J.; Grant, C. D.; Jr., Magana, D.; Zhang, J. Z. *J. Phys. Chem. B.* **2002**, *106*, 7005.

22) Gai, P. L.; Harmer, M. A. *Nano Lett.*, **2002**, *2*, 771.

23) a) Jin, R.; Cao, Y.; Mirkin, C. A.; Kelly, K. L.; Schatz, G. C.; Zheng, J. G. *Science*, **2001**, *294*, 1901. b) Ahmadi, T. S.; Wang, Z. L.; Green, T. C.; Henglein, A.; El-Sayed, M. A. *Science*, **1996**, *272*, 1924.

24) Marks, L. D. *Rep. Prog. Phys.* **1994**, *57*, 603.

25) Hao, E.; Kelly, K. L.; Hupp, J. T.; Schatz, G. C. *J. Am. Chem. Soc.* **2002**, *124*, 15182.

26) a) Pastoriza-Santos I.; Liz-Marzan, L. M. *Nano Lett.* **2002**, *2*, 903. b) Malikova, N.; Pastoriza-Santos, I.; Schierhorn, M.; Kotov, N. A.; Liz-Marzan, L. M. *Langmuir.* **2002**, *18*, 3694.

27) a) Rao, B.R.R. *Industrial Crops and Products*, **2002**, *16*, 133. b) Husain, A. *Status Report on Aromatic and Essential Oil-Bearing Plants In NAM Countries* (Centre For Science And Technology Of The Non-aligned and Other Developing Countries), **1994**, 93.

28) a) Garg, H.S. ; Bhakuni, D. S. *Phytochemistry* **1984**, *23*, 2115. b) Siddiqui, B. S. ; Afshan, F. ; Faizi, G. S. ; Naqvi, S. N. H. ; Tariq, R. M. ; *Phytochemistry* **2000**, *53*, 371.

Chapter IV

Synthesis of Flat Triangular and Hexagonal Gold Particles Using Lemongrass Leaf Extract

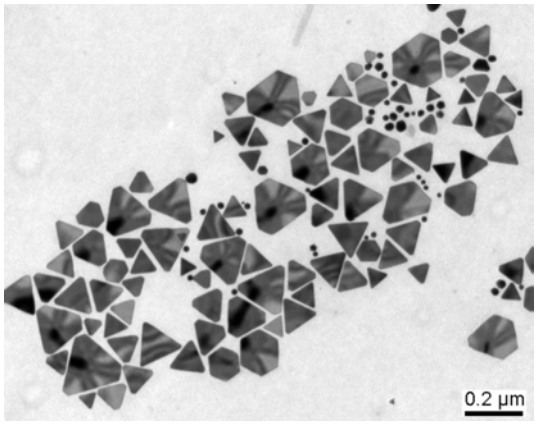

Following the synthesis of metal nanoparticles using plant extracts as discussed in previous chapter, lemongrass (cymbopogon flexuosus) leaf extract was observed to have remarkable ability to promote the growth of large percentage of flat triangular and hexagonal gold particles. In this chapter synthesis and growth of these flat gold triangular and hexagonal particles has been discussed. Following the kinetics of the formation of triangles it could be inferred that the growth of flat gold particles proceeds through initial formation of spherical particles followed by their assembly and room temperature sintering. These flat particles have large absorption in the near-infrared (NIR) region and the absorption position can be tuned by modulating their size with simple variations in the experimental conditions. The chapter also discusses the potential application of these flat gold particles to fabricate NIR absorbing optical coatings on glass substrates.

Part of the work presented in this chapter has been published:

(1) Shankar, S. S.; Rai, A.; Ankamwar, B.; Singh, A.; Ahmad, A.; Sastry, M. *Nat. Mater*. **2004**, *3*, 482. (2) Shankar, S. S.; Rai, A.; Ahmad, A.; Sastry, M. *Chem. Mater.* **2005**, *17*, 566.

4.1 Introduction.

Everyday we come across materials in a myriad of shapes, each tailor made to provide solutions for specific utilities. These bulk materials regardless of their shape, however complex or simple, generally tend to exhibit same physical and chemical properties. The recent obsession of the nanotechnologists to create materials of different sizes and shapes in nano-dimensions arise from the unforeseen properties pertaining to these variations. It is interesting to learn that nanoparticles of different sizes melt at different temperatures, [1] and that a change in their shape could lead to change in their colors [2] and might also lead to different catalytic activities [3]. The size and shape [1-4] dependent physicochemical and optoelectronic properties of metal and semiconductor nanoparticles render them applicable in catalysis [5], biosensing [6], recording media [7] and optics [8]. Anticipating such unique properties and potential applications, various shapes viz., nanocubes [9], nanorods/nanowires [10], nanodisks [11], nanotapes/nanobelts [12], nanodumbbells [13], nano-teardrops/arrows/tetrapods [14], and a number of other shapes [15] have been synthesized by chemical and physical methods. Of the many shapes of nanoparticles that have been synthesized till date, formation of gold nanotriangles in small percentages was reported by Turkevich in as early as 1951 using sodium citrate reduction method [16]. In recent past, a number of synthesis protocols of silver nanotriangles/nanoprisms have been reported [17]. However, synthesis of gold nanotriangles in large percentage could be achieved only lately [18]. Apart from occasional sighting of gold nanotriangles previously, Malikova et al had succeeded in achieving a spectroscopically legible anisotropic flat gold nanoparticles using salicylic acid reduction method [18c]. As mentioned previously, the syntheses of anisotropic metal nanostructures have been achieved by different chemical and physical methods. The mechanisms that explain the formation of nanoparticles of different shapes can be classified into the following categories: a) nucleation and growth mechanism [19], b) seeded growth, where the anisotropy is directed by the defects in the seed [19j,k,20], c) anisotropy as a consequence of physical confinements of the rigid templates during growth of nanoparticles [19j,21] and d) shape evolution of preformed nanoparticles induced by chemical [22] or physical means [17d,23]. In the nucleation and growth mechanism, first nuclei starts forming in solution induced by the supersaturation of

solute, and later by a diffusive mechanism, more and more solute species get deposited on it leading to crystal growth [19a-g]. Presence of surface-active agents that passivate certain crystallographic planes can direct the evolution of different shapes both during growth from freshly formed nuclei [19j,k] or from preformed seed particle [19j,k,20]. In some of the cases, initial growth process may also be followed by a ripening process [17b,19g,h] or by an aggregation based secondary particle formation leading to interesting final structures [24]. It is to be noted that all these methods either involve multiple steps and reagents and/or require very precise control of experimental conditions to achieve the desired shape control.

In this chapter we discuss the single step synthesis of triangular gold nanoparticles using lemongrass leaf extract in a green chemistry approach. A large percentage of flat triangular and hexagonal gold nanoparticles could be achieved by this route bettering previous attempts to synthesize them following purely chemical approaches. These flat particles appear to grow by a process involving rapid reduction, assembly and room temperature sintering of the spherical particles. The solution of triangular and hexagonal gold particles exhibits large near infrared (NIR) absorption. The NIR absorption of the triangular and hexagonal particles is dependent on their edge lengths and could be conveniently tuned by varying the concentration of the lemongrass leaf extract acting as a natural reducing agent. These NIR absorbing gold nanoparticles may find application in hyperthermia of cancer cells [25] and could possibly be good candidates as conducting tips for scanning tunneling microscopy (STM). These flat particles would also block radiation in the NIR region of the solar spectrum and thus could serve as efficient NIR blocking optical coatings for glass windows to reduce temperature-rise in an enclosed room [26]. In this chapter, the preliminary experimental investigations to test the NIR blocking efficiency of these flat gold particles on glass substrates have also been described.

4.2 Synthesis of triangular and hexagonal gold particles using lemongrass leaf extract.

4.2.1 Experimental Details:

The leaf extract was prepared by boiling 100 g of thoroughly washed and finely cut lemongrass leaves (*Cymbopogon flexuosus*) in 500 mL of sterile distilled water. In a typical experiment, 5 mL of this lemongrass extract was added to 45 mL of 10^{-3} M aqueous $HAuCl_4$ solution. The reduction of $AuCl_4^-$ ions was monitored by recording the UV-vis absorption spectra as a function of time of reaction of this mixture. After completion of the reaction, UV-vis-NIR spectra was recorded for the above reaction mixture on solution-cast films of the gold nanoparticles on a quartz substrate. In order to enhance the percentage of gold nanotriangles/hexagons in the crude reaction medium, 3 cycles of centrifugation at 4,000 rpm followed by redispersion in water was attempted resulting in an increase in gold triangles population from 45 to 90 %. An attempt was made to identify the nature of the biomolecules present in the leaf extract that might be responsible for the formation of flat gold particles. First, solvent extraction of the components in the broth (500 mL from 100 g of lemongrass) was followed by adding it to $CHCl_3$ (100 mL) and vigorously shaking the biphasic solution for separation, based on the polarity of the molecules. The dried $CHCl_3$ and water-soluble fractions weighed 0.078 g and 5 g respectively. The aqueous fraction was further separated into 12 fractions by column chromatography using silica gel (100 – 200 mesh) in a glass column of inner diameter 1.4 cm and length 30 cm as stationary phase and chloroform – ethylacetate – methanol gradient as the eluting system. The flow rate was set at 100 mL/h. The 12 fractions eluted successively were designated W1 – W12 respectively. The amounts of each fraction W1-W12 obtained were 45, 138, 19, 36, 56, 132, 216, 231, 122, 284, 360 and 547 mg respectively. The fractions were dried, weighed and tested for reaction with aqueous $HAuCl_4$. UV-vis-NIR spectra were recorded for 10^{-3} M aqueous $HAuCl_4$ solution after reaction with W1 – W12 fractions. The crude lemongrass extract, the aqueous fraction after solvent extraction and the W12 fraction that was observed to show the shape directing ability were further characterized by FTIR. The W12 fraction was additionally characterized by nuclear magnetic resonance (NMR) measurement using D_2O as solvent. The kinetics of formation of gold nanoparticles during reduction of $AuCl_4^-$ ions by lemongrass leaf extract was monitored by transmission electron microscopy (TEM), laser light scattering particle size distribution analyzer and by measuring the change in conductivity of the reaction mixture as function of time. Prior to

laser light scattering measurement, the lemongrass broth was passed through a 0.22 μm membrane filter. The conductivity measurements were followed using a conductivity cell with a cell constant of 1.0 cm^{-1}. The gold particles synthesized by crude lemongrass leaf extract and other fractions were characterized by TEM and scanning electron microscopy (SEM). Atomic force microscopy (AFM) analysis in contact mode was done to find out the thickness of the flat gold particles. High resolution transmission electron microscopy (HRTEM) analysis was also carried out to image the lattice planes of the flat gold particles. X-ray photoelectron spectroscopy (XPS) analysis of the lemongrass reduced gold and sodium borohydride reduced spherical gold nanoparticles were also carried out.

To control the size of the triangular and hexagonal gold particles a more concentrated lemongrass leaf extract was used by boiling 100 g of thoroughly washed and finely cut leaves in 100 mL of sterile distilled water. 0.1 to 1.6 mL of this leaf extract was added to 5 mL of 10^{-3} M aqueous $HAuCl_4$ solution separately and the volume was made upto 7 mL with addition of appropriate amount of water. UV-vis-NIR spectra were recorded after allowing the reaction medium to stand for 48 h when reduction of $AuCl_4^-$ ions in all the reaction mixtures had reached saturation. TEM measurements were carried out for particles formed in each of these reaction mixtures.

Study of the ability of gold nanotriangle-coated glass to reduce the temperature rise within an enclosed compartment on irradiation with light as compared to uncoated glass was done. For this purpose variation in temperature as a function of time within an enclosed box of cardboard of dimensions 20 cm X 10 cm X 10 cm with a window opening of dimensions, 2 cm X 2.5 cm covered with a) uncoated glass, b) glass coated with spherical gold nanoparticles (7.3 mg/cm^2), c) glass with single coat of gold nanotriangles (4.4 mg/cm^2), d) with three coats of gold nanotriangles (13.3 mg/cm^2), and e) glass with three coats of gold nanotriangle solution followed by heat treatment at 300 ^oC for 3 h was measured. The box fitted with required glass sample was irradiated with a 250 W tungsten filament IR lamp, kept at a distance of 20 cm from the box.

4.2.2 Transmission electron microscopy (TEM) analysis:

A representative transmission electron microscopy (TEM) image of the gold ion-lemongrass extract solution after 6 h of reaction shows the presence of a large number of

triangular and spherical gold nanoparticles (Figure 4.1A and 4.1B). Nearly 45 % of the total gold particle population are triangular in shape and is significantly higher than that reported earlier [18a-c]. Similar large percentage of gold triangles can also be observed by SEM as shown in Figure 4.1F. The triangular particles range in size from 0.05-2 μm and often show truncated vertices similar to that observed for triangular silver [17] and gold nanoprisms [18] synthesized by chemical/photochemical methods. The contrast within triangular and hexagonal nanoparticles (Figure 4.1A, 4.1B) is believed to arise due to stresses in the particles due to buckling of the extremely thin nanosheets. Figure 4.1C shows TEM image of one of the gold nanotriangles standing upright (indicated by an arrow) that was fortuitously grabbed when an underlying polymer support of the carbon coated copper grid was curling due to the incident electron beam of the microscope. From this image, the thickness of the gold nanotriangles is observed to be ca. 8 nm. The

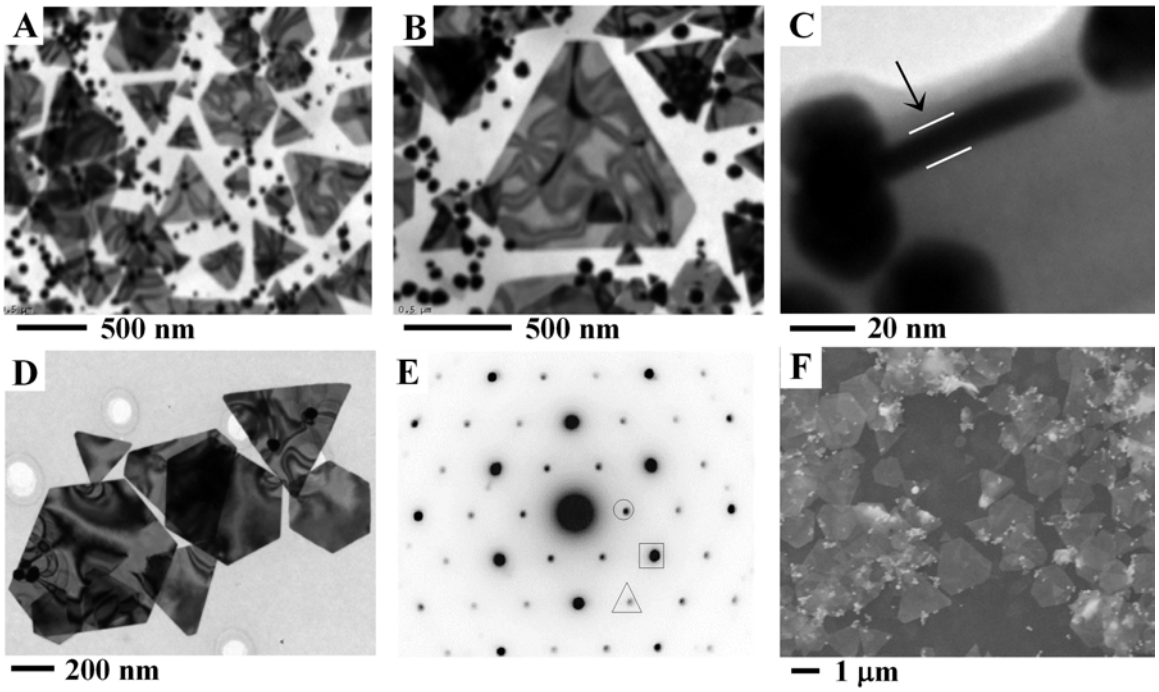

Figure 4.1: *A-C) Representative TEM images of triangular gold particles synthesized by the reduction of aqueous $AuCl_4^-$ ions by lemongrass extract. D) Gold nanotriangles purified by repeated centrifugation and redispersion in water. E) Selected area electron diffraction pattern from a single triangular gold particle. The circled spots, boxed spots and spots circumscribed by triangles correspond to 1/3{422}, {220} and {311} Bragg reflections with lattice spacings of 2.5, 1.44 and 1.23 Å respectively. F) Representative SEM image of lemongrass leaf extract reduced unpurified gold particles.*

percentage of gold nanotriangles in the reaction medium could be considerably enhanced upto 90 % of the nanoparticle population by repeated centrifugation (at 4,000 rpm), washing and redispersion. Figure 4.1D shows a representative TEM image of the purified gold nanotriangles indicating negligible amounts of spherical particles. The selected area electron diffraction (SAED) pattern (Figure 4.1E) from one of the gold nanotriangles in Figure 4.1B clearly shows that it is single crystalline. The hexagonal nature of the diffraction spots is a clear indication that the triangular gold nanoprisms are highly [111] oriented with the top normal to the electron beam. The spots could be indexed based on

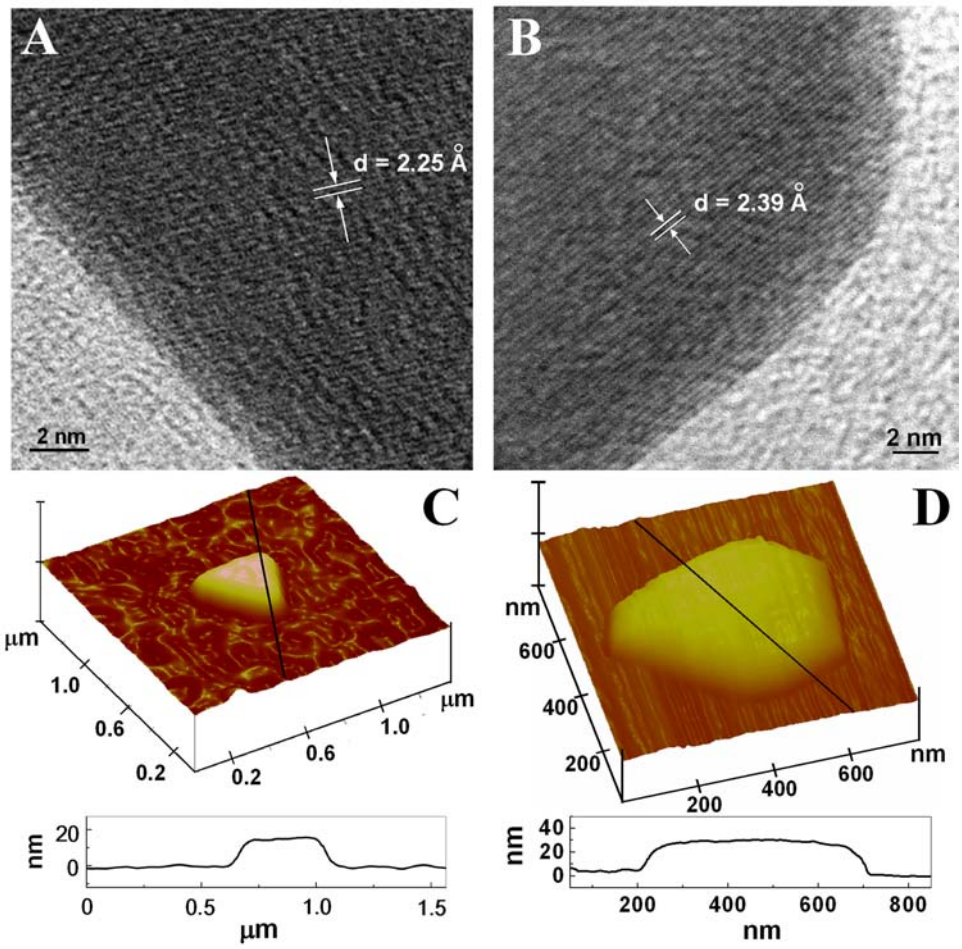

Figure 4.2: *A) HRTEM image from the edge of one of the hexagonal gold particles synthesized by reduction of $AuCl_4^-$ ions using lemongrass leaf extract. B) HRTEM image from the vertex of one of the hexagonal gold particles C-D) AFM images of each one of the triangular and hexagonal gold particles. The bottom plot in each AFM image represents topographic height analysis of the triangle and hexagon along the line marked in the AFM micrograph.*

the face centred cubic (fcc) structure of gold. The circled spots, boxed spots and spots circumscribed by triangles correspond to the forbidden 1/3{422} and allowed {220} and {311} Bragg reflections with lattice spacing of 2.5, 1.44 and 1.23 Å respectively. The presence of the 1/3{422} reflections indicates that the gold triangles could have stacking faults along the <111> direction [19k,27].

Figure 4.2A and 4.2B show the HRTEM images taken from the edge and vertex of a hexagonal gold particle respectively. It would be worth mentioning here that though the lattice planes could be imaged at particular instances, in general, the lattices were very unstable under the incident electron beam of the microscope and could not be imaged. The lattice spacing obtained from the captured images were ca. 2.25 Å and 2.39 Å for the lattice planes observed at the edge and the vertex of a hexagonal gold particle respectively (Figure 4.2A and 4.2B). These lattice spacing could not be indexed to any of the reported lattice planes. The lattice planes observed in Figure 4.2B are parallel to one of the edges of the hexagon and has a lattice spacing of ca. 2.39 Å that is nearest to the standard value 2.355 Å for the fcc gold (111) lattice. Since these flat particles are observed to be <111> oriented it may imply that the observed hexagonal particle is not lying perpendicular to the incident beam but could be at an angle ~ 19.5^{o} while imaging, making it possible to view the $(11\bar{1})$ or the $(1\bar{1}\bar{1})$ lattice planes that are at a dihedral angle of ~ 70.5^{o} and 109.5^{o} relative to {111} lattice respectively.

4.2.3 Atomic force microscopy (AFM) measurements:

Figures 4.2C and 4.2D show atomic force microscopy (AFM) images of triangular and hexagonal gold particles, the surface profile plots of which (lower panels in Figures 4.2C and 4.2D) shows that the particles have a thickness of 14 nm and 25 nm respectively. The edge length of the triangular and hexagonal gold particle was found to be ~ 400 and 440 nm respectively. AFM analysis of a number of nanotriangles indicated that their thickness ranged from 8 to 25 nm.

4.2.4 UV-vis spectroscopy:

On visual inspection it is observed that, by mixing lemongrass leaf extract with 10^{-3} M aqueous $HAuCl_4$, the faint yellow color of the solution turns yellowish brown that gradually fades and becomes faint blue-green in color within next 2 hours. After 2 to 3

hours, the color of the solution turns reddish brown and intensifies within next half an hour. UV-vis spectra recorded as a function of time of reaction of lemongrass leaf extract with 10^{-3} M $HAuCl_4$ solution at room temperature (Figure 4.3A) show the appearance of a surface plasmon resonance (SPR) band at ca. 580 nm after 90 min of reaction that gradually blue-shifts to 500 nm and increases in intensity with time. This is also accompanied by an increase in the absorption in the NIR region of the electromagnetic

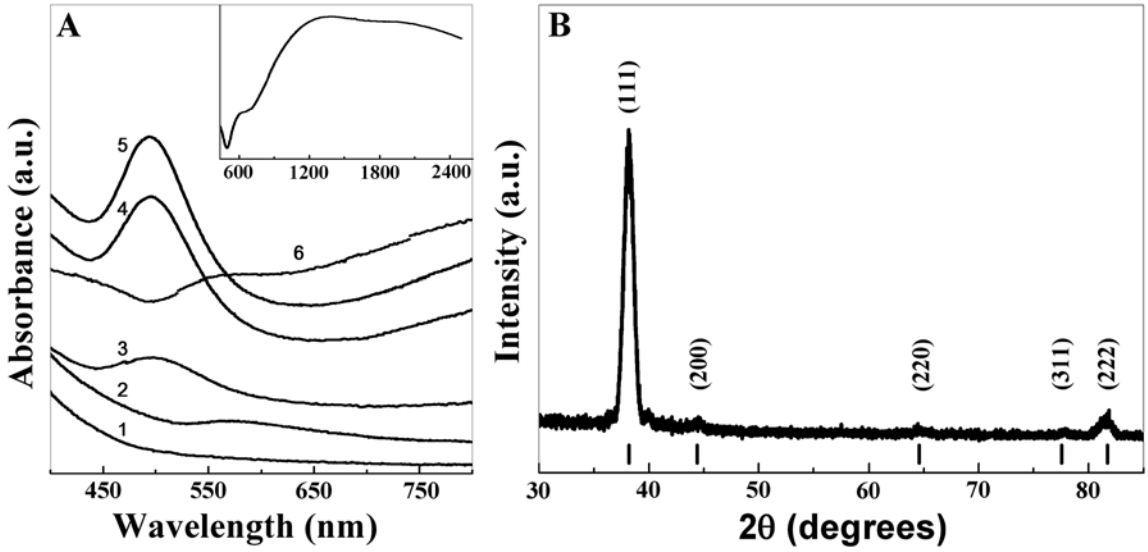

Figure 4.3: *A) UV-vis spectra recorded as a function of time of reaction of lemongrass extract with aqueous gold ions; curves 1-5 correspond to spectra recorded after 1, 90, 160, 220 and 340 min of reaction. Curve 6 - spectrum obtained from the purified gold nanotriangle solution; inset - UV-vis-NIR spectrum of a solution-cast film of purified gold nanotriangles on a quartz substrate. The axes notations for the inset figure are the same as that for the corresponding main figure. B) X-ray diffraction pattern of lemongrass leaf extract synthesized gold particles solution drop cast on a glass substrate without any purification. The bars below the curve represent the standard 2θ values for fcc gold.*

spectrum. These time-dependent features observed in the UV-vis spectra shown in Figure 4.3A are characteristic of either formation of spherical gold nanoparticles that aggregate with time [6a,28], formation of anisotropic particles whose aspect ratio increases with time [4e,h,11a] or a combination of both processes. From the TEM images of the lemongrass extract reduced gold nanoparticles, where a large percentage of triangular gold particles were observed with hardly any signs of aggregated particles, it can be concluded that the large NIR absorption observed in the corresponding UV-vis-NIR

absorption spectra (Figure 4.3A) is clearly due to the highly anisotropic shape of the gold particles. Curve 6 in Figure 4.3A represents the UV-vis spectra of the lemongrass leaf extract synthesized gold particles subjected to purification by the repeated centrifugation method. A prominent red shift in the lower wavelength SPR band from 500 to 575 nm is observed along with a significant loss in its absorbance value, while the absorbance feature above 600 nm remains unaltered relative to the unpurified sample. This indicates that, while the NIR absorbing flat gold particles are retained in the solution, the spherical particles contributing to the absorbance around 500 nm could be separated significantly. The absorption band observed at 575 nm is due to the transverse component of the SPR band originating from the out-of-plane plasmon vibrations in the triangular and hexagonal gold particles [4i]. The inset of Figure 4.3A shows the UV-vis-NIR spectra of the purified gold triangles, solution cast as films by solvent evaporation on to a quartz substrate. The increasing absorbance value observed above 600 nm in the UV-vis spectra of the lemongrass reduced gold solution can now be seen as a clear absorption band with a maxima at 1400 nm (inset Figure 4.3A). The extremely large NIR absorption observed in UV-vis-NIR spectrum (inset of Figure 4.3A) of the purified flat gold triangular and hexagonal particles drop-coated onto a quartz substrate is a consequence of the longitudinal absorption band originating from the in-plane plasmon vibrations [4i]. In the UV-vis-NIR spectra corresponding to gold triangles film on quartz (inset Figure 4.3A) a shoulder at 640 nm is also observed and corresponds to the band at 575 nm observed in the UV-vis spectra of the gold triangles in solution phase. The observed large red-shift in the peak position can be attributed to the change in dielectric environment of the gold triangles on forming a dry film from an aqueous solution phase [29].

4.2.5 X – Ray Diffraction measurements:

XRD measurements of a drop cast film of lemongrass leaf extract reduced gold on a glass substrate (Figure 4.3B) showed only one very intense Bragg reflection at 38.2^{o} and a weaker one at 81.9^{o}. The reflections could be indexed to {111} and {222} set of lattice planes for fcc gold. The intense Bragg reflection corresponding to {111} set of lattice planes and almost negligible intensities corresponding to other lattice plane indicates that the particles are highly [111] oriented and supports the conclusions drawn from the TEM and SAED analysis.

4.3 Growth of triangular and hexagonal gold particles.

The kinetics of formation of the gold triangles in the $HAuCl_4$–lemongrass reaction medium was followed by TEM (Figure 4.4), light scattering (Figures 4.5A-D) and conductivity measurements (Figure 4.5E). At very early stage of reaction (1 h, Figure 4.4A), spherical nanoparticles of gold are seen densely populating the surface of the grid. Light scattering measurements of the $AuCl_4^-$ -lemongrass reaction solution (2 min of reaction, Figure 4.5A) indicate very rapid reduction of gold ions and formation of large aggregates of particles in the size range 0.3-5 μm. The nanoparticles are in close contact and this could be responsible for the initial large red shift in the SPR band (580 nm, Figure 4.3A) [30] observed at early stages of reaction. After 3 h of reaction, sintering of the gold nanoparticles is evident leading to rudimentary triangular structures (Figures

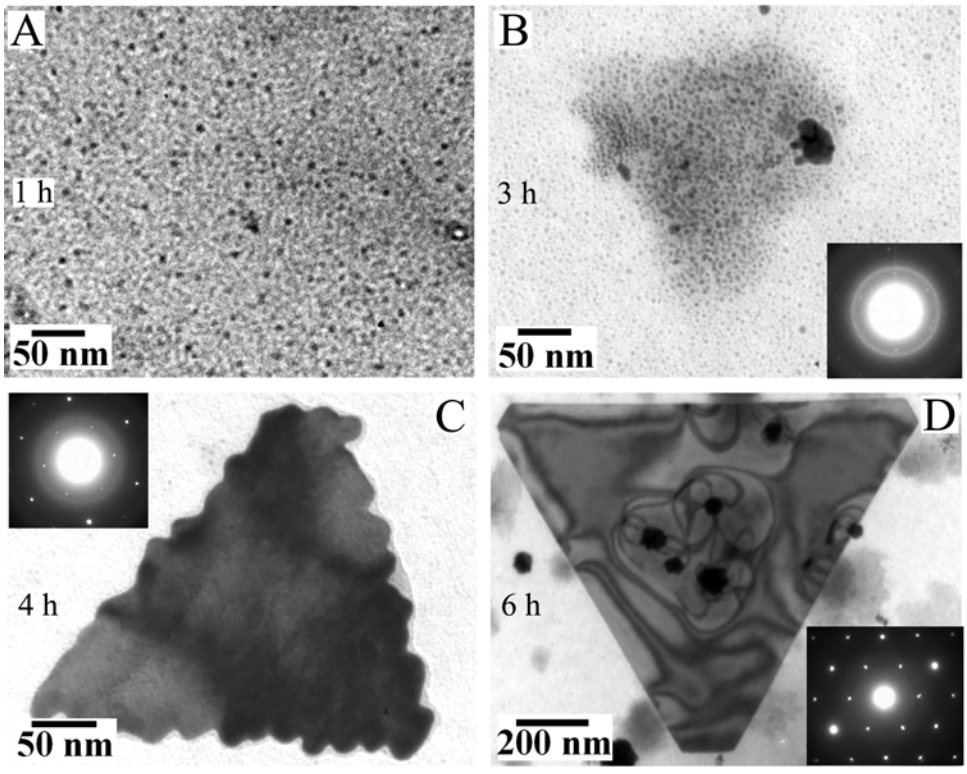

Figure 4.4: *TEM images of gold nanoparticles as a function of time of reaction of aqueous chloroaurate ions with lemongrass extract. A) 1 h; B) 3 h; C) 4 h and D) 6 h. The insets in panels B, C and D show SAED patterns of the gold nanostructures in the main part of the respective figures.*

4.4B and 4.4C). The ring structure of the SAED pattern from this assembly is characteristic of polycrystalline gold (inset, Figure 4.4B). The peak at 0.1-0.3 μm in the light scattering data (Figure 4.5B) is consistent with the growth of larger, single particles of gold. After 4 h of reaction, triangular particles with corrugated edges are seen (Figure 4.4C) with an SAED pattern that shows diffraction spots superimposed on a ring structure (inset, Figure 4.4C). The individual gold nanoparticles that were evident after 3 h of

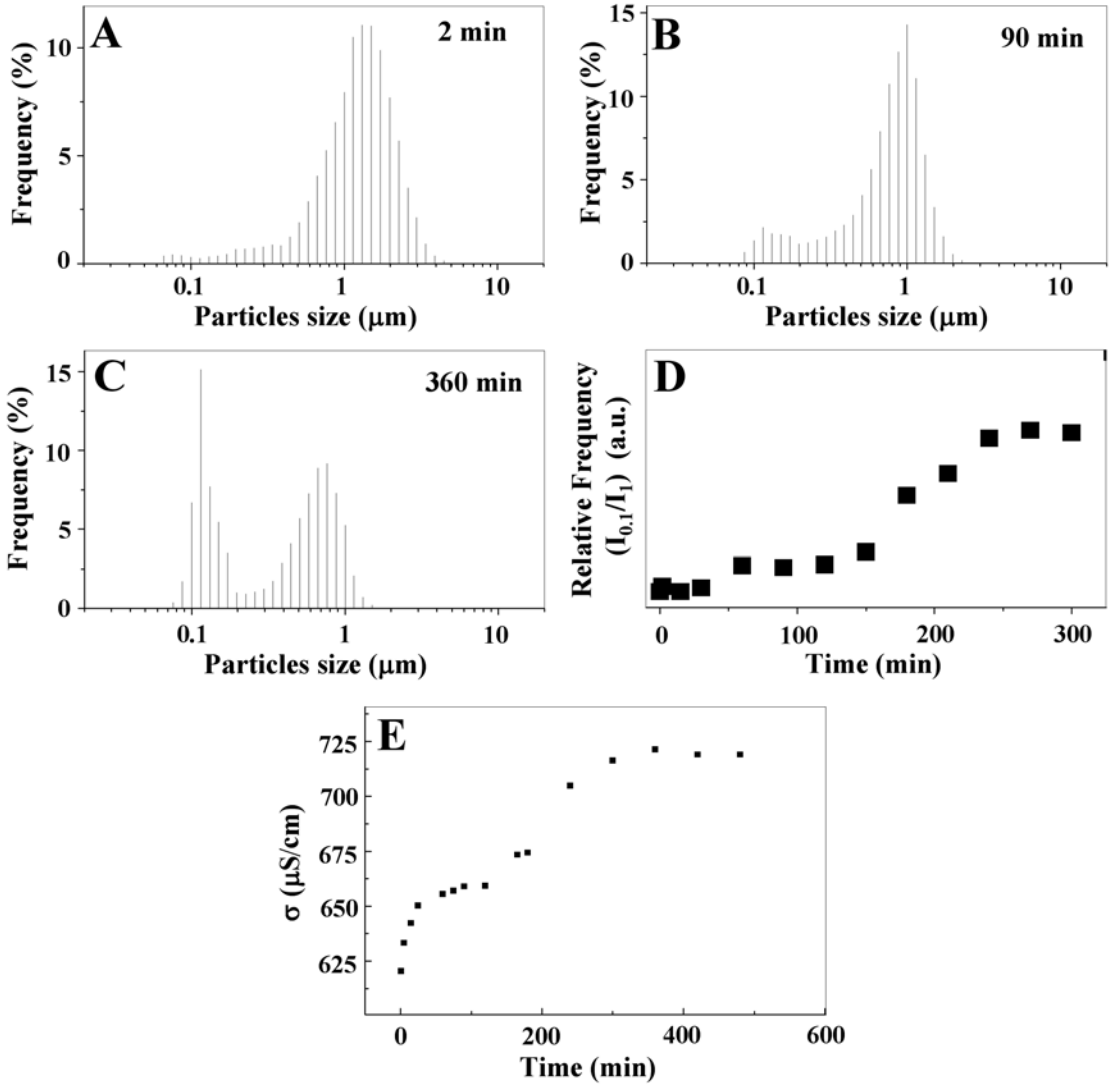

Figure 4.5: *Laser light scattering measurements of gold nanoparticles as a function of time of reaction of aqueous chloroaurate ions with lemongrass extract. A-C) Laser light scattering particle size histograms during reaction in the $HAuCl_4$ –lemongrass solution. D) Ratio of particle size population at 0.1 ($I_{0.1}$) and 1 μm (I_1) as a function of time of reaction of the$HAuCl_4$ – lemongrass solution from light scattering studies. E) Plot of conductivity of $HAuCl_4$ – lemongrass leaf extract solution as a function of time of the reaction.*

reaction (Figure 4.4B) are no longer visible. After 6 h of reaction, compact triangles with sharp edges are observed (Figure 4.4D) that show hexagonally arranged diffraction spots characteristic of single crystalline (111)-oriented gold nanocrystals (inset, Figure 4.4D). A large increase in the population of nanoparticles of ca. 0.1 μm size is accompanied by a loss in large aggregates of nanoparticles (ca. 1 μm size, Figure 4.5C) after 6 h of reaction and is consistent with the TEM results. The consumption of small gold nanoparticles in the aggregates with time due to formation of gold nanotriangles is clearly shown in the ratio of populations at 0.1 μm/1.0 μm in light scattering measurements plotted against time (Figure 4.5D). In a parallel experiment, the conductivity of the solution was measured as a function of time after addition of lemongrass leaf extract to 10^{-3} M $HAuCl_4$ and was observed to increase rapidly for 30 min after which the conductivity remains nearly constant with only marginal increase for the next 2 hours (Figure 4.5E). The initial conductivities of $HAuCl_4$ and lemongrass leaf extract solution after making up to the same dilution as in the reaction medium were 4375 μS and 496.5 μS respectively. The conductivity measured soon after mixing lemongrass leaf extract in $HAuCl_4$ solution was found to be 620.4 μS that is not significantly higher than that measured for plain lemongrass leaf extract but much less compared to the value for $HAuCl_4$ solution. The lower than expected conductivity value (i.e., nearly the sum of individual conductivities of $HAuCl_4$ and lemongrass leaf extract) possibly implies that the $AuCl_4^-$ ions form some kind of adduct with the biomolecules of the extract, thus preventing their net individual contribution to the conductivity of the solution. The increase in conductivity might be attributed to the reduction of the $AuCl_4^-$ leading to the formation of Au^0 and $4Cl^-$ ions resulting in the net increase in the number of charged species contributing to the conductivity of the solution. Assuming this to be the case, it implies that a rapid reduction of the gold ions occurs during the first 30 min without any appreciable reduction in the next 2 hours. During this period it is very likely that only formation of nanoparticles from the reduced $AuCl_4^-$ ions takes place and then assembly occurs as evident from the TEM kinetic (Figures 4.4A and 4.4B) and light scattering measurements (Figure 4.5A-D). Interestingly, after 3 hours again an increase in conductivity of the solution is observed that saturates within 5 to 6 hours after the initiation of the reaction. In this time period as observed from TEM measurements (Figures 4.4C and 4.4D) the assembled structures

grow into well-formed triangular structures. Possibly, the sintering of the particles to form flat particles is also assisted by a secondary growth on the assembled structures observed after 3 hours of reaction (Figure 4.4B), which might be analogous to the seeded growth of gold nanorods, in which case reduction of gold ions by ascorbic acid occurs only in the presence of seed particles [20a]. Possibly, when the sintering commences, a simultaneous rapid reduction of the remaining $AuCl_4^-$ ions at the highly energetic defect regions of the grain boundaries occurs facilitating the growth of these particles. Such a reduction process might explain the observed increase in conductivity of the solution after three hours of reaction. While, formation of single crystalline particles by such a mechanism is not common, it is not surprising that spherical gold particles could come together and assemble in such a geometric fashion [31] or that individual nanoparticles can come together and sinter [32]. In fact, Klabunde's group have observed such assembly of monodisperse spherical particles into triangular and hexagonal superlattices in solution [31a,b], though the further sintering of the superlattices to form a single crystalline particle was not observed. Transformation of spherical metal particles to other single crystalline structures have been reported in a couple of other instances [17c,23a]. The extremely small size of the initially formed gold nanoparticles having high surface energy and the strong influence of the capping biomolecules of the lemongrass leaf extract in the present case possibly has a major role to play in the formation of these flat gold particles.

4.4 Fractionation of Lemongrass leaf extract and their ability towards synthesizing triangular and hexagonal gold particles.

4.4.1 Fractionation:

The fluidity required by the spherical gold nanoparticles to form triangular/hexagonal gold single crystals at room temperature must be provided by biomolecules present in the lemongrass extract. To investigate further into the nature of the different biomolecules present in the lemongrass extract and their effect on the kinetics of nanotriangle formation, the following experiments were undertaken. The crude lemongrass extract was separated into water and chloroform-soluble fractions (98.5 : 1.5 wt. % respectively, obtained by measuring their respective dry weight) and

individually tested for reaction with aqueous $AuCl_4^-$ ions. The UV-vis-NIR spectrum recorded from a 10^{-3} M aqueous solution of $HAuCl_4$ after 6 h of reaction with the chloroform-soluble component (dispersed in water using methanol, Figure 4.6A, curve 1) shows negligible absorption in the region 400-800 nm. On the other hand the water

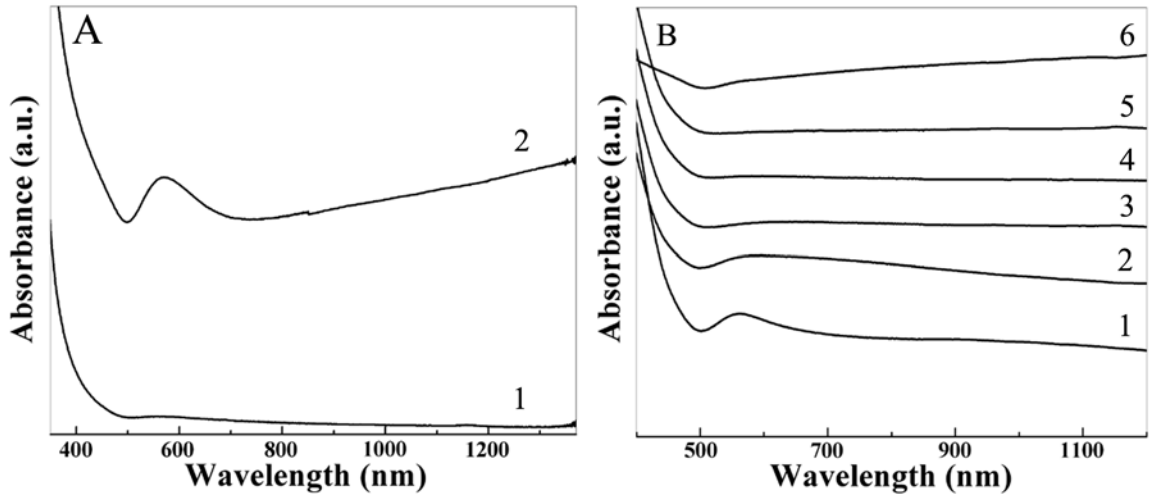

Figure 4.6: *A) UV-vis-NIR absorption spectra of the reaction mixture of aqueous $HAuCl_4$ solution with: curve 1) the $CHCl_3$ soluble component of the crude lemongrass extract and curve 2) the remaining water soluble component of the crude lemongrass leaf extract. B) UV-vis-NIR absorption spectra of gold particles synthesized by the reduction of aqueous $AuCl_4^-$ ions by water-soluble fractions W1, W6, W7, W9, W11 and W12 (curves 1-6 respectively).*

soluble component shows activity similar to the crude lemongrass extract (Figure 4.6A, curve 2). The water-soluble fraction of the lemongrass is thus implicated in the formation of triangular gold particles as evident from the SEM image (Figure 4.7A) obtained after reaction with 10^{-3} M aqueous solution of $HAuCl_4$ for 6 h. The water-soluble fraction was further fractionated by column chromatography into 12 fractions (W1 – W12 in order of increasing polarity). Fractions W1, W6, W7, W9, W11 and W12 reduced $AuCl_4^-$ ions to varying degrees and the UV-vis-NIR spectra recorded from these fractions are shown as curves 1-6 respectively in Figure 4.6B. Among all the positive reactions, the one involving fraction W12 showed the largest NIR absorption (curve 6, Figure 4.6B) with almost monotonous increase of absorbance in the NIR region with no discernible transverse SPR band as opposed to that observed in previous instances. Figure 4.7B is the representative

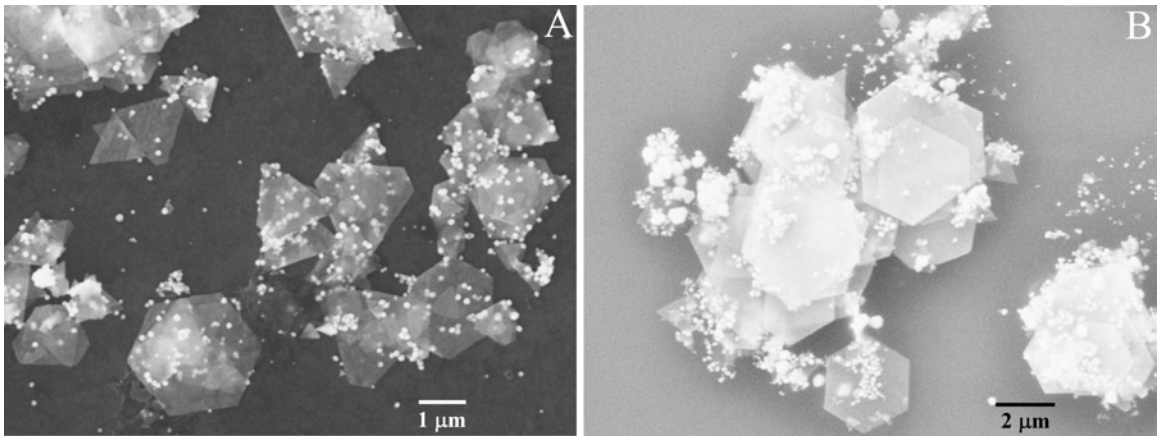

Figure 4.7: *SEM images of gold particles synthesized by reacting $HAuCl_4$ solution with A) water-soluble component of the lemongrass leaf extract remaining after separation of the less polar biomolecular components of the crude aqueous extract with $CHCl_3$ extraction. B) W12 fraction of the above mentioned water soluble component of the crude lemongrass leaf extract.*

SEM image of the gold particles synthesized by reacting W12 fraction with 10^{-3} M aqueous solution of $HAuCl_4$, a large number of mainly hexagonal gold particles can be seen. The observed feature in the UV-vis-NIR spectra can be attributed to the presence of these very large micron sized gold nanoparticles that do not have similar optical response as gold particles of few nanometer dimensions would have. Clearly W12 fraction seems

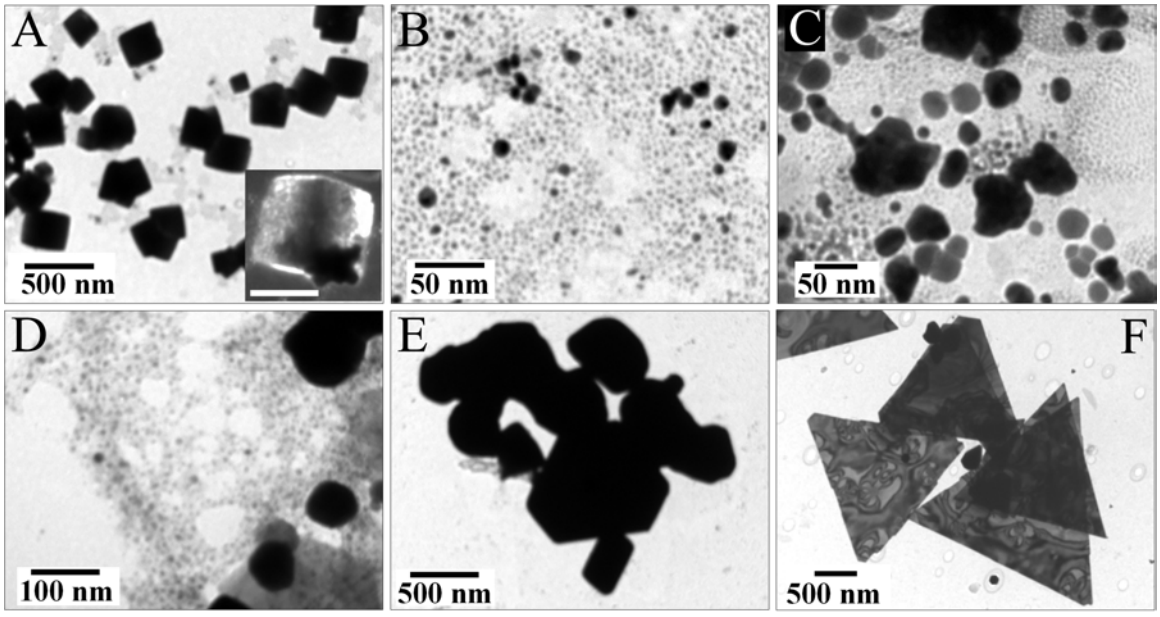

Figure 4.8: *A – F) TEM images of gold nanoparticles synthesized by reacting $HAuCl_4$ solution with water-soluble W1, W6, W7, W9, W11 and W12 lemongrass fractions respectively.*

to be mainly responsible for triangular and hexagonal gold particles formation during reduction of $HAuCl_4$ solution with lemongrass leaf extract. TEM images recorded for the gold nanoparticles synthesized using the above-mentioned active fractions of the water soluble component of the lemongrass leaf extract are shown in Figure 4.8. Interestingly, cubic particles were observed from the W1 fraction-gold ions reaction (Figure 4.8A), that on closer examination appear to be composed of spherical nanoparticle assemblies and can be noticed from the dark field image of one such particle shown in the inset of Figure 4.8A.The other fractions resulted mainly in some spherical or irregularly shaped particles (Figure 4.8B-E) and thus these fractions apparently only contribute in the reduction of $AuCl_4^-$ ions with less contribution towards directing the evolution of triangular and hexagonal gold particles.

4.4.2 FTIR and NMR measurements:

The Fourier transform infrared (FTIR) spectra recorded from the lemongrass reduced gold, crude lemongrass extract, the water soluble component of the extract and the W12 fraction are shown in Figure 4.9A represented by the curves 1, 2, 3 and 4 respectively. In all the spectra, many common features are observed. All have vibrational frequencies in the range 1700-1750, 1615-1550 and 1010-1090 cm^{-1} corresponding to

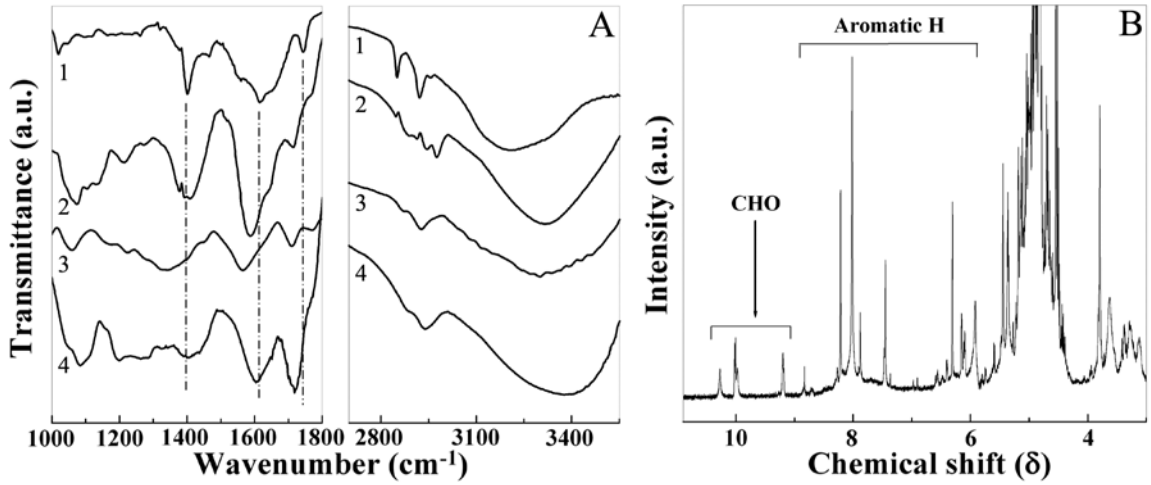

Figure 4.9: *A) FTIR spectra of : curve1) gold particles synthesized by lemongrass leaf extract, curve 2) lemongrass leaf extract, curve 3) water soluble component of lemongrass leaf extract obtained after solvent extraction with $CHCl_3$ and curve 4) W12 fraction of the water soluble component of the lemongrass leaf extract in the spectral region 1000 – 1800 cm^{-1} and 2700 – 3550 cm^{-1}. B) Proton NMR spectrum recorded from the W12 lemongrass fraction.*

carbonyl stretching, carboxylate anion or aromatic C=C stretching and to C–O stretching of polysaccharides [33] respectively apart from the methyl/methylene bending frequencies in the range 1325-1445 cm^{-1}. Figure 4.9B shows the NMR spectrum of W12 fraction revealing the presence of aldehydic protons at 10.3, 10 and 9.2 ppm and a number of aromatic protons in the range 6 – 9 ppm [34]. It thus appears that the biomolecules present in the lemongrass leaf extract are some ketone/aldehyde compounds, most likely saccharides with aromatic moieties. With this rudimentary inference at this juncture, it would be worth mentioning here that Fuhrhop and coworkers have demonstrated that gold nanoparticles synthesized in the presence of acetone result in the formation of flat gold platelets with a fluid-like surface [22a]. We believe that the formation of gold nanotriangles in this study might be due to reduction of aqueous chloroaurate ions by the reducing sugars (aldoses), while the aldehydes/ketones bind to the nascent spherical nanoparticles rendering them 'liquid-like' and amenable to sintering at room temperature (TEM results, Figure 4.4).

4.4.3 XPS measurements:

A chemical analysis of lemongrass-reduced gold nanoparticles was also followed by XPS and compared with that of nanoparticles obtained by standard sodium borohydride reduction of aqueous $HAuCl_4$ [35]. Figures 4.10A and B show the C 1s and Au 4f core levels respectively for sodium borohydride reduced gold nanoparticles. The C 1s core level has only one chemically distinct component centered at 285 eV binding energy (BE) and is due to adventitious carbon in the sample (Figure 4.10A). The Au $4f_{7/2}$ core level could be decomposed into two chemically distinct components centered at 83.6 and 85.5 eV BEs that correspond to Au(0) and Au(I) respectively (Figure 4.10B). The relatively small amount of Au(I) present on the surface of the gold nanoparticles is responsible for the high BE peak and is believed to stabilize the particles electrostatically against aggregation in solution [35]. In the case of lemongrass-reduced gold nanotriangles and hexagons, the C 1s photoemission spectrum is more complex and could be decomposed into four chemically distinct components (Figure 4.10C). In addition to the adventitious C 1s peak at 285 eV BE, peaks at 282.2, 286.6 and 288.7 eV BE are observed. The low BE peak at 282.2 eV is attributed to aromatic carbons of biomolecules bound to the surface of the gold nanotriangles. The high BE peak at 288.7 eV BE is

attributed to electron emission from carbons in carbonyl groups (aldehydic, ketonic or carboxylic carbons) [36], while the peak at 286.6 eV BE is most likely from carbons α to the carbonyl carbons. Induction effects are known to influence the BEs of carbon complexed with electron withdrawing functional groups such as carbonyls [37]. It is also possible that this peak in the C 1s spectrum could arise from carbon coordinated to hydroxyl groups in sugar derivatives present in the lemongrass leaf extract [38] and

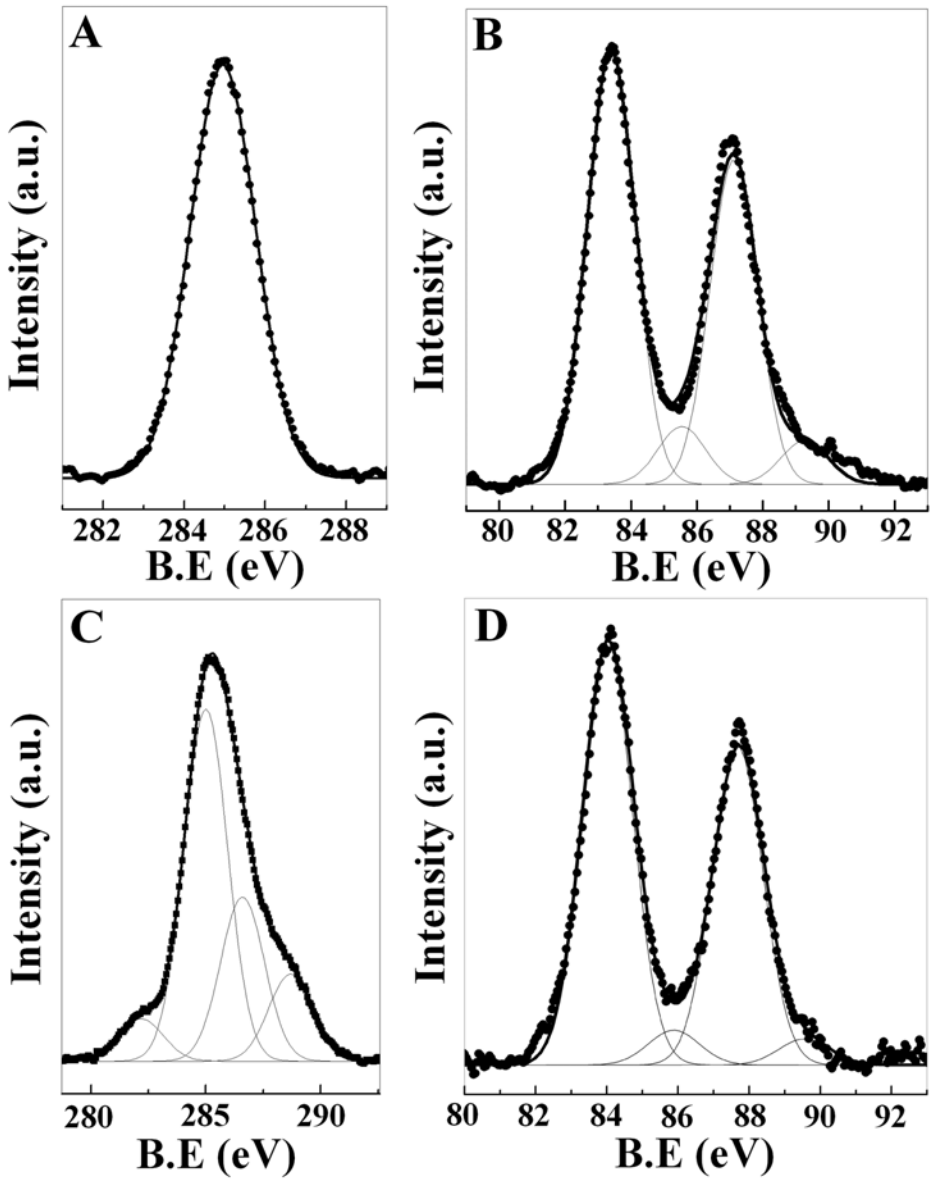

Figure 4.10: *A) and B) XPS C 1s and Au 4f core level spectra respectively recorded from sodium borohydride reduced gold nanoparticles. C) and D) XPS C 1s and Au 4f core level spectra respectively from lemongrass leaf extract reduced gold nanoparticles.*

complexed with the gold nanotriangles. Figure 4.10 D shows the Au 4f core level spectra for lemongrass reduced gold particles. The Au $4f_{7/2}$ core level could be decomposed into two chemically distinct components centered at 84 and 85.8 eV BEs that correspond to Au(0) and Au(I) respectively (Figure 4.10D), similar to the case of sodium borohydride reduced gold. Since, a clear indication of the presence of Au(I) is observed most likely from the surface of the gold particles, it is possible that the carbonyl compounds present in the lemongrass extract interact with the nascent gold particles formed in the $HAuCl_4$ – lemongrass extract reaction through these surface bound Au (I) species and thus influence the shape evolution [22a].

4.5 Controlling the size of triangular gold particles.

Figure 4.11 shows representative TEM images of gold nanoparticles synthesized by the reaction of aqueous $AuCl_4^-$ ions by different amounts of lemongrass extract after

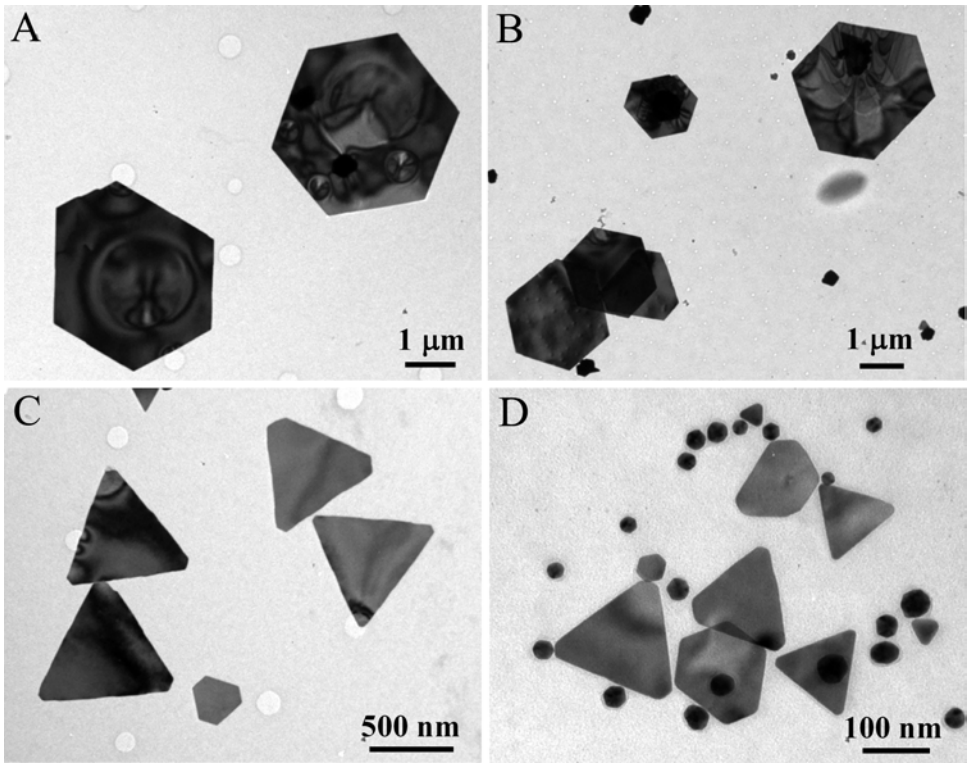

Figure 4.11: *Representative TEM images of gold nanoparticles synthesized by the reduction of 5 mL of 10^{-3} M aqueous $HAuCl_4$ solution with A) 0.2 mL, B) 0.3 mL, C) 0.5 mL and D) 1.0 mL of lemongrass leaf extract.*

48 h of reaction. It is observed that with increasing amount of extract added to the $HAuCl_4$ solution, the average size of the triangular and hexagonal particles decreases. Another observation is that the ratio of the number of spherical nanoparticles to triangular/hexagonal particles increases with increasing amount of lemongrass extract in the reaction medium (compare for example Figures 4.11A and D). Figure 4.12A shows a plot of the average edge length of the triangular and hexagonal gold particles formed as a function of volume percentage of lemongrass extract added to the 10^{-3} M $HAuCl_4$ solution. The triangular and hexagonal particles formed in each case are not monodisperse and show a large spread in the edge lengths. However, the average edge length determined from 100 triangular/hexagonal particles in each reaction does show a correlation with the amount of reducing agent (lemongrass extract) in the reaction medium (Figure 4.12A) – the edge length decreases monotonically with increasing amount of lemongrass. Further evidence for the lemongrass concentration dependent variation of triangle size is provided by UV-vis-NIR spectroscopic analysis of the different solutions (Figure 4.12B). Two important observations are made from these spectra. The first is that, as the amount of lemongrass extract in the reaction medium increases, the SPR band centered at 525 nm increases in intensity and indicates an

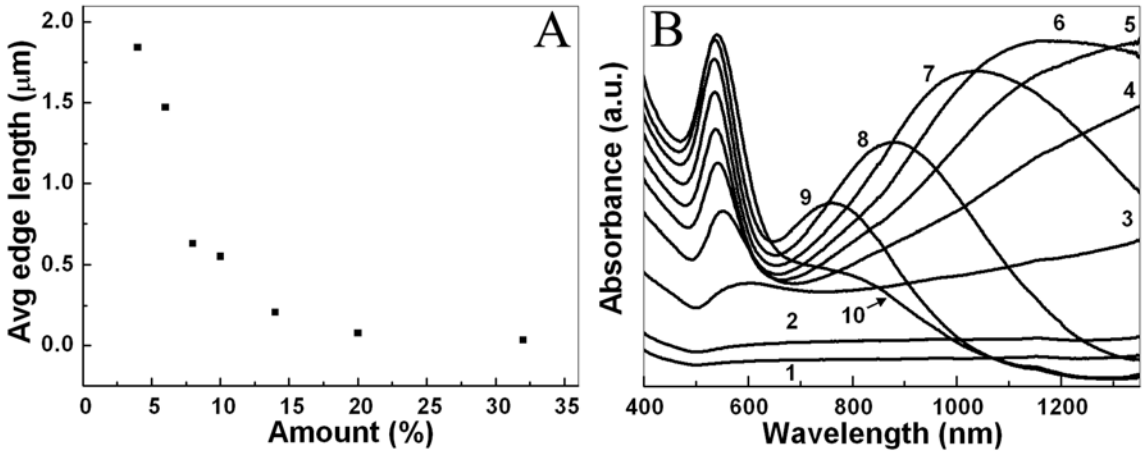

Figure 4.12: *A) Plot of the average edge length variation in gold nanotriangles and truncated triangles as a function of volume percentage of lemongrass extract in 10^{-3} M $HAuCl_4$ solution. B) UV-vis-NIR spectra of gold nanoparticles synthesized by adding different amount of lemongrass leaf extract to 5 mL of 10^{-3} M $HAuCl_4$ solution. Curves 1 – 10 correspond to solutions with 0.2, 0.3, 0.4, 0.5, 0.6, 0.7, 0.8, 1.0, 1.2 and 1.6 mL of lemongrass leaf extract in 5 mL of 10^{-3} M $HAuCl_4$ solution respectively.*

increase in the number of spherical nanoparticles in the reaction medium. This is borne out by the TEM results (Figure 4.11D) where a large percentage of small spherical gold nanoparticles are seen to coexist with triangular and hexagonally shaped nanoparticles. The second is that this increase in the SPR band intensity at 525 nm is accompanied by a blue-shift of the longitudinal SPR component appearing in the NIR region (Figure 4.12B). The shift to longer wavelengths with lesser amount of lemongrass extract in the reaction medium is consistent with TEM analysis of the particles that showed an increase in the average edge length of the anisotropic particles (Figure 4.11 and Figure 4.12A). Thus, it is possible to vary the edge length of the synthesized gold nanotriangles by simple variation of the amount of reducing agent (lemongrass extract) in the reaction medium. The consequent variation in nanoparticle aspect ratio results in the ability to tune the wavelength of absorption in the NIR region with important implications in optical coating technology and hyperthermia of cancer cells. In biological applications, tuning of the NIR absorption band in the gold nanoparticles is important since they need to be selectively excited without exciting and hence damaging other tissues [39]. We would like to mention here that in the reactions involving low concentrations of lemongrass extract in solution (0.2 and 0.3 mL of lemongrass extract), the edge lengths of the gold nanotriangles were large (1.8 ± 0.4 μm and 1.5 ± 0.6 μm respectively) and the particles settled with time at the bottom of the test tube as a golden colored precipitate. Ultrasonication of this precipitate resulted in reasonably stable dispersions in water as well as organic solvents such as chloroform and toluene thereby leading to the possibility of forming films of the nanotriangles on different substrates.

Figure 4.13 shows TEM images of single nanotriangles/hexagonal gold particles and the corresponding electron diffraction patterns of particles obtained under conditions of low lemongrass concentration in the reaction medium (0.2 and 0.3 ml of lemongrass extract). In the former case (Figures 4.13A and 4.13D) the triangular and hexagonal particles were single crystalline fcc structured and [111] oriented as observed from the diffraction pattern in Figure 4.13D [29]. In the latter case too (Figures 4.13B and 4.13E) an electron diffraction pattern that appears like a single crystalline diffraction pattern is observed but most of the triangular and hexagonal gold particles also show additional diffraction spots around the direct beam and around the spots corresponding to {200} and

{422} set of planes as shown in Figure 4.13E. Due to the weak intensity of the diffraction spots corresponding to the 1/3{422} planes, similar hexagonal pattern of spots could not be confirmed around them. Such multiple spot electron diffraction pattern is reported for polycrystalline aggregates of cubic phase [α-$Al_9(Mn,Fe)_2Si_2$], in which the entire motifs are parallel [40]. It is thus evident here that the flat particles tend to form by an initial oriented aggregation mechanism. In this particular case, since the amount of added reducing agent is very less, it is likely that the second stage of reduction assisting the conversion of the aggregates into a single crystalline particle as observed during solution conductivity measurements (Figure 4.5E), is not proceeded to completion. The fact that the forbidden 1/3{422} reflections are also very negligible suggests that these particles are not atomically flat and do not have prominent stacking faults [29]. These stacking faults possibly develop only after complete conversion of the aggregates into single crystalline particles in order to relieve any residual strain in the particles. In other words it means that when a single crystal is formed, only then the (111) planes develop that extend throughout out the crystal plane and then a possibility of stacking fault arises. In case where the whole particle is rather constituted of oriented granular domains, the

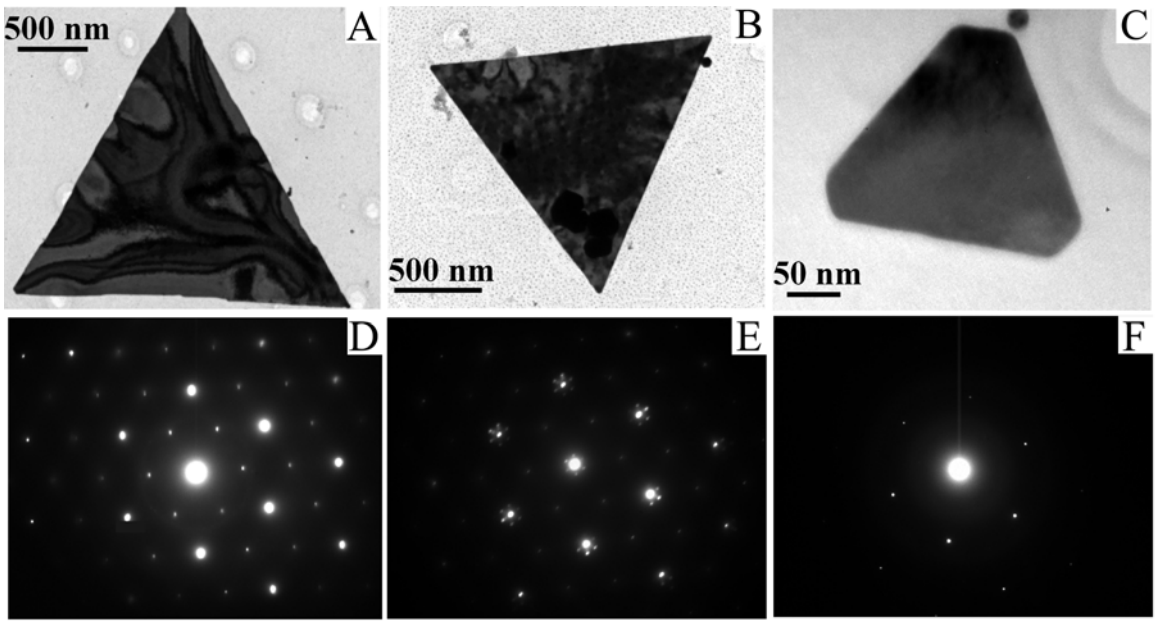

Figure 4.13: *TEM images and the corresponding electron diffraction patterns of gold nanotriangles and hexagons formed on addition of A) and D) 0.2 mL, B) and E) 0.3 mL and C) and F) 1.0 mL of lemongrass leaf extract to 5 mL of 10^{-3} M $HAuCl_4$ solutions, respectively.*

stacking fault would be confined only to individual grains and would not extend uniformly throughout the particles and thus lead to a low intense 1/3{422} reflections. At lower concentration of lemongrass extract in solution (0.2 ml), the degree of truncation of the triangular particles was observed to be higher with more hexagonal particles in solution (Figure 4.11A). The electron diffraction pattern of the hexagonal gold nanoparticle shown in Figure 4.13C is represented in Figure 4.13F. The diffraction pattern is similar to that obtained for the triangular nanoparticles and indicates <111>-orientation of single crystals [29]. When the added amount of lemongrass extract exceeds 0.7 mL per 5 mL of 10^{-3} M $HAuCl_4$, the stable gold nanoparticle solution obtained consists only of a small fraction of triangular and hexagonal nanoparticles, the major fraction being spherical. We have also observed that the time taken for completion of reaction reduces progressively from 32 h to 3 h as the concentration of lemongrass extract in solution increases from 0.2 ml to 1.6 ml in the reaction medium. This may be rationalized on the basis of two models. The first is based on the formation of spherical 'seeds' that then act as centers around which nanotriangle growth occurs through the interaction of shape-directing molecules present in solution. Such a mechanism as discussed earlier has been invoked by Mirkin et al in their study on the growth of silver nanoprisms by a photo-irradiation process [17c]. For such a process to occur in this study, the rate of formation of spherical nuclei should be slow enough to enable deposition of gold in the form of triangles around the spheres and would clearly be facilitated under conditions of low lemongrass concentration in solution as observed. The second possible model could be one in which the rate of creation of spherical gold nanoparticles competes with assembly and sintering of the particles to triangular/hexagonal structures. In the case of reduction of $AuCl_4^-$ ions using lemongrass extract it is possible that the shape evolution of the gold particles from a spherical to flat triangular or hexagonal shape involves both these mechanisms. A change in the amount of lemongrass extract used for the reduction of $AuCl_4^-$ ions most likely alters the delicate balance between the rate of nucleation and growth and thus controls the size and shape of the gold particles formed in the process. Further in depth studies are still required to unequivocally claim the mechanism responsible for the lemongrass leaf extract mediated formation of the triangular and hexagonal gold particles.

4.6 Infrared absorbing optical coatings of gold nanotriangles.

The energy in the solar spectrum is primarily centered around the visible and infrared region of the electromagnetic spectrum [41]. For architectural constructions in high temperature geographical locations, it is required for glass coatings to be optically transparent but infrared opaque. Such coatings reduce the temperature rise within enclosed rooms, thus considerably reducing power expenditure on cooling of interiors. This may be accomplished either by designing coatings that reflect [26] or absorb IR radiation. In current architectural applications, the former approach is preferred. The possibility of tuning the longitudinal SPR absorption band over a wide range of wavelengths from ~ 700 nm to well into the NIR region of the electromagnetic spectrum for the anisotropic triangular and hexagonal gold nanoparticles make them well suited for architectural applications [26]. We show below through a simple experiment that glass coatings with IR absorbing elements such as those provided by the lemongrass-extract synthesized triangular and hexagonal gold particles could provide an interesting alternative. In this experiment, the temperature rise within a cardboard box with an aperture to fix various glass substrates due to exposure to an infrared lamp was recorded as a function of time of exposure. A representative experimental setup used for these temperature measurements is shown in scheme 4.1. Curves 1 and 2 in Figure 4.14A correspond to the UV-vis-NIR transmission spectra recorded from a glass substrate with 3 coats of triangular and hexagonal gold particles obtained in the 0.2 ml lemongrass reaction medium before and after heating at 300 ^{o}C for 3 h, respectively. In the case of as-prepared coating, the transmission in the NIR region is quite low due to absorption by the triangular and hexagonal gold particles (curve 1). After heat treatment of the film, the transmission in the NIR increases (curve 2) indicating some sintering of the triangular and hexagonal gold particles and loss in their anisotropic structure. The as-deposited triangular and hexagonal gold particles film has a pretty bluish color (inset of Figure 4.14B, photograph corresponding to filled triangles) and could thus serve dual purposes of providing tinted glass (indeed, the color of the coating could be varied from light pink to blue to dark gray) as well as an IR absorbing coating. After heat treatment, the film color turned to a golden hue (inset of Figure 4.14B, photo corresponding to open

triangles) and in spite of the increased IR transmission (curve 2, Figure 4.14A), the coating was still effective in blocking IR radiation, as is further discussed below.

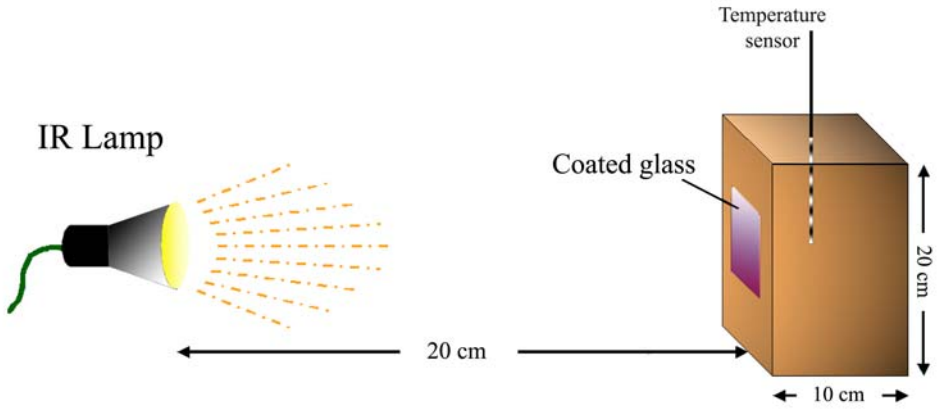

Scheme 4.1: *The schematic shows the experimental set up used for measuring the rise in temperature in an enclosed cardboard box with a coated glass window on irradiation with a tungsten filament IR lamp.*

Figure 4.14B shows plot of the variation of temperature within an enclosed box of cardboard with a window covered with, a) uncoated glass (filled squares) and glass with : b) a coat of spherical, borohydride reduced gold nanoparticles (7.3 mg/cm^2, circles), c) a single coat of triangular and hexagonal gold particles (4.4 mg/cm^2, stars), d) three coats of triangular and hexagonal gold particles (13.4 mg/cm^2, solid triangles), and with e) three coats of triangular and hexagonal gold particles after heating at 300 ^{o}C for 3 h (open triangles) as a function of time exposure to an IR lamp positioned at a distance of 20 cm from the window. It is observed that after irradiation with a tungsten filament lamp using either uncoated glass (squares) or the glass coated with spherical gold nanoparticles (open circles) as a window, the temperature rise follows a similar trend and that the temperature within the enclosure increases by 32 ^{o}C relative to the ambient room temperature (28 ^{o}C) within 30 min. of exposure. Thus, spherical gold nanoparticles do not lead to a drop in temperature within the enclosure, a result consistent with the fact that spherical gold nanoparticles do not absorb in the NIR region. In the case of the glass with single coat of triangular and hexagonal gold particles (stars), the temperature rise within the enclosure could be brought down to 27 ^{o}C while on using the glass with three coats of triangular and hexagonal gold particles (solid triangles), the difference in temperature with respect

to the ambient temperature could be brought down to as low as 23 ^{o}C. This drastic reduction in temperature due to infrared blocking by the film of triangular and hexagonal gold particles on the glass can clearly lead to a huge savings in the expenditure

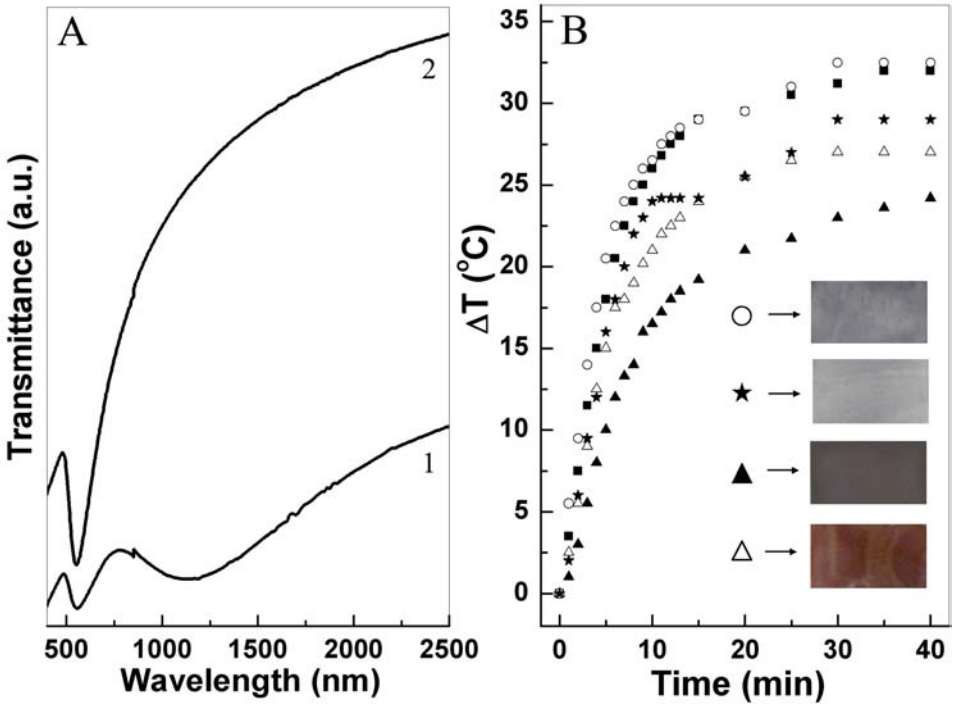

Figure 4.14: *A) UV-vis-NIR transmission spectra of lemongrass reduced gold nanotriangles. Curve 1: film of gold nanotriangles spray-coated onto a glass substrate maintained at 80 ^{o} C; curve 2 : after heat treatment of the above film at 300 ^{o} C for 3 h. B) Plot of temperature difference (with respect to ambient temperature = 28 ^{o} C vs. time measured inside a thermally insulated box exposed to an IR lamp with a window blocked with uncoated glass (squares); glass coated with spherical gold nanoparticles (open circles); glass coated with one layer of lemongrass-extract prepared gold nanotriangles (stars) and three layers of gold nanotriangles (solid triangles); and the three layer gold nanotriangle sample after heat treatment (open triangles). The inset shows photographs of the different glass samples with coatings identified by the corresponding symbols.*

required to cool interiors of structures in geographically hot locations. In order to test the role of heat treatment of the film on the infrared absorbing capability of the triangular and hexagonal gold particles coatings, the 3-coat film of triangular and hexagonal gold particles on glass was heated at 300 ^{o}C for 3 h in air. On using the heat-treated triangular and hexagonal gold particles coated glass as a window, it is observed that the temperature rise inside the enclosure now increases to 26 ^{o}C (open triangles). Thus, there is a small loss in IR absorbing efficiency of the triangular and hexagonal gold particles coating after this heat treatment and is consistent with the increased IR transmission measured for this

film (Figure 4.14A, curve 2). After this heat treatment, it was observed that the color of the film changed to a golden hue (when viewed at slightly off normal) and that the color was more uniform over the surface. Even after this heat treatment, it is seen that the film is still capable of blocking out a considerable amount of IR radiation (compare with behavior of plain glass, squares). Since the synthesis of triangular and hexagonal gold particles used in the coatings is a solution method employing plant-extract based reducing agents, we believe it would be an economically viable approach to form infrared absorbing thin coatings on different surfaces.

4.7 Conclusions.

In conclusion, an efficient shape controlled synthesis of flat gold triangular and hexagonal particles has been demonstrated through a very convenient and environmentally benign single step process. The ability of the this green chemistry approach as an alternative to usual chemical and physical approaches was further demonstrated by the ease with which the size of triangular and hexagonal gold particles could be controlled by a mere change in the amount percentage of the natural reducing agent used. It was observed that the size of the flat gold particles tend to increase as lesser amount of the lemongrass leaf extract is used for their synthesis and also that, on using higher amount of the extract, the percentage of spherical particles in the solution tend to increase. The extremely thin flat gold particles with thickness in the range 8 to 25 nm seem to be formed by initial formation of spherical particles that subsequently assemble and sinter to ultimately form single crystalline flat gold particles. The formation of gold particles is believed to occur due to the reduction of $AuCl_4^-$ ions by reducing sugars present in the lemongrass leaf extract and the growth of flat structures by assembly and sintering mechanism apparently is facilitated by ketonic/aldehydic compounds. The possibility of tuning the longitudinal SPR component of the flat gold particles in NIR region by controlling their size makes these particles suitable for use as efficient optical coatings on glass windows for architectural applications. It is observed that glass coated with flat gold particles are able to reduce the temperature rise within an enclosed compartment appreciably as compared to plane glass or glass coated with spherical particles on irradiation with vis-IR light.

4.8 References:

1) a) Buffat, P.; Borel, J.-P. *Phys. Re*v. *A* **1976**, *13*, 2287. b) Castro, T.; Reifenberger, R.; Choi, E.; Andres, R. P. *Phys. Re*v. *B* **1990**, *42*, 8548. c) Beck, R. D.; St. John, P.; Homer, M. L.; Whetten, R. L. *Science* **1991**, *253*, 879. d) Martin, T. P.; Naher, U.; Schaber, H.; Zimmermann, U. *J. Chem. Phys.* **1994**, *100*, 2322.

2) a) Link, S.; El-Sayed, M. A. *Annu. Rev. Phys. Chem.* **2003**, *54*, 331. b) Link, S.; El-Sayed, M. A. *Int. Rev. Phys. Chem.* **2000**, *19*, 409. c) Peng, X. G.; Manna, L.; Yang, W. D.; Wickham, J.; Scher, E.; Kadavanich, A.; Alivisatos, A. P. *Nature* **2000**, *404*, 59. d) El-Sayed, M. A. *Acc. Chem. Res.* **2001**, *34*, 257. e) Murphy, C. J.; Jana, N. R. *Adv. Mater.* **2002**, *14*, 80.

3) a) Narayanan, R.; El-Sayed, M. A. *Nano Lett.* **2004**, *4*, 1343. b) Narayanan, R.; El-Sayed, M. A. *J. Phys. Chem. B* **2004**, *108*, 5726.

4) a) P. Claus,; A. Bruckner,; C. Mohr,; H. Hofmeister *J. Am. Chem. Soc.* **2000,** *122,* 11430. b) Sanchez, A.; Abbet, S.; Heiz, U.; Schneider, W.-D.; Hakkinen, H.; Barnett, R. N.; Landman**,** U. *J. Phys. Chem. A* **1999,** *103,* 9573. c) Alivisatos, A. P. *J. Phys. Chem*. **1996**, *100*, 13226. d) Aizpura, J.; Hanarp, P.; Sutherland, D. S.; Käll, M.; Bryant, G. W.; García de Abajo, F. J. *Phys.Rev.Lett.* **2003**, *90*, 057401. e) Landes, C. F.; Link, S.; Mohamed, M. B.; Nikoobakht, B.; El-Sayed, M. A. *Pure Appl. Chem.* **2002**, *74*, 1675. f) Valden, M.; Lai, X.; Goodman, W. *Science* **1998**, *281*, 1647. g) Davis, R. J. *Science* **2003**, *301*, 926-927. h) Burda, C.; Chen, X.; Narayanan, R.; El-Sayed, M. A. *Chem. Rev.* **2005**, *105*, 1025. i) Kelly, K. L.; Coronado, E.; Zhao, L. L.; Schatz, G. C. *J. Phys. Chem. B* **2003**, *107*, 668-677.

5) Moreno-Manas, M.; Pleixats, R. *Acc. Chem. Res.* **2003**, *36*, 638.

6) a) Mirkin, C, A.; Letsinger, R. L.; Mucic, R. C.; Storhoff, J. J. *Nature* **1996**, *382*, 607. b) Han, M., Gao, X., Su, J.Z. & Nie, S. *Nature Biotechnol*. **2001**, *19*, 631.

7) Sun, S., Murray, C.B., Weller, D., Folks, L. & Moser, A. *Science* **2000**, *287*, 1989.

8) Kamat, P. V.; *J. Phys. Chem. B***, 2002**, *106*, 7729.

9) a) Sun, Y.; Xia, Y. *Science* **2002**, *298*, 2176. b) Xiong, Y.; Chen, J.; Wiley, B.; Xia, Y.; Yin, Y.; Li, Z. Y. *Nano Lett.* **2005**, *5*, 1237.

10) a) Hutchinson, T. O.; Liu, Y.-P.; Kiely, C.; Kiely, C. J.; Brust M. *Adv.Mater.* **2001**, *13*, 1800. b) Peng, X.; Manna, L.; Yang, W.; Wickham, J.; Scher, E.; Kadavanich, A.; Alivisatos A. P. *Nature* **2000**, *404*, 59. c) Busbee, B. D.; Obare, S. O.; Murphy, C. J.; *Adv. Mater.* **2003**, *15*, 414. d) Jana, N.; Gearheart, L.; Murphy, C. J. *Chem. Mater.* **2001**, *13*, 2313.

11) a) Hao, E.; Kelly, K. L.; Hupp, J. T.; Schatz, G. C. *J.Am.Chem.Soc.* **2002**, *124*, 15182. b) Puntes, V. F.; Zanchet, D.; Erdonmez, C. K.; Alivisatos, A. P. *J. Am. Chem. Soc.;* **2002**, *124*, 12874.

12) Sun, Y.; Mayers, B.; Xia, Y. *Nano.Lett.* **2003**, *3*, 675.

13) Huang, C.-C.; Yang, Z.; Chang, H.-T. *Langmuir* **2004**, *20*, 6089.

14) a) Manna, L.; Scher, E. C.; Alivisatos, A. P. *J.Am.Chem.Soc.* **2000**, *122*, 12700. b) Chen, S.; Wang, Z. L.; Ballato, J.; Foulger, S. H.; Carroll, D. L. *J. Am. Chem. Soc.* **2003**, *125*, 16186.

15) a) Sau, T. K.; Murphy, C. J. *J. Am. Chem. Soc.* **2004**; *126*, 8648. b) Hu, J.; Zhang, Y.; Liu, B.; Liu, J.; Zhou, H.; Xu, Y.; Jiang, Y.; Yang, Z.; Tian, Z. –Q. *J. Am. Chem. Soc.* **2004**, *126*, 9470.

16) Turkevich, J.; Stevenson, P. C.; Hiller, J. *Discussions Faraday, Soc.*, **1951**, *11*, 55.

17) a) Chen, S.; Carroll, D. L. *Nano.Lett.* **2002**, *2*, 1003. b) Haes, A. J.; Zhao, J.; Zou, S.; Own, C. S.; Marks, L. D.; Schatz, G. C.; Van Duyne, R. P.; *J. Phys. Chem. B.* **2005**, *109*, 11158. c) Jin, R.; Cao, Y.; Mirkin, C. A.; Kelly, K. L.; Schatz, G. C.; Zheng, J. G. *Science* **2001**, *294*, 1901. d) Jin, R.; Cao, Y. C.; Hao, E.; Métraux, G. S.; Schatz, G. C.; Mirkin, C. A. *Nature* **2003**, *425*, 487. e) Callegari, A.; Tonti, D.; Chergui, M. *Nano Lett.* **2003**, *3*, 1565. f) Sun, Y.; Mayers, B.; Xia, Y. *Nano Lett.* **2003**, *3*, 675. g) Sun, Y.; Xia, Y. *Adv. Mater.* **2003**, *15*, 695. h) Chen, S.; Carroll, D. L. *J. Phys. Chem. B* **2004**, *108*, 5500. i) Métraux, G. S.; Mirkin C. A. *Adv. Mater.* **2005**, *17*, 412

18) a) Milligan, W. O.; Morriss. *J. Am. Chem. Soc.* **1964**, *86*, 3461. b) Chiang, Y. S.; Turkevich, J. *J. Colloid Sci* **1963**, *18*, 772. c) Malikova, N., Pastoriza-Santos, I., Schierhorn, M., Kotov, N.A. & Liz-Marzan, L.M. *Langmuir*, **2002**, *18*, 3694. d) Sarma, T. K.; Chattopadhyay, A.; *Langmuir* **2004**, *20*, 3520. e) Li, Z.; Liu, Z.; Zhang, J.; Han, B.; Du, J.; Gao, Y.; Jiang, T. *J. Phys. Chem. B* **2005**, *109*, 14445. f)

Millstone, J. E.; Park, S.; Shuford, K. L.; Qin, L.; Schatz, G. C.; Mirkin, C. A. *J. Am. Chem. Soc.* **2005**, *127*, 5312. g) Kim, F.; Connor, S.; Song, H.; Kuykendall, T.; Yang, P. *Angew. Chem., Int. Ed. Engl.* **2004**, *43*, 3673-3677.

19) a) Mullin, J. W. *Crystallization*, Butterworth-Heinemann, Woburn, MA, 1997. b) Turkevich, J. Stevenson, P. C.; Hillier, J. *J. Phys. Chem.* **1953**. *57*, 670. c) Hu, J. Q.; Chen, Q.; Xie, Z. X.; Han, G. B.; Wang, R. H.; Ren, B.; Zhang, Y.; Yang, Z. L.; Tian, Z. Q. *Adv. Funct. Mater.* **2004**, *14*, 183. d) Wiley, B.; Sun, Y.; Xia, Y.; *Langmuir*, **2005**, *21*, 8077. e) Chen, J.; Herricks, T.; Geissler, M.; Xia, Y.; *J. Am. Chem. Soc.* **2004**, *126*, 10854. f) Watzky, M. A.; Finke, R. G. *J. Am. Chem. Soc.*, **1997**, *119*, 10382. g) Murray, C. B.; Norris, D. J.; Bawendi, M. G. *J. Am. Chem. Soc.* **1993**, *115*, 8706. h) Reiss, H. *J. Chem. Phys.* **1951**, *19*, 482. i) Sato, T.; Ruch, R. *Stabilization of Colloidal Dispersions by Polymer Absorption;* Marcel Dekker: New York, 1980; pp 46-51. j) Xia, Y.; Yang, P.; Sun, Y.; Wu, Y.; Mayers, B.; Gates, B.; Yin, Y.; Kim, F.; Yan, H. *Adv. Mater.* **2003**, *15*, 353. k) Lofton, C,; Sigmund, W. *Adv. Funct. Mater.* **2005**, *15*, 1197.

20) a) Gai, P. L.; Harmer, M. A. *Nano Lett.* **2002**, *2*, 771. b) Zhang, S. –H.; Jiang, Z. –Y.; Xie, Z. –X.; Xu, X.; Huang, R. –B.; Zheng, L. –S. *J. Phys. Chem. B* **2005,** *109,* 9416. c) Zhang, J.; Kambayashi, M.; Oyama, M. *Electroanalysis*, **2005**, *17*, 408.

21) a) Hulteen, J. C.; Martin, C. R. *J. Mater. Chem.* **1997**, *7*, 1075. b) Martin, C. R. *Acc. Chem. Res.* **1995**, *28*, 61. c) Martin, C. R. *Science* **1994**, *266*, 1994. d) Gao, T.; Meng, G.; Zhang, J.; Sun, S.; Zhang, L. *Appl. Phys. A* **2002**, *74*, 403. e) Barbic, M.; Mock, J. J.; Smith, D. R.; Schultz, S. S. *J. Appl. Phys.* **2002**, *91*, 9341. f) Molares, M. E. T.; Buschmann, V.; Dobrev, D.; Neumann, R.; Scholtz, R. Schuchert, I. U.; Vetter, J. *Adv. Mater.* **2001**, *13*, 62. g) Bhattacharyya, S.; Saha, S. K.; Chakravorty D. *Appl. Phys. Lett.* **2000**, *77*, 3770. h) Ajayan, P. M.; Stephan, O.; Redlich, Colliex, C. *Nature*, **1995**, *375*, 564. i) Braun, E.; Eichen, Y.; Sivan, U.; Ben-Yoseph, G. *Nature*, **1998**, *391*, 775. j) Jorritsama, J.; Gijs, M. A. M.; Kerkhof, J. M.; Stienen, J. G. H. *Nanotechnology* **1996**, *7*, 263.

22) a) Li, G.; Lauer, M.; Schulz, A.; Boettcher, C.; Li, F.; Fuhrhop, J. H. *Langmuir* **2003,** *19,* 6483. b) Jana, N. R.; Gearheart, L.; Obare, S. O.; Murphy, C. J. *Langmuir* **2002**, *18*, 922.

23) Tsuji, T.; Higuchi, T.; Tsuji, M. *Chem. Lett.* **2005**, *34*, 476.

24) a) Penn, R. L., Banfield, J. F. *American Mineralogist*, **1998**, *83*, 1077. b) Privman, V.; Goia, D. V.; Park, J.; Matijevic, E. *J. Colloid Interface Sci.* **1999**, *213*, 36.

25) a) Loo, C.; Lin, A.; Hirsch, L.; Lee, M. H.; Barton, J.; Halas, N.; West, J.; Drezek, R. *Technology in Cancer Research and Treatment* **2004**, *3*, 33. b) Hirsch, L. R.; Stafford, R. J.; Bankson, J. A.; Sershen, S. R.; Rivera, B.; Price, R. E.; Hazle, J. D.; Halas, N. J.; West, J. L. *Proc. Natl. Acad. Sci. USA*, **2003**, *100*, 13549. c) Nanospectra biosciences, Inc. Huston Texas, www.nanospectra.com.

26) a) Arnaud, A. *J. Non-Cryst. Solids* **1997**, *218*, 12. b) Manning, T. D.; Parkin, I. P. *J. Mater. Chem.* **2004**, *14*, 2554-2559. c) Xu, X.; Stevens, M.; Cortie, M. B. *Chem Mater.* **2004**, *16*, 2259-2266.

27) Germain, V.; Li, J.; Ingert, D.; Wang, Z. L.; Pileni, M. P. *J. Phys. Chem. B* **2003**, *107*, 8717.

28) a) Storhoff, J. J.; Lazaides, A. A.; Mucic, R. C.; Mirkin, C. A.; Letsinger, R. L.; Schatz, G. C. *J. Am. Chem. Soc.* **2000**, *122*, 4640. b) Turkevich, J. ; Garton, G.; Stevenson P. C. *J. Colloid Interface Sci. Suppl.* **1954**, *9*, 26. c) Mangeney, C.; Ferrage, F.; Aujard, I.; Artzner, V. -M.; Jullien, L.; Ouari, O.; Rekai, E. D.; Laschewsky, A.; Vikholm, I.; Sadowski, J. W. *J. Am. Chem. Soc.* **2002**, *124*, 5811.

29) a) Mulvany, P. *Langmuir* **1996**, *12*, 788. b) Kreibig, U.; Vollmer, M. *Optical Properties of Metal Clusters*; Springer Series in Material Science, 25; Springer-Verlag: Berlin, 1995. c) Seker, F.; Malenfant, P. R. L.; Larsen, M.; Alizadeh, A.; Conway, K.; Kulkarni, A.; Goddard, G.; Garaas, R. *Adv. Mater.* **2005**, *17*, 1941.

30) Wessels, J. M.; Nothofer, H.-G.; Ford, W. E.; von Wrochem, F.; Scholz, F.; Vossmeyer, T.; Schroedter, A.; Weller, H.; Yasuda, A. *J. Am. Chem. Soc.* **2004,** *126*, 3349.

31) a) Stoeva, S.I.; Prasad, B.L.V.; Uma, S.; Stoimenov, P.K.; Zaikovski, V.; Sorensen, C.M.; Klabunde, K.J. *J. Phys. Chem. B* **2003**, *107*, 7441. b) Smetana, A. B.; Klabunde, K. J.; Sorensen C. M. *J. Colloid Interface Sci.* **2005**, *284*, 521. c) Talapin, D. V.; Shevchenko, E. V. Gaponik, N.; Radtchenko, I. L.; Kornowski, A.; Haase, M.; Rogach, A. L.; Weller, H. *Adv. Mater.* **2005**, *17*, 1325. d) Zhang, Z. L.; Glotzer, S. C. *Nano Lett.* **2004**, *4*, 1407.

32) Jose-Yacaman, M.; Wing, C. -G.; Miki, M.; Yang, D.-Q.; Piyakis, K. N.; Sacher, E. *J. Phys. Chem. B* **2005,** *109,* 9703.

33) Ciardelli, G.; Chiono, V.; Vozzi, G.; Pracella, M.; Ahluwalia, A.; Barbani, N.; Cristallini, C.; Giusti, P. *Biomacromolecules* **2005,** 6, 1961.

34) Silverstein, R.M., & Basseler, G.C. Spectrometric identification of organic compounds (John Wiley & Sons, Inc., New York) **1967**, chapter 4.

35) Liu, Y. C.; Chuang, T. C. *J. Phys. Chem. B.* **2003**, *107*, 12383.

36) Miyama, T.; Yonezawa, Y. *Langmuir* **2004**, *20*, 5918.

37) Sastry, M.; Ganguly, P. *J. Phys. Chem. A.* **1998**, *102*, 697.

38) Kowbel, W.; Shan, C. H. *Carbon*, **1990**, *28*, 287.

39) a) Simpson, C. R.; Kohl, M.; Essenpreis, M.; Cope, M. *Phys. Med. Bio.* **1998**, *43*, 24652478. b) Anderson, R. R.; Parrish, J. A. *J. Invest. Dermatol.* **1981**, *77*, 13.

40) Bendersky, L. A.; W. Gayle, F. *J. Res. Natl. Inst. Stand. Technol.* **2001**, *106*, 997.

41) ASTMG 159 – 98. Standard tables for references solar spectral irradiance at air mass 1.5: Direct normal and hemispherical for a 37^{o} tilted surface; American society for testing and materials: West Conshohocken, PA, 1998.

Chapter V

Study of Gold Nanotriangles: Formation and Their Morphological Changes Induced by Chemical and Physical Means

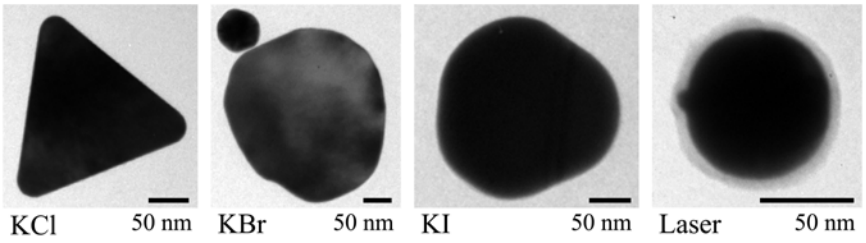

In this chapter, using citric acid reduction method for the synthesis of gold nanoparticles as a model system, attempt has been made to understand the growth of gold nanotriangles and the factors favoring their formation. TEM measurements were performed to observe the intermediate stages during the growth of gold nanotriangles. Attempt has been made to draw attention towards the possible crucial role of Cl^- ions in promoting the growth of <111> oriented gold nanotriangles. Furthermore, the significant role of halide ions has been stressed by demonstrating their ability to influence the shape of gold nanoparticles during their synthesis as well as on preformed nanoparticles. As a physical means of shape transformation, studies on the effect of laser irradiation on the lemongrass reduced gold nanotriangles has been discussed.

Part of the work presented in this chapter has been published in:

Shankar, S. S.; Bhargava, S.; Sastry, M. *J. Nanosci. Nanotech.* **2005**, *5*, 1721.

5.1 Introduction.

In the previous chapter the synthesis of triangular and hexagonal gold particles was discussed and the growth of the anisotropic particles appeared to follow through an aggregation of initially formed spherical gold nanoparticles. In the lemongrass leaf extract – $HAuCl_4$ aqueous growth medium the number of molecular components are enormous and could at least be a few hundreds or more, thus making it difficult to single out the contributing factors responsible for such interesting growth of anisotropic structures in large percentage. The molecules responsible for the triangular and hexagonal gold particles formed have been broadly classified as carbonyl group containing compounds, possibly some sugar molecules with specific structure. The situation still remains very complex and the observed triangular and hexagonal gold particle formation may not be under the influence of a single type of molecule but could also be a synergistic effect of many molecules that are able to intereact with the initially formed gold nuclei. To bring down the complexity of the situation, in this chapter an attempt has been made to study the growth of the gold nanotriangles and nanohexagons using a system where the contribution of different components can be accounted for with greater clarity. In this chapter we have attempted to study the formation of gold nanotriangles using the commonly used citric acid reduction method. Synthesis of gold nanoparticles using sodium citrate as a reducing agent has been extensively studied by Turkevich et. al. [1] and they have also showed that gold nanotriangles are formed along with spherical nanoparticles by using citric acid as a reducing agent. This observation motivated us to further study the formation of gold nanotriangles using citric acid mediated reduction of aqueous $HAuCl_4$ solution as a model system. Plate-like structures were also later reported by Suito and Uyeda using salicylic acid as reducing agent [2] and were followed by a few more reports on the formation of triangular and large micron sized flat gold particles [3]. The large plate-like structures have been proposed to form by a spiral growth mechanism [4] and by an aggregation and recrystallization process [3c]. Turkevich and coworkers in their study on gold nanoparticle formation using sodium citrate as reducing agent have focused mainly on the rate of nucleation, the rate of growth and on the size of the spherical gold nanoparticles. We have attempted to reinvestigate the citric acid reduction method to bring forth the unaddressed issue of the agents that assist in the formation of

the flat gold nanotriangles. This is a surfactantless and templateless method, therefore these agents must be preventing the uniform three dimensional growth of nuclei to form the thermodynamically favorable spherical nanoparticles in some manner. In the work reported by Turkevich et. al., emphasis was laid on the role of acetone dicarboxylate ions, the oxidized product of citric acid, as a key factor in facilitating the nucleation process [1a,b,d]; but a mention on the species facilitating the growth of the nuclei to form flat gold nanotriangles was lacking. In our experiments with the citric acid reduction method to form gold nanoparticles, we attempted to study the effect of the temperature of the reaction medium on the size and percentage of the gold nanotriangles formed. In the room temperature reduction of $AuCl_4^-$ ions, in which case a good percentage of gold nanotriangles could be observed, time dependent UV-vis-NIR spectroscopy and TEM analysis were carried out to study the intermediate stages in the formation of these gold nanotriangles. In this study we intend to draw attention to the possible crucial role of chloride ions, that have so far not been given due emphasis, in the growth process in promoting the formation of gold nanotriangles. We observe that the presence of halide ions in solution during $AuCl_4^-$ ion reduction by citric acid critically affects the morphology of the particles. While added Cl^- ions promote the formation of gold nanotriangles, Br^- and I^- ions inhibit the growth of gold nanotriangles significantly. Bromide and iodide ions are known to be capable of replacing chemisorbed Cl^- ions from the gold surface [5] and thus can potentially control the growth of the nano nuclei unlike the F^- ions that are unable to do so. Surface chemistry of the citric acid reduced gold nanoparticles was analyzed by X-Ray photoelectron spectroscopy (XPS) measurements and their relevance to the crystal growth mechanism of gold nanotriangles has been attempted. The role of halide ions is not unique to the citric acid reduction reinvestigated here, but has been recently gaining importance in the crystal growth mechanism in few other systems too [6]. Pileni's group have demonstrated that though the presence of halide ions do not affect the structure of the micellar template, drastic changes in the shape of the copper nanoparticles formed in their presence could be observed [6a-f]. In their study, while NaCl addition was observed to promote rod like structures and NaBr promoted the formation of cubic copper nanoparticles, NaF was not observed to impart any specific shape, though presence of small cubes have been claimed [6a, e]. Similarly,

importance of the Cl^- on the structure of the nanoparticles formed has also been claimed by Roberts et. al. and Xia et. al. in their reports on the synthesis of copper [6g] and silver nanoparticles [6h] respectively.

The role of halide ions seems so prominent that they are able to impart morphological distortions even in an aqueous solution of preformed gold nanotriangles. The halide ions thus also serve as chemical agents to induce morphological changes to well formed gold nanoparticles [7]. Studies on the morphological changes induced by laser irradiation on preformed gold nanotriangles have also been carried out. Nd-YAG laser with an emission wavelength of 1064 nm was used to selectively excite and melt the gold nanotriangles synthesized using lemon grass leaf extract and thus served as a physical means to induce morphological changes to the gold nanotriangles. Shape transformation of gold nanorods induced by laser irradiation has been well studied by a number of groups [8] and has also been demonstrated in the case of silver nanotriangles and micron sized gold flakes [9]. In this chapter we have extended these studies to gold nanotriangles and observe similar formation of spherical gold nanoparticles on irradiation along with some fragmentation.

5.2 Experimental Details.

In a typical experiment, 10 ml of 10^{-3} M aqueous $HAuCl_4$ solution was diluted to 90 mL and was subsequently mixed with 10 mL of 10^{-2} M aqueous citric acid solution at different temperatures (20, 30, 40, 60 ^oC and at boiling temperature) and allowed to react for 12 hours except in the case of boiling condition where the reaction was carried out only for 10 min after mixing. For purification of the gold nanotriangles (enhancement of the percentage of gold nanotriangles in the mixture), the gold nanoparticle solution synthesized at 20 ^oC was centrifuged at 3000 rpm for 15 min. The settled pellet was thereafter redispersed in deionized water by sonication and again subjected to centrifugation as before. The cycle of centrifugation and redispersion was repeated 4 times to obtain enhanced percentage of gold nanotriangles. During the third and fourth cycles of purification, the pellet was redispersed in aqueous 10^{-5} M KCl to prevent irreversible aggregation of the gold nanoparticles due to depletion of the stabilizing ions around the nanoparticle [10]. The kinetics of formation of the gold nanotriangles was

followed by UV-vis-NIR spectroscopic measurements at regular intervals after mixing citric acid and $HAuCl_4$ solution in above mentioned proportions at room temperature. TEM at various intermediate reaction times were also carried in parallel by solution-casting nanoparticle films onto the TEM grids but taking care to ensure rapid evaporation of water by placing the grids in a chamber evacuated to 10^{-3} Torr pressure. In this way, the TEM samples could be routinely prepared within 2 min.

To study the effect of halide ions on the morphology of gold nanoparticles during their synthesis by citric acid reduction of $AuCl_4^-$ ions, 1 mL of 10^{-2} M aqueous citric acid solution was added at room temperature (27 ^oC) to 9 mL of aqueous $HAuCl_4$ solution in the presence of different potassium halides (KX, X = F, Cl, Br, I) with the concentration of each maintained at 10^{-4} M. These solutions were allowed to react for 24 h at room temperature. UV-Vis-NIR spectroscopy and TEM analysis were pursued to characterize the gold nanoparticles formed in each of these solutions. X-ray photoelectron spectroscopy (XPS) analysis of the samples of citric acid reduced gold nanoparticles formed under different conditions, prepared by solution casting in the form of a film on Si (111) wafers, was done to analyze the surface chemistry. The core level binding energies (BEs) were aligned with reference to the Au $4F_{7/2}$ BE of 84 eV. For all the XPS measurements, the gold nanoparticle solution was centrifuged and redispersed 4 times in deionized water to free the nanoparticles from any unbound ions/molecules present in the initial solution.

To study the effect of halide ions on the preformed citric acid reduced gold nanoparticles, 2 mL each of aqueous 10^{-2} M KF, KCl, KBr and KI solutions were added to 20 mL of citric acid reduced gold nanoparticles solution synthesized at 27 ^oC and allowed to stand for two days. Isothermal titration calorimetric (ITC) measurements were carried out to characterize the interaction between citric acid reduced gold nanoparticles synthesized at 27 ^oC and the aqueous solutions of 10^{-3} M KF, KCl, KBr and KI. Deionized water was taken as standard in the reference cell and 1.47 ml of 10^{-3} M aqueous citric acid reduced gold nanoparticles solution in the titration cell was titrated against 10^{-3} M aqueous solutions of KF, KCl, KBr and KI separately by adding 10 μL of the respective potassium halide solution per injection at regular intervals of 2 min. In order to correct for calorimetric response arising from dilution of the potassium halides in

water, control experiments were performed wherein 10^{-3} M aqueous potassium halide solutions were titrated against deionized water.

As a physical means for inducing shape transformation in the gold nanotriangles laser irradiation studies were carried out. The laser source used for irradiating the sample is a home made Nd:YAG Q-switched laser. The output laser was of wavelength 1064 nm and had a repetition rate of 1 Hz with a pulse width of 20 ns. The triangles used for these studies were synthesized by lemongrass leaf extract based method with which a large percentage of triangular gold particles could be obtained conveniently. Synthesis of gold nanotriangles was followed as discussed in Chapter 4, Section 4.2.1, by adding 0.6 mL of the lemongrass leaf extract to 5mL of 10^{-3} M aqueous $HAuCl_4$ solution. The gold nanoparticles synthesized by this method after 48 h of reaction were subjected to repeated centrifugation and redispersion in deionized water four times at a speed of 4000 rpm and 10 min duration to yield in an increased percentage of the gold nanotriangles. Using these proportions of lemongrass leaf extract and $HAuCl_4$ solution, gold nanotriangles exhibiting longitudinal SPR band centered at 1200 nm could be obtained favoring large absorbance at the laser wavelength used. The average size of gold nanotriangles was in the range 100 to 300 nm.

For the laser irradiation experiment, a 2μL sample of gold nanotriangle solution was placed in a glass capillary of 2 cm path length and 2 mm diameter sealed from one end using wax. To study the effect of energy of laser on the gold nanotriangles, two set of experiments were performed. In the first set of experiment, irradiation was carried out for duration of 5 min and varying the laser fluence in the range 2 – 35 mJ/cm^2 at 1064 nm. In the second set of experiment, laser fluence was kept constant at 30 mJ/cm^2 and the time of irradiation was varied in between 2 – 14 min. The changes in the gold nanotriangles solution were monitored by recording the UV-visible-NIR absorption spectra, XRD and TEM measurements after each laser irradiation experiment. Control experiment was also carried out to assess the effect of 1064 nm laser irradiation on solution containing only spherical gold nanoparticles with no absorbance in the NIR region of electromagnetic spectra. Gold nanoparticles for this purpose were synthesized by reducing 100 mL of 10^{-4} M $HAuCl_4$ aqueous solution using 10 mL of 0.1% aqueous sodium borohydride ($NaBH_4$)

solution, and exhibited only a single SPR band at 512 nm with negligible absorbance in the NIR region.

5.3 Gold nanotriangles by citric acid reduction.

5.3.1 Temperature dependence on the formation of gold nanotriangles:

Figure 5.1A shows the UV-vis-NIR absorption spectra recorded from the reaction of 10^{-4} M aqueous $HAuCl_4$ with citric acid (net concentration 10^{-3} M) at different temperatures. Under boiling conditions (the standard citric acid reduction method), the spectrum shows a sharp absorption band at 525 nm with negligible absorption beyond 600 nm. The absorption at 525 nm is due to excitation of surface plasmon (SP) vibrations in the gold particles and is responsible for the striking ruby red-pink color of gold hydrosols. Interesting differences in the UV-vis-NIR absorption spectra are seen for the reactions carried out at 20, 30, 40 and 60 ^{o}C (Figure 5.1A). In addition to the absorption at 525 nm, these solutions exhibit an additional absorption band at longer wavelengths; the position of the long wavelength absorption band being clearly a function of the reaction temperature and shows a shift to longer wavelengths as the reaction temperature

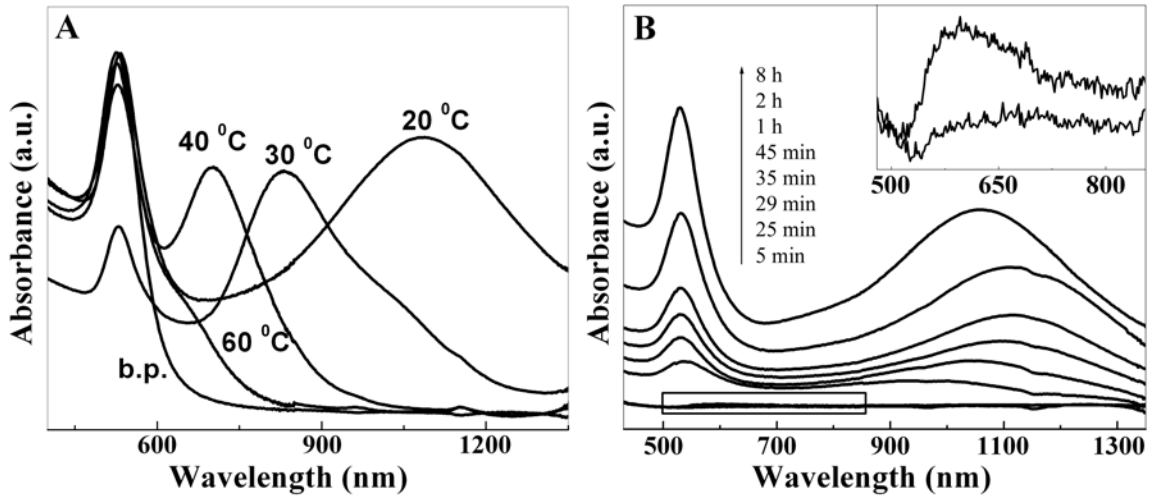

Figure 5.1: *A) UV-vis-NIR absorption spectra of citrate reduced gold nanoparticles prepared at different reaction temperatures (indicated next to the respective curves). B) UV-vis-NIR absorption spectra of citrate reduced gold nanoparticles as a function of time of reaction at room temperature. The inset shows an expanded view of the boxed region with axes notation same as that of the corresponding main figure.*

is reduced. At 60^{o} C, the long wavelength component appears as a shoulder in the UV-vis-NIR spectrum. The long wavelength absorption as discussed in the previous chapter may arise due to : 1) aggregation of the gold particles into open, string-like structures [11] or, 2) due to shape anisotropy in the particles [12] or due to a combination of these two factors.

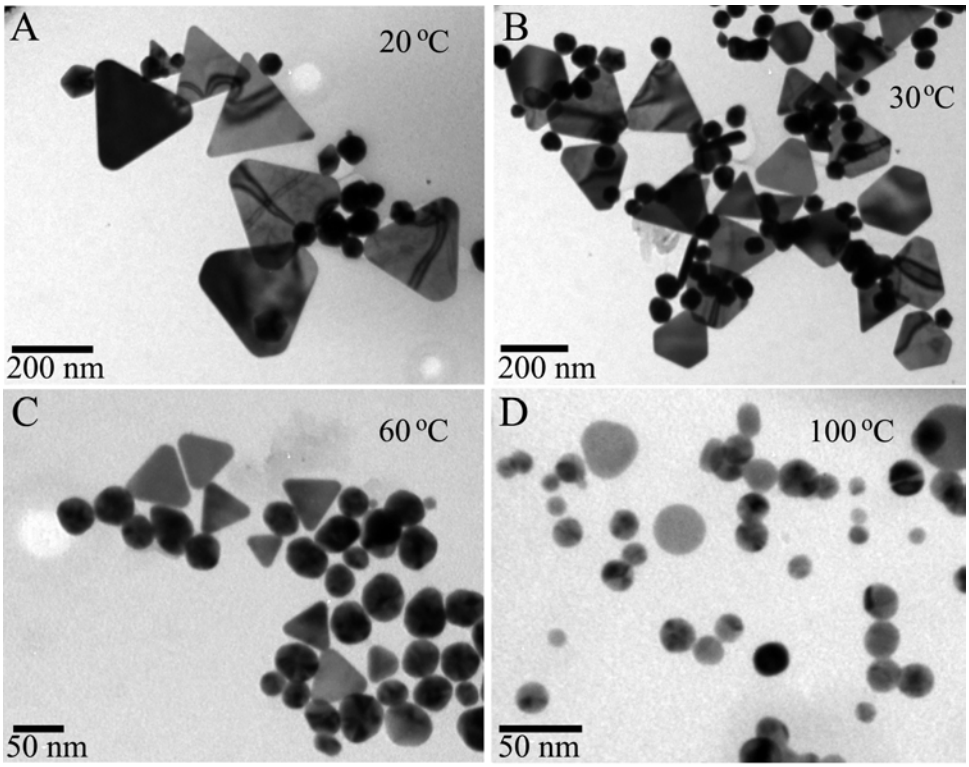

Figure 5.2: *Representative TEM images of citric acid reduced gold nanoparticles synthesized at A) 20, B) 30, C) 60 ^{o}C and D) at 100 ^{o}C as indicated.*

Figure 5.2 A-D shows representative TEM images of gold nanoparticles obtained in the reactions carried out at 20, 30, 60 and 100 ^{o}C respectively. It is observed that a reasonably large percentage of triangular nanoparticles are formed when reactions are carried out at or below 40 ^{o}C. The percentage of triangular particles formed was estimated to be approximately 18 and 27% when gold ion reduction was carried out at 20 and 30 ^{o}C respectively (Figure 5.2 A,B). Only a small percentage of triangles (< 10 %) was observed when reduction was carried above 40 ^{o}C (Figure 5.2C,D). It is clear that the long wavelength absorption observed in the UV-vis-NIR spectra recorded from these solutions (Figure 5.1A) is due to shape anisotropy (flat gold nanotriangles) and not due to

assembly of spherical nanoparticles. An analysis of a number of TEM images recorded from the triangular nanoparticles prepared at different temperatures yielded the following average edge lengths : 250, 190, 106 and 58 nm for reactions at 20, 30, 40 and 60 ^{o}C respectively. The rest of the particles synthesized under these conditions were mainly spherical or decahedral with size less than 50 nm. In case of gold nanoparticles synthesized under boiling conditions, negligible amount of nanotriangles were observed. The particles in this case were mainly spherical with size in the range 10 – 20 nm (Figure 5.2D). There is thus a clear correlation in both the number of triangles in the nanoparticle population and their size (quantified in terms of the edge length) with the reaction temperature; both increase as the reaction temperature is reduced. However, a small reduction in the percentage of triangles relative to spherical gold particles is observed on reducing the reaction temperature below room temperature. Since, the gold nanotriangles synthesized at 20 ^{o}C are nearly 30 % larger as compared to those synthesized at 30 ^{o}C the amount of gold consumed in the formation of gold nanotriangles is essentially same. That the triangles are larger at lower temperatures is also consistent with the UV-vis-NIR spectra that exhibited a progressive red shift in the longitudinal plasmon absorption band with decreasing reaction temperature (Figure 5.1A).

Increasing the temperature during citric acid reduction of $AuCl_4^-$ ions results in an increase in the metal ion reduction rate and thus the rate of growth of the gold nanoparticles. The reaction times vary from few minutes, when carried under boiling conditions, to 10 h when carried at 20 ^{o}C. The UV-vis-NIR absorption spectra recorded during citrate reduction of aqueous gold ions at room temperature (27 ^{o}C) is shown in Figure 5.1B. As the reaction proceeds, the transverse SPR band at 510 nm grows in intensity and is accompanied by a concomitant increase in absorption at ca. 1100 nm (longitudinal SPR band). At very early stages of reaction, a broad absorption band at ca. 625 nm with very low absorbance is observed (inset of Figure 5.1B). As the reaction proceeds, an absorption band starts developing in near infrared (NIR) region and red shifts gradually to longer wavelengths. After 2 h of reaction, the NIR absorption band again blue shifts but to a lesser extent when compared to the red shift observed during the initial stages of reaction. The optical absorption spectra show no detectable changes after 8 h of reaction indicating complete reduction of $AuCl_4^-$ ions. In any of the reactions

discussed above, we do not observe exclusive formation of gold nanotriangles (Figure 5.2A-D); however, they can be separated and purified very efficiently by repeated centrifugation and redispersion of the pellet that settles during centrifugation. Figure 5.3A shows the UV-vis-NIR spectra of the gold nanotriangle solution synthesized at 20 ^{o}C before (curve 1) and after purification by repeated centrifugation and redispersion (4 cycles, curve 2). A comparison of these two curves shows that the ratio of intensities of the longitudinal SPR band at 1050 nm to the transverse SPR band at 510 nm increases after repeated centrifugation and redispersion. This indicates that the fraction of gold nanotriangles in solution has increased and it is indeed 'purified'. The enhancement in population of the gold nanotriangles is unequivocally seen in the TEM image recorded from the purified solution (Figure 5.3B).

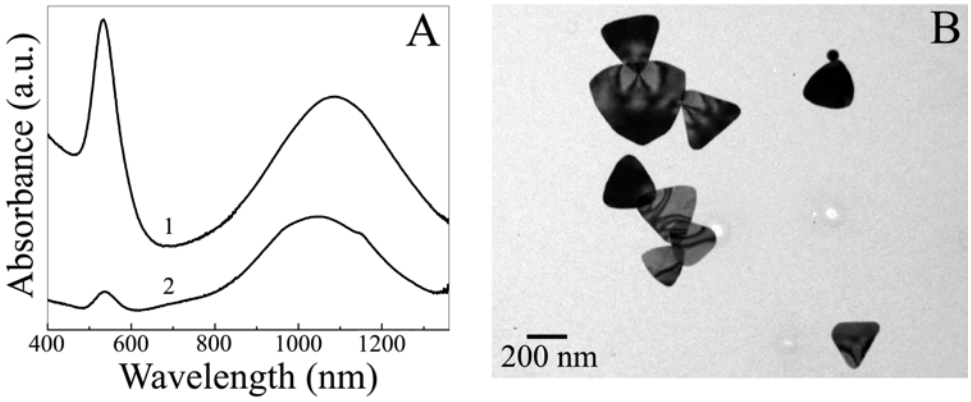

Figure 5.3: *A) UV-Vis-NIR absorption spectra of citrate reduced gold nanoparticles synthesized at 20 ^{o}C (curve 1) and after separating the gold nanotriangles (curve 2) from spherical gold nanoparticles by repeated centrifugation and redispersion of the settled pellet. B) Representative TEM image of the purified citrate reduced gold nanotriangles (corresponding to curve 2 in A).*

5.3.2 Growth kinetics of gold nanotriangles during room temperature synthesis:

The morphological evolution of the gold nanoparticles synthesized in the room temperature citrate reduction experiment was followed by time-dependent TEM studies, representative images of which are shown in Figure 5.4. After 10 min of reaction (Figure 5.4A), a large number of irregularly shaped particles are seen that range in size from 50 nm to 150 nm. At higher magnification (Figure 5.4B1-B4), the nanoparticles are observed to possess a fibrous structure with a semblance of triangular morphology.

Surprisingly, very few spherical particles could be found at this initial stage of reaction. This indicates that the rate of nucleation is not high and the initially formed nuclei tend to grow instead of forming fresh nuclei. More interestingly, the nuclei appear to grow two dimensionally. We recall that the SP band from the nanoparticles was extremely broad

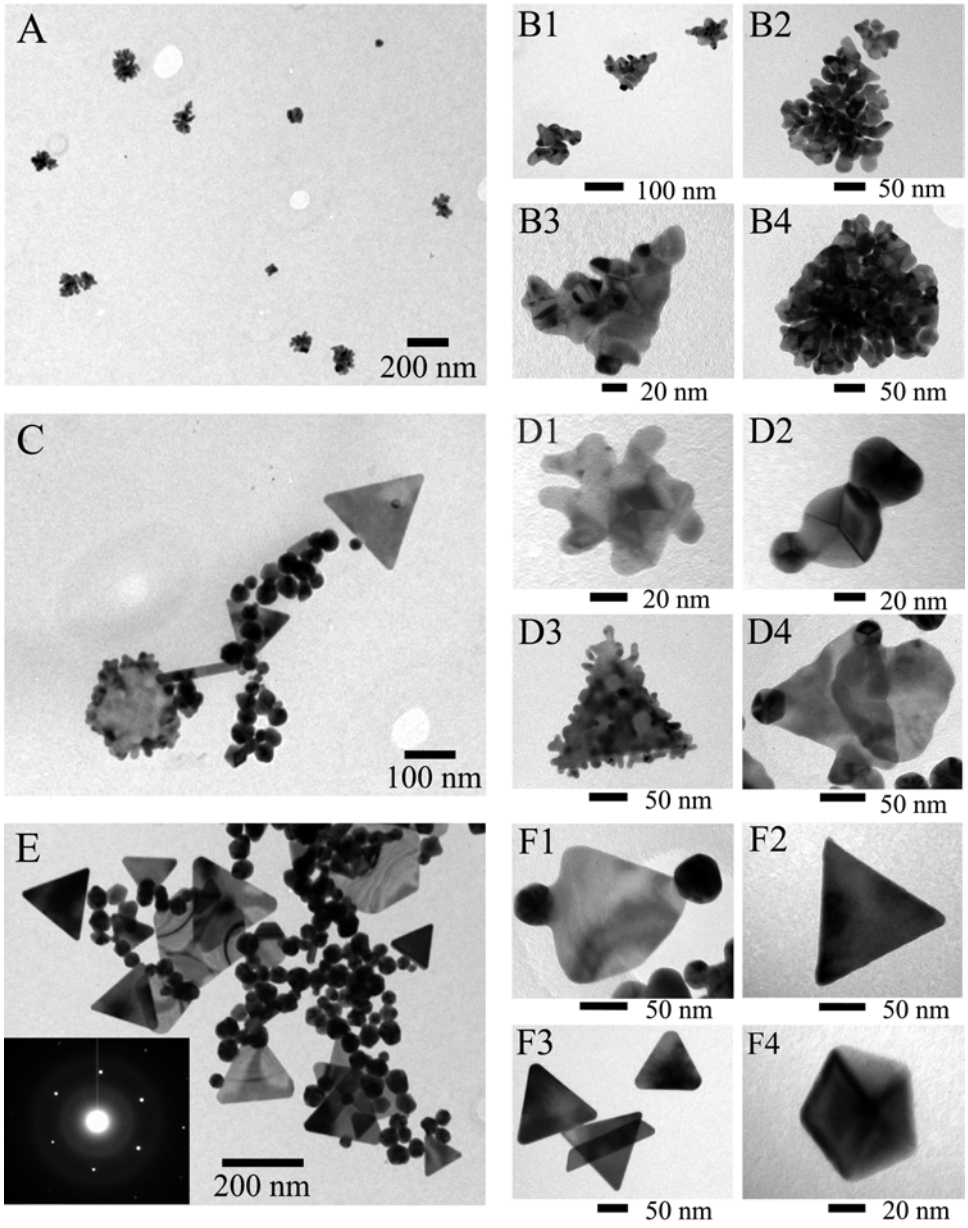

Figure 5.4: *Representative TEM images from nanoparticles synthesized in the room temperature citrate reduction of aqueous gold ions at various times of reaction. A), C) and E) : Low magnification images at 10 min, 1 h and 6 h respectively. The inset in E is the SAED pattern from a fully formed nanotriangle. High magnification TEM images – B1-B4 : 10 – 20 min; D1 -D4 : 30 min – 1 h; F1-F4 : 2 – 6 h.*

and weak after 10 min of reaction (inset, Figure 5.1B); these irregular structures could be responsible for the observed absorption at 625. After 1 h of reaction (Figure 5.4C), much bigger particles are seen that present a variety of morphologies. Well-resolved spherical particles together with triangular, hexagonal and a small amount of rod-like particles are observed at this stage. The higher magnification images of the gold nanoparticles in the reaction time interval 30 min – 1 h are quite revealing. At the center of one irregularly shaped particle in Figure 5.4D1, the pentagonal outline of a multiply twinned decahedral structure can be seen on careful observation. Such multiply twinned nanoparticles were not observed at earlier stages of reaction (Figure 5.4A,B). Figure 5.4D2 shows the growth of two particles from a well-defined multiply twinned decahedral particle. One of the particles is of triangular morphology while the other one is quasi-spherical. This image reveals again the propensity of the multiply twinned particle to grow two dimensionally and could possibly be acting as a seed for the growth of nanotriangles. Indeed, that the multiply twinned particles could be seeds for the growth of the nanotriangles is very clearly seen in the image of triangle shown in Figure 5.4D4, where two multiply twinned particles are observed at two of the vertices of the larger triangle in the image. In addition to the almost regular gold nanotriangles in Figure 5.4D4, we also observe highly irregular but triangular structures (Figure 5.4D3) that in many ways resemble the structures formed at the initial stages of reaction (Figure 5.4A,B). This suggests that the irregular nanotriangles (Figure 5.4D3) evolve into well-defined equilateral triangles with time (Figure 5.4D4) either via a seed-mediated mechanism or by a room temperature annealing process. The growth of gold nanorods with decahedral multiply twinned particles as seeds has been explained previously by invoking ion transport along defect directions in the twinned structure [13]. In the case of nanotriangle growth, the process involving twinned particles is likely to be much more complex given that at completion of the reaction, each one of the triangle is a single crystal. Indeed, the complexity of the process related to triangle growth is highlighted by nanostructures such as those shown in Figure 5.4D3 that clearly possess a triangular morphology but show no evidence of multiply twinned particles within their manifold.

As the reaction proceeds to completion, the triangular particles growing out of the irregular fibrous nanoparticles (Figure 5.4F1) are fully transformed into regular and well

faceted triangular particles (Figure 5.4E,F2,F3) that are single crystalline and [111] oriented (SAED pattern, inset of Figure 5.4E). The red-shift in the longitudinal SP vibration band of the gold nanoparticles (Figure 5.1B) during the initial stages of particle formation supports the above mode of growth, i.e. the smaller irregular planar structures tend to form larger and more regular triangles with time of reaction. The small blue-shift in the longitudinal SP band at the latter stages of growth of gold nanotriangles might possibly be an indication of thickening of gold nanotriangles, leading to a decrease in its aspect ratio. During growth of gold nanotriangles, the particles that do not grow in a planar fashion, grow without any preferred orientation to form faceted (almost spherical) particles or multiply twinned decahedrons (Figure 5.4F4). It may be noted here that the decahedral gold nanoparticles are also bound by {111} facets [14]. This further indicates a high preference for formation of gold nanoparticles bound by {111} set of planes under the above mentioned reaction conditions.

The tendency to form large triangles in addition to radially growing spherical particles depending on the reaction temperature may be explained on the basis of variation in the nucleation and growth rate of the gold particles. At higher reaction temperature, the rate of nucleation would be expected to be high [1a,b]. Low rates of nucleation at lower temperatures and a delayed growth process would possibly facilitate crystal formation with specific crystallographic orientations, thus leading to anisotropic structures. Under high rates of reduction, the rapid creation of fresh nuclei would consume gold atoms that would otherwise deposit on existing nuclei. The preference for two dimensional growth of gold nanoparticles to form [111] oriented triangular particles at lower temperatures is intriguing and at this point, not understood. Though the {111} set of planes are known to be the most stable faces in fcc crystals, the formation of thin triangular gold nanoparticles with extended (111) faces indicates inhibition of crystal growth along certain [111] directions. This inhibition of growth along certain [111] directions could arise from surface complexation of any of the following species present in the nanoparticles growth medium: excess unoxidized citrate ions, acetonedicarboxylate ions (product of citrate ion oxidation) and their further oxidation products viz. formic acid, formaldehyde and CO_2 [1a] and/or chloride ions (from the $AuCl_4^-$ ions). It is well known that Cl^-, Br^- and I^- ions very efficiently chemisorb on the surface of gold and that

while bromide and iodide ions are capable of replacing chloride ions from the surface of gold, fluoride ions do not [5]. Further discussion on the oriented growth of the gold nanoparticles to attain triangular shape is continued below during the study of the reduction of $HAuCl_4$ in presence of different halide ions.

5.3.3 Growth of gold nanoparticles in presence of Halide ions:

Figure 5.5A shows the UV-Vis-NIR spectra of citric acid reduced gold nanoparticle synthesized at room temperature (27 ^{o}C) in the absence (dotted curve) and presence of different potassium halides (Au : KX, 1 : 1, X=F, Cl, Br, I). The as-prepared solution (dotted curve) shows two distinct absorption bands centered at 528 nm (transverse SPR band) and 865 nm (longitudinal SPR band) and have been discussed in detail earlier. Representative TEM images recorded from the different reactions are shown in Figure 5.5B-F. On carrying the reaction in the presence of KF, only a small blue shift of the in-plane SP vibration band relative to the nanoparticles prepared in the absence of halide was observed (Figure 5.5A). The size and shape of the gold nanotriangles formed in the absence (Figure 5.5B) and presence of KF (Figure 5.5C) are essentially similar and thus in agreement with the UV-vis-NIR results. The presence of KCl in the reaction medium results in a large red-shift of the in-plane SP vibration band from 865 nm to 1125 nm (Figure 5.5A). The TEM image of the gold nanotriangles formed in the presence of KCl (Figure 5.5D) shows that the gold nanotriangles are indeed larger than those obtained in the control experiment (Figure 5.5B, absence of halide ions) and have an average edge length of ~ 270 nm as compared to ~ 160 nm in the control experiment, indicating that their formation is being favored in this condition. The synthesis of gold nanoparticles in the presence of KBr or KI leads to a significant or complete suppression of formation of gold nanotriangles (Figure 5.5E and F respectively). Some small flat gold nanoparticles are formed in presence of KBr (Figure 5.5E) and explains the presence of a significantly reduced and red-shifted surface plasmon absorption band at ca. 760 nm (Figure 5.5A). The gold nanoparticles formed in the presence of KI are almost all spherical with no noticeable faceting (Figure 5.5F), again consistent with the UV-vis-NIR spectrum recorded from this sample that shows just a single absorption band centered at 555 nm (Figure 5.5A). From the TEM images of these gold nanoparticles, a small percentage of aggregates were also observed (inset of

Figure 5.5F). Similar aggregates were observed by Cheng et. al. in their study of the effect of aqueous KI solution on the morphology of spherical citrate reduced gold nanoparticles solution (synthesized under boiling conditions) [7].

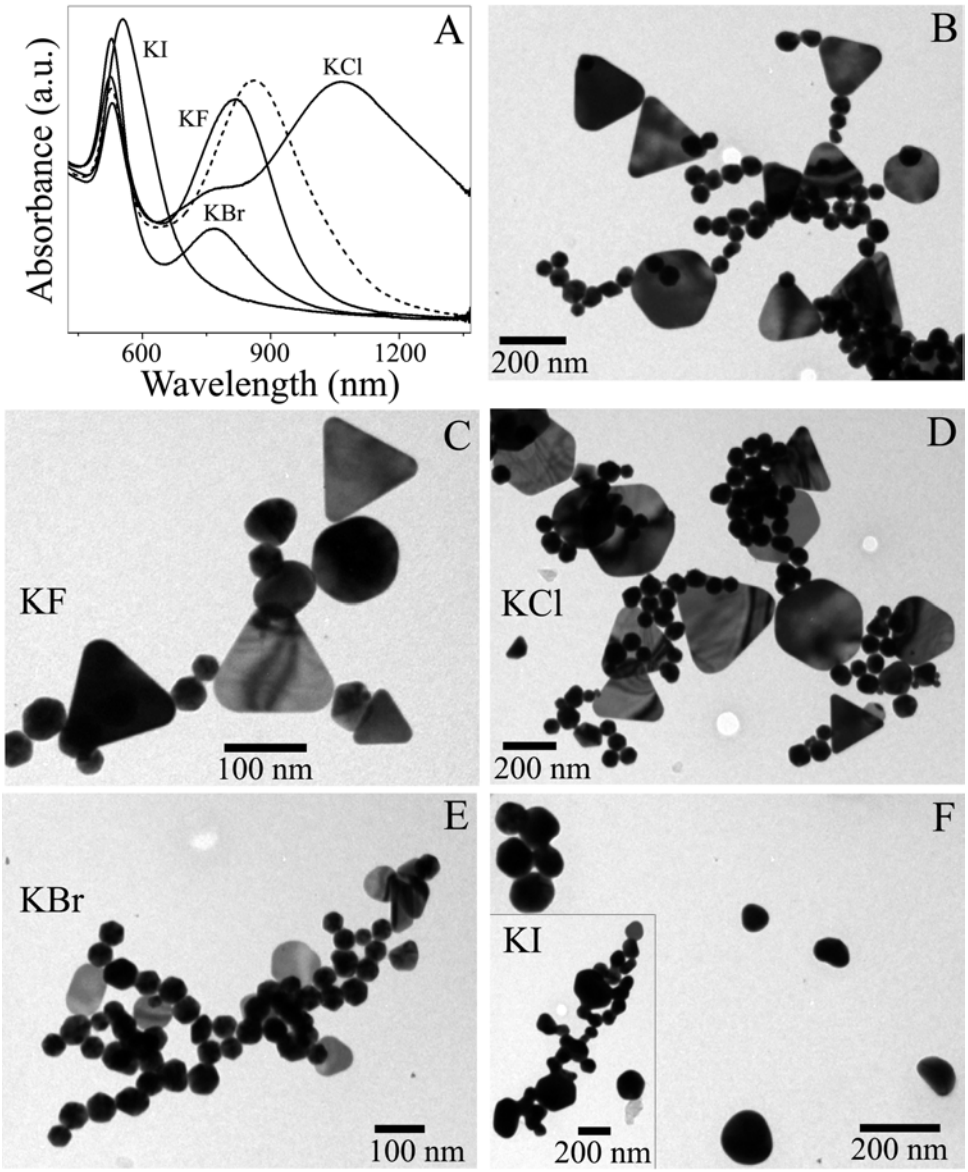

Figure 5.5: *A) UV-vis-NIR spectra of citric acid reduced gold nanoparticles synthesized at 27 ^{o}C in the presence of different potassium halides (KX, X = F, Cl, Br and I). The dotted curve corresponds to citric acid reduced gold nanoparticles synthesized in the absence of a halide. Representative TEM images of citric acid reduced gold nanoparticles synthesized at 27 ^{o}C in : B) the absence of a halide and in the presence of C) KF, D) KCl, E) KBr and F) KI. The inset in F shows an aggregate of gold nanoparticles grown in the presence of KI.*

A chemical analysis of the gold nanoparticles synthesized in the absence and presence of different halide ions was carried out using XPS. The pellet of the particles obtained by centrifugation were washed throughly prior to casting in thin film form for XPS analysis on Si substrate. While a very weak Cl 2p signal was recorded from the gold nanotriangles synthesized in the absence of halide ions [Figure 5.6A] and clearly is due to Cl^- ions produced during reduction of aqueous $AuCl_4^-$ ions, a stronger Cl 2p signal was obtained from the nanoparticles synthesized in the presence of KCl [Figure 5.7A]. The additional Cl^- coverage of the gold nanotriangles in this experiment thus seems to play crucial role in promoting nanotriangle formation (Figure 5.5D). The low intensity of the 2p core level of Cl species can be attributed to its low photoemission cross-section. The Au 4f core level signal in the citric acid reduced gold nanoparticles showed the presence of two chemically distinct spin-orbit pairs centered at 84 and 85.7 eV binding energy [Figure 5.6B] that corresond to Au^0 and Au^+ species respectively from the core and surface

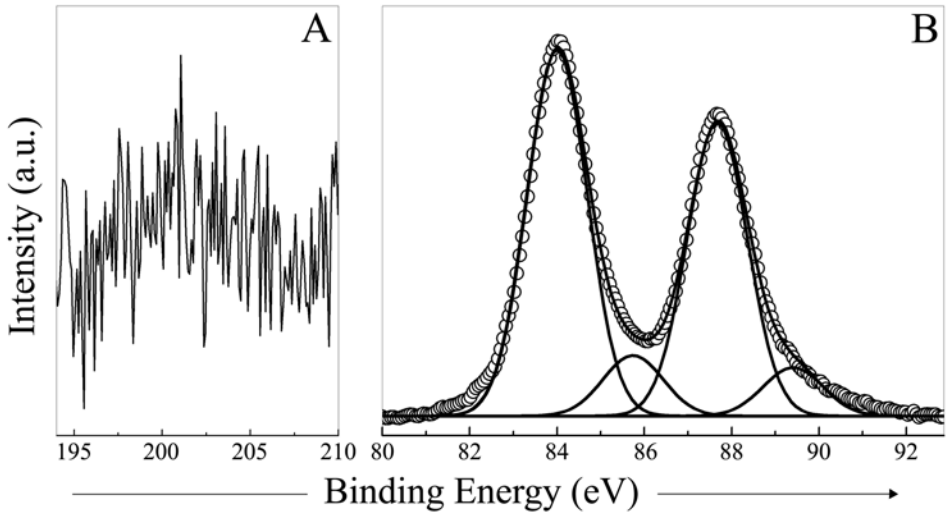

Figure 5.6: *XPS spectra of A) Cl 2p and B) Au 4f core levels from citric acid reduced gold nanoparticles synthesized at room temperature in the absence of halide ions.*

bound ionic species. Reasonably strong Br 3d and I 3d signals were observed in the gold nanotriangles prepared in the presence of KBr and KI respectively [Figure 5.7B and C] and the F 1s signal was below detection limits [Figure 5.7D] for gold nanoparticles synthesized in presence of KF. These results are consistent with the gold nanoparticle

morphology variation observed in the TEM images; the presence of Br^- and I^- ions changes the morphology and optical properties significantly relative to the control particles (Figure 5.5A, B, E, F) while F^- ions do not cause any such considerable changes (Figure 5.5A, B, C).

The effect of different halide ions on the morphology of gold nanoparticles synthesized by citric acid reduction may possibly be rationalized as follows. F^- ions are not known to chemisorb on the surface of gold nanoparticles [5] and would therefore be

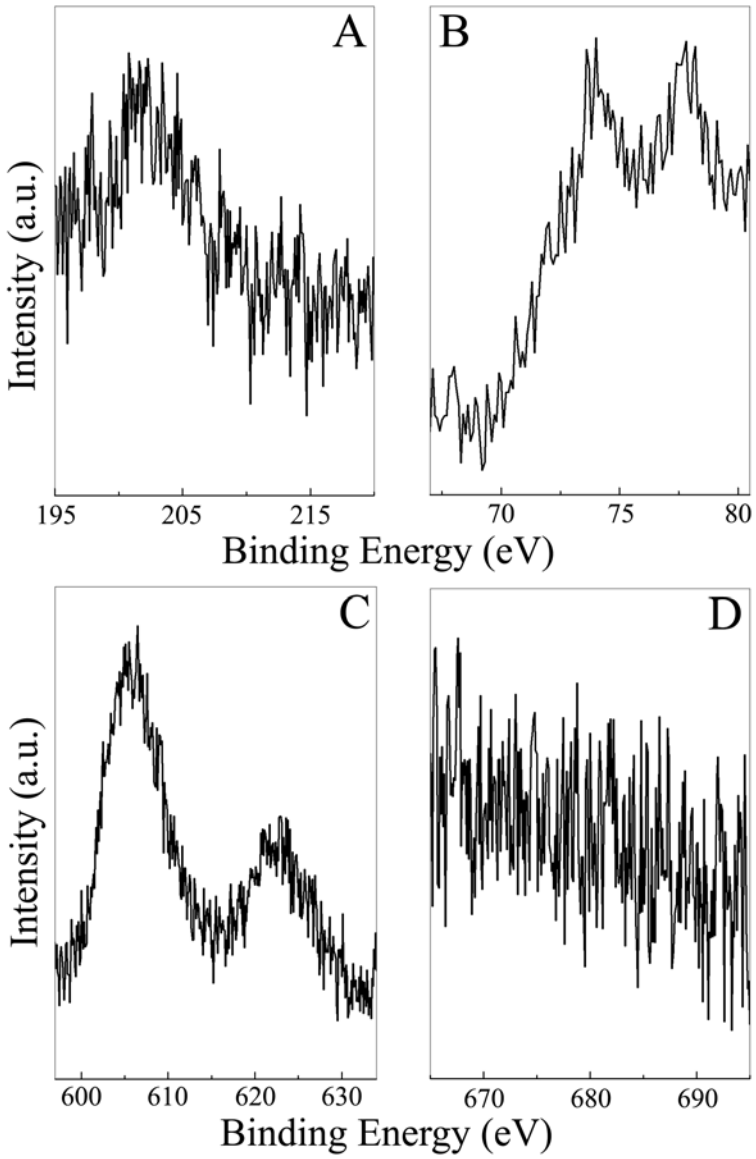

Figure 5.7: *XPS spectra of A) Cl 2p, B) Br 3d, C) I 3d and D) F 1s core levels from citric acid reduced gold nanoparticles synthesized in presence of KCl, KBr, KI and KF respectively at room temperature.*

incapable of influencing any significant change in either the size or mophology of the gold nanoparticles synthesized in their presence. This is consistent with the observations derived from the XPS, UV-vis-NIR and TEM analysis. On the other hand, Cl^-, Br^- and I^- ions have the ability to chemisorb on the Au surface, forming Au-X bonds with force constants in the order I > Br > Cl [5,15]. The inability of F^- ions and the ability of Br^- and I^- ions to compete with gold-surface bound Cl^- ions in complexing with the surface of gold could be because of their comparative ligating ability. This could also be the reason why molecules to functional groups that have better polarizability (thiols, phosphines,etc.) and charge transfer ability are able to interact with the surface of the gold nanoparticles as compared with molecules bearing other functional groups viz. alcohols [16]. That the Cl^-, Br^- and I^- ions are present on the gold nanoparticles formed in their presence is clearly indicated in the XPS measurements (Figure 5.6 and 5.7). The structure of the adlayers of Cl^-, Br^- and I^- ions on the Au surface has been well

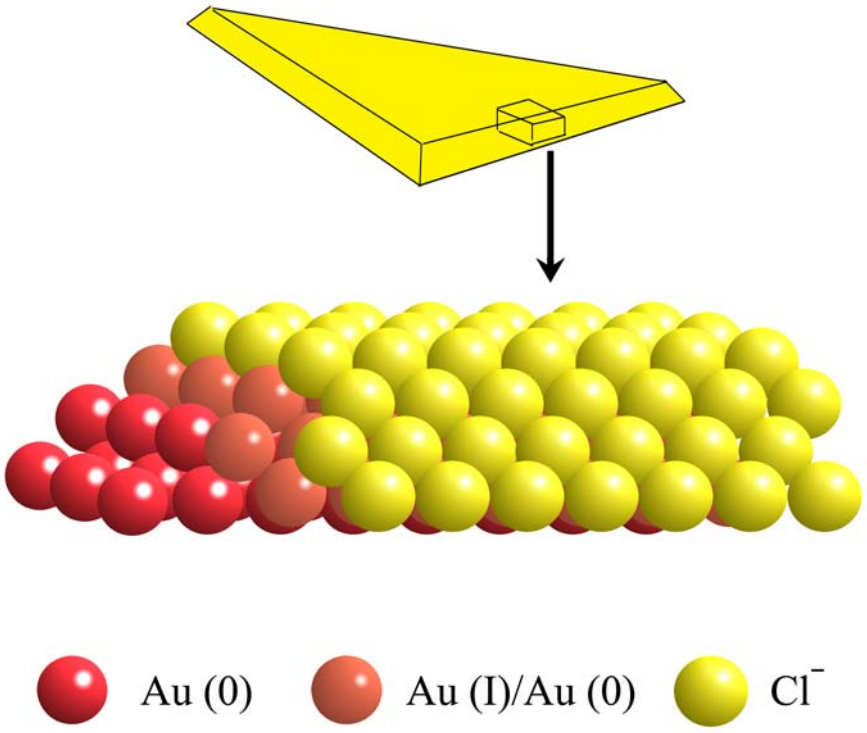

Scheme 5.1: *Schematic showing the probable structure at the surface of gold nanotriangles with an adlayer of Cl^- ions above the faces forming the triangular gold single crystal. The complete surface coverage with Cl^- ions is an ideal representation excluding the presence of citrate ions and its oxidation products that could in reality be existing in a small percentage in direct coordination with the surface gold atoms.*

characterized [17]. It is reported that all the three halides form an incommensurate adlayer on gold (no lateral registry). Among these halides, Cl^- and Br^- ions form a hexagonal-close-packed adlayer of which the Cl^- adlayer is better aligned with the underlying Au (111) lattice plane. The slight mismatch between the Cl^- adlayer and the underlying atomic Au (111) lattice planes might cause some residual strain at the surface and lead to the development of defects like twin planes, few atomic layers below them, in order to facilitate relaxation in the lattice structure. The development of these twin plane defects might possibly be playing the crucial role in directing the two dimensional growth of gold nanoparticles as demonstrated by Lofton and Sigmund [18], instead of a more favorable octahedron shape with all {111} faces. Apart from the two dimensional growth, the ultimate formation of triangular and hexagonal shapes are a result of the geometrical constraints of the stable crystallographic lattice planes forming the edges of the <111> oriented flat fcc crystals. The planes forming the facets at the edges are reported to be from among the {111} and the next stable {100} set of planes [19]. Similar preference for the formation of triangular gold nanoparticles in the presence of Cl^- ion as a counter ion for the cationic surfactant has been reported by Murphy and co-workers [20]. Based on these inferences the probable structure of the gold nanotriangles at the surface is shown in Scheme 5.1 wherein a surface monolayer of Cl^- ions bound to the gold surface through an intermediate layer of Au(1) species is depicted. It may be noted that the schematic is an idealized representation and the surface would in fact have complexed citrate ions and other oxidation products of citric acid in addition to the Cl^- ions, the major shape directing agent. The I^- ion adlayer has the largest mismatch with the Au (111) lattice plane compared with other halides and would thus be highly strained to an extent that it dose not favor the formation of (111) faces. We believe this might ultimately prevent two dimensional growths of the nuclei, leading to nanoparticles with spherical morphology (Figure 5.5F). It may be noted that the gold nanoparticles formed in presence of I^- ions lack any proper faceting (Figure 5.5F) unlike in other cases. Further, the aggregated structures observed in presence of I^- ions can be attributed to the increased covalency of the Au–I bond [7,15] leading to lower surface charge and consequent instability of the gold nanoparticles. Br^- ions have an intermediate mismatch [17] and also since they do not have as strong affinity as I^- ions to replace the surface

bound Cl^- ions [5,15], a complete suppression of gold nanotriangles formation is not observed. We recollect that for such halide-mediated gold nanoparticle shape control to happen, a delayed growth rate is essential that is facilitated at low temperatures and by slow reduction rates of the $AuCl_4^-$ ions.

5.3.4 Morphological transformations induced by the halide ions on preformed Au nanotriangles:

Figure 5.8A shows the UV-Vis NIR spectra of citric acid reduced gold nanoparticles solution synthesized at room temperature (27 ^oC) and after addition of 2 mL of 10^{-3} M potassium halide solutions separately to 20 mL of it. The spectra of citric acid reduced gold nanoparticles solution was taken after adding appropriate amount of water to account for the dilution. The as prepared solution had two absorption bands at 531 nm (out-of-plane SPR component) and 949 nm (in-plane SPR component)

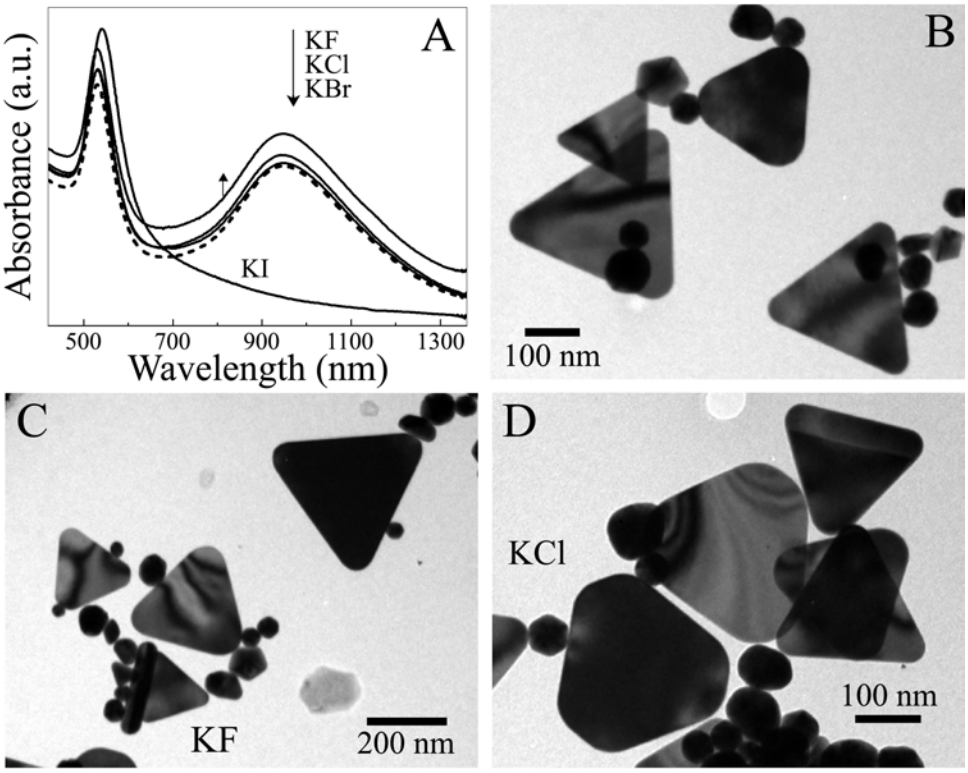

Figure 5.8: *A) UV-vis-NIR spectra of citric acid reduced gold nanoparticles synthesized at 27 ^oC (dotted curve) and of the same solution after addition of different potassium halides as indicated. The curve corresponding to addition of KF aqueous solution has been shifted upwards, indicated by a small upward arrow for clarity of the spectra. TEM of B) citric acid reduced gold nanoparticles synthesized at 27 ^oC, after addition of C) KF and D) KCl aqueous solutions.*

represented by dotted curve in Figure 5.8A. On treatment of citric acid reduced gold with KF, KCl or KBr aqueous solutions, no marked difference in the UV-vis-NIR spectra and only a small increase in the intensity of the absorbance of the transverse and longitudinal SPR band could be observed without any shift in the peak positions in case of added KF or KCl (Figure 5.8A). Dramatic changes in the UV-vis NIR spectra of the citric acid reduced gold were observed after addition of aqueous KI solution. The absorbance peak at 949 nm (longitudinal SPR component) was completely suppressed and the absorbance peak at 531 nm was red shifted to 540 nm and increased considerably in intensity, resembling the usual absorbance spectra obtained for spherical gold nanoparticles. This result is surprisingly in contrast to the changes in UV-Vis NIR spectra observed by Cheng et. al. on addition of aqueous KI solution to citrate reduced spherical gold solution, where they observe an appearance of a new absorbance band at higher wavelength [7].

Figure 5.8B is a representative TEM image of the gold nanoparticles synthesized by citric acid reduction at room temperature (27 ^{o}C). It is observed that the triangles formed posses' well-defined faceted edges with some degree of curvature at the vertices. Addition of aqueous solutions of KF and KCl did not show any noticeable changes in the shape of the gold nanoparticles as observed from TEM images shown in Figure 5.8C and D respectively. This was also evident from the UV-Vis NIR spectra for above-mentioned two cases. The small increase in intensity of absorbance could be merely a result of change in ionic strength and change in ionic atmosphere around the gold nanoparticles leading to a change in the charge density around it on addition of aqueous solutions of KCl and KF. The TEM images of citric acid reduced gold nanoparticles solution after addition of aqueous KBr solution showed some interesting features (Figure 5.9A,B). The triangular particles after exposure to KBr were observed to have undergone some noticeable changes in the morphology; the edges of the planar particles were now more irregular and had lost the faceted structure at the edges observed before exposure to KBr. The KBr solution thus seems to be able to specifically interact more with the edges of the gold nanotriangles as shown in Scheme 5.2 depicting the preferential chemisorption of Br^{-} ions at the edges as opposed to the flat (111) faces of the gold nanotriangles. The edges of the triangles, as discussed before are bound by the (110) and (111) faces [19]. It

appears that the Br^- ions have better chemisorption on the (110) planes as compared to Cl^- ions as is also evident in the gold nanorods formation [21]. A clear indication to this effect comes from the observation that even with the same surfactant chains better nanorods bound by {110} set of planes along their length are formed in presence of Br^- rather than Cl^- as counter ions [21c]. With citric acid synthesized gold nanotriangles, the Br^- ions after preferential absorption on the edges are observed to induce reconstruction leading to the deformation of the well faceted triangular morphology to form disc like or ill faceted triangles. The inability to observe any significant UV-vis-NIR spectral changes (Figure 5.8A) in spite of the morphological changes observed from TEM analysis might imply that the observed distortion of the edges does not lead to much change in the net lateral dimensions and in the thickness of the gold nanotriangles. Figures 5.9C and D show representative TEM images of citric acid reduced gold nanoparticles after addition

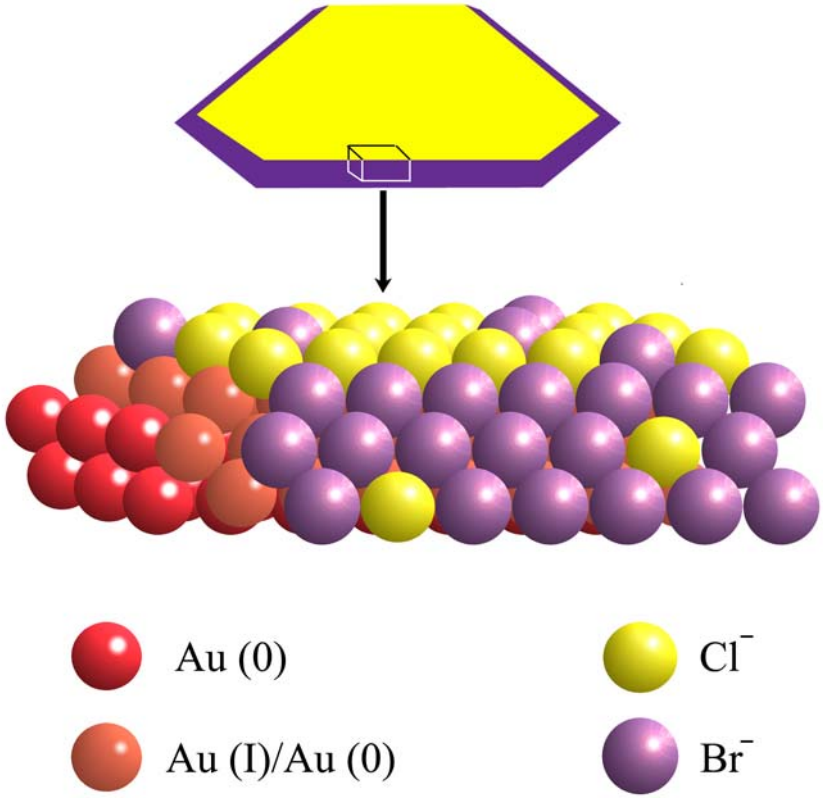

Scheme 5.2: *Schematic showing the probable structure at the surface of the citric acid reduced gold nanotriangles and hexagons after treatment with aqueous KBr solution. A preferential chemisorption of Br^- ions replacing the preexisting Cl^- ions adlayer at the edges of the triangular and hexagonal gold single crystals is proposed, that eventually are supposed to distort the edges.*

of aqueous KI solution. As can be predicted from the corresponding UV-vis NIR spectra (Figure 5.8A), all the nanoparticles observed were nearly spherical. On a careful observation, it may be observed that almost all the deformed gold nanoparticles lack

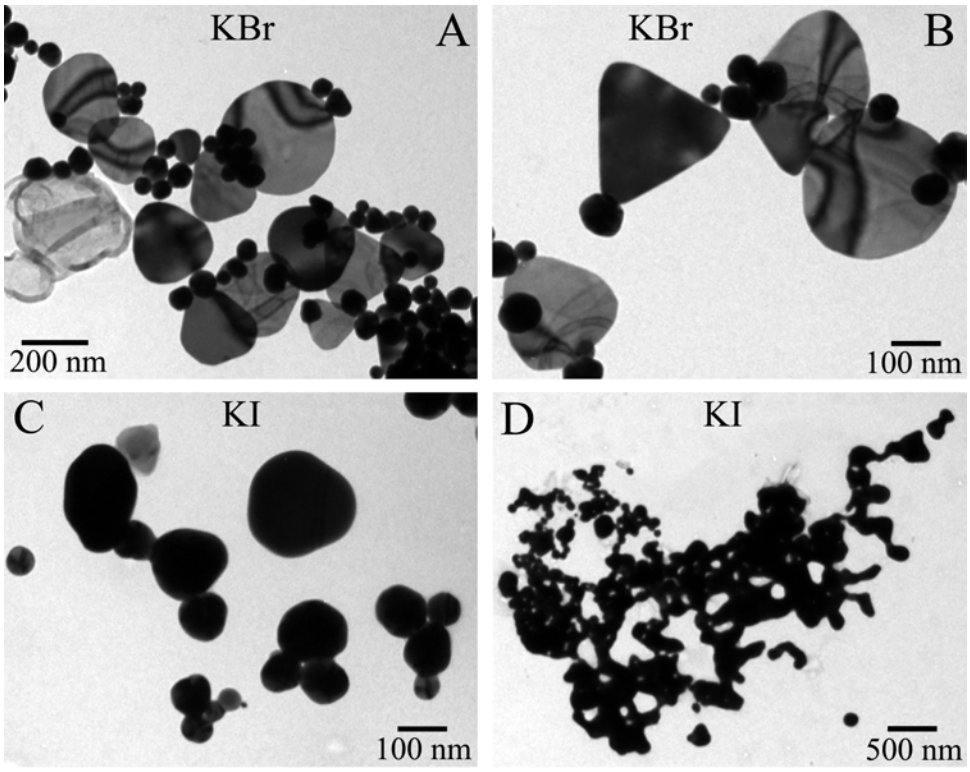

Figure 5.9: *TEM of citric acid reduced gold nanoparticles synthesized at 27 ^{o}C, two days after addition of A and B) aqueous KBr solution, C and D) aqueous KI solution*

proper faceting and have more rounded curvatures similar to gold nanoparticles synthesized by citric acid reduction in presence of KI (Figure 5.5F). Among all the halides, I^- ions are reported to have highest mismatch with the (111) lattice of gold and thus would be expected to develop considerable strain on the surface inducing deformation as shown in Scheme 5.3. In fact, I^- are known to induce surface reconstruction even in case of bulk gold [17d]. Since, gold nanotriangles are only few nm thick, the strain developed at the surface due to the chemisorbed I^- ions translates throughout the crystal and leads to complete change in the morphology of the triangular particles. The larger size nanoparticles observed after exposure of citric acid reduced gold nanoparticles with KI solution are possibly the triangular gold nanoparticles that have undergone drastic change in morphology. It is also observed that many of the

nanoparticles exist in the form of small aggregates along with occasional observation of very large aggregates (Figure 5.9D) similar to the report of Cheng et. al. [7]. The aggregates observed can be explained on the basis of lowered surface charge, i.e. ζ potential, due to adsorbed I^- [7,15] as discussed earlier about the aggregation observed in gold nanoparticles synthesized in presence of KI.

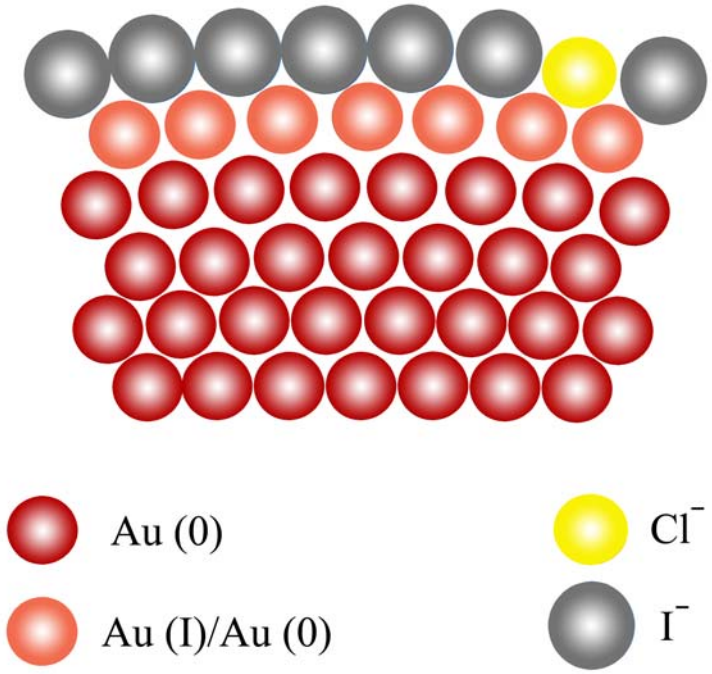

Scheme 5.3: *Schematic representing the distortion initiating at the topmost layers of gold nanotriangles and hexagons due the strain developed between the I^- ions adlayer and the underlying Au lattice as a consequence of their considerable lattice mismatch. This strain is believed to propagate throughout the underlying atomic layers of the thin gold nanotriangles and hexagons leading to their complete morphological transformation in an attempt to relieve the strain.*

Isothermal calorimetric (ITC) measurements were carried out to study the binding efficiencies of different halide ions during addition of corresponding potassium halides to citric acid reduced gold nanoparticles solution. Figure 5.10A-D show the ITC data obtained during addition of aqueous KF, KCl, KBr and KI respectively. Addition of aqueous KF solution shows a large endothermic reaction that decreases linearly with successive injections (Figure 5.10A), with KCl solution only a very low endothermicity is observed (Figure 5.10B). Addition of aqueous KBr solution leads to an initially small

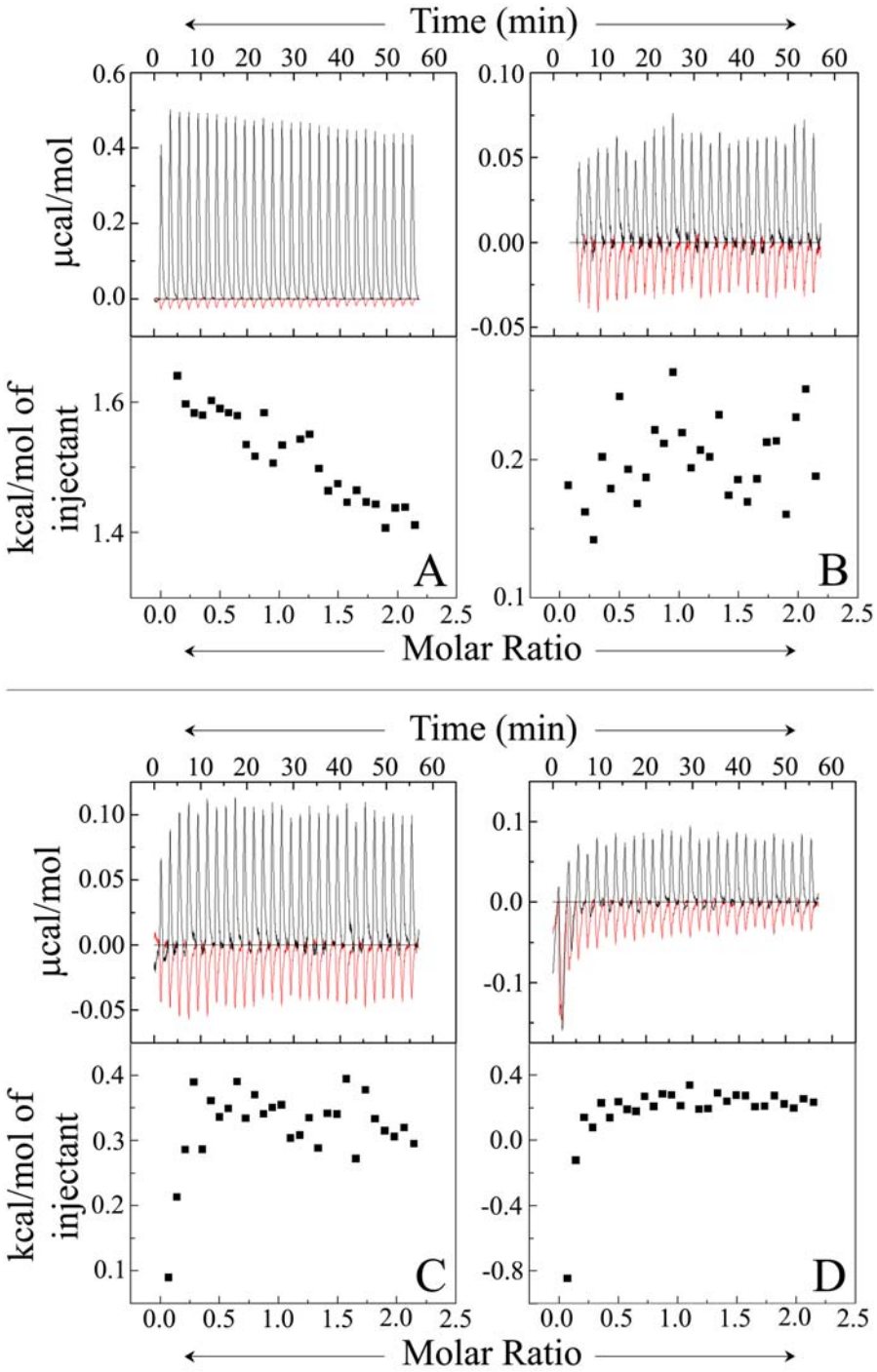

Figure 5.10: *Isothermal titration calorimetric data recorded during successive injections of 10 µl aqueous 10^{-3} M solutions of A) KF, B) KCl, C) KBr and D) KI into the titration cell containing 1.47 ml of aqueous citric acid reduced gold nanoparticles synthesized at 27 ^{o}C. The data in red corresponds to the ITC response recorded during titration of potassium halide solutions against deionized water to account for dilution effect. The lower frame shows the binding isotherm obtained by integration of the raw data shown in the upper panel after conversion of the reacting potassium halide and aqueous citric acid reduced gold nanoparticles to molar ratio in the titration cell.*

endothermic reaction, magnitude of which increases within the first few injections and is nearly constant thereafter (Figure 5.10C). On the other hand addition of aqueous KI solution led to an initial exothermic reaction that decreased in the first few injections and was again followed by an endothermic reaction in the successive injections (Figure 5.10D). Endothermic reactions indicate the occurrence of entropically favored process whereasexothermic reactions indicate formation of enthalpically favored processes, possibly, by formation of more stable bonds.

On comparing the TEM and the ITC results, few conclusions could be made as follows. In case of addition of aqueous KF solution no noticeable changes have been observed in the morphology of the gold nanoparticles but an endothermic reaction is inferred from the ITC measurements. This may imply that the F^- ions instead of binding to the surface of gold nanoparticles as has been observed by others [5], merely modifies the composition of the diffused double layer around the gold nanoparticles as an entropically favored process leading to the endothermic energy change. On similar grounds it may be claimed that the very low endothermicity observed on addition of KCl solution is due to the minimal variations in the composition of the diffuse double layer around the gold nanoparticles as the Cl^- ions are already present in the solution. In case of addition of aqueous KBr solution to citric acid reduced gold solution an overall endothermic process is observed. However, the endothermic values in the first few injections are very low and could be a net outcome of an exothermic and endothermic process. The exothermic process being the replacement of the surface chemisorbed Cl^- ions by the Br^- ions [5]. The endothermic process being the same as in the former cases. The exothermic process is more prominently observed on adding KI solution to the citric acid reduced gold nanoparticles solution. The high exothermicity clearly indicates the strong affinity of the I^- ions towards chemisorption on the gold nanoparticles surface by replacement of the existing Cl^- ions [5,15], which varies as $I^- > Br^-$.

It thus seems very likely that the citric acid reduced gold nanoparticles have Cl^- ions directly chemisorbed to their surface to a large extent. These Cl^- ions are possibly interacting with the gold nanoparticles through the surface bound Au^+ species as evident from the XPS measurements. The extent of replacement of the chemisorbed Cl^- ions by

the Br^- and the I^- ions seem to occur with an efficiency depending on the force constants of the Au-X bond [5,15].

Through these studies we have tried to draw attention towards the important role of halide ions on the shape of gold nanoparticles. The influence of halide ions has been explained on the basis of possible formation of a close packed adlayer on different crystallographic faces of fcc gold as compared to relatively larger sized anionic molecules *viz*. citrate anions or the acetonedicarboxylate anion and other oxidation products of citric acid. The molecular anions in the citric acid reduced gold nanoparticles are possibly restricted largely to the diffuse double layer around the particle.

5.4 Laser induced morphological transformations in gold nanotriangles.

To study the effect of laser irradiation, gold nanotriangles synthesized using lemongrass leaf extract were used. Since the wavelength of the output pulse of the Nd-YAG laser was 1064 nm and the gold nanotriangles solution exhibited its longitudinal SPR band centered at 1200 nm (dotted curve Figure 5.11A) high degree of absorption can be expected on laser irradiation. The choice of using lemongrass reduced gold nanotriangles was based on the convenience in using small quantities of highly

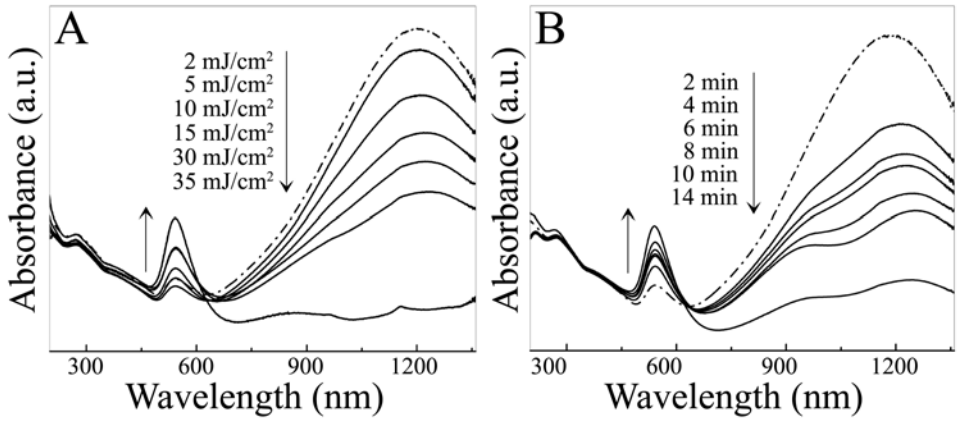

Figure 5.11: *UV-vis-NIR spectra of the lemongrass leaf extract reduced gold nanotriangles after irradiation using 20 ns laser pulses of wavelength 1064 nm by A) varying the fluence in the range 2 – 35 mJ/cm^2 while keeping the time of irradiation fixed at 5 min in each case. B) varying the time of irradiation in between 2 to 14 min as indicated keeping the laser fluence constant at 30 mJ/cm^2. The dotted curve in each figure corresponds to the unirradiated lemongrass leaf extract reduced gold nanotriangles solution. The small upward arrow in each figure indicates the increasing trend of the transverse SPR band, concurrent to the decreasing trend of the longitudinal SPR band.*

concentrated gold nanotriangles solutions without irreversible aggregation in cappilary tubes for further charectrization. The large intensity of the longitudinal SPR band relative to the transverse SPR band is a good indirect indicator of the presence of a large percentage of triangular gold nanoparticles as opposed to spherical gold nanoparticles. Figure 5.11A shows the change in the UV-vis-NIR spectra of the aqueous gold nanotriangles solution after irradiation with varying laser fluence in the range 2 – 35 mJ/cm^2 for 5 min. Irradiation with laser of fluence 2 mJ/cm^2 yielded very small changes in the UV-vis-NIR spectra while a near complete loss in the longitudinal SPR band was observed on irradiation with laser of fluence 35 mJ/cm^2. For intermediate laser fluences, the loss in the intensity of the longitudinal SPR band was proportional to the increasing laser fluence. A gradual decrease in the longitudinal SPR band of the gold nanotriangles with increased fluence of the 1064 nm laser pulses was accompanied by a proportional increase in the absorbance of the transverse SPR band centered at 542 nm. The loss in the intensity of the longitudinal SPR band indicates a loss in the anisotropy of the gold nanoparticles. Laser irradiation experiments were also carried out by varying the time of irradiation on the aqueous gold nanotriangles solution. Figure 5.11B shows the variation in the UV-vis-NIR absorbance spectra of the gold nanotriangles solution on laser irradiation for different time durations between 2 to 14 minutes with constant fluence of

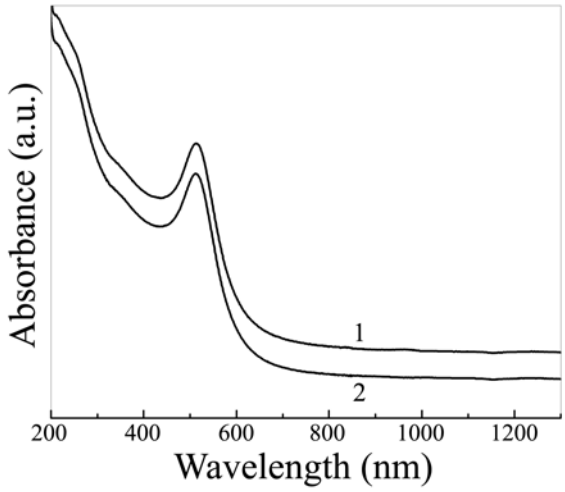

Figure 5.12: *UV-vis-NIR spectra of the spherical gold nanoparticles, synthesized by $NaBH_4$ reduction method, before (curve 1) and after (curve 2) irradiation using laser of pulse width 20 ns, fluence 30 mJ/cm^2 and wavelength 1064 nm for 15 min.*

30 mJ/cm^2. Analogous to the variation observed on changing the fluence of the laser pulses, longitudinal SPR band of the gold nanotriangles solution reduces in intensity with increasing time of irradiation. The concomitant increase in the absorbance at 542 nm as in the previous instance suggests the formation of spherical gold nanoparticles. As a control experiment, laser irradiation was done with gold nanoparticles synthesized by sodium borohydride reduction that yields only spherical nanoparticles with a single absorbance band in the visible region at 512 nm (curve 1, Figure 5.12) due to single mode surface plasmon resonance [12]. Since the $NaBH_4$ reduced spherical gold nanoparticles do not have any absorbance in the higher wavelength NIR region, no change in the UV-vis-NIR spectra was observed (curve 2, Figure 5.12) on irradiation with 30 mJ/cm^2 laser pulses for 15 min.

Figure 5.13A shows the TEM image of gold nanotriangles synthesized using lemongrass leaf extract. The gold nanotriangles with well faceted structure, largely with edge lengths in the range 100 – 300 nm are observed. Figure 5.13B – D show the

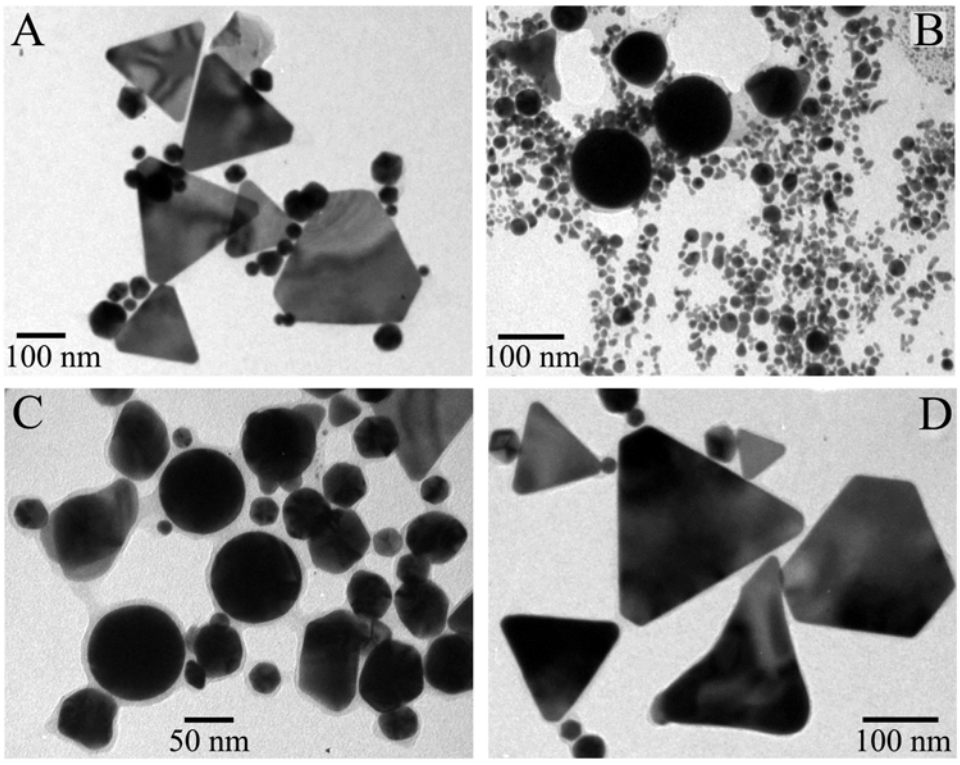

Figure 5.13: *TEM images of lemongrass leaf extract reduced gold nanotriangles A) before carrying out the laser irradiation experiment and B, C and D) after irradiation using laser of pulse width 20 ns, fluence 30 mJ/cm^2 and wavelength 1064 nm for 14 min.*

representative TEM images of gold nanotriangles solution after laser irradiation for 14 minutes with fluence 30 mJ/cm^2. After laser irradiation, a large number of completely spherical gold nanoparticles with size greater than 70 nm are observed (Figure 5.13B and D) along with many small gold nanoparticles of size less than 10 nm (Figure 5.13B). The observation of the large gold nanoparticles can be attributed to the melting of gold nanotriangles [8]. The presence of the small gold nanoparticles in the laser irradiated gold nanotriangles solution that were not observed prior to irradiation is attributed to the fragmentation of the gold nanotriangles accompanying their melting [8g,h]. The observed changes in the gold nanotriangles are similar to the changes occurring on exciting gold nanorods and silver nanotriangles by laser irradiation. Laser irradiation of nanoparticles have been explained to transfer energy to the electron gas mainly through excitation of the broad plasmon mode and the superimposed single electron modes [22]. In such irradiations the pump laser has been explained to induce a change in the electron energy distribution due to the formation of a low-density non-thermalized highly energetic electron population. The energy acquired by these electrons is equilibrated by electron-electron and electron-phonon relaxation modes. The electron thermallization is reported to usually occur in femotsecond time domain, while the thermallization of the hot electrons with the lattice by electron-phonon relaxation and interactions with the nanoparticle surface, as well as with defects and impurities (if present) has been reported to occur in the 1 – 3 picoseconds [22c,23]. Following these pathways the excess thermal energy in the nanoparticles is then removed by thermal diffusion toward the surrounding medium on a time scale of few tens of picoseconds. Finally, the whole ensemble of nanoparticle and medium reaches the initial temperature of the sample on a time scale of hundreds of picoseconds [22c,d,24]. Melting of the nanoparticles is believed to occur during the electron-phonon relaxation process that leads to lattice thermallization. Reckoning these time scales, El-Sayed and coworkers [8g] have concluded that gold nanorods on irradiation with nanosecond laser pulses will be continuously pumped with energy for a time longer than ~ 100 ps required for complete loss of heat to the surrounding medium through phonon-phonon relaxation. The nanosecond laser was thus reported to heat the lattice of nanorods continuously beyond the melting stage leading to their fragmentation [8g]. On similar grounds it may be explained that during laser

irradiation of gold nanotriangles with pulse width of 20 ns and 1064 nm wavelength, the particles having maximum absorbance at this wavelength gain maximum amount of energy resulting in their fragmentation. However, the gold nanotriangles exhibiting longitudinal SPR band away from the 1064 nm would not gain similar amount of energy and thus would only melt to form spherical particles instead of fragmenting. In addition, it is observed that the extent of fragmentation is not as extensive as with gold nanorods and a high percentage of completely spherical large gold nanoparticles can be observed. The total energy absorbed per particle has been reported to be proportional to its volume and the heat dissipation proportional to the total surface area [25]. Since a triangular gold nanoparticle has a greater surface to volume ratio as compared to nanorods it is expected to have greater tendency for dissipation of energy at a faster rate, explaining the observed lower percentage of their fragmentation. In Figure 5.13D a gold nanotriangle partially deformed under the influence of laser irradiation can be observed and appears that the melting is faster at the edges as compared to the tips of the gold nanotriangles.

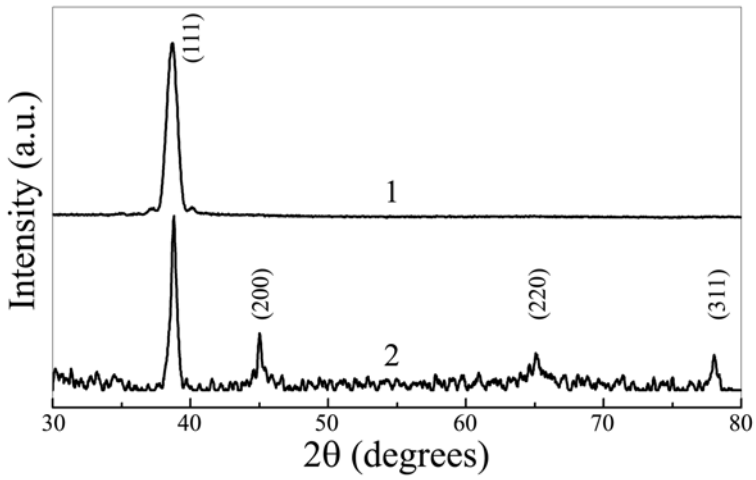

Figure 5.14: *XRD pattern of lemongrass leaf extract reduced gold nanotriangles before (curve 1) and after irradiation(curve 2) using laser of pulse width 20 ns, fluence 30 mJ/cm^2 and wavelength 1064 nm for 14 min.*

Figure 5.14 shows the XRD pattern of gold nanotriangle solution synthesized by lemongrass leaf extract reduction before and after laser irradiation for 14 minutes at a fluence of 30 mJ/cm^2. Curve 1 of Figure 5.14, corresponding to gold nanotriangles before laser irradiation shows a single intense Bragg reflection that can be indexed to (111)

lattice planes based on the fcc structure of gold. Curve 2 of Figure 5.14, corresponding to gold nanotriangles after laser irradiation shows the appearance of a number of new Bragg reflections at higher 2θ values that could be well indexed to the (200), (220) and (311) lattice planes of fcc structured gold. Clearly the appearance of all the usually observed Bragg reflections for fcc gold is a result of the loss of highly oriented anisotropic morphology of the gold nanotriangles leading to the formation of spherical gold nanoparticles that supports the observation made from the UV-vis-NIR and TEM measurements.

5.5 Conclusions.

In summary, we have demonstrated the role of temperature on the formation of gold nanotriangles using citric acid reduction by controlling the rate of nucleation and growth in the reaction medium. Following the TEM kinetics allows us to track the growth of the gold nanotriangles could be tracked at intermediate stages of their formation. The formation of gold nanotriangles in case of citric acid reduction appears to be occurring through nucleation and growth process unlike in case of lemongrass reduction where apparently growth occurs by aggregation and room temperature sintering of the nuclei. In this chapter we have also highlighted the crucial role of Cl^- ions on the evolution of the triangular morphology of gold nanoparticles during citric acid reduction of the $AuCl_4^-$ ions. Cl^- ions are known to form an ordered layer on the (111) lattice plane of gold and thus have a greater probability of passivating (111) face, inhibiting the growth along <111> direction. The formation of flat triangular and hexagonal gold nanoparticles rather than a thermodynamically more favorable octahedron bound by {111} set of planes has been attributed to the mismatch between the Cl^- adlayer and the underlying (111) Au lattice. The possibility of twin plane defects in the <111> direction originating from the strain induced by chloride ion adlayer mismatch is believed to promote the twin plane defect assisted two dimensional growth perpendicular to the <111> direction as reported recently. Based on these arguments it has been demonstrated that Br^- and I^- ions, having better ability to bind with gold surface, not only inhibit the formation of triangular and hexagonal gold nanoparticles but also induce shape transformation even on preformed gold nanotriangles and nanohexagons. As a physical means of shape transformation, it

has been demonstrated that nanosecond pulsed laser irradiation of the aqueous gold nanotriangles leads to transformation of triangular and hexagonal gold particles to spherical nanoparticles and also to their fragmentation. The extent of fragmentation is believed to be limited by the possibility of rapid dissipation of heat by nanotriangles as compared to nanorods owing to their higher surface area.

5.6 References:

1) a) Turkevich, J.; Hiller, J.; Stevenson, P. C. *Discussions Faraday Soc.* **1951**, *11*, 55. b) Turkevich, J.; Stevenson, P. C.; Hillier J. *J. Phys. Chem.* **1953**, *57*, 670. c) Enüstün, B. V.; Turkevich J. *J. Am. Chem. Soc.;* **1963**, *85*, 3317. d). Turkevich, J. *Gold Bull.* **1985**, *18*, 86. e) Lewis, J.; Turkevich, J. *A. B. Thesis*, Princeton University, Princeton, New Jersey, 1957.

2) Suito, E.; Uyeda, N. *Proc. Intern. Conf. Elect. Micro.*, London, 1954, 224.

3) a) Milligan, W. O.; Morriss, R. H. *J. Am. Chem. Soc.* **1964**, *86*, 3461. b) Malikova, N., Pastoriza-Santos, I., Schierhorn, M., Kotov, N.A. & Liz-Marzan, L.M. *Langmuir*, **2002**, *18*, 3694. c) Chiang, Y. S., Turkevich, J. *J. Colloid Sci.* **1963**, *18*, 772. d) Brüche, B. *Kolloid-Z.* **1960**, *170*, 97.

4) a) Suito, E.; Uyeda, N. *Nature* **1960,** *185*, 453. b) Suito, E.; Uyeda, N. *J. Electronmicroscopy* **1960,** *8*, 25. c) Frank, F. C. *Discussions Faraday Soc.* **1949**, *5*, 48. d) Frank, F. C. *Acta Cryst.* **1951**, *4*, 497. e) Kossel, W., *Ann. Physik* **1934**, *21*, 457. f) Stranski, I. N. *Z. Phys. Chem.* **1928**, *136*, 259.

5) Gao, P. Weaver, M. J. *J. Phys. Chem.*, **1986**, *90*, 4057.

6) a) Pileni, M. -P. *Nat. Mater.* **2003**, *2*, 145. b) Filankembo, A.; Pileni M. P. *Appl. Surf. Sci.* **2000**, *164*, 260. c) Filankembo, A.; Pileni M. P. *J. Phys. Chem. B* **2000**, *104*, 5865. d) Pileni M. P. *Langmuir* **2001,** *17,* 7476 e) Pileni M. P. *C. R. Chimie* **2003**, *6*, 965. f) Filankembo, A.; Giorgio, S.; Lisiecki, I.; Pileni M. P. *J. Phys. Chem. B* **2003,** *107,* 7492. g) Kitchens, C. L.; McLeod, M. C.; Roberts C. B. *Langmuir* **2005,** *21,* 5166. h) Im, S. H.; Lee, Y. T.; Wiley, B.; Xia Y. *Angew. Chem., Int. Ed. Engl.* **2005**, *44*, 2154.

7) Cheng, W.; Dong, S.; Wang, E. *Angew. Chem. Int. Ed.*, **2003**, *42*, 449.

8) a) Hu, M.; Wang, X.; Hartland, G. V.; Mulvaney, P.; Juste, J. P.; Sader, J. E. *J. Am. Chem. Soc.* **2003**, *125*, 14925. b) Hartland, G. V.; Hu, M.; Wilson, O.; Mulvaney, P.; Sader, J. E. *J. Phys. Chem. B.*, **2002**, *106*, 743. c) Link, S.; Hathcock, D. J.; Nikoobakht, B.; El-Sayed, M. A. *Adv. Mater.* **2003**, *15*, 393. d) Wang, Y.; Dellago, C. *J. Phys. Chem. B.,* **2003**, *107*, 9214. e) Chang, S.-S.; Shih, C.-W.; Chen, C.-D.; Lai, W.-C.; Wang, C. R. C. *Langmuir*, **1999**, *15*, 701. f) Link, S.; Wang, Z. L.; El-

Sayed, M. A.; *J. Phys. Chem. B.*, **2000**, *104*, 7867. g) Link, S.; Burda, C.; Mohamed, M. B.; Nikoobakht, B.; El-Sayed, M. A. *J. Phys. Chem. A.*, **1999**, *103*, 1165. h) Link, S.; Burda, C.; Nikoobakht, B.; El-Sayed, M. A. *J. Phys. Chem. B.*, **2000**, *104*, 6152.

9) a) Zhao, Q.; Hou, L.; Zhao, C.; Gu, S.; Huang, R.; Ren, S. *Laser Phys. Lett.* **2004**, *1*, 115. b) Kawasaki, M.; Masuda, K. *J. Phys. Chem. B.*, **2005**, *109*, 9379.

10) Rasa, M.; Philipse, A. P. Nature, **2004**, 429, 857.

11) Mirkin, C. A.; Letsinger, R. L.; Mucic, R. C.; Storhoff, J. J. *Nature* **1996**, *382*, 607.

12) a) El-Sayed, M. A. *Acc.Chem.Res.* **2001**, *34*, 257; b) Narayanan, R.; El-Sayed, M. A. *Langmuir* **2005**, *21*, 2027. c) Kelly, K. L.; Coronado, E.; Zhao, L. L.; Schatz, G. C. *J. Phys. Chem. B*, **2003**,*107*, 668.

13) Gai P. L.; Harmer, M. A. *Nano Lett.* **2002**, *2*, 771.

14) Wang, Z. L. *J. Phys. Chem. B*, **2000**, *104*, 1153.

15) Wasileski S. A.; Weaver, M. J. *J. Phys. Chem. B*, **2002**, *106*, 4782.

16) a) Zhang, P.; Sham, T. K. *Phys. Rev. Lett.*, **2003**, *90*, 245502. b) Prasad, B. L. V.; Stoeva, S. I.; Sorensen, C. M.; Klabunde, K. J. *Chem. Mater.*, **2003**, 15, 935.

17) a) Magnussen, O. M.; Ocko, B. M.; Adzic R. R.; Wang. J. X. *Phys. Rev.*, *B* **1995**, *51*, 5510. b) Magnussen, O. M.; Ocko, B. M.; Wang J. X.; Adzic, R. R. *J. Phys. Chem.*, **1996**, *100*, 5500. c) Ocko B. M.; Watson, G. M.; Wang, J. *J. Phys. Chem.*, **1994**, *98*, 897. d) Gao, X.; Weaver, M. J. *J. Phys. Chem.*, **1993**, *97*, 8685.

18) Lofton, C.; Sigmund, W. *Adv. Funct. Mater.* **2005**, *15*, 1197.

19) a) Germain, V.; Li, J.; Ingart, D.; Wang Z. L.; Pieni, M. P. *J. Phys. Chem. B* **2003**, *107*, 8717. b) Maillard, M.; Giorgio, S.; Pileni, M. P. *Adv. Mater.* **2002**, *14*, 1084. c) Wang, Z. L. *J. Phys. Chem. B*, **2000**, *104*, 1153.

20) Gao, J.; Bender C. M.; Murphy, C. J. *Langmuir*, **2003**, *19*, 9065.

21) a) Nikoobakht, B.; El-Sayed, M. A. *Chem. Mater.* **2003,** *15,* 1957 b) Aguirre, C. M.; Kaspar, T. R.; Radloff, C.; Halas, N. J. **2003**, *3*, 1707. c) Pérez-Juste, J.; Liz-Marzán, L. M.; Carnie, S.; Chan, D. Y. C.; Mulvaney, P. *Adv. Funct. Mater.* **2004**, *14*, 571. d) Link, S.; Burda, C.; Nikoobakht, B.; El-Sayed, M. A. *J. Phys. Chem. B* **2000**, *104*, 6152. e) Nikoobakht, B.; El-Sayed, M. A. *J. Phys. Chem. A* **2003**, *107*, 3372.

22) a) Kreibig, U. *J. Phys. F* **1974**, *4*, 999. b) Ekart, W.*Phys. Rev. B* **1985**, *31*, 6360. c) Stella, A.; Nisoli, M.; De Silvestri, S.; Svelto, O.; Lanzani, G.; Cheyssac P.; Kofman, R. *Phys. Rev. B* **1996**, *53*, 15497.

23) a) Ahmadi, T. S.; Logunov, S. L.; El-Sayed, M. A. *J. Phys. Chem.* **1996**, *100*, 8053. b) Ahmadi, T. S.; Logunov, S. L.; El-Sayed, M. A.; Khoury, J. T.; Whetten, R. L. *J. Phys. Chem. B* **1997**, *101*, 3713. c) Perner, M.; Bost, P.; Plessen, G.; Feldmann, J.; Becker, U.; Mennig, M.; Schmidt, H. *Phys. Re*V. *Lett.* **1997**, *78*, 2192. d) Hodak, J. K.; Martini, I.; Hartland, G. V. *J. Phys. Chem. B* **1998**, *102*, 6958. e) Schoenlein, R. W.; Lin, W. Z.; Fujimoto, J. G.; Eesley, G. L. *Phys. Rev. Lett.* **1987**, *58*, 1680. f) Sun, C.-K.; Vallée, F.; Acioli, L.; Ippen, E. P.; Fujimoto, J. G. *Phys. Rev. B* **1993**, *48*, 12 365. g) Elsayed-Ali H. E.; Juhasz, T. *Phys. Rev. B* **1993**, *47*, 13 599. h) Sun, C.-K.; Vallée, F.; Acioli, L. H.; Ippen, E. P.; Fujimoto, J. G. *Phys. Rev. B* **1994**, *50*, 15 337.

24) a) Hodak, J. H.; Henglein, A.; Hartland, G. V. *J. Phys. Chem. B* **2000**, *104*, 9954. b) Link, S.; El-Sayed, M. A. *Int. Re*v. *Phys. Chem.* **2000**, *19*, 409.

25) Bloemer, M. J.; Haus, J. W.; Ashley, P. R. *J. Opt. Soc. Am. B* **1990**, *7*, 790.

Chapter VI

Thermally Evaporated Lipid Thin Films for the Synthesis and Assembly of Inorganic Nanoparticles

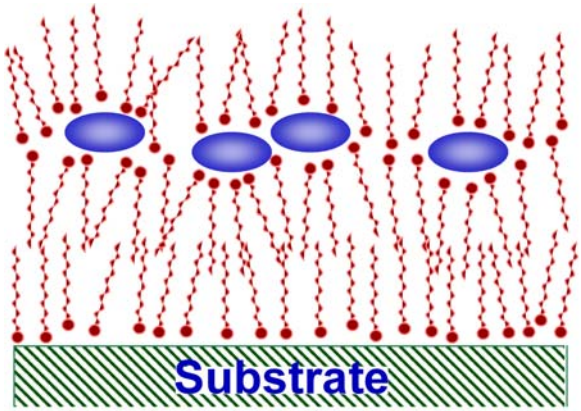

This chapter discusses the use of thermally evaporated lipid thin films for the immobilization of metal nanoparticles and synthesis of metal oxide and metal sulfide nanoparticles. Immobilization of biologically synthesized gold nanoparticles in thermally evaporated fatty amine and fatty acid lipid thin films has been demonstrated. These lipid thin films are observed to exhibit some size and shape dependent preference towards nanoparticles from a polydisperse solution. The synthesis of TiO_2, ZrO_2 and CdS nanoparticles within thermally evaporated lipid thin films is achieved by a simple immersion based method. By sequential immersion of the ionizable lipid thin films into suitable solutions, first metal ions can be entrapped and then chemically treated to synthesize the nanoparticles within the lipid matrix.

Part of the work presented in this chapter has been published:
(1) Shankar, S. S.; Ahmad, A.; Pasricha, R.; Khan, M. I.; Kumar, R.; Sastry, M. *J. Colloid Interface Sci.* **2004**, *274*, 69-75. (2) Shankar, S. S.; Rautaray, D.; Pasricha, R.; Pavaskar, N. R.; Mandale, A. B.; Sastry, M. *J. Mater. Chem.* **2003**, *13*, 1108–1111. (3) Shankar, S. S.; Joshi, H.; Pasricha, R.; Pavaskar, N. R.; Mandale, A. B.; Sastry, M. *J. Colloid Interface Sci.* **2004**, *269*, 126-130. (4) Shankar, S. S.; Chatterjee, S.; Sastry, M. *PhysChemComm,* **2003**, *6*, 36-39.

6.1 Introduction.

Synthesis of nanoparticles by solution based chemical methods, also termed wet chemical methods, is the most commonly followed route because of its many associated advantages. The advantages include the possibility of scaling up of the reaction with control over the size, shape, composition and/or surface functionality of the resultant nanoparticles. Wet chemical methods though mainly applied to in-solution synthesis of homogeneously distributed nanoparticles, have also been used to synthesize nanoparticles/nanostructures heterogeneously on support materials or other confined spaces, e.g for the synthesis of nanoparticles within mesoporous hosts [1], at liquid-liquid or air-water interfaces [2] and for the fabrication of freely suspended nanoparticle arrays [3]. Synthesis protocols alternative to wet chemical methods do not have such wide applicability. However, because of their unique features, they cater to the needs of some specific experimental requirements. One such requirement is the fabrication of nanoparticulate thin films or two dimensional nanoparticle arrays of various materials. Nanoparticulate thin films are of high commercial and technological importance due to their potential applications, e.g., in high-density magnetic media [4], optical/electronic/optoelectronic devices [5], solar cells, [6] and in biosensors [7], etc. An interesting aspect of nanoparticles is that apart from their ability to exhibit unique properties [8] when compared to their bulk counterparts they may also exhibit collective properties that differ from the properties of individual nanoparticles themselves [9]. The unique collective properties of two dimensionally assembled nanoparticles and the structural feasibility offered by the nanoparticulate thin films for above-discussed applications demand the improvement of existing methods and development of new methods for the synthesis of nanoparticulate thin films. The synthesis of nanoparticulate thin films or two-dimensional arrays of nanoparticles have been achieved by both physical and chemical processes. Traditionally thin films have been fabricated by methods like molecular beam epitaxy, sputtering, chemical vapor deposition, atomic layer deposition, etc.[10] More recently methods based on simple solvent evaporation,[11,9a] electrophoretic deposition, [12] sol-gel route, [13] Langmuir-Blodgett (LB) technique, [14] molecular self assembled monolayer (SAM) templates,

[15] polymeric matrices, [16] and biotemplates, [17] have been applied to synthesize thin films of various nanoparticles. Most of the latter techniques rely on covalent or electrostatic interactions between nanoparticles and the molecular templates for the organization or synthesis of nanoparticles in the form of thin films.

This chapter presents the use of thermally evaporated lipid thin films as a versatile host for the immobilization and syntheses of various inorganic nanoparticles. The technique adopted here is a combination of physical and chemical processes and in few aspects, is conceptually analogous to the LB technique. In the LB technique, a lipid monolayer with ionizable functional groups is first spread at the air water interface (Langmuir monolayer) and then allowed to electrostatically complex with oppositely charged species present in the aqueous subphase. The charged species may range from simple ions to large biomacromolecules or suitably surface functionalized nanoparticles. The lipid monolayer along with the charged species electrostatically complexed with it can then be lifted on to a desired substrate to get mono- or multi-layers of the desired species. Using this LB technique, assembled layers of many metal and metal oxide nanoparticles have been achieved by electrostatic complexation [18]. Alternatively, metal and metal oxide thin films have been synthesized by first electrostatically complexing the metal ions to the Langmuir lipid monolayer followed by their chemical or thermal treatment [19]. In the lipid-based methodology that will be discussed in this chapter, thin films of ionizable lipid molecules are obtained by thermal evaporation in a vacuum chamber on desired substrates with desired thickness. The deposited films are then used for electrostatic entrapment of metal ions that after necessary chemical treatment lead to the formation of a nanoparticulate thin film.

6.2 Thermally evaporated lipid thin films as host for synthesis and assembly of inorganic nanoparticles.

Thermally evaporated thin films of lipid molecules behave as a flexible host rendering them possible to entrap charged species of different size and shape unlike clay materials that can intercalate only small charged species. On immersion of thermally evaporated lipid thin films into aqueous solutions at appropriate pH, the functional groups of the lipid molecules (e.g. –COOH or $–NH_2$) get ionized (e.g. $–COO^-$ or $–NH_3^+$)

forming anionic or cationic templates that facilitate the diffusion of oppositely charged species present in the solution into charged lipid matrix. Such lipid thin films with entrapped metal ions have been reported to have an ordered lamellar structure of 'bilayer stacks' [20] similar to that observed in LB films as shown in Scheme 6.1. With this technique, it is possible to fabricate patterned structures and thus direct the assembly or synthesis of nanoparticles. Synthesis or assembly of nanoparticles can be achieved in two

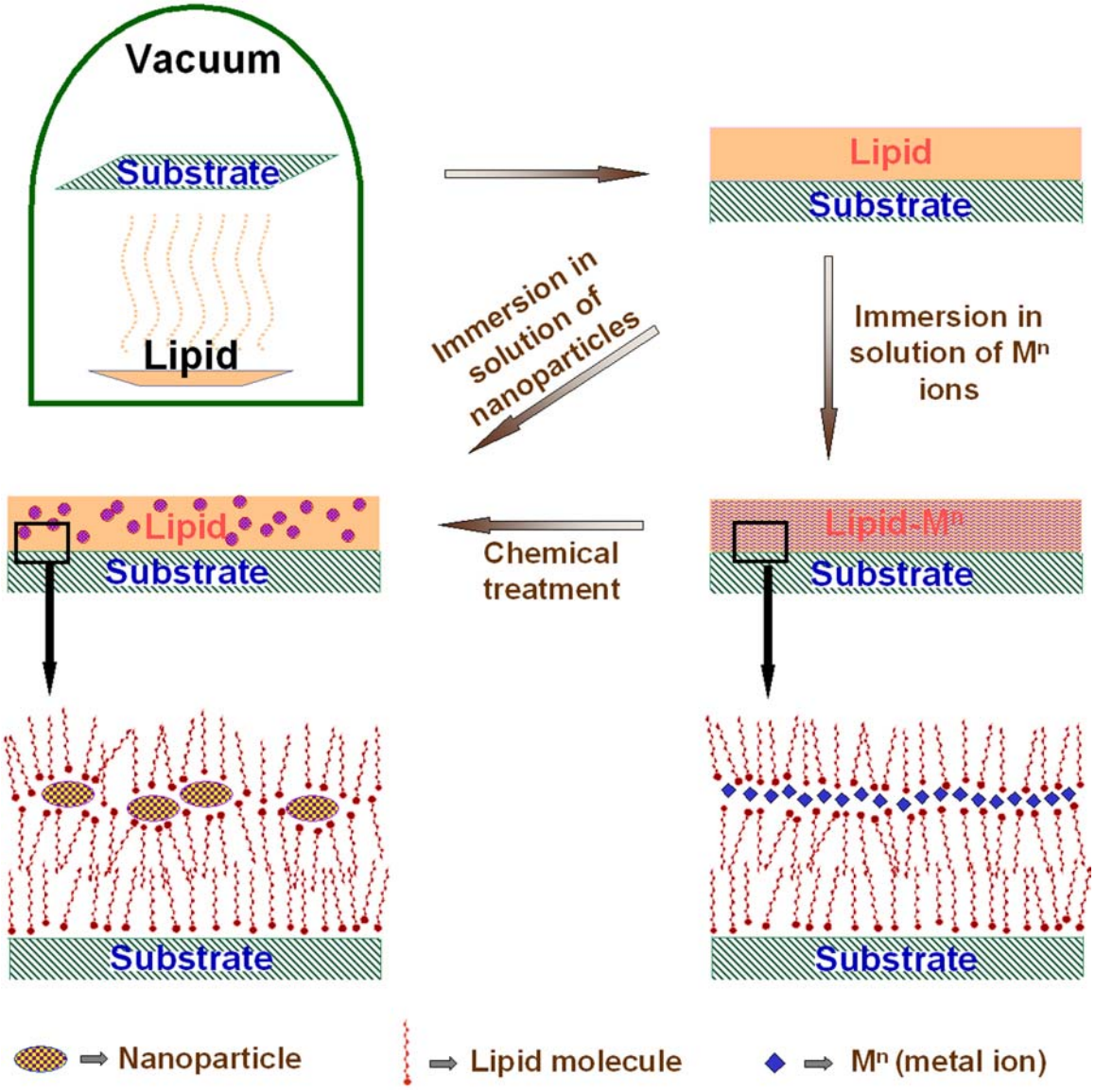

Scheme 6.1: *Schematic illustrating the synthesis of lipid-nanoparticle composite thin films. The thermally vacuum deposited lipid thin film can either be immersed in a solution of charged nanoparticles or be immersed in a solution of suitable metal ions and further chemically treated to synthesize lipid-nanoparticle composite thin film.*

ways analogous to the LB technique. In the first method, metal ions may be entrapped in thermally evaporated lipid films [21] and thereafter, reduced/chemically treated to yield metal or metal sulphide nanoparticles within the lipid matrix. Alternatively suitably functionalized nanoparticles can be electrostatically entrapped in a charged lipid matrix [22]. In this laboratory thermally evaporated lipid thin films have been successfully used in the immobilization of a broad range of inorganic species like metal ions [20] and nanoparticles [22, 14h] as well as biomacromolecules like proteins/enzymes [23] and DNA [24]. In addition, synthesis of metal and semiconducting nanoparticles has also been achieved within the lipid thin films. [21]

In this chapter an attempt has been made to extend the lipid based technique to:

1) Immobilize biosynthesized nanoparticles both into cationic and anionic lipid thin films as opposed to the immobilization of chemically synthesized nanoparticles into either cationic or anionic lipid films limited by their inherent charge.
2) Study the preferential entrapment of biologically synthesized nanoparticles into the lipid thin films based on their size and shape.
3) Synthesize metal oxides (titania and zirconia) and sulfide (CdS) nanoparticles within lipid thin films.

6.3 Immobilization of biologically synthesized gold nanoparticles in thermally evaporated lipid thin films.

As mentioned in chapters 1 and 3, there is an ever-growing current interest in the biological synthesis of nanoparticles and much work has been pursued in this laboratory to use microorganisms for the synthesis of nanoparticles both intra- and extra-cellularly. The nanoparticles synthesized using microorganisms are capped with proteins/biomacromolecules that act as efficient stabilizing agents. Following the discussion in the introduction part of this chapter, it would be of great interest from an application point of view to study the feasibility of immobilization of biologically synthesized nanoparticles to form their thin films. In earlier studies, it has been demonstrated in this laboratory that metal nanoparticles can be entrapped into oppositely

charged lipid thin films after suitable surface modification. [22] The suitability of thermally evaporated lipid thin films for immobilizing nanoparticles has thus been demonstrated, however it still faces a constraint that either anionic or cationic lipid thin films can only be used for a given counter-charged nanoparticles. Though this seems to be a constraint for the immobilization of nanoparticles, proteins have been observed to be more immune to this limitation and can be immobilized both into cationic and anionic lipid thin films [23b,f]. An interesting aspect of proteins is their amphoteric nature. Each protein has a specific isoelectric point (pI) depending on its constituting amino acids. The proteins are cationic when the pH of the medium is below their pI value and on increasing the pH of the medium above their pI value the proteins become anionic. This feature of the proteins have been capitalized and based on their pI values different proteins have been immobilized in either cationic or anionic regions in an array of thermally evaporated lipids to form patterned protein films [23c]. While it is possible to immobilize proteins into both cationic and anionic lipid thin films, assisted by electrostatic and/or secondary interactions (hydrogen bonding or hydrophobic interactions) [23b,f], it would be of interest to study if proteins can help the nanoparticles to infiltrate along with them both into cationic and anionic lipid thin films. Further, once the nanoparticles are able to diffuse into two different kinds of lipid thin films, it would also be of interest to study whether the lipid films exhibit any selectivity towards their entrapment, especially when the nanoparticles are polydisperse. The ability to entrap nanoparticles into both anionic and cationic lipid thin films would increase the scope of the possible templates that can be used for thin film fabrication. Biologically synthesized nanoparticles are known to be capped with proteins and thus may be a good candidate for these studies.

In this section, an attempt has been made to study the entrapment of biologically synthesized nanoparticles into lipid thin films, keeping in view the above-mentioned aspects. For this purpose, gold nanoparticles synthesized using the fungus *Fusarium oxysporum* [25] and those synthesized using the leaf extract of geranium plant were used and thermally evaporated thin films of octadecylamine (ODA) and stearic acid (StA) were used as cationic and anionic hosts respectively for their immobilization.

6.3.1 Immobilization of the gold nanoparticles synthesized using the fungus *Fusarium oxysporum* into thermally evaporated lipid thin films:

6.3.1a Synthesis of gold nanoparticles using the fungus *Fusarium oxysporum*:

The gold nanoparticles used for immobilization into lipid thin films were synthesized using the fungus *Fusarium oxysporum* [25] and geranium leaf extract. Synthesis of gold nanoparticles using the fungus, *Fusarium oxysporum* as reported in ref. 25 is described below. The synthesis of gold nanoparticles using geranium leaf extract has already been discussed in chapter 3 and is therefore not repeated here.

The fungus *Fusarium oxysporum* was obtained from the National Collection of Industrial Microorganisms (NCIM), National Chemical Laboratory, Pune, India. *Fusarium oxysporum* was routinely maintained by subculturing on potato-dextrose agar slants at 25 ^{o}C. The fungus was grown in 500 mL Erlenmeyer flasks each containing 100 mL MGYP media, composed of malt extract (0.3%), glucose (1.0%), yeast extract (0.3%), and peptone (0.5%) at 25-28 ^{o}C under shaking condition (200 rpm) for 96 h. After 96 h of fermentation, mycelia were separated from the culture broth by centrifugation (5000 rpm) at 10 °C for 20 min and the settled mycelia were washed thrice with sterile distilled water. Ten grams of the harvested mycelial mass was then re-suspended in 100 mL sterile distilled water in 500 mL conical flasks at pH = 5.5 - 6.0 and to this suspension, 100 mL of an aqueous solution of 10^{-3} M chloroauric acid ($HAuCl_4$) was added. The whole mixture was thereafter put into a shaker at 28 °C (200 rpm) and the reaction was carried out for a period of 72 h. Optical absorption spectra showed a strong peak at 548 nm indicating the formation of gold nanoparticles. The solution was filtered and centrifuged at 5000 rpm at 10 °C for 10 min to remove traces of mycelia. Thereafter, the supernatant was again centrifuged at 10,000 rpm at 10 °C for 15 min to separate out protein-capped gold nanoparticles from free proteins suspended in the solution. UV-Vis absorption spectra of the redispersed pellet and the supernatant were taken. The pellet was redispersed in 50 mL of distilled water in a 100 mL conical flask.

6.3.1b Entrapment of the fungus *Fusarium oxysporum* synthesized gold nanoparticles into ODA and StA lipid thin films:

10 mL aqueous solution of gold nanoparticles synthesized using the fungus, *Fusarium oxysporum* was taken in four separate 25 mL beakers. A pH of 6.6 was observed for this solution. The pH of three such solution in the beakers were adjusted to 4.5, 5.5 and 8.5 respectively by adding necessary amount of 0.1 M HCl for acidic pH and 0.1 M NH_4OH for basic pH. Buffer solutions were not used so as to avoid the presence of competitive ions for diffusion into the lipid film. 500 Å thick octadecylamine (cationic lipid, ODA) and stearic acid (anionic lipid, StA) films were deposited on Si (111) wafers, quartz substrates, gold-coated 6 MHz AT-cut quartz crystal microgravimetry (QCM) crystals and carbon-coated TEM copper grids by vacuum thermal evaporation

6.3.1c QCM measurements:

The kinetics of gold nanoparticle incorporation in the ODA/StA films was followed by immersing the ODA/StA films deposited on QCM crystals in the biologically synthesized gold nanoparticle solutions maintained at different pHs and by

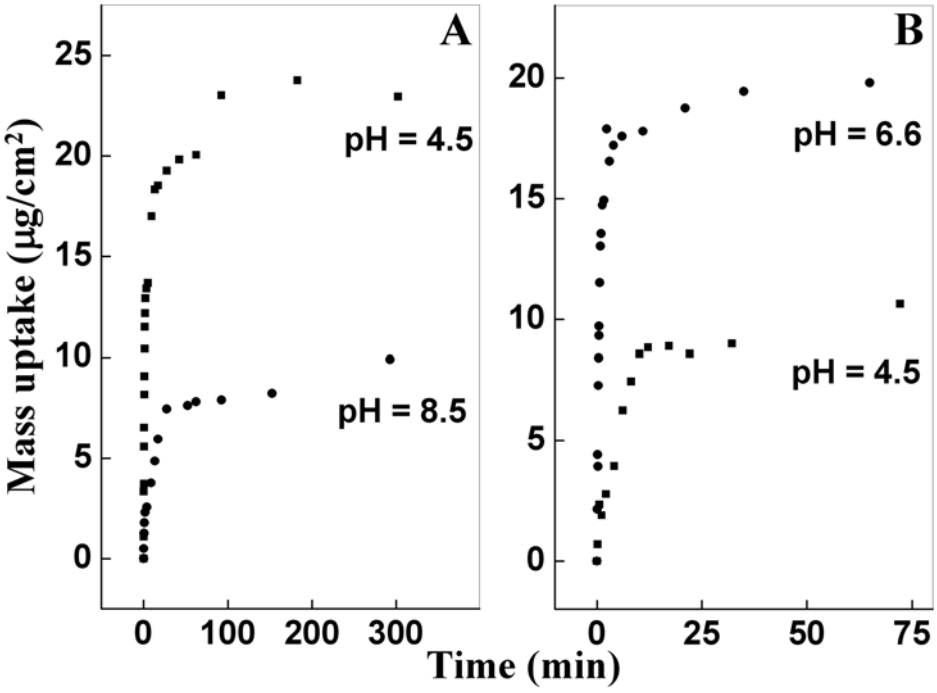

Figure 6.1: *(A) QCM mass uptake kinetics for a 500 Å thick stearic acid film immersed in solutions of gold nanoparticles synthesized with the fungus, Fusarium oxysporum and maintained at pH values 4.5 (squares) and 8.5 (circles). (B) QCM mass uptake kinetics for a 500 Å thick octadecylamine film immersed in solutions of gold nanoparticles synthesized with the fungus, Fusarium oxysporum and maintained at pH values 4.5 (squares) and 6.6 (circles).*

measuring the frequency change *ex situ* after thorough washing and drying of the crystals. The change in the quartz crystal resonance frequency was measured and converted to a mass loading using the Sauerbrey formula [26]. The kinetics of gold nanoparticle diffusion was studied for the following experimental conditions : (1) StA film of 500 Å thickness immersed in the biologically synthesized gold nanoparticle solutions at pH values 4.5 and 8.5 and, (2) ODA films of 500 Å thickness immersed in biologically synthesized gold nanoparticle solutions at pH values 4.5 and 6.6. The ex-situ QCM kinetics measurements are shown in Figure 6.1. The mass uptake in 500 Å thick StA films immersed in the gold nanoparticle solutions maintained at pH 4.5 and 8.5 is represented by solid squares and circles respectively in Figure 6.1A. As shown, the mass uptake in the StA film at pH 4.5 is around 3.5 times higher than for the film immersed in the gold nanoparticle solution at pH 8.5. The kinetics of mass uptake in 500 Å thick ODA films during immersion in gold nanoparticle solutions maintained at pH 4.5 and 6.6 are shown in Figure 6.1B and are represented by squares and circles respectively. The mass uptake in the case of ODA is 2 times higher for the gold nanoparticle solution maintained at pH 6.6 than that of pH 4.5 gold solution. The mass uptake by lipid thin films as discussed above is determined largely by the electrostatic interactions between nanoparticles and charged lipid molecules. It is also observed that in cases where there is low mass uptake, the rate of nanoparticles uptake is also slow. From the mass uptake observed in the QCM data, it can be concluded that the extent of charge on the gold particles depends on the pH of the solution. In an earlier report from our laboratory, it has been shown that the gold nanoparticles synthesized by *Fusarium oxysporum* are capped with proteins [25]. Comparison of Figure 6.1A and Figure 6.1B shows that the pH dependence of gold nanoparticles incorporation in StA and ODA is inverse to each other. It is well known that StA is negatively charged above pH 4.5 (pK_a of StA ~ 4.5) while ODA is charged positively below pH 10.1 (pK_b of ODA ~ 10.1). Within the pH range of the experiments explained above, the determining factor for gold nanoparticle incorporation in the lipid film is thus the charge on the protein capped gold nanoparticles.

6.3.1d UV-vis measurements:

Gold nanoparticle incorporation in the lipid films was studied using UV-vis absorption spectroscopy. StA and ODA films of 500 Å thickness deposited on quartz

substrates were immersed in the biologically synthesized gold sols maintained at pH values of 4.5, 5.5, 6.6 and 8.5 respectively for 48 h.

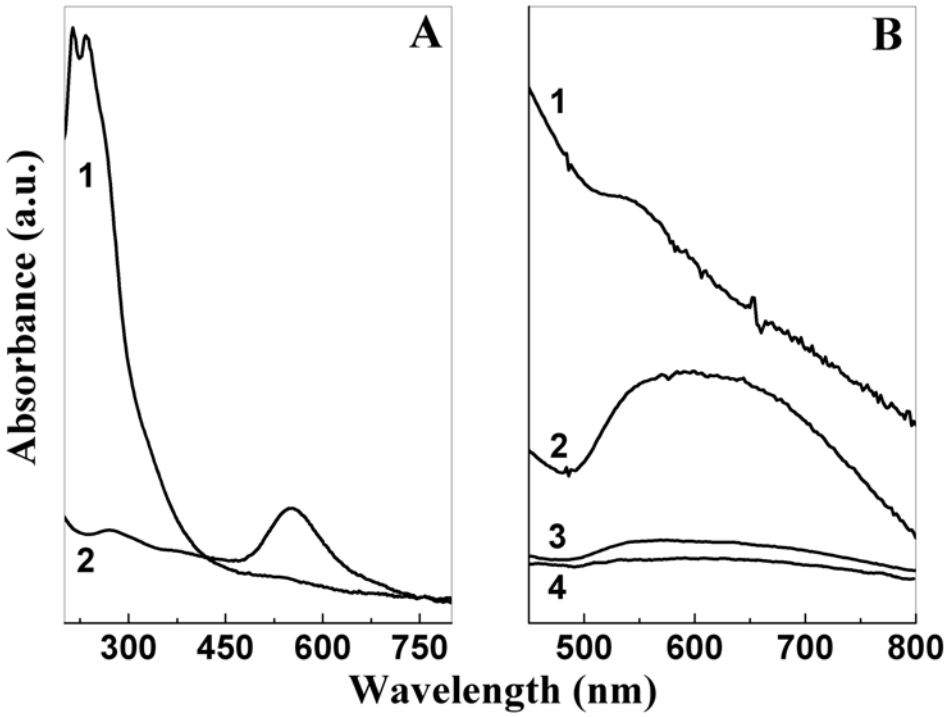

Figure 6.2: *A) UV-vis absorption spectra of supernatant collected after centrifugation of the gold nanoparticle solution synthesized by the reduction of aqueous $AuCl_4^-$ ions by the fungus, Fusarium oxysporum, (curve 1) and of the redispersed pellet (curve 2, text for details). (B) UV-Vis absorption spectra recorded from a 500 Å thick ODA film immersed in the gold nanoparticle solution obtained from Fusarium oxysporum and maintained at pH 6.6 (curve 1) and at pH 4.5 (curve 4). The spectra recorded from a 500 Å thick stearic acid film immersed in the biologically synthesized gold nanopartice solution from the same microorganism maintained at pH 4.5 (curve 2) and pH 5.5 (curve 3) are also shown.*

After exposure of the aqueous chloroauric acid solutions to the fungal biomass for 72 h, the gold nanoparticle solutions was separated and subjected to centrifugation as described in the experimental section. Figure 6.2A shows the UV-vis absorption spectra of supernatant and the redispersed pellet of the fungus-reduced colloidal gold solution. The redispersed pellet solution gave a relatively sharp absorbance peak at 550 nm (curve 2, Figure 6.2A) that was absent in the absorption spectrum corresponding to the supernatant (curve 1, Figure 6.2A) indicating absence of gold nanoparticles in the supernatant and their complete removal by centrifugation. In curve 1 of Figure 6.2A (corresponding to the supernatant), a strong absorption peak centered at 280 nm arising due to π-π* transition in the tryptophan and tyrosine residues of the proteins present in

the solution can be seen [27]. Absorbance due to these components in the case of the redispersed pellet solution (curve 2, Figure 6.2A) is drastically decreased. Thus by centrifugation, it was possible to separate out the free, uncapped proteins from the protein-capped nanoparticles in the biologically synthesized gold nanoparticle solution. Figure 6.2B shows the UV-vis absorption spectra recorded from 500 Å thick StA and ODA films immersed in the redispersed pellet solutions of the biologically synthesized gold nanoparticles maintained at different pH values. Although there was mass uptake by both StA and ODA films at all the pH values mentioned above (Figure 6.1), it was observed that the optical absorption spectra of the films showed a strong peak corresponding to gold nanoparticles (identified by the surface plasmon resonance at 600 nm) only for the StA film immersed in the gold nanoparticle solutions maintained at pH below 5.5 (curve 2, Figure 6.2B) and for ODA films above a pH value 5.5 (curve 1, Figure 6.2B). This shows that there is significant immobilization of gold nanoparticles only in these pH intervals. Though the complete nature of the encapsulating protein is yet to be elucidated, with reference to the QCM data it can be argued that the *Fusarium oxysporum* synthesized gold nanoparticles are positively charged below pH 5.5 and negatively charged above pH 5.5. This rationalizes the observed intake of protein-capped gold nanoparticles in StA films below pH 5.5 and a similar intake in the ODA films immersed in the nanoparticle solutions maintained at pH above 5.5. These results thus give a rough estimate of the pI of the encapsulating protein to be around 5.5.

A striking difference can be observed on comparing the optical absorption spectra of the gold nanoparticles immobilized in ODA and StA films (Figure 6.2B, curves 1 and 2 respectively) with that of the parent biologically synthesized gold nanoparticle solution (Figure 6.2A, curve 2). The absorption peak arising due to excitation of surface plasmons in the gold nanoparticles entrapped in the lipid matrix is broadened and also shows a red shift relative to the parent gold solution used for immobilization. This feature is more pronounced in the case of gold nanoparticles immobilized in films of StA than ODA. This could be due to aggregation of the nanoparticles within the film [28] or due to a large variation in the size distribution of the incorporated particles [29]. Aggregation is favored within the lipid film because the charged functional groups of the lipid film matrix help in screening the repulsion between the similarly charged protein-capped gold

nanoparticles. In the case of the parent gold nanoparticle solution, such screening agents which decrease the repulsive forces acting between the gold nanoparticles are absent and hence the particles tend to be dispersed forming a stable nanoparticle solution. Observations from the TEM images are consistent with the above explanations and are discussed below.

6.3.1e FTIR measurements:

FTIR measurements were taken for the 500 Å thick StA and ODA films on Si (111) substrates immersed in the biologically synthesized gold sols maintained at pH 4.5 and 6.6 respectively. Thorough washing and drying of the films was done prior to FTIR measurements.

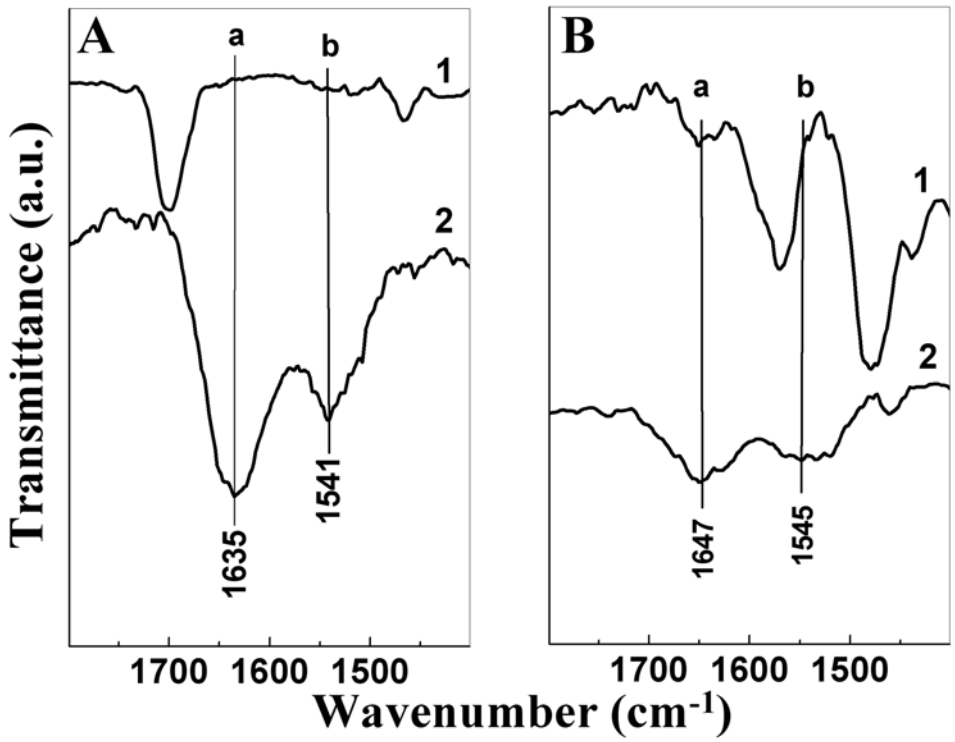

Figure 6.3: *FTIR spectra recorded from- (A) 500 Å stearic acid film (curve 1) and this film immersed in Fusarium oxysporum synthesized gold nanoparticle solution at pH 4.5 (curve 2); (B) 500 Å thick ODA film (curve 1) and this film after immersion in Fusarium oxysporum synthesized gold nanoparticle solution at pH 6.6 (curve 2).*

FTIR spectra recorded from 500 Å thick StA and ODA films immersed in the *Fusarium oxysporum* synthesized gold nanoparticle solutions (pH 4.5 for StA and 6.6 for

ODA, where maximum gold nanoparticle loading has been observed) are shown in Figures 6.3A and B respectively (curve 2 in both cases). FTIR spectra from pure StA and ODA films have also been shown in the respective figures for comparison (curves 1 in both cases). In both gold nanoparticle-incorporated thin films, the presence of strong amide I and II bands due to carbonyl stretch and -N-H stretch vibrations respectively of amide linkages of proteins can be seen (Figures 6.3A and B, curve 2) [30]. The presence of protein bands in the cationic and anionic lipid hosts clearly shows that the immobilized gold nanoparticles are capped with proteins, these proteins being responsible for the pH-dependent mass uptake of the gold nanoparticles observed in the QCM and UV-vis spectroscopy studies (Figures 6.1 and 6.2). In the case of ODA thin films, the amide I band was observed at 1647 cm^{-1} and a broad amide II band was observed within the range 1509-1569 cm^{-1} (Figure 6.3B) while in the case of StA films, these bands are shifted slightly to lower wavenumbers (1635 cm^{-1} and 1541 cm^{-1} respectively, Figure 6.3A). This shift is possibly due to the stronger interaction of the amide linkages of the proteins capping the gold nanoparticles with carboxylic functional groups of StA molecules relative to that of the amine groups in ODA.

6.3.1f TEM measurements:

TEM measurements were carried out using 500 Å thick StA and ODA films deposited on carbon-coated TEM grids immersed in the gold sols maintained at pH values 4.5 and 8.5 respectively for 48 h. Prior to TEM analysis, the samples were washed by gently rinsing in distilled water in order to get rid of any loosely bound nanoparticles on the surface of the lipid thin film coated copper grids. Figure 6.4 shows the TEM image of the gold nanoparticles as prepared using the fungus, *Fusarium oxysporum*. As

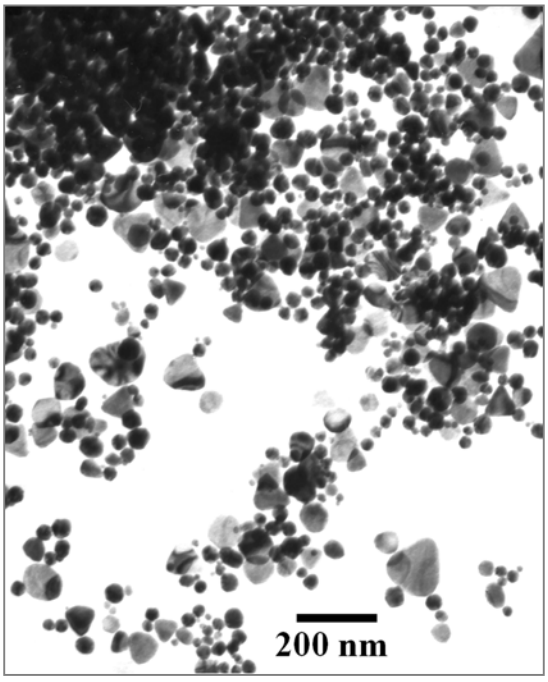

Figure 6.4: *Representative TEM image of gold nanoparticles biologically synthesized using the fungus, Fusarium oxysporum.*

shown the spherical gold nanoparticles are polydisperse and are in the size range ca. 10 - 35 nm along with a large number of flat gold nanoparticles in the range 50 – 130 nm. The Figures 6.5A and B are the representative images of the StA and ODA films immobilized with *Fusarium oxysporum* synthesized gold nanoparticles from the same solution maintained at pH 4.5 and 6.6 respectively. Clearly, there is efficient immobilization of polydisperse gold nanoparticles within both StA and ODA thin films. As already mentioned regarding possible aggregation of gold nanoparticles within the lipid films, it can be observed that there is infact such aggregation explaining the broadening and red

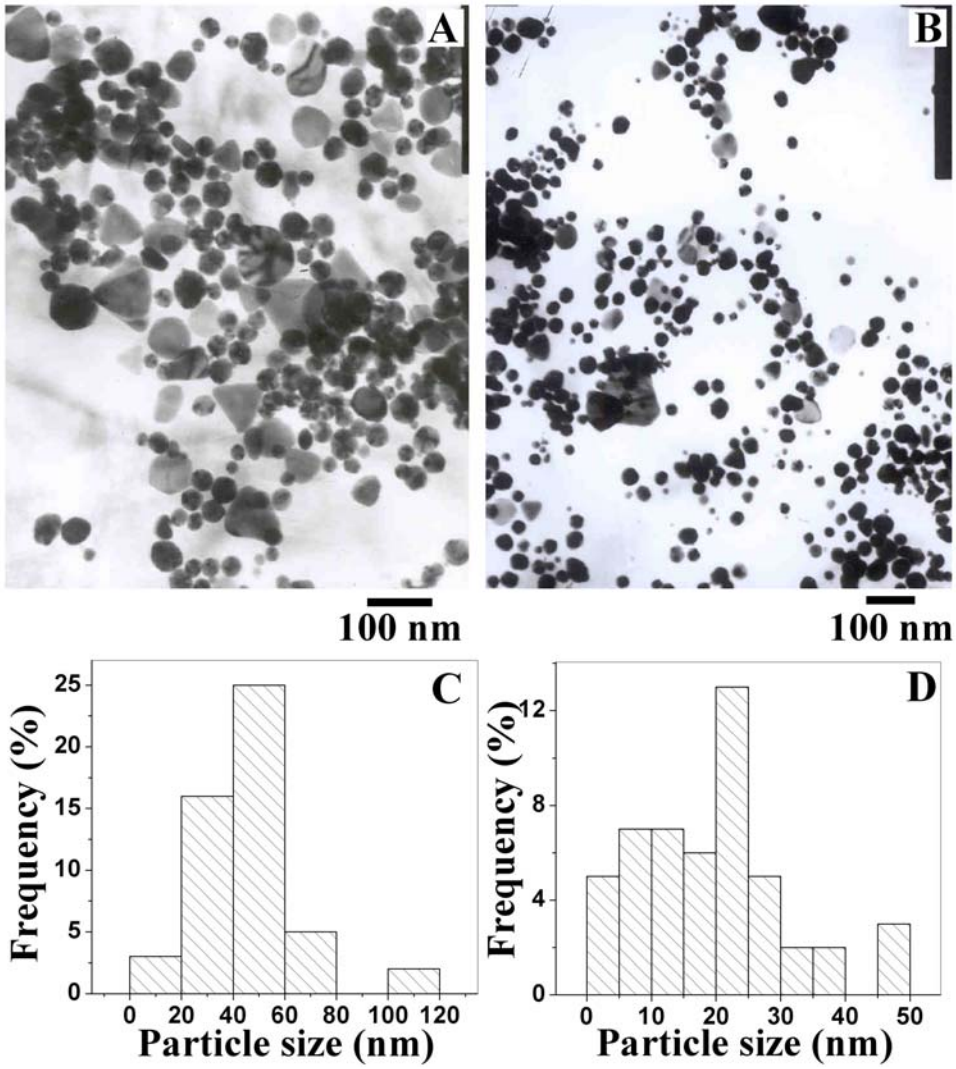

Figure 6.5: *Representative TEM images of Fusarium oxysporum synthesized gold nanoparticles immobilized in a 500 Å thick STA film at pH 4.5 (A) and in a 500 Å thick ODA film at pH 6.6 (B). C and D show the particle size distribution histograms determined from the TEM images A and B respectively for gold nanoparticles immobilized in STA and ODA thin films.*

shift in the optical absorption peaks recorded in the films. In case of the StA film, the gold nanoparticles seem to be more aggregated relative to gold nanoparticles incorporated in the ODA film. Furthermore, on comparing both the images (Figure 6.5A and 6.5B) it is observed that the two lipid films have different size and shape selectivity towards the immobilized gold nanoparticles. Though the same parent solution was used in the immobilization experiment, the particle size distribution is different for gold nanoparticles incorporated in StA and ODA thin films. The gold nanoparticles in the StA film were of average size ca. 46 nm (Figure 6.5C). A large number of triangular gold nanoparticles are also observed in the StA thin films. The triangular particles are of 70 nm average size and are essentially planar. The gold nanoparticles incorporated in the ODA film were of comparatively smaller dimensions with an average size ca. 21 nm (Figure 6.5D). The particles were mostly spherical with a very low percentage of triangular nanoparticles. The triangular nanoparticles in the ODA matrix rarely exceeded 30 nm in dimension.

6.3.2 Selectivity in the entrapment of the gold nanoparticles synthesized using geranium leaf extract into thermally evaporated lipid thin films:

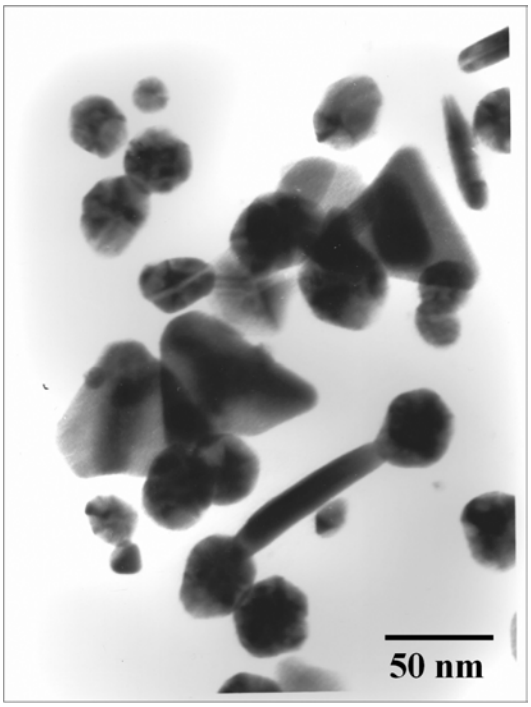

In a different set of experiments, gold nanoparticles synthesized using geranium (*Pelargonium graveolens*) leaf broth were used for their immobilization within thermally evaporated lipid thin films. The gold nanoparticles for this purpose were synthesized using geranium leaf broth as described in section 3.2.1 of chapter 3. The pH of as-prepared gold nanoparticle solution using geranium leaf broth was 2.8. The pH of this solution was adjusted to 4.5 and 6.6 in two

Figure 6.6: *Representative TEM image of gold nanoparticles synthesized using geranium leaf extract as described in chapter 3.*

different beakers by adding 0.1 M NH_4OH solution. Thereafter, immobilization of the geranium synthesized gold nanoparticles in the different lipid films was done as described above for gold nanoparticles synthesized using *Fusarium oxysoprum*.

In a previous study, as disscused in chapter 3, we observe that reaction of aqueous gold ions with geranium leaf extract resulted in the formation of polydisperse gold nanoparticles with a variety of shapes. Figure 6.6 shows the representative TEM image of gold nanoparticles synthesized using geranium leaf extract before their use for

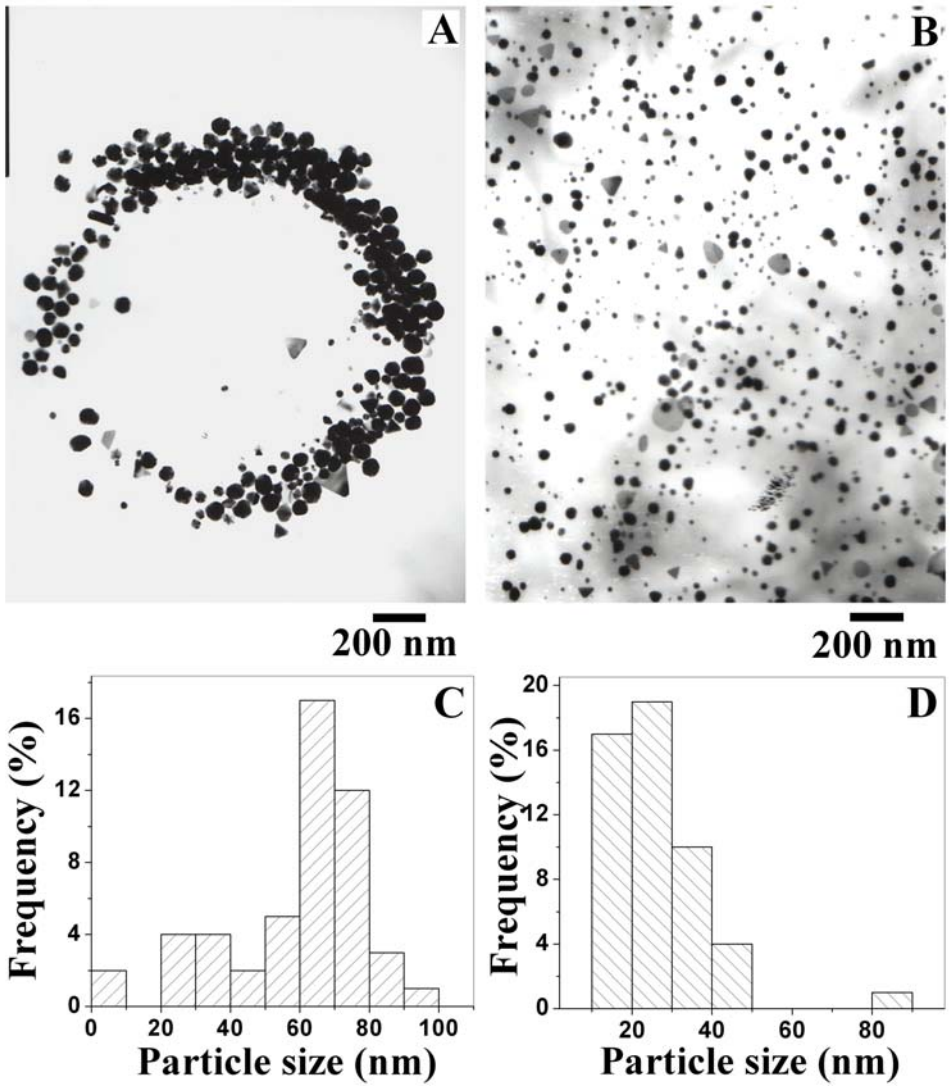

Figure 6.7: *Representative TEM images of geranium leaf extract synthesized gold nanoparticles immobilized in a 500 Å thick STA film at pH 4.5 (A) and in a 500 Å thick ODA film at pH 6.6 (B). C and D show the particle size distribution histograms determined from the TEM images A and B respectively for gold nanoparticles immobilized in STA and ODA thin films.*

entrapment in lipid thin films. With this experiment, we were interested to see whether the lipid thin films were capable of size and shape-selective incorporation of geranium leaf extract synthesized gold nanoparticles. The geranium synthesized gold nanoparticles were incorporated into 500 Å thick StA and ODA thin films at pH values of 4.5 and 6.6 respectively by simple immersion of the films in the gold nanoparticle solutions and analyzed by TEM. As in case of immobilization of *Fusarium oxysporum* synthesized gold nanoparticles (Figure 6.5), we observe significant differences in both the size and shape of geranium synthesized gold nanoparticles immobilized in the two lipid matrices (Figures 6.7A and B). In the StA thin film (Figure 6.7A), the gold nanoparticles (average particle size of ca. 69 nm) were larger than those immobilized in the ODA thin film (Figure 6.7B, average size ~ 23 nm). Another exciting observation is the assembly of these gold nanoparticles in a circular pattern within the StA film (Figure 6.7A) that is absent in the ODA thin film. The circular assemblies of gold nanoparticles in the StA film were present uniformly on the grid surface and were of average diameter 1.3 μm. TEM images recorded at higher magnification shows that the geranium synthesized gold nanoparticles immobilized in the StA thin film consist of larger percentage of flat triangular particles (Figure 6.8A). In the ODA thin film, the nanoparticles were very uniformly dispersed with no signs of aggregation throughout the film (Figure 6.8B). Furthermore, the geranium synthesized gold nanoparticles in the ODA matrix are predominantly spherical in morphology with a very small percentage of triangular particles (Figure 6.8B). We are thus able to observe that from a sol of polydisperse gold nanoparticles the two lipid thin films have very different size and shape selectivity towards the gold nanoparticles. The pH dependence of the nanoparticle entrapment shows that for geranium synthesized gold nanoparticles, the driving force for immobilization is electrostatic attraction. In both fungus and geranium synthesized gold nanoparticles, the nature of the capping agents are not known presently and consequently, the mechanistic aspects relating to the shape and size selectivity exhibited by the StA and ODA films is not clear. In addition to the nanoparticle capping agent, differences in the internal molecular arrangement within the lipid thin films may also contribute to the size and shape selectivity observed. The observation of circularly arranged gold nanoparticles selectively in StA thin film and not in ODA thin film is also exciting. Ohara *et al* have

previously reported such circular assembly which is shown to be a result of pinning of holes that have nucleated in sufficiently thin films of dilute solutions of particles that wet the substrate on which they are spread [31]. It is unlikely that such a mechanism is responsible for the ring formation observed in the present study since the gold nanoparticles are expected to be intercalated within the lipid bilayers of the ODA and StA matrix.

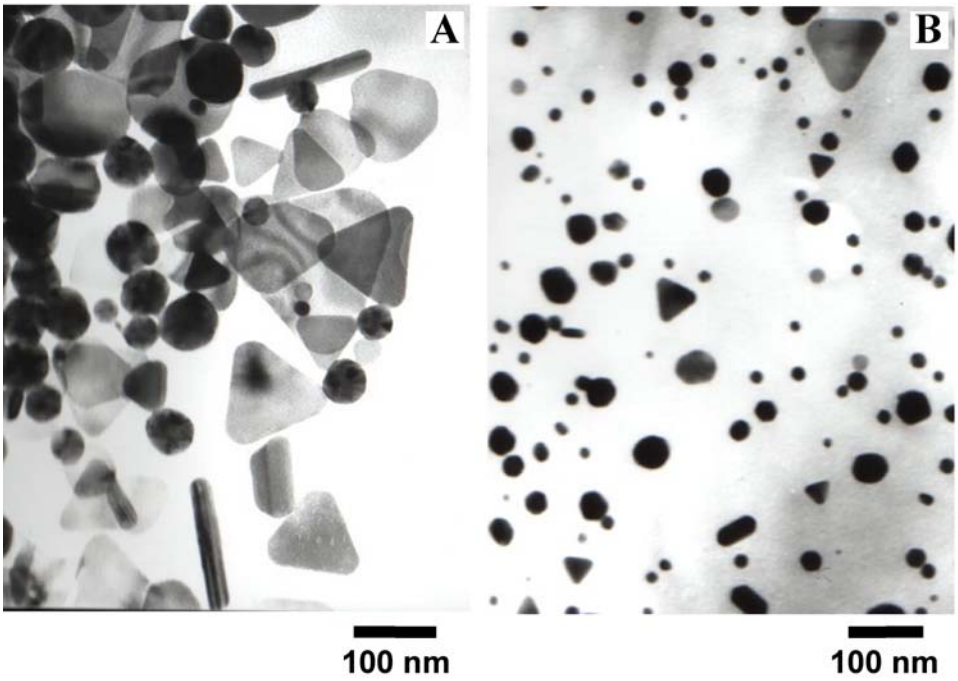

Figure 6.8: *Representative higher magnification TEM images recorded from geranium leaf broth gold nanoparticles immobilized in a 500 Å thick STA film at pH 4.5 (A) and in a 500 Å thick ODA film at pH 6.6 (B).*

6.4 Synthesis of metal oxide and sulfide nanoparticles in thermally evaporated lipid thin films.

As already discussed in this chapter, thermally evaporated thin films have been used to synthesize thin films of metal and bimetallic nanoparticles [21]. In this section, as a part of our ongoing studies on the use of thermally evaporated lipid films in the synthesis of inorganic nanostructures, we describe our attempts to extend this lipid based methodology to metal oxides like titania (TiO_2) and zirconia (ZrO_2). We also describe here the use of aerosol OT thin films as an efficient host for the synthesis of

nanoparticulate thin films of CdS with better size control as compared to our previous attempts [21a]. The nanomaterials like TiO_2, ZrO_2 and CdS that we have attempted to synthesize in the form of thin films, belong to a class of technologically important materials having some common and unique applications. Titania has useful dielectric and refractory properties and finds applications in microelectronics [32], optical cells [33], solar energy conversion [34], highly efficient catalysts [35], microorganism photolysis [36], antifogging and self-cleaning coatings [37], gratings [38], gate oxides in MOSFET (metal-oxide-semiconductor field effect transistor) [39], sensors [40] and in electrochromic devices [41]. Zirconia in its pure form has high hardness, low wear resistance, low coefficient of friction, high elastic modulus, chemical inertness, good ionic conductivity, low thermal conductivity, and high melting temperature. These unique properties enable application of zirconia in a wide range of fields such as structural materials, thermal barrier coatings, solid-state electrolytes [42], solid fuel cells [43], gate dielectrics [44], oxygen sensors [45] and as heterogeneous catalysts [46]. Similarly, cadmium sulfide particles that exhibit significant quantum size effect below the size limit of 6 nm have potential applications in optoelectronic devices [47], lasers [48], photocatalysts[49], electrochemical cells[50] and in fluorescent labeling of cell organelles[51]. Fabrication of thin films of these materials in a reproducible manner is a requisite for many of the above mentioned applications. This serves as a motivation for us to attempt synthesizing thin films of these materials using thermally evaporated thin films.

For the synthesis of nanoparticulate thin films of titania and zirconia and their various characterization, 250 Å thick octadecylamine (ODA, $CH_3(CH_2)_{17}NH_2$) films were deposited on Si (111) wafers, quartz pieces, gold-coated 6 MHz AT cut quartz crystals and carbon-coated TEM copper grids by thermal evaporation under vacuum. The film thickness/deposition rate was monitored *in situ* by quartz crystal microgravimetry (QCM). QCM measurements of the kinetics of entrapment of TiF_6^{2-}/ ZrF_6^{2-} ions in the ODA films were carried out by immersing the ODA film deposited on quartz crystals in freshly prepared 10^{-3} M K_2TiF_6/K_2ZrF_6 solution (pH 3.6) for different times and measuring the frequency change *ex-situ* after thorough washing of the crystals in distilled water and drying. The exact time of drying of the ODA-coated quartz crystal after each

cycle of immersion was extremely important. During immersion of the film in the electrolyte solution, the lipid bilayers swell leading to a large uptake of water. After removal of the film from solution, the frequency of the ODA-coated quartz crystal was monitored as a function of time to record evaporation of entrapped water from the film. It was observed that drying the film for 10 minutes resulted in stabilization of the crystal frequency indicating complete evaporation of water in this time interval and consequently, the film was dried for 15 minutes prior to each successive immersion cycle. It may be mentioned here that the frequency with which the QCM measurements were carried out (by varying the time interval between measurements) did not result in a significant difference in the ion mass uptake kinetics. The mass change in the ODA-TiF_6^{2-} and ODA-ZrF_6^{2-} composite film was thereafter monitored during immersion of the film in 1 % and 10 % ammonia solution respectively held at 50 ^oC. The optimum times of immersion of the ODA films in K_2TiF_6/K_2ZrF_6 and ammonia solutions as determined from QCM measurements was used in the preparation of titania/Zirconia nanoparticle films on other substrates for further analysis. For optical absorption spectroscopy studies, the ODA-titania/ODA-Zirconia nanoparticle films on quartz were used. For X-ray photoemission spectroscopy (XPS) analysis, the general scan and C 1s, Ti 2p and Zr 3d core level spectra were recorded from the ODA-TiF_6/-ZrF_6 and ODA-titania/ODA-zirconia, nanoparticle films synthesized on Si (111) wafers. The core level spectra were background corrected using the Shirley algorithm and the chemically distinct species resolved using a nonlinear least squares procedure. The core level binding energies (BEs) were aligned with the adventitious carbon binding energy of 285 eV. Transmission Electron Microscopy (TEM) measurements of titania and zirconia nanoparticles synthesized within ODA thin film matrix deposited on carbon-coated TEM grids were carried out. X-ray diffraction (XRD) measurements of the ODA-TiF_6/-ZrF_6 as well as the ODA-titania/zirconia nanoparticle composite films were also carried out.

Similar procedure was followed for the synthesis of nanoparticulate thin film of CdS. As an anionic lipid host for the entrapment of Cd^{2+} ions, 500 Å thick film of sodium bis(2-ethylhexyl)sulfosuccinate (AOT) was deposited onto quartz piece, Si (111) wafers, carbon-coated copper TEM grids and gold-coated AT-cut quartz crystals. To monitor the kinetics of entrapment of Cd^{2+} ions and formation of CdS, QCM measurements were

carried out by first immersing the AOT film deposited on quartz crystals in 10^{-3} M $CdCl_2$ solution for different times and measuring the frequency change *ex-situ* after thorough washing of the crystals in distilled water and drying. After saturation of the entrapment of Cd^{2+} ions into AOT thin film, QCM measurements were continued by measuring the mass uptake during the second step of immersion of the AOT thin film into an aqueous solution of 10^{-3} M Na_2S to monitor the formation of CdS. Synthesis of CdS was further characterized by UV-vis spectroscopy, FTIR, EDAX and TEM.

6.4.1 Synthesis of titania and zirconia nanoparticles within thermally evaporated thin films of octadecylamine:

6.4.1a QCM measurements:

The kinetics of incorporation of TiF_6^{2-} and ZrF_6^{2-} ions into a 250 Å thick ODA film during immersion in freshly prepared 10^{-3} M K_2TiF_6 and K_2ZrF_6 solution was followed by QCM and the data obtained is shown in Figure 6.9. It is observed that there is a fairly rapid mass increase due to electrostatically driven diffusion for both TiF_6^{2-} and ZrF_6^{2-} ions into the ODA matrix, the equilibration of the metal ion concentration in the ODA matrix occurring within ca. 3 h and 4 h of immersion respectively. As mentioned in section 6.2, the uptake of TiF_6^{2-} and ZrF_6^{2-} ions in ODA is driven to a large extent by electrostatic interaction between their negative charge and the positive charge of the protonated amine groups in ODA thin film under the pH conditions of the solution (pH 3.6). The mass uptake by the ODA thin film when immersed in solution of TiF_6^{2-} and ZrF_6^{2-} ions is observed to be ca. 9.6 μg/cm^2 and ca. 40.9 μg/cm^2 respectively. QCM kinetics was also followed during the second step of immersion of the composite film ODA-TiF_6^{2-} and ODA-ZrF_6^{2-} in 1 % and 10% ammonia solution respectively at 50 °C for their complete hydrolysis to yield TiO_2 and ZrO_2 nanoparticles respectively within the lipid matrix. As shown in Figure 6.9, hydrolysis of ODA-TiF_6^{2-} film led to an apparent additional mass uptake of 6.3 μg/cm^2 and with ODA-ZrF_6^{2-} film almost no mass change was observed even after complete hydrolysis. Though in both cases of ODA-TiF_6^{2-} and ODA-ZrF_6^{2-} films, a decrease in mass during first few minutes of hydrolysis followed by an increase in mass was observed, the initial decrease was more prominent in the latter case. It is interesting to observe here that the two systems though being apparently

analogous, exhibit very different mass uptake behavior as implied by the QCM kinetics measurements during initial metal ion incorporation and during their subsequent hydrolysis. The observed 4 times greater mass uptake by 250 Å thick ODA film immersed in K_2ZrF_6 solution as compared to K_2TiF_6 solution is possibly influenced by factors such as, higher atomic weight of Zr (Zr, at. wt. 91.224, Ti, at. wt. 47.867) and

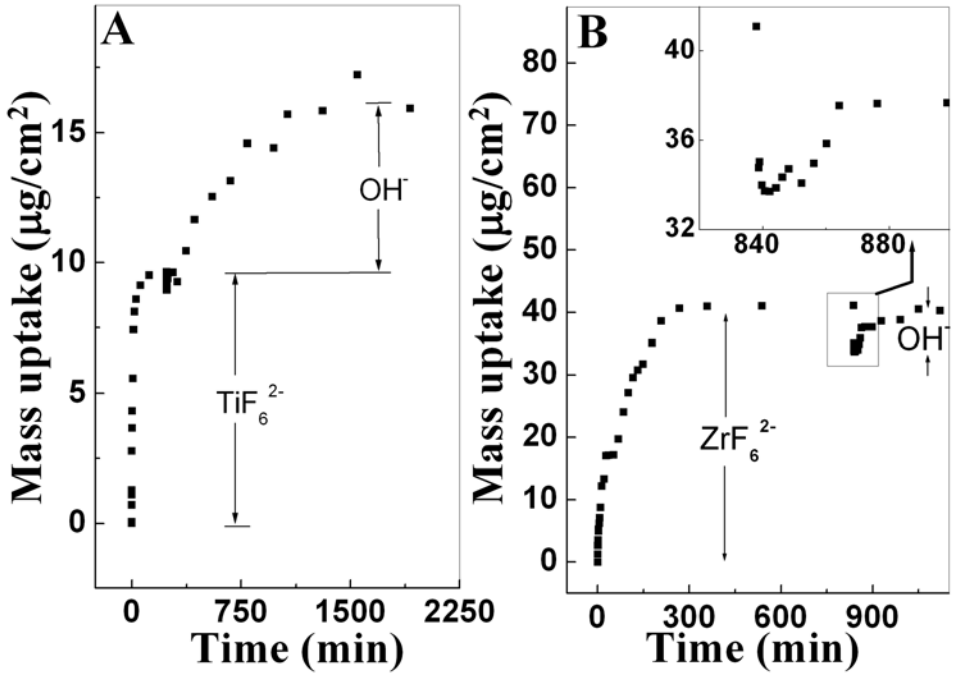

Figure 6.9: *QCM mass uptake kinetics for a 250 Å thick ODA film during A) immersion in 10^{-3} M $K_2TiF_6^{2-}$ solution and its subsequent immersion in 1 % ammonia solution at 50 °C and B) immersion in 10^{-3} M $K_2ZrF_6^{2-}$ solution and its subsequent immersion in 10 % ammonia solution at 50 °C.*

larger radius of Zr complex relative to Ti complex leading to greater increase in thickness of the lipid film, though these factors may not completely account for it. Varying degree of intake of TiF_6^{2-} and ZrF_6^{2-} ions could also be as a consequence of different extent of hydrolysis of MF_6^{2-} ions (M = Ti or Zr) to $MF_{(6-n)}(OH)_n^{2-}$ that though, dose not change the net charge of the complex but may have different diffusivity into the lipid matrix. During hydrolysis of the composite film the initial reduction in mass change (mass release) is due to conversion of the MF_6^{2-} complex ion to MO_2 with release of F^- ion. In case of ODA-ZrF_6^{2-} composite film the reduction was more prominent. The release of F^- ions during hydrolysis of the ODA-MF_6^{2-} composite film has been characterized by XPS (as has been discussed later) which shows the absence of F^- ions to detectable limit. The

mass uptake observed in the later part of hydrolysis leading to no net mass change with ODA-ZrF_6^{2-} composite film but a high mass gain with ODA-TiF_6^{2-} composite film is unusual. It may be mentioned here that the inferred mass uptake is derived from the observed frequency change in the Quartz crystal. The frequency change, due to the damping of the acoustic waves at the surface of the coated quartz crystal is dependent on the material properties, viz, density and viscoelastic properties of the coated material. Hence, it is possible that the observed discrepancies both during uptake of TiF_6^{2-}/ZrF_6^{2-} ions and during hydrolysis of the ODA-TiF_6^{2-}/ODA-ZrF_6^{2-} composite film could be a result of the different acoustic properties of these materials. This effect seems to be more pronounced during the later part of hydrolysis when the oxide nanoparticles start forming after initial release of F^- ions. As it is used now, the analysis makes no allowance for such a change in the acoustic properties and treats the film after hydrolysis as being similar to the precursor film. In any case, changes in the apparent 'mass' of the film with time may be viewed indirectly as an indicator of changes in the ODA-TiF_6^{2-} film during hydrolysis and will be viewed in this sense. The optimum times of immersion of the ODA films in K_2TiF_6/K_2ZrF_6 and ammonia solutions determined from the QCM measurements were used in the preparation of ODA-TiF_6^{2-}/ ODA-ZrF_6^{2-} and ODA-titania/ODA-Zirconia nanoparticle samples for additional studies.

6.4.1b UV-Vis measurements:

The optical absorption spectrum recorded from a 250 Å thick ODA film after entrapment of TiF_6^{2-}/ZrF_6^{2-} ions and their subsequent hydrolysis is shown in Figure 6.10. It is observed that the ODA-TIF_6^{2-} film, after hydrolysis (curve 2, Figure 6.10A) exhibits a sharp absorption edge at ca. 350 nm (3.6 eV). The band gap for bulk titania is 3.2 eV [52] and therefore the existence of an absorption edge blue-shifted relative to the bulk counterpart is indicative of the formation of nanoscale titania in the ODA matrix. The observed blue-shift occurs due to quantum confinement effects and is a standard signature of the formation of nanoparticles [52]. The optical absorption spectrum after hydrolysis of ODA-ZrF_6^2 thin film exhibits a sharp absorption edge below 260 nm (curve 2, Figure 6.10B), which is comparable with that of previously reported for zirconia [53]. For ODA-ZrF_6^{2-} film before hydrolysis (curve 1, Figure 6.10B), the optical absorption curve showed a very small absorption in the UV region. The presence of absorption

above 230 nm is characteristic of monoclinic phase of zirconia [53] and suggests that the product obtained by the hydrolysis of ZrF_6^{2-} ions in the ODA film is monoclinic zirconia.

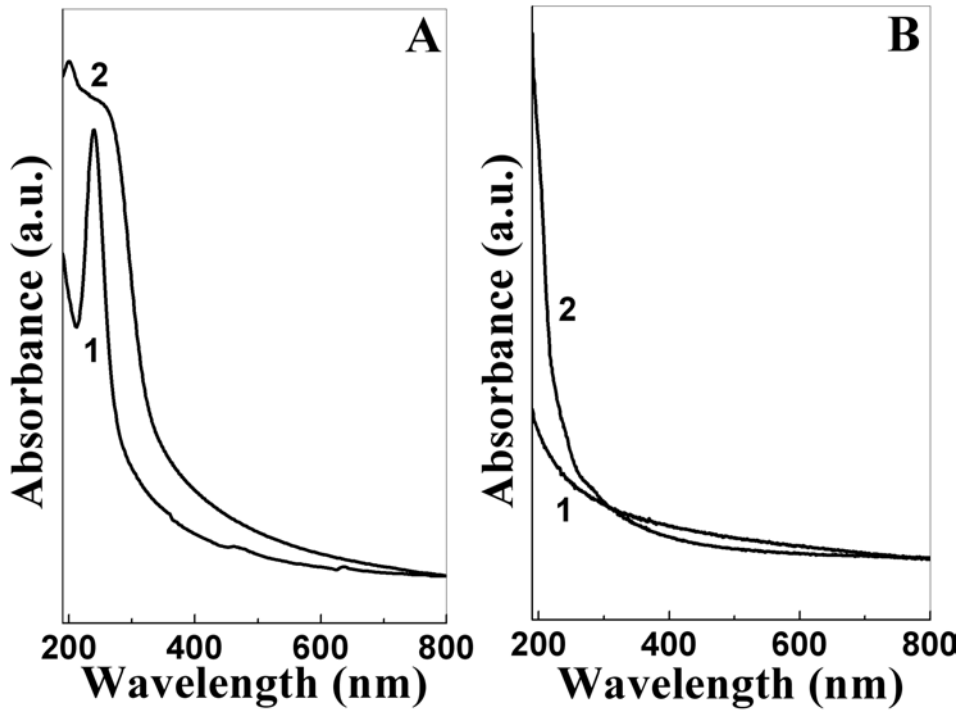

Figure 6.10: *UV-Vis spectra of a 250 Å thick ODA film after A) immersion in 10^{-3} M $K_2TiF_6^{2-}$ solution (curve 1) and its subsequent immersion in 1 % ammonia solution (curve 2) at 50 °C and B) immersion in 10^{-3} M $K_2ZrF_6^{2-}$ solution (curve 1) and its subsequent immersion in 10 % ammonia solution (curve 2) at 50 °C.*

6.4.1c FTIR measurements:

Figures 6.11A - D show the FTIR spectra in different spectral regions for the ODA thin films before and after entrapment of TiF_6^{2-} and ZrF_6^{2-} ions and after their subsequent hydrolysis. It is observed that after immersion of the ODA film into K_2TiF_6 solution, the peak in the FTIR spectra corresponding to N-H stretching frequency broadens and shifts from 3331 cm^{-1} to lower wavenumber centered at 3115 and 3144 cm^{-1} respectively. This indicates the complexation of the TiF_6^{2-}/ZrF_6^{2-} ions with the protonated amine group ($-NH_3^+$) of the ODA molecules during immersion of ODA thin film in aqueous K_2TiF_6/K_2ZrF_6 solutions. The broad peak may also have contribution from the water molecules hydrating the TiF_6^{2-}/ZrF_6^{2-} ions. Entrapment of TiF_6^{2-} ions into ODA thin film also leads to a shift in the NH_2 bending modes from 1644 and 1559 cm^{-1} to 1598

and 1530 cm^{-1} respectively, while on entrapment of ZrF_6^{2-} ions, doublets at 1596 and 1615 cm^{-1}; and at 1541 and 1524 cm^{-1} are observed in their place (Figure 6.11B and D).

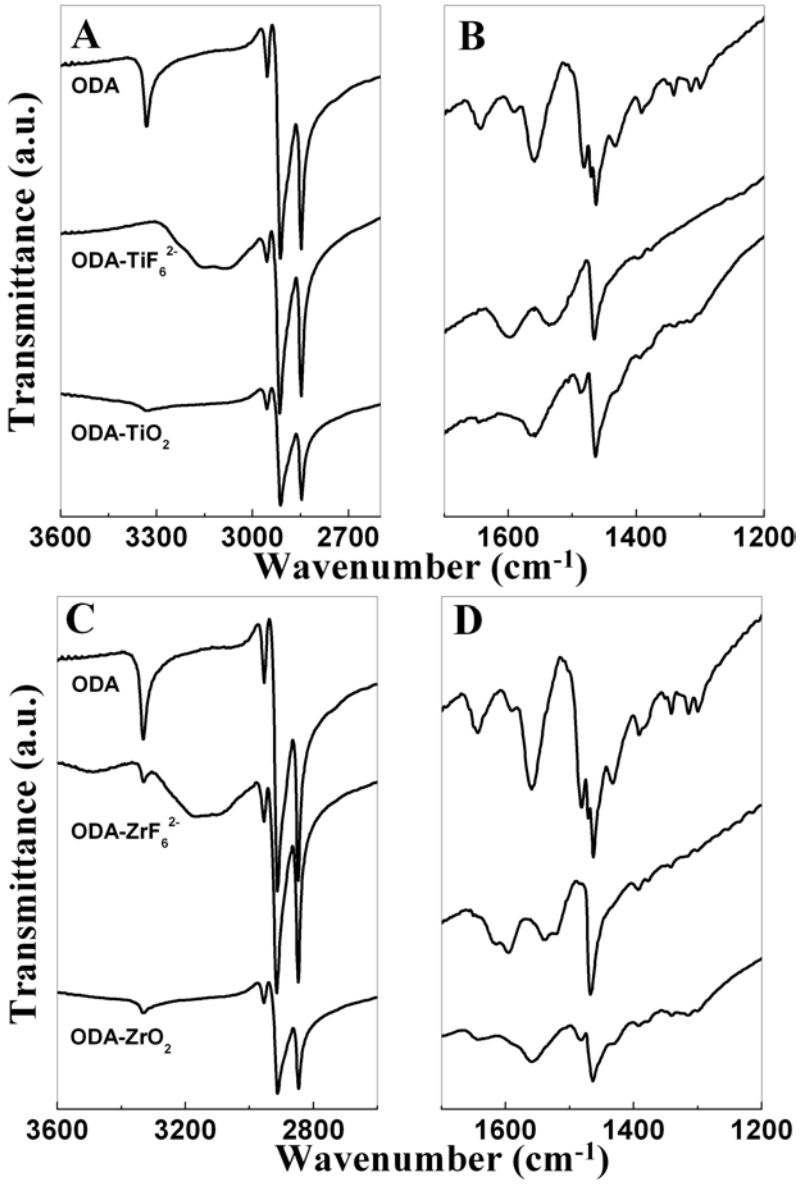

Figure 6.11: *FTIR spectra of a 250 Å thick ODA film and its spectra after its immersion in A) 10^{-3} M $K_2TiF_6^{2-}$ solution (ODA-$K_2TiF_6^{2-}$) and its subsequent immersion in 1 % ammonia solution (ODA-TiO_2) at 50 °C and B) 10^{-3} M $K_2ZrF_6^{2-}$ solution (ODA-$K_2ZrF_6^{2-}$) and its subsequent immersion in 10 % ammonia solution (ODA-ZrO_2) at 50 °C.*

The doublet observed in the region corresponding to NH bending modes and existence of weak peak at 3330 cm^{-1} indicates the presence of two different kinds of amine groups present in the film. Possibly there are few ODA molecules that are not complexed with the ZrF_6^{2-} ions. On further hydrolysis of the ODA-TiF_6^{2-}/ODA-ZrF_6^{2-} composite film, the

-NH_2 stretching and bending frequencies are regenerated although with reduced peak intensity. The reappearance of -NH_2 stretching and bending frequencies to values corresponding to plane ODA thin film is due to the release of the amine groups from a complexed state to a free state during the formation of TiO_2/ZrO_2 nanoparticles.

6.4.1d XPS measurements:

A detailed chemical characterization of the ODA film on Si (111) wafers was effected at different stages of treatment. Figure 6.12 shows the XPS of Ti 2p core level spectra recorded from a 250 Å thick ODA film after entrapment of TiF_6^{2-} ions (A) and after their subsequent hydrolysis (B). In both cases, the Ti 2p signal had to be resolved into two chemically shifted spin-orbit pairs. In the case of the ODA-TiF_6 composite film, the binding energies of the chemically distinct Ti $2p_{3/2}$ components were found from the fitting analysis to be 457.6 (**1**) and 460.1 eV (**2**). The intensity of the low BE component is much smaller than the 460.1 eV component in the as-prepared ODA-TiF_6 film. The 457.6 eV BE agrees well with the values reported from this laboratory in an earlier study of TiO_2 nanoparticles formed in solution [52]. The high BE component is clearly due to coordination of titanium atoms to a more electronegative element and is assigned to

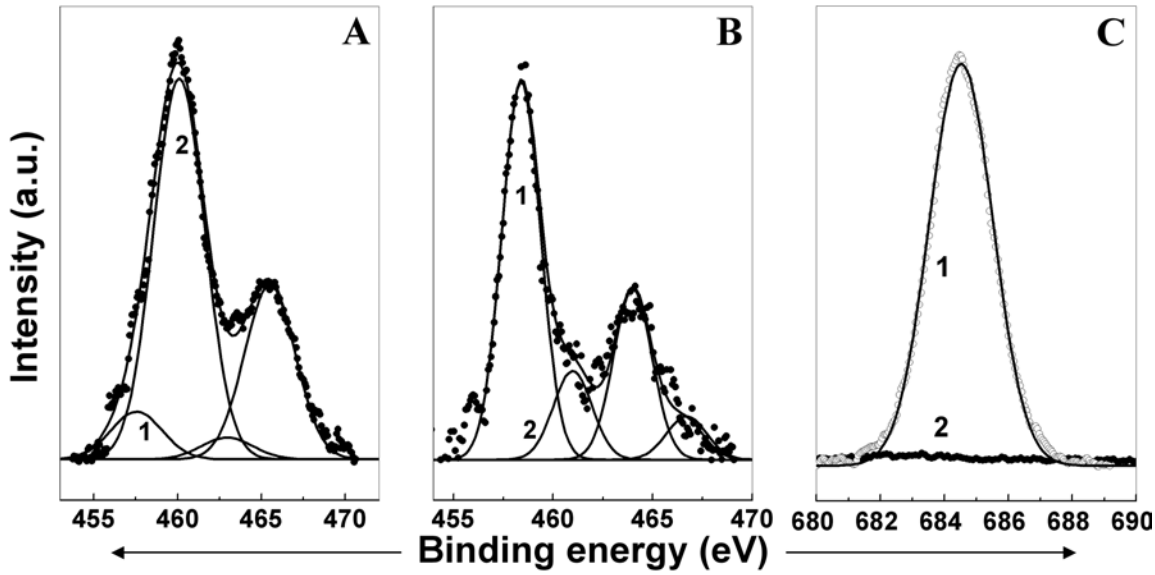

Figure 6.12: *XPS Ti 2p core level spectra decomposed into two chemically distinct species and their corresponding spin-orbit components: A) after entrapment of TiF_6^{2-} ions into a 250 Å thick ODA film and, B) after hydrolysis of TiF_6^{2-} entrapped in a 250 Å thick ODA film. C) F 1s core level spectra after entrapment of TiF_6^{2-} ions (curve 1) and their subsequent hydrolysis (curve 2).*

electron emission from the TiF_6^{2-} ions in the ODA matrix. The XPS results of Figure 6.12A thus clearly show that while the titanium ions in the ODA matrix are present predominantly as TiF_6^{2-} ions, a very small percentage of the titanium ions do undergo hydrolysis to yield a TiO_2 phase in the as-prepared sample. Figure 6.12B shows a similar analysis of the Ti 2p core level carried out on the ODA-TiF_6^{2-} composite film after hydrolysis. It is clearly seen that the low BE component (BE = 458 eV) has increased significantly in intensity relative to the high BE (BE = 461 eV) component. This indicates that a large fraction of the TiF_6^{2-} ions have undergone hydrolysis and have transformed to titania. As shown from the UV-vis measurements of Figure 6.10A, the outcome of the hydrolysis reaction is clearly the formation of quantum size titania nanoparticles. It would be interesting to follow the fate of the F^- ions after hydrolysis. There is a possibility that the F^- ions could complex with the $-NH_3^+$ groups in the ODA matrix after hydrolysis leading to a mass increase in the film as suggested by the QCM results (Figure 6.9A). Figure 6.12C shows the XPS spectra of F 2p core level recorded from the ODA-TiF_6 composite film before (curve 1) and after hydrolysis (curve 2). A significant reduction in the F 2p signal intensity is observed on hydrolysis indicating that the F^- ions

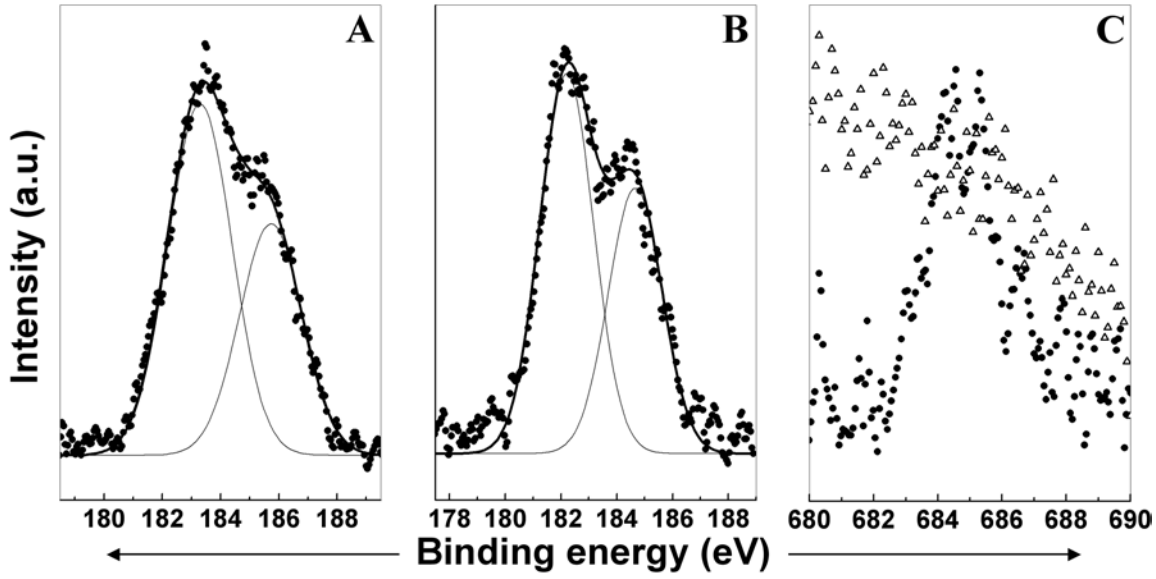

Figure 6.13: *XPS Zr 3d core level spectra decomposed into two chemically distinct species and their corresponding spin-orbit components: A) after entrapment of ZrF_6^{2-} ions into a 250 Å thick ODA film and, B) after hydrolysis of ZrF_6^{2-} entrapped in a 250 Å thick ODA film. C) F 1s core level spectra after entrapment of ZrF_6^{2-} ions (plot of solid circles) and their subsequent hydrolysis (plot of hollow triangles).*

do not remain within the ODA matrix. Similar characterization of the ODA thin film after entrapment of ZrF_6^{2-} ions and their subsequent hydrolysis was undertaken by XPS. Figure 6.13A and 6.13B show the Zr 3d core level spectra recorded from a 250 Å thick ODA film after entrapment of ZrF_6^{2-} ions (A) and subsequent hydrolysis of ODA-ZrF_6^{2-} film (B). In both cases, the Zr 3d signal was stripped into their respective spin-orbit components. In the case of ODA-ZrF_6^{2-} composite film, the binding energies (BE) of Zr $3d_{5/2}$ and Zr $3d_{3/2}$ components were found from the fitting analysis to be 183.3 and 185.7 eV respectively (A). After hydrolysis of the ODA-ZrF_6^{2-} film, the BEs of the Zr $3d_{5/2}$ and Zr $3d_{3/2}$ spin-orbit components were shifted to 182.2 and 184.7 eV respectively (B). The shift in BE of the Zr 3d core levels after hydrolysis towards lower values similar to the previous case indicates the coordination of Zr atoms with a less electronegative element as would happen during transformation of ZrF_6^{2-} to ZrO_2. That this is the likely scenario is supported by the fact that the Zr $3d_{5/2}$ BE of 182.2 eV recorded from the ODA-ZrF_6^{2-} film after hydrolysis agrees excellently with the Zr $3d_{5/2}$ BE of 182.4 eV reported in the literature for zirconia [54]. In Figure 6.13C photoelectron emission spectra for the F 1s core levels recorded before and after hydrolysis of the ZrF_6^{2-} ions entrapped in the ODA thin film is shown. While a clear peak corresponding to F 1s core level is observed before hydrolysis of the entrapped ZrF_6^{2-} ions, after hydrolysis a mere background is observed in the binding energy region corresponding to F 1s core level. The absence of signal for the F 1s core level after hydrolysis indicates the release of the F^- ions from the ZrF_6^{2-} complex and its expulsion from the ODA thin film in the process. The XPS results of Figure 6.13 thus clearly show that there is a complete hydrolysis of ZrF_6^{2-} ions to yield ZrO_2.

6.4.1e TEM measurements:

While in principle it is possible to make a rough estimate of the titania nanoparticle size from the shift in the absorption edge relative to bulk titania, a more direct analysis based on TEM would be desirable. Figure 6.14A shows a representative TEM images recorded from a 250 Å thick ODA film deposited on carbon-coated TEM grids after one cycle of TiF_6^{2-} entrapment and hydrolysis. It can be seen from this figure that there is a very high concentration of nanoparticles uniformly distributed over the surface of the film. The particles are fairly uniform in size, an analysis of which yields an

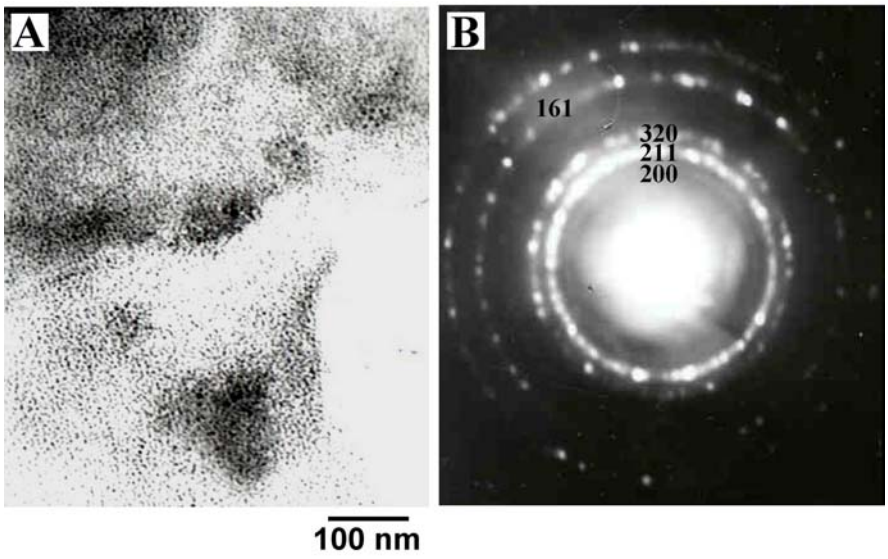

Figure 6.14: *A) Representative TEM micrograph of titania nanoparticles synthesized within a 250 Å ODA thin film (see text for details). B) SAED pattern recorded for titania nanoparticles synthesized within a 250 Å ODA thin film.*

average diameter of ~ 4 nm. Selected area electron diffraction (SAED) analysis of the nanoparticles shown in Figure 6.14A yielded a sharp diffraction pattern (Figure 6.14B) indicating that the particles are crystalline. The diffraction rings could be indexed based on the brookite structure of titania. Figure 6.15A and B show representative TEM images recorded from a 250 Å thick ODA film deposited on carbon-coated TEM grids after one

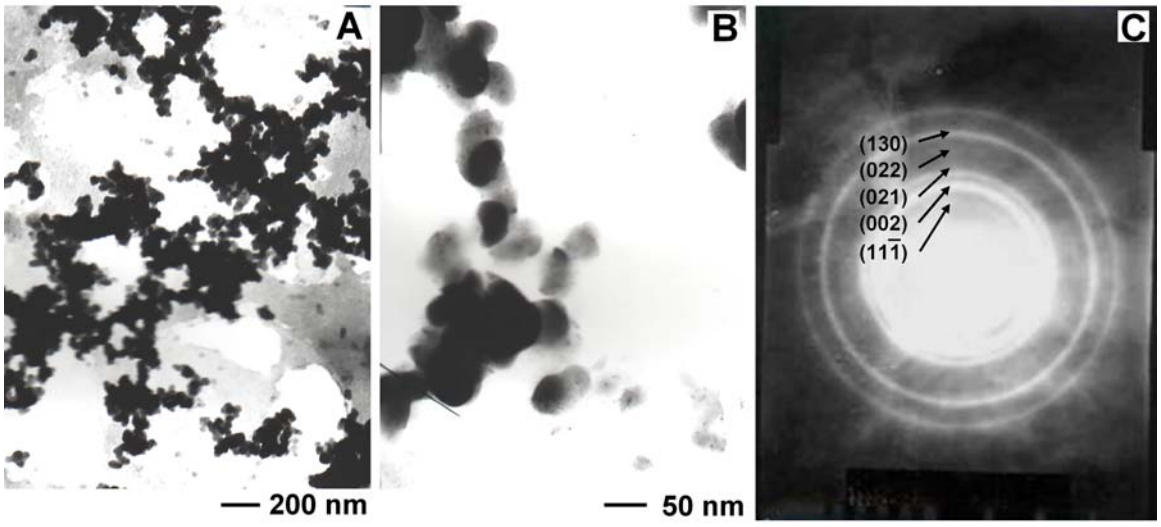

Figure 6.15: *A and B- Representative TEM images of zirconia nanoparticles synthesized within a 250 Å ODA thin film at different magnifications. C) SAED pattern recorded from zirconia nanoparticles synthesized within a 250 Å ODA thin film.*

cycle of ZrF_6^{2-} entrapment and hydrolysis under different magnifications. At lower magnification (Figure 6.15A), it can be seen that there is a very high concentration of nanoparticles distributed over the surface of the film. The particles are fairly uniform in size with an average diameter of ~ 40 nm (Figure 6.15B). Selected area electron diffraction (SAED) analysis of the nanoparticles shown in Figure 6.15A yielded a sharp diffraction pattern (Figure 6.15C) indicating that the particles are crystalline. The diffraction rings could be indexed based on the monoclinic structure of zirconia. It is thus observed that, while in case of titania the particle size is ~ 4 nm, the particle size of zirconia nanoparticles synthesized in a similar way is ~ 40 nm. This difference in particle size apart from the different inherent properties of TiO_2 and ZrO_2 nanoparticles may also be a reason for the different acoustic properties of the ODA-TiO_2/ODA-ZrO_2 composite filmsleading to the different apparent mass uptake observed during QCM measurements as discussed in section 6.4.1-a.

6.4.1f XRD measurements:

Figure 6.16A and 6.17A shows the XRD pattern recorded from a 250 Å thick ODA film on Si (111) substrate after entrapment of TiF_6^{2-} and ZrF_6^{2-} ions respectively. The diffraction pattern shows sharp (0 0 l) Bragg reflections with a characteristic odd-even intensity oscillation that is symptomatic of lamellar c-axis ordering of the titanium or zirconium complex ions in the ODA matrix [20]. From the separation between the (0 0 l) Bragg reflections, the bilayer thickness in the ODA-TiF_6^{2-} and ODA-ZrF_6^{2-} composite thin film was found to be ca. 50.9 nm and 50.7 nm respectively. This repeat distance is in good agreement with the dimensions of the ODA molecule and the TiF_6^{2-} and ZrF_6^{2-} complex ions. Since, more intense and higher order (00l) reflections are observed in case of ODA-ZrF_6^{2-} thin films, it appears that ZrF_6^{2-} ions lead to better ordering of the ODA thin film as compared to TiF_6^{2-} ions. The XRD pattern recorded from the ODA-TiF_6 composite film after hydrolysis is shown in Figure 6.16B. It can be seen from this figure that there are a number of Bragg reflections (which were absent prior to the hydrolysis step) indicating that the titania nanoparticles are quite crystalline. Analysis of the diffraction pattern indicated that the Bragg reflections correspond mostly to the brookite phase and to a small extent to the rutile phase. The various Bragg reflections have been indexed in Figure 6.16B with the prefix 'B' and 'R' corresponding to the brookite and

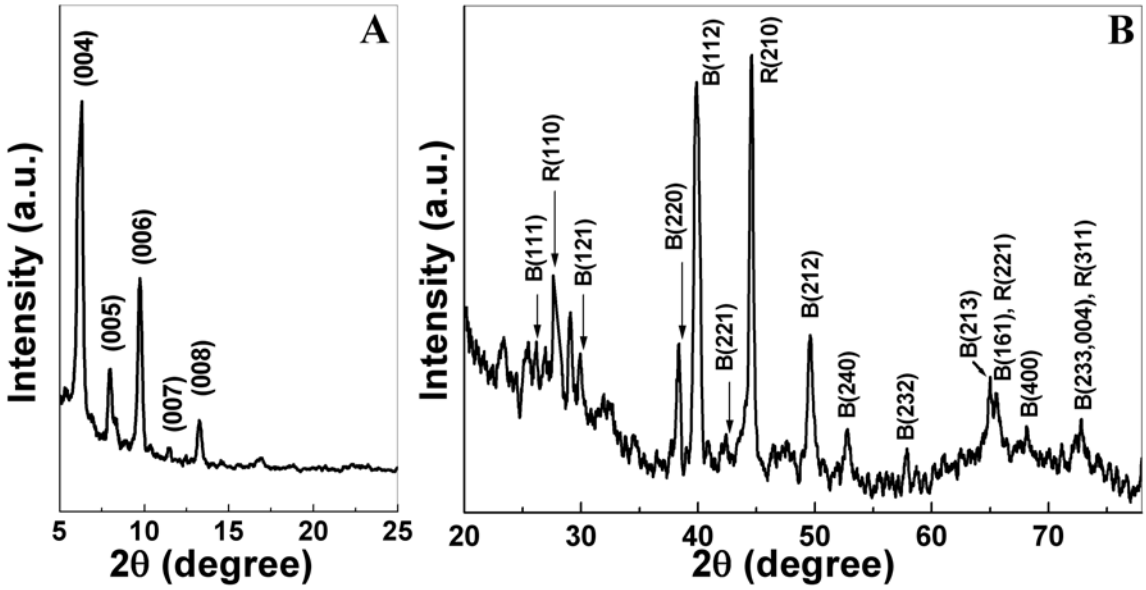

Figure 6.16: *XRD pattern of 250 Å thick ODA film A) after entrapment of TiF_6^{2-} anions, indicating lamellar ordering within the film with a periodicity of ca. 50.9 nm. B) ODA composite thin film after hydrolysis of entrapped TiF_6^{2-} anions with 1 % ammonia solution.*

rutile phases respectively. An important feature of the diffraction pattern is that the intensity ratios of the different Bragg reflections from a particular crystallographic phase are quite different from that of reported powder diffraction patterns. This clearly indicates that the titania crystallites in the lipid matrix are oriented with specific crystallographic planes parallel to the substrate. It is observed that oriented growth of the brookite phase along the (112) and (212) directions has taken place. The commonly observed products of hydrolysis of titanium compounds[55] in solution are anatase and rutile. In some cases, brookite is observed as a by-product when the hydrolysis of titanium complexes is carried out in an acidic medium at low temperatures[55e,f,56] or when the precipitate formed from $TiCl_4$ and ammonia is aged for a 15 month period [57]. Classically, brookite is obtained as large crystals by hydrothermal methods at high temperatures and pressure ($200 \leq T \leq 400$ °C, $10 \leq P \leq 400$ bar) in aqueous [58] or in organic media [59]. It has been reported that the presence of some alkaline and alkaline earth metal ions induces the formation of brookite phase. Though sodium has been observed to produce in some cases pure brookite phase, potassium has been observed to result in a mixture of brookite and anatase forms [59]. In this study, we obtain a mixed phase of brookite and rutile unlike in the above report where the second phase obtained was anatase. The most interesting feature of the titania nanoparticle synthesis procedure described in this paper is that even

under basic solution and very mild temperature conditions (50 ^{o}C), the ODA film is able to favor the formation of brookite rather than the more stable forms, anatase and rutile. Oriented growth of the brookite nanocrystals as discussed above indicates that there is some degree of epitaxy between specific crystallographic faces of this polymorph and the ODA bilayer template, thus stabilizing the brookite phase. Other possibilities for stabilizing the brookite phase include the presence of potassium ions within the interlamellar regions of the ODA bilayer structure and a locally acidic environment that

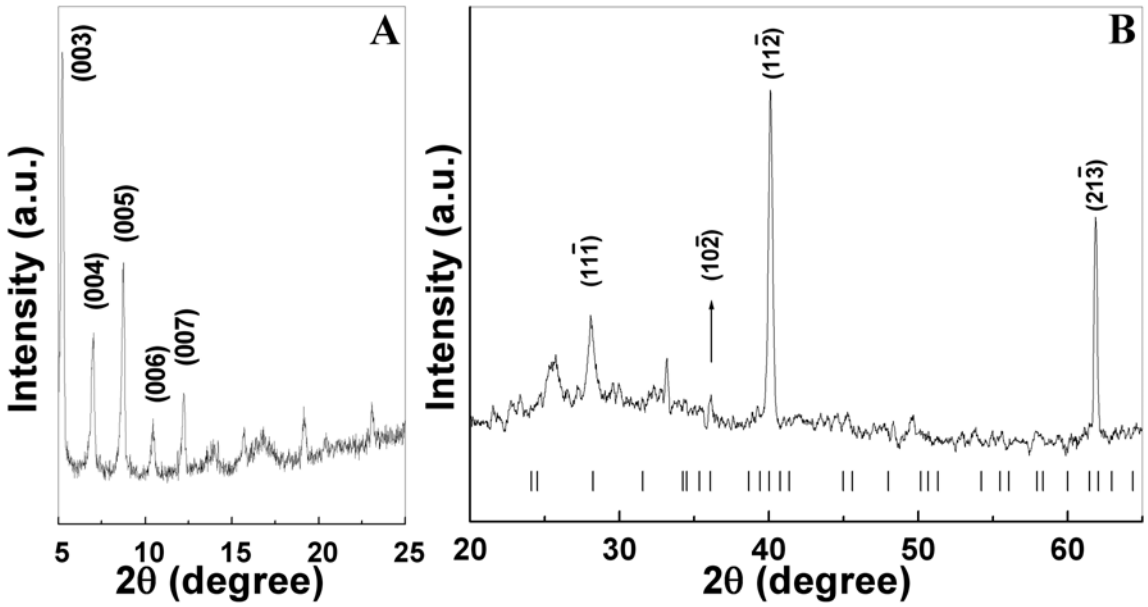

Figure 6.17: *XRD pattern of 250 Å thick ODA film A) after entrapment of ZrF_6^{2-} anions, indicating lamellar ordering within the film with a periodicity of ca. 50.9 nm. B) ODA composite thin film after hydrolysis of entrapped ZrF_6^{2-} anions with 10 % ammonia solution. The bars represent standard 2θ values of Bragg reflections for the monoclinic phase of zirconia.*

arises due to the presence of F^- ions released during the conversion of TiF_6^{2-} ions to their oxide form in the film. Analysis of the XRD pattern of the ODA-ZrF_6^{2-} composite film after hydrolysis, shown in the Figure 6.17 indicated that the Bragg reflections correspond to the monoclinic phase of zirconia, which is known to be the stable form of zirconia below 1200 ^{o}C [60]. As in the previous case the intensity ratios of the different Bragg reflections are quite different from that of typical powder diffraction patterns of zirconia and indicate a preferred orientation along the (11-2) direction in them.

6.4.2 Synthesis of CdS nanoparticles within thermally evaporated thin films of AOT:

6.4.2a QCM measurements:

Figure 6.18 shows the QCM kinetics data for the mass uptake by the 500 Å AOT film during immersion in the $CdCl_2$ solution at regular intervals. From the equilibrium mass loading of the cadmium ions (48 $\mu g/cm^2$) in the thin film and the knowledge of the AOT mass deposited initially, an AOT:Cd^{2+} molar ratio of 1:42 was calculated. The above observation clearly indicates considerable overcompensation of the negative charge due to the sulfate groups in the AOT matrix by the Cd^{2+} ions. Such charge overcompensation (though not to this extent) is known to occur in the layer-by-layer electrostatically assembled systems [61]. This 'apparently' large charge overcompensation could also be due to a large change in the acoustic properties of the AOT film consequent to Cd^{2+} entrapment as observed in the previous section during entrapment of ZrF_6^{2-} ions into ODA thin film. During the next cycle of treatment of the cadmium-sulfosuccinate film in Na_2S solution for the formation of CdS nanoparticles

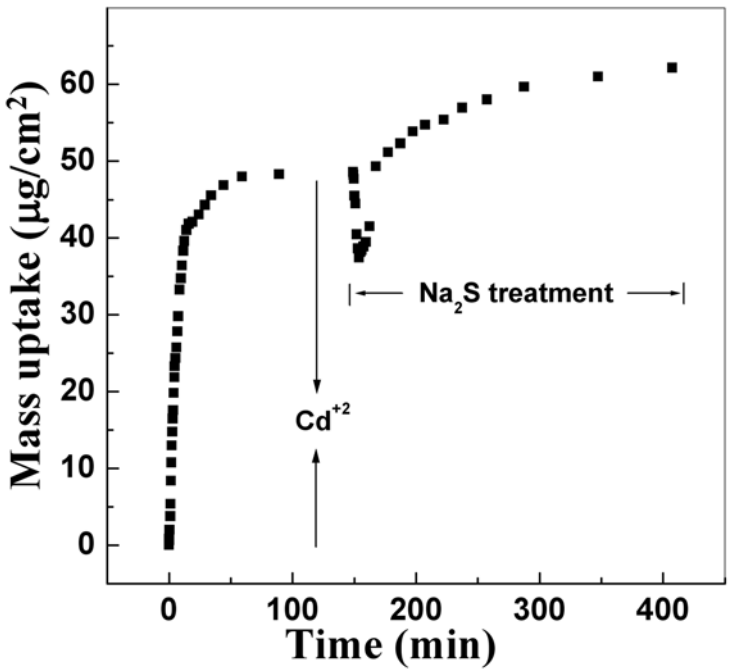

Figure 6.18: *Quartz crystal microgravimetry measurements of the Cd^{2+} mass intake in a 500 Å thick AOT film as a function of time of immersion in the $CdCl_2$ solution and thereafter, reaction with sulfide ions by immersion in Na_2S solution.*

(Figure 6.18), it is observed that there is an initial decrease in mass of the film. The mass change in the film reaches a minimum after approximately 5 minutes of immersion with a ca. mass loss of 10.2 μg/cm^2. This fall in mass is followed by an increase giving a subsequent mass uptake of ca. 24.8 μg/cm^2 after 6 hrs of immersion leading to a net mass uptake of 14.7 μg/cm^2 relative to the Cd^{2+} ions entrapped AOT film. Such anomalous variation in mass change was also observed during hydrolysis of ODA-TIF_6^{2-} /ODA-ZrF_6^{2-} composite and may be explained on the basis of similar arguments discussed above. The initial mass loss could be due to partial leaching out of the cadmium ions or the nitrate ions that could have been entrapped within the AOT film as a counter ion to compensate the excess charge accumulated dueto the excess intake of Cd^{2+} ions in AOT thin film as observed from QCM measurements. The mass increase observed thereafter could be explained on the basis that during formation of CdS, an uncharged entity, fresh sulfonate groups are regenerated leading to the possibility of complexation of positively charged Na^+ ions within the film. Another possible contributing factor as discussed in the above section for the metal oxide systems, the observed mass increase could be a consequence of the large change in the acoustic properties of the composite nanoparticulate thin film of AOT with entrapped semiconducting nanoparticles.

6.4.2b UV-vis spectroscopy measurements:

The cadmium-sulfosuccinate film following Na_2S treatment exhibited a yellowish tinge clearly indicating the formation of CdS nanoparticles. Figure 6.19 shows the UV/vis spectrum recorded from the 500 Å thick film after treatment with S^{2-} ions. From the UV/vis absorption spectrum,

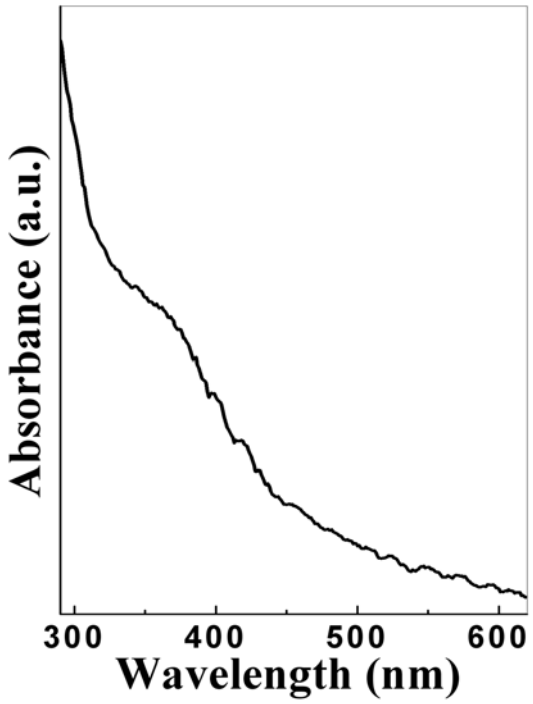

Figure 6.19: *UV/Vis absorption spectrum of CdS nanoparticles synthesized within a 500 Å thick AOT film deposited on a quartz substrate by electrostatic entrapment of Cd^{2+} ions followed by treatment with S^{2-} ions.*

it is seen that an absorption band with an onset of absorption located at ca. 413 nm occurs in the chemically treated cadmium-sulfosuccinate thin film. This absorption edge is blue-shifted relative to bulk form of CdS, which is known to occur at 510 nm. The blue-shift in the absorption edge observed here with AOT thin films is an indicator that the CdS

$$E(R_0) = E_0 + \frac{\hbar^2 \pi^2}{2}\left(\frac{1}{m_e} + \frac{1}{m_h}\right)\frac{1}{R_0{}^2} - \frac{1.8e^2}{\varepsilon}\cdot\frac{1}{R_0} + \frac{e^2}{R_0}\overline{\sum_{n=1}^{\infty}\alpha_n\left(\frac{S}{R_0}\right)^{2n}} \qquad \textbf{……..(1)}$$

nanoparticles formed within the AOT matrix are in the quantum dot regime. An estimate of the CdS nanoparticle size may be made from the following equation obtained by Brus [62] for the lowest direct interband transition energy of a spherical quantum dot of radius R_0 in the effective mass approximation :

where E_0 is the band gap in the bulk form, m_e and m_h are the effective mass of electrons and holes respectively, e the electronic charge, ε the dielectric constant of the material, α_n a function of dielectric constants and S is electron-hole separation. The second term in the right hand side of equation (1) represents the quantum localization energy. The third and fourth terms correspond to the Coulomb potential and polarization energy respectively. For nanoparticles of CdS with radius in the range 1 to 4 nm, the polarization term is typically one third of the Coulomb term with opposite sign [62]. Incorporation of correction for the polarization term by appropriately rescaling the coefficient of the coulomb term leads to the following simplified expression for the energy E(R) for CdS particles of radius R, E_0 = 2.43 eV and ε = 5.7.

From equation (2), the radius of the CdS quantum dots synthesized within the AOT thin films was estimated to be 1.8 nm. We would like to emphasize here that the size of the

$$E(R) = 2.43 + \frac{2.446}{R^2} - \frac{0.3031}{R} \qquad \textbf{…….. (2)}$$

CdS nanoparticles grown in AOT thin films is significantly smaller than that observed in an earlier study from this laboratory on CdS growth in thermally evaporated stearic acid films where the absorption band edge was observed at 470 nm [21a].

6.4.2c FTIR measurements:

FTIR measurements for the AOT thin film of thickness 500 Å were done at each

stage of treatment to study the complexation of the Cd^{2+} ions to the AOT molecules after immersion in $CdSO_4$ solution and after treatment with Na_2S solution for CdS nanoparticle synthesis. The spectrum corresponding to a pure AOT thin film represented as curve 1 in Figure 6.20 showed peaks at 1160 cm^{-1} and 1052 cm^{-1} corresponding to asymmetric and

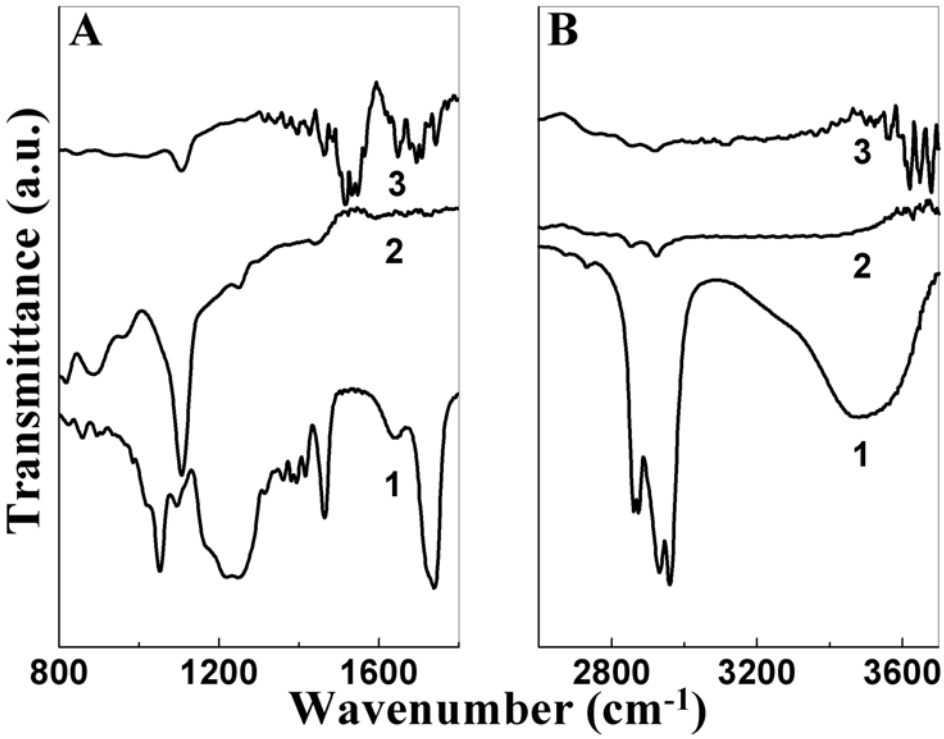

Figure 6.20: *FTIR spectra recorded from a 500 Å thick AOT film (curve 1) on Si (111) wafer, the AOT film shown as curve 1 after entrapment of Cd^{2+} ions (curve 2) and the Cd-AOT film shown as curve 2 after treatment with Na_2S solution (curve 3) in two different spectral windows.*

symmetric stretch vibrations of the sulfonate groups and at 1247 cm^{-1} which corresponds to the ester stretch (-C(=O)-O-C) [63]. A shift in S-O stretching frequency from 1160 to 1113 cm^{-1} was observed in the AOT film after immersion in $CdCl_2$ solution (curve 2, Figure 6.20). After formation of CdS (curve 3, Figure 6.20A), there is no further shift in the peak value corresponding to S-O stretching vibrational mode indicating that the AOT molecules are still bound to the cadmium ions on the surface of the CdS nanocrystals or could possibly be due to the presence of Na^+ ions as discussed above in relation to the observed QCM mass change. The intense peaks at 2854 and 2924 cm^{-1} corresponding to methylene antisymmetric and symmetric vibrational modes in AOT (curve 1) as shown in Figure 6.20 are reduced in intensity after incorporation of Cd^{2+} ions (curve 2) and further reduced after formation of CdS (curve 3) indicating randomization in the orientation of

the hydrocarbon chains consequent to ion entrapment.

6.4.2d EDAX measurements:

The elemental composition of the composite CdS-AOT thin film was determined using energy dispersive analysis of X-rays (EDAX). The EDAX spectrum recorded from a 500 Å thick AOT film after formation of CdS nanoparticles is shown in Figure 6.21. A quantitative analysis of the film revealed that the atomic ratio of Cd and S in the film is *ca.* 1 : 2.2. It should be noted here that the contribution of the S atoms in the EDAX spectrum comes from S atoms present in the AOT molecules and from those in the CdS nanoparticles and this probably explains the larger than unity molar ratio of sulfur relative to cadmium.

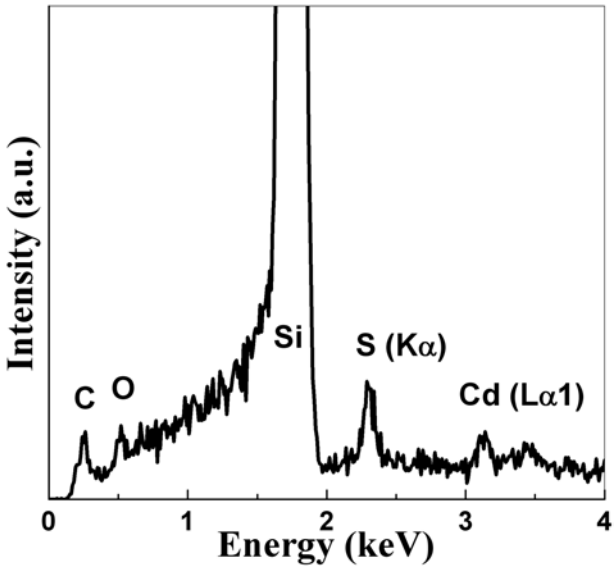

Figure 6.21: *EDAX spectrum showing the presence of cadmium and sulfur in a 500 Å thick composite CdS nano-AOT film.*

6.4.2e TEM measurements:

Figure 6.22A shows a low magnification TEM image of CdS nanoparticles formed in a 500 Å thick AOT thin film as described earlier. While an exact estimate of the particle size cannot be made from this image, it is clear that the CdS nanoparticles are formed at sufficiently high density within the AOT film. A better idea of the particle size and shape may be drawn from the high magnification TEM image of the nano CdS-AOT composite film shown in Figure 6.22B. From this image, it is clearly seen that the particles are essentially spherical and fairly monodisperse. Figure 6.22C shows the particle size distribution histogram measured from a number of CdS nanoparticles shown in Figure 6.22B and other similar images. From a Gaussian fit to the histogram (solid line, Figure 6.22C), an average CdS nanoparticle size 3 ± 0.6 nm was estimated.

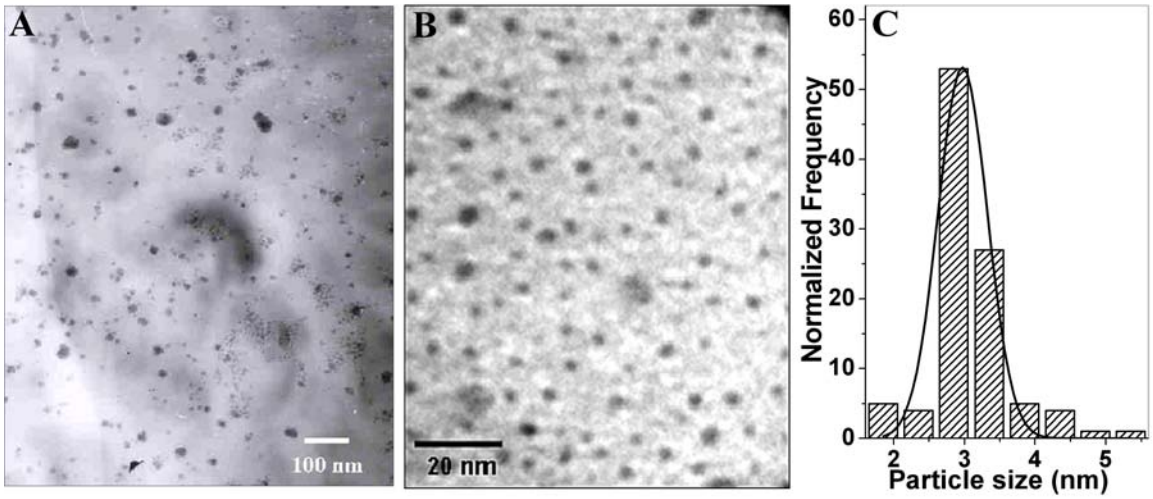

Figure 6.22: *A) Low magnification and B) high magnification TEM images of CdS nanoparticles synthesized in a 500 Å thick thermally evaporated AOT film. C) Particle size distribution of CdS nanoparticles formed in a thermally evaporated 500 Å thick AOT film deposited on a carbon-coated copper TEM grid. The solid line is a Gaussian fit to the particle size distribution histogram.*

6.4.2f XRD measurements:

From XRD measurements as shown in Figure 6.23, it was concluded that the particles are hexagonal CdS nanocrystals [64]. XRD measurement of the AOT thin film after incorporation of Cd^{2+} ions showed no lamellar ordering which is commonly

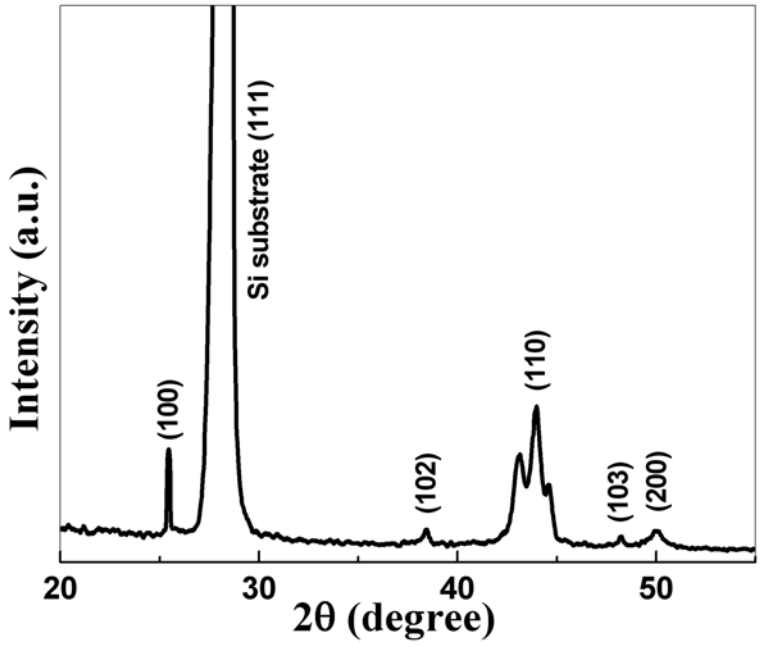

Figure 6.23: *XRD pattern of 500 Å thick AOT film after entrapment of Cd^{2+} ions and its subsequent immersion in aqueous Na_2S solution.*

observed in case of stearic acid or octadecyl amine [20]. AOT has double hydrocarbon chains, and unlike them stearic acid and octadecyl amine molecules are single chained molecules and tend to pack in planar structures in the form of bilayer stacks [20]. AOT as mentioned above has an inherent tendency to form spherical reverse micelles. Perhaps due to this nature, AOT is able to inhibit the growth of the CdS nanoparticles and thus helps in forming quantum dots with a better size control.

6.5 Conclusion.

We have shown the possibility of entrapping biologically synthesized protein capped gold nanoparticles both into cationic and anionic lipid thin films by simply varying the pH of the solution. Electrostatic entrapment of nanoparticles is facilitated into anionic lipid thin films when the pH of the biosynthesized gold nanoparticles solution is lesser than the pI value of the capping protein, and conversely into a cationic lipid thin film when the pH is above the pI value. It has been shown that the anionic stearic acid films have greater propensity towards immobilization of larger and flat nanoparticles as compared to the cationic octadecylamine thin films. It has also been observed that the electrostatic entrapment of simple metal ions or their complex ions within AOT or fatty amine thin films provides an efficient route for the synthesis of CdS, titania and zirconia nanoparticles with a fair degree of size control. Using patterned thin films of lipids and entrapping inorganic nanoparticles in these confined regions by either direct electrostatic entrapment of nanoparticles or the metal ions followed by their chemical treatment can prove to be an efficient route for fabricating a great variety of intricate nanoparticulate structures.

6.6 References:

1) Bandyopadhyay, M.; Birkner, A.; van den Berg, M. W. E.; Klementiev, K. V.; Schmidt, W.; Grunert, W.; Gies H. *Chem. Mater.*, **2005,** *17,* 3820.
2) Selvakannan, PR.; Kumar, P. S.; More, A. S.; Shingte, R. D.; Wadgaonkar, P. P.; Sastry M. *Adv. Mater.*, **2004**, *16*, 966. b) Sastry, M.; Swami, A.; Mandal S.; Selvakannan, PR. *J. Mater. Chem.*, **2005**, *15*, 3161.
3) Jiang, C.; Markutsya, S.; Shulha, H.; Tsukruk V. V. *Adv. Mater.*, **2005**, *17*, 1669.
4) a) Liu , X.; Fu, L.; Hong, S.; Dravid, V. P.; Mirkin C. A. *Adv. Mater.*, **2002**, *14*, 231. b) Koike, K.; Matsuyama, H.; Hirayama, Y.; Tanahashi, K.; Kanemura, T.; Kitakami, O.; Shimada, Y. *Appl. Phys. Lett.*, **2001**, *78*, 784.
5) a) Beecroft L. L.; Ober C. K. *Chem. Mater.*, **1997**, *9*, 1302. b) Jacobs, H. O.; Whitesides, G. M. *Science*, **2001**, *291*, 1763. c) Ho, P. K. H.; Thomas, D. S.; Friend, R. H.; Tessler, N. *Science*, **1999**, *285*, 233.
6) O'Regan, B.; Grätzel, M. *Nature (London)*, **1991**, *353*, 737.
7) a) Renault, J. P.; Bernard, A.; Juncker, D.; Michel, B.; Bosshard, H. R.; Delamarche, E. *Angew. Chem., Int. Ed.*, **2002**, *41*, 2320. b) Pirrung, M. C. *Angew. Chem., Int. Ed.*, **2002**, *41*, 1276.
8) a) Kreibig, U. *Z. Physik* **1970**, *234*, 307. b) Alivisatos, A. P. *Science*, **1996**, *271*, 933. b) Landes, C. F.; Link, S.; Mohamed, M. B.; Nikoobakht, B.; El-Sayed, M. A. *Pure Appl. Chem.*, **2002**, *74*, 1675. c) Kreibig, U.; Genzel, L. *Surface. Sci.*, **1985**, *156*, 678. d) Brus, L. *J. Phys. Chem.*, **1986**, *90***,** 2555. e) Henglein, A. *Top. Curr. Chem.*, **1988**, *143*, 113. f) Paterson, M. W.; Micic. O. I..; Nozik, A. J. *J. Phys. Chem.*, **1988**, *92*, 4160.
9) a) Pileni, M. P. *J. Phys. Chem. B*, **2001**, *105*, 3358. b) Petit, C.; Taleb, A.; Pileni, M. P. *J. Phys. Chem. B*, **1999**, *103*, 1805. c) Yuen, K. P.; Law, M. F.; Yu, K. W.; Sheng P. *Phys. Rev. E*, **1997**, *56*, R1322. d) Bieganski, P.; Dobierrzewska-Mozrzymas, E.; Peisert, J. *Physica* A, **1989**, *157***,** 323. e) Doremus, R. H. *J. Appl. Phys.*, **1966**, *37*, 2775. f) Collier, C.P.; Henrichs, S.E.; Shiang, J.J.; Saykally R.J.; Heath, J.R. *Science*, **1997**, *277*, 1978. g) Maier, S. A.; Brongersma, M. L.; Kik, P. G.; Meltzer, S.; Requicha, A. A. G.; Atwater, *Adv. Mater.*, **2001**, *13*, 1501.

10) a) Gao, G. *Nanostructures and Nanomaterials: Snthesis, Properties and Applications*, Imperial College Press, London, Chapter 5, **2004**. b) H.S.Nalwa (ed.), *Handbook of Thin Film Materials, Vol. 1: Deposition and Processing of Thin Films*, Academic Press, San Diego, CA, **2002**. c) Liang, J.; Chik, H.; Yin, A.; Xu, J. *J. Appl. Phys.*, **2002**, *91*, 2544. d) Crouse, D.; Lo, Y. H.; Miller, A. E.; Crouse, M. *Appl. Phys. Lett.*, **2000**, *76* 49. e) Knaack, S. A.; Eddington, J.; Leonard, Q.; Cerrinia, F.; Onellion, M. *Appl. Phys. Lett.*, **2004**, *84*, 3388. f) Bullen, H. A.; Garrett, S. J. *Nano Lett.*, **2002**, *2*, 739. g) Masuda, H,; Yasui, K.; Nishio, K. *Adv. Mater.*, **2000**, *12*, 1031. h) Sander, M. S.; Tan, L. S. *Adv. Funct. Mater.*, **2003**, *13*, 393.

11) a) Murray, C. B.; Kagan, C. R.; Bawendi, M. G. *Annu. Rev. Mater. Sci.*, **2000**, *30*, 545. b) Sarathy, K. V.; Raina, G.; Yadav, R. T.; Kulkarni, G. U.; Rao, C. N. R. *J. Phys. Chem. B*, **1997**, *101*, 9876. c) Sarathy, K. V.; Kulkarni, G. U.; Rao, C. N. R. *Chem. Comm.*, **1997**, 537.

12) a) Hayward, R. C.; Saville, D. A.; Aksay I. A. *Nature*, **2000**, *404*, 56. b) Trau, M.; Saville, D. A.; Aksay, I. A. *Science*, **1996**, *272*, 706. c) Böhmer, M. *Langmuir*, **1996**, *12*, 5747. d) Giersig, M.; Mulvaney, P. *J. Phys. Chem.*, **1993**, *97*, 6334. e) Giersig, M.; Mulvaney, P. *Langmuir*, **1993**, *9*, 3408.

13) a) Kovtyukhova, N. I.; Buzaneva, E. V.; Waraksa, C. C.; Martin, B. R.; Mallouk, T. E. *Chem. Mater.*, **2000**, *12*, 383. b) Burnside, S. D.; Shklover, V.; Barbe, C.; Comte, P.; Arendse, F.; Brooks, K.; Gratzel, M. *Chem. Mater.*, **1998**, *10*, 2419.

14) a) Mamedov, A. A.; Kotov, N. A. *Langmui*, **2002**, *16*, 5530. b) Mamedov, A.; Ostrander, J.; Aliev, F.; Kotov, N. A. *Langmuir*, **2000**, *16*, 3941. c) Yi, K. C.; Fendler, J. H. *Langmuir*, **1990**, *6*, 1519. d) Yang, J.; Meldrum, F. C.; Fendler, J. H. *J. Phys. Chem.*, **1995**, *99*, 5500. e) Yang, J.; Fendler, J. H. *J. Phys. Chem.*, **1995**, *99*, 5505. f) Yang, J.; Fendler, J. H.; Jao, T. C.; Laurion, T. *Microsc. Res. Technol.*, **1993**, *27*, 402. g) Sastry, M., Ed. Nalwa, H. S., "Handbook of Surfaces and Interfaces of Materials" Vol 3, p 87, Academic Press, San Diego, 2001. h) Sastry, M.; Rao, M.; Ganesh, K. N. *Acc. Chem. Res.*, **2002**, *35*, 847. i) Swami, A.; Kumar, A.; Selvakannan, PR.; Mandal, S.; Sastry, M. *J. Colloid Int. Sci.*, **2003**, *260*, 367. j)

Selvakannan, PR.; Swami, A.; Srisathiyanarayanan, D.; Shirude, P. S.; Pasricha, R.; Mandale, A. B.; Sastry, M. *Langmuir*, **2004**, *20*, 7829.

15) a) Colvin, V. L.; Goldstein, A. N.; Alivisatos A. P. *J. Am. Chem. Soc*., **1992**, *114*, 5221. b) Colvin, V. L.; Alivisatos A. P.; Tobin, J. G. *Phys. Rev. Lett.*, **1991**, *66*, 2786. c) Gole, A.; Sainker, S. R.; Sastry, M. *Chem. Mater.*, **2000**, *12*, 1234. d) Bandopadhyay, K.; Patil, V.; Vijaymohanan, K.; Sastry, M. *Langmuir*, **1997**, *13*, 5244.

16) a) Sohn, B. H.; Seo, B. H. *Chem. Mater.*, **2001**, *13*, 1752.

17) a) McMillan, R. A.; Paavola, C. D.; Howard, J.; Chan, S. L.; Zaluzec, N. J.; Trent. *Nat. Mater.*, **2002**, *1*, 247. b) Shenton, W.; Pum, D.; Sleytr, U. B.; Mann, S. *Nature*, **1997**, *389*, 585. c) Mertig, M.; Kirsch, R.; Pompe, W.; Engelhardt, H. *Eur. Phys. J. D*, **1999**, *9*, 45. d) Wahl, R.; Mertig, M,; Raff, J.; Pobell, S. S.; Pompe, W. *Adv. Mater.*, **2001**, *13*, 736. e) Lam, S. S.; Harauz, G.; Beveridge, T. J. *J. Bacteriol.*, **1992**, *174*, 7971. f) Dieleuweit, S.; Pum, D.; Sleytr, U. B. *Supramol. Sci.*, **1998**, *5*, 15.

18) a) Muramatsu, K.; Takahashi, M.; Tajima, K.; Kobayashi, K. *J.Colloid Interface Sci.*, **2001**, *242*, 127. b) Lee, D.K.; Kang, Y.S.; Lee, C.S.; Stroeve, P. *J.Phys.Chem.B*, **2002**,*106*, 7267. c) Patil, V.; Mayya, K. S.; Pradhan, S. D.; Sastry, M. *J. Am. Chem. Soc.*, **1997**, *119*, 9281. d) Sastry, M.; Mayya, K. S.; Patil, V. *Langmuir*, **1998**, *14*, 5291. e) Mayya, K. S.; Patil, V.; Sastry, M. *Langmuir*, **1997**, *13*, 2575. f) Sastry, M.; Mayya, K. S.; Patil, V.; Paranjape, D. V.; Hegde, S. G. *J. Phys. Chem. B*, **1997**, *101*, 4954. g) Mayya, K. S.; Patil, V.; Sastry, M. *J. Chem. Soc. Faraday Trans.*, **1997**, *93*, 3377. h) Mayya, K. S.; Sastry, M. *J. Phys. Chem. B*, **1997**, *101*, 9790. i) Mayya, K. S.; Sastry, M. *Langmuir*, **1998**, *14*, 2575. j) Mayya, K. S.; Patil, V.; Kumar, P. M.; Sastry, M. *Thin Solid Films*, **1998**, *312*, 308. k) Sastry, M.; Mayya, K. S. *J. Nanopart. Res.*, **2000**, *2*, 183.

19) a) Furlong, D.N.; Urquhart, R.S.; Grieser, F.; Matsuura, K.; Okahata, Y. *J.Chem.Soc.,Chem.Commun.*, **1995**, 1329. b) Paranjape, D.V.; Sastry, M.; Ganguly, P. *Appl.Phys.Lett.*, **1993**, *63*, 18. c) Amm, D.T.; Johnson, D.; Laursen, T.; Gupta, S.K. *Appl.Pys.Lett.*, **1992**, *61*, 522. d) Taylor, D.M.; Lambi, J.N. *Thin Solid Films*, **1994**, *243*, 384. e) Seidl, M.; Schurr, M.; Brugger, A.; Volz, E.; Voit, H.

Appl.Phys.A, **1999**, 68, 81. f) Amm, D.T.; Johnson, D.J.; Matsuura, N.; Laursen, T.; Palmer, G. *Thin Solid Films*, **1994**, *242*, 74. g) Sastry, M. *Colloids and Colloid Assemblies : Synthesis, Modification, Organization and Utilization of Colloid Particles*, F. Caruso (ed.), Wiley-VCH, Berlin, Chapter 12, **2003**.

20) Ganguly, P.; Sastry, M.; Pal S.; Shashikala, M.N. *Langmuir*, **1995**, *11*, 1078.

21) a) Mandal, S.; Damle, C.; Sainkar, S. R.; Sastry, M. *J. Nanosci. Nanotechnol.*, **2001**, *1*, 281. b) Mandal, S.; Sainkar, S. R.; Sastry, M. *Nanotechnology*, **2001**, *12*, 358. c) Kumar, A.; Damle, C.; Sastry, M. *Appl. Phys. Lett.*, **2001**, *79*, 3314. d) Damle, C.; Biswas, K.; Sastry, M. *Langmuir*, **2001**, *17*, 7156. e) Mandal, S.; Phadtare, S.; Selvakannan, PR.; Pasricha R.; Sastry M. *Nanotechnology* **2003**, *14*, 878.

22) a) Patil, V.; Mayya, K. S.; Sastry, M. *Langmuir*, **1998**, *14*, 2707. b) Sastry, M.; Patil, V.; Mayya, K. S. *Langmuir*, **1997**, *13*, 4490. c) Sastry, M.; Patil, V.; Sainkar, S. R. *J. Phys. Chem. B*, **1998**, *102*, 1404. d) Patil, V.; Sastry, M. *Langmuir*, **2000**, *16*, 2207. e) Patil, V.; Sastry, M. *Langmuir* **1997**, *13*, 5511. f) Patil, V.; Malvankar, R. B.; Sastry, M. . *Langmuir*, **1999**, *15*, 8197. g) Patil, V.; Sastry, M. *J. Chem. Soc., Faraday Trans.*, **1997**, *93*, 4347.

23) a) Gole, A.; Dash, C.; Rao, M.; Sastry, M. *J. Chem. Soc., Chem. Commun.*, **2000**, 297. b) Gole, A.; Dash, C.; Mandale, A. B.; Rao, M.; Sastry, M. *Anal. Chem.*, **2000**, *72*, 4301. c) Gole, A.; Sastry, M. *Biotechnol. Bioeng.*, **2001**, *74*, 172. d) Gole, A.; Chaudhari, P.; Kaur, J.; Sastry, M. *Langmuir*, **2001**, *17*, 5646. e) Gole, A.; Vyas, S.; Sainkar, S. R.; Lachke, A. L.; Sastry, M. *Langmuir*, **2001**, *17*, 5964-5970. f) Phadtare, S.; Parekh, P.; Gole, A.; Patil, M.; Pundle, A.;Prabhune, A.; Sastry, M. *Biotechnol. Prog.*, 2002, *18,* 483.

24) a) Sastry, M.; Ramakrishnan, V.; Pattarkine, M.; Ganesh, K. N. *J. Phys. Chem. B*, **2001**, *105*, 4409. b) Sastry, M. *Trends Biotech.*, **2002**, *20*, 185.

25) Mukherjee, P.; Senapati, S.; Mandal, D.; Ahmad, A.; Khan, M. I.; Kumar, R.; Sastry, M. *ChemBioChem.*, **2002**, *5*, 461.

26) G. Sauerbrey, *Z. Phys*., **1959**, *155*, 206.

27) Stoscheck, C.M., *Met. Enzymology*, **1990**, *182*, 50.

28) Connolly, S.; Rao, S. N.; Fitzmaurice, D. *J. Phys. Chem. B*, **2000**, *104***,** 4765.

29) Link, S.; El-Sayed, A. M., *Int. Rev. Phys. Chem.*, **2000**, *19*, 409.

30) a) Gole, A.; Dash, C.; Ramakrishnan, V.; Sainkar, S.R.; Mandale, A.B.; Rao, M.; Sastry, M. *Langmuir*, **2001**, *17*, 1674. and references therein. b) Kumar, C.V., and McLendon, G.L., *Chem. Mater.*, **1997**, *9*, 863.

31) Ohara, P. C.; Heath, J. R.; Gelbart, W. M. *Angew. Chem. Int. Ed. Engl.*, **1997**, *36*, 1077.

32) Burns, G. P. *J. Appl. Phys.*, **1989**, *65*, 2095.

33) Yoldas, B. E.; O'Keeffe, T. W. *Appl. Opt.*, **1979**, *18*, 3133.

34) Butler, M. A.; Ginley, D. S. *J. Mater. Sci.*, **1980**, *15*, 19.

35) a) Carlson, T.; Giffin, G. L. *J. Phys. Chem.*, **1986**, *90*, 5896. b) Fujishima, A.; Honda, K. *Nature*, **1972**, *238*, 37. c) Mills, A.; Hunte, S. L. *J. Photochem. Photobiol. A*, **1997**, *108*, 1. d) Hoffmann, M. R.; Martin, S. T.; Choi, W.; Bahnemann, D. W. *Chem. Rev.*, **1995**, *95*, 69.

36) Matsunaga, T.; Tomoda, R.; Nakajima, T.; Komine, T. *Appl. Environ. Microbiol.*, **1988**, *54*, 330.

37) Wang, R.; Hashimoto, K.; Fujishima, A. *Nature*, **1997**, *388*, 431.

38) Borenstain, S. I.; Arad, U.; Lyubina, I.; Segal, A.; Warschawer, Y. *Thin Solid Films* **1999**, *75*, 2659.

39) a) Peercy, P. S. *Nature* **2000**, *406*, 1023. b) Wang, D.; Masuda, Y.; Seo, W. S.; Koumoto, K. *Key Eng. Mater.*, **2002**, *214*, 163.

40) a) Takahashi, Y.; Ogiso, A.; Tomoda, R.; Sugiyama, K.; Minoura, H.; Tsuiki, M. *J. Chem. Soc., Faraday Trans. 1*, **1982**, *78*, 2563. b) Ferroni, M.; Guidi, V.; Martinelli, G.; Nelli P.; Sberveglieri, G. *Sensors and Actuators B: Chemical*, **1997**, *44*, 499.

41) Bechinger, C.; Ferrere, S. ; Zaban, A.; Sprague, J.; Gregg, B. A. *Nature*, **1996**, *383*, 608.

42) Birkby, I.; Stevens, R.; *Key Eng. Mat.*, **1996**, *122*, 527.

43) Minh, N. Q., *J. Am. Ceram. Soc.*, **1993**, *76*, 563.

44) Copel, M.; Gribelyuk, M.; Gusev, E. *Appl.Phys .Lett.*, **2000**, *76*, 436.

45) Xie, Y., *J. Am. Ceram. Soc.*, **1999**, *82*, 768.

46) a) Yamaguchi, T. *Catal. Today* **1994**, *20*, 199. b) Corma, A. *Chem. Rev.*, **1995**, *95*, 559.

47) a) Colvin, V. L.; Schlamp, M. C.; Alivisatos, A. P. *Nature*, **1994**, *370*, 354. b) Dabbousi, B. O.; Bawendi, M.G.; Onitsuka, O. *App. Phys. Lett*., **1995**, *66*, 1316.

48) Pavesi, L.; Negro, L. D.; Mazzoleni, C.; Franzo, G.; Priolo F. *Nature*, **2000,** *408*, 440.

49) Grazel, C. K.; Gratzel, M. *J. Am. Chem. Soc.*, **1979**, ***101***, 7741.

50) Hagfeldt, A., Gratzel, M. *Chem. Rev.*, **1995**, *95*, 49.

51) Bruchez, Jr M.; Moronne, M.; Gin, P.; Weiss, S.; Alivisatos, A. P. *Science*, **1998**, *281*, 2013.

52) Kumar, P.M.; Badrinarayanan, S.; Sastry, M. *Thin Solid Films*, **2000**, *358*, 122.

53) Lopez, E. F.; Escribano, V. S.; Panizza, M.; Carnascialic, M. M.; Busca, G. *J. Mater. Chem.*, **2001**, *11*, 1891.

54) Valov, I.; Stoychev, D.; Marinova, Ts. *Electrochimica Acta*, **2002**, *47*, 4419.

55) a) Santacesaria, E.; Tonello, M.; Storti, G.; Pace R. C.; Carra, S. J. *J. Colloid Interface Sci.*, **1986**, *111*, 44. b) Matijevic, E.; Budnick M.; Meites, L. *J. Colloid Interface Sci*., **1977**, *61*, 302. c) Bekkerman, L. I.; Dobrovol'skii I. P.; Ivakin, A. A. *Russ. J. Inorg. Chem.,* **1976**, *21*, 223. d) Chemseddine A.; Moritz, T. *Eur. J. Inorg. Chem.,* **1999**, *2*, 235. e) Bischoff B. L.; Anderson, M. A. *Chem. Mater.* **1995**, *7*, 1772. f) Arnal, P.; Corriu, J. P. R.; Leclercq, D.; Mutin P. H.; Vioux, A. *J. Mater. Chem.*, **1996**, *6*, 1925. g) Arnal, P.; Corriu, J. P. R.; Leclercq, D.; Mutin P. H.; Vioux, A. *Chem. Mater.*, **1997**, *9*, 694.

56) a) Music, S.; Gotic, M.; Ivanda, M.; Popovic, S.; Turkovic, A.; Trojko, R.; Sekulie A.; Furie, K. *Mater. Sci. Eng., B*, **1997**, *47*, 33. b) Bokhimi, X.; Morales, A.; Novaro, O.; Lopez, T.; Sanchez E.; Gomez, R. *J. Mater. Res.*, **1995**, *10*, 2788.

57) Jalava, J. P.; Heikkila, L.; Hovi, O.; Laiho, R.; Hiltunen, E.; Hakanen A.; Harma, H. *Ind. Eng. Chem. Res.*, **1998**, *37*, 1317.

58) Keesmann, I. *Z. Anorg. Allg. Chem.*, **1966**, *346*, 31.

59) Kominami, H.; Kohno M.; Kera, Y. *J. Mater. Chem.*, **2000**, *10*, 1151.

60) Woudenberg, F. C. M.; Sager, W. F. C.; Sibelt, N. G. M.; Verweij H. *Adv. Mater.* **2001**, *13*, 514.

61) Cuvillier, N.; Rondelez, F. *Thin Solid Films*, **1998**, *19*, 327.

62) Brus L. E. *J. Chem. Phys.*, **1984**, *80*, 4403.

63) Takuya, N.; Bunsho, O.; Kohei, U. *J. Phys. Chem. B*, **1998**, *102*, 1571.

64) Razik, N. *J. Mater. Sci. Lett.* **1987**, *6*, 1443.

Chapter VII

Conclusions

This chapter contains concluding remarks on the salient features of the work described in the thesis and future potential developments in the area.

7.1 Summary of the work.

The main emphasis of the work presented in this thesis has been to demonstrate the synthesis of metal nanoparticles using plant extracts as an environmentally benign alternative to chemical methods and the fabrication of thin films of inorganic nanoparticles using thermally evaporated lipid films. The aspects that have been covered in this thesis are: 1) Synthesis of gold and silver nanoparticles using extracts from different parts of the plant geranium and using neem leaf extract, 2) synthesis and the study of the formation of triangular and hexagonal gold particles using lemongrass leaf extract, 3) study of the growth of gold nanotriangles using citric acid reduction method as a model system and the effect of halide ions on their formation and on preformed gold nanotriangles, 4) shape transformation of gold nanotriangles on laser irradiation and 5) fabrication of thin films of inorganic nanoparticles by entrapment of the charged nanoparticles or the precursor metal ions in thermally evaporated lipid films.

Synthesis of stable silver and gold nanoparticles using extracts of geranium leaf, stem and root was demonstrated to be a rapid process when compared with the parallel biosynthetic process using microorganisms that require 2 – 4 days for the same. While synthesis of silver nanoparticles could be achieved within 3 h using geranium root extract, gold nanoparticles could be synthesized in just 10 min using geranium stem extract. The majority of the silver and gold nanoparticles synthesized by this route were observed to be spherical and polydisperse that varied in size between 8 – 40 nm. Synthesis of gold nanoparticles using extracts of different parts of geranium was shown to be accompanied by a small percentage of gold nanotriangles and hexagons. On using geranium leaf extract as reducing agent, even a small percentage of gold nanorod formation was observed. Similarly using neem leaf extract as reducing agent a rapid synthesis of silver and gold nanoparticles and bimetallic Au-Ag nanoparticles was demonstrated. Flat gold nanoparticles were also observed to be formed in small fraction along with the spherical gold nanoparticles on using neem leaf extract as a reducing agent. A clear indication of the propensity of the plant extract to direct the shape of the nanoparticles was demonstrated. Synthesis of silver nanoparticles using the extracts from different parts of the plant geranium was shown to be always accompanied with partial precipitation of AgCl due to the presence of Cl^- ions in the plant extracts. Based on the

functional group characterization by FTIR analysis, the biomolecules responsible for the reduction and stability of the metal nanoparticles was proposed to be some reducing sugars and terpenoids present in large percentage in the plant extracts. Further, using lemongrass leaf extract as a reducing agent, large percentage of triangular and hexagonal gold particles was achieved. The triangular and hexagonal gold particles were shown to apparently grow by an initial formation of spherical nuclei followed by their assembly and room temperature sintering. It was demonstrated that by simple variation of the amount of lemongrass leaf extract used for the reduction of $AuCl_4^-$ ions, the size of the triangular and hexagonal gold particles could be controlled. With increasing amount of the lemongrass leaf extract used for reduction, the average size of the flat gold particles was observed to decrease along with the formation of greater percentage of spherical gold nanoparticles. By controlling the average size of the triangular and hexagonal gold nanoparticles the optical absorption features in the NIR region could also be very well tuned. The high absorption in the NIR region by the triangular and hexagonal gold particles was tested for their possible applications in NIR blocking optical coatings. It was demonstrated that the optical coatings of triangular and hexagonal gold particles on glass could considerably retard the rise in temperature across it.

The reinvestigation of the citric acid reduction method for the synthesis of gold nanotriangles has shown that the evolution of the triangular shape in this case occurs by initial nucleation followed by its two dimensional growth. The formation of gold nanotriangles was observed to be favored at lower temperatures when the growth rate is also slow. On studying the citric acid reduction of $AuCl_4^-$ ions in presence of different halide ions it was demonstrated that Cl^- ions have a high tendency to promote the formation of gold nanotriangles. Br^- and I^- ions on the other hand have greater tendency to bind to the surface of gold and were observed to inhibit the formation of gold nanotriangles to different extents. It was proposed that Cl^- ions having the ability to chemisorb on the (111) lattice of fcc gold with a hexagonal closed packed structure could be responsible for the formation of <111> oriented gold nanotriangles and nanohexagons. The prominent effect of the halide ions has been further demonstrated by their ability to induce morphological transformation even in preformed gold nanotriangles. Br^- ions were demonstrated to transform the triangular and hexagonal gold nanoparticles to disc-

like morphology with irregular edges due to their preferential chemisorption on the edges. In comparison, I^- ions were observed to completely transform the triangular and hexagonal gold nanoparticles into spherical morphologies. The shape transformation has been attributed to the strain induced by the surface adlayer of I^- ions on the underlying lattice of gold. Shape transformation has also been demonstrated by laser irradiation using 20 ns pulses and wavelength 1064 nm. The gold nanotriangles were observed to undergo both melting and fragmentation on irradiation.

In the last part of the thesis immobilization of gold nanoparticles synthesized using the fungus, *Fusarium oxysporum* and the leaf extract of geranium into thin films of cationic and anionic lipid thin films have been demonstrated. The immobilization of gold nanoparticles into both cationic and anionic lipid thin films was facilitated by the charge switching of the capping biomolecules on varying the pH of solution. The protein capping of the *Fusarium oxysporum* synthesized gold nanoparticles apparently had a pI of 5.5 and thus could be immobilized into anionic stearic acid thin film below pH 5.5 and into cationic octadecylamine thin films above pH 5.5. An interesting shape selectivity of the stearic acid and octadecylamine thin films has also been demonstrated. It was observed that the stearic acid thin films had a tendency towards preferential immobilization of larger sized spherical and flat gold nanoparticles whereas the octadecylamine thin films had a propensity towards immobilizing only smaller size spherical gold nanoparticles. The thin film based method was further utilized for the synthesis of nanoparticulate thin films of metal oxides like titania and zirconia and of semiconducting quantum dots of cadmium sulfide. The synthesis of these nanoparticles within lipid thin films was demonstrated by initial electrostatic entrapment of the precursor metal ions. Titania and zirconia nanoparticles were synthesized within thermally evaporated thin films of octadecyl amine by hydrolyzing the electrostatically entrapped TiF_6^{2-} and ZrF_6^{2-}. Similarly CdS quantum dots were synthesized by electrostatically entrapping the Cd^{2+} ions in thermally evaporated sodium bis(2-ethylhexyl)sulfosuccinate thin films followed by their treatment with Na_2S solution. Using this method it was demonstrated that a range of inorganic nanoparticles can either be entrapped or synthesized in confined spaces using non-specific electrostatic interactions.

7.2 Scope for future work.

The synthesis of triangular and hexagonal gold particles is an interesting result and can have many potential applications. It would be interesting to use these gold particles having high absorbance in the NIR region for hyperthermic treatment of cancerous cells. Since the body tissues can sufficiently transmit light in the range 800 – 1100 nm, irradiation of suitably surface modified gold nanotriangles, selectively localized near the cancerous tissue, may kill the cells in the local vicinity.

In the study of gold nanotriangle, though the importance of Cl^- ions has been demonstrated, it is worth noting that gold nanoparticles synthesized by various methods described in this thesis show a prominent presence of Au(I) species from the XPS measurements. The presence of Au(I) and their role in the surface composition would be worth following. Studies carried out in case of gold nanorods have demonstrated that the addition of Ag^+ ions greatly enhances their formation [1-4]. It thus seems likely that cationic heavy metal ions have an important role in providing stability to the surface. Many important insights regarding the surface chemistry of nanoparticles may be gained by trying to understand the subtle role of these cations.

7.3 References:

1) Chang, S. S.; Shih, C. W.; Chen, C. D.; Lai, W. C.; Wang, C. R. C. *Langmuir* **1999**, *15*, 701.
2) Jana, N. R.; Gearheart, L.; Murphy, C. J. *Adv. Mater.* **2001**, *13*, 1389.
3) Kim, F.; Song, J. H.; Yang, P. *J. Am. Chem. Soc.* **2002**, *124*, 14316.
4) Nikoobakht, B.; El-Sayed, M. A. *Chem. Mater.* **2003**, *15*, 1957.

List of Publications

1) **Shankar**, **S. S.**; Rautaray, D.; Pasricha, R.; Pavaskar, N. R.; Mandale, A. B.; Sastry, M. *J. Mater. Chem.* **2003**, *13*, 1108–1111.
2) **Shankar**, **S. S.**; Joshi, H.; Pasricha, R.; Pavaskar, N. R.; Mandale, A. B.; Sastry, M. *J. Colloid Interface Sci.* **2004**, *269*, 126-130.
3) **Shankar**, **S. S.**; Chatterjee, S.; Sastry, M. *PhysChemComm.* **2003**, *6*, 36-39.
4) **Shankar**, **S. S.**; Ahmad, A.; Pasricha, R.; Sastry, M. *J. Mater. Chem.* **2003**, *13*, 1822–1826.
5) **Shankar**, **S. S.**; Ahmad, A.; Sastry, M. *Biotechnol. Progr.* **2003**, *19*, 1627-1631.
6) **Shankar**, **S. S.**; Ahmad, A.; Pasricha, R.; Khan, M. I.; Kumar, R.; Sastry, M. *J. Colloid Interface Sci.* **2004**, *274*, 69-75.
7) **Shankar**, **S. S.**; Rai, A.; Ahmad, A.; Sastry, M. *Applied Nanoscience* **2004**, *1*, 69-77.
8) **Shankar**, **S. S.**; Rai, A.; Ahmad, A.; Sastry M. *J. Colloid Interface Sci.* **2004**, *275*, 496-502.
9) Rautaray, D.; Sinha, K.; **Shankar**, **S. S.**; Adyanthaya, S. D.; Sastry, M. *Chem. Mater.* **2004,** *16,* 1356-1361
10) **Shankar**, **S. S.**; Rai, A.; Ankamwar, B.; Singh, A.; Ahmad, A.; Sastry, M. *Nat. mater.* **2004**, *3*, 482-488.
11) **Shankar**, **S. S.**; Patil, U. S.; Prasad, B. L. V.; Sastry, M. *Langmuir* **2004**, *20*, 8853-8857.
12) **Shankar**, **S. S.**; Rai, A.; Ahmad, A.; Sastry, M. *Chem. Mater.* **2005**, 17, 566.
13) **Shankar**, **S. S.**; Bhargava, S.; Sastry, M. *J. Nanosci. Nanotechnol.* **2005**, *5*, 1721.